JAMES COOK UNIVERSITY

A MULTI-FREQUENCY ANALYSIS OF RADIO SUPERNOVA REMNANTS AND THEIR ENVIRONMENTS IN SCULPTOR GROUP SD GALAXY NGC 300 AND THE SMALL MAGELLANIC CLOUD

A THESIS SUBMITTED TO THE
FACULTY IN CANDIDACY FOR THE DEGREE OF
DOCTOR OF PHILOSOPHY IN ASTRONOMY

CENTRE FOR ASTRONOMY

BY

JEFFREY LYNN PAYNE, B. S., M. ASTRON., M. D.

Townsville, QLD, 4811, Australia

APRIL, 2008

To Miroslav Filipović and Graeme White for their heroic work

in the developement of Internet based Astronomy Education.

STATEMENT OF ACCESS

I, Jeffrey Lynn Payne, author of this work, understand that James Cook University will make this thesis available for use within the University Library and, via the Australian Digital Theses network, for use elsewhere.

I understand that, as an unpublished work, a thesis has significant protection under the Copyright Act and; I do not wish to place any further restriction on access to this work.

Jeffrey Lynn Payne

Date

STATEMENT OF SOURCES

DECLARATION

I declare that this thesis is my own work and has not been submitted in any form for another degree or diploma at any university or other institution of tertiary education.
Information derived from the published or unpublished work of others has been acknowledged in the text and a list of references is given.

Jeffrey Lynn Payne _____ Date _____

CONTRIBUTION OF OTHERS

Chapter 1

The introduction to this thesis was originally reviewed by Miroslav Filipović, my advisor, and Graeme White. I wish to thank them for their time and useful suggestions.

Chapter 2

Chapter 2 was originally published as a "Multi-frequency Study of extragalactic supernova remnants and H II regions. Sculptor group Sd galaxy NGC 300", in Astronomy and Astrophysics, 2004, volume 425, pages 443–456. In this paper, I analysed and presented multi-wavelength data, including radio data from the Australia Telescope Compact Array and the Very Large Array (VLA). The Compact Array data was originally obtained and reduced by M. D. Filipović, P. A. Jones, N. Duric and G. L. White. The VLA data was obtained from T. G. Pannuti. I reduced and analysed X-ray observations obtained from the *XMM-Newton* Science Operations Centre archive at http://xmm.vilspa.esa.es/ . W. Pietsch and A. Read allowed me to use their *ROentgen SATellite* (*ROSAT*) image of NGC 300 for analysis. W. Blair graciously provided me with [S II] and Hα images of NGC 300 used in Blair & Long (1997). Those Los Campanas Observatory observations were transferred from tape and sent to me at his request. Finally, E. M. Berkhuijsen deserves heartfelt thanks for her advice and kind patience.

Chapter 3

Chapter 3, originally entitled, "An ATCA radio-continuum study of the Small Magellanic Cloud - II. Source identification and classification" was published in 2004 by the Monthly Notices of the Royal Astronomical Society (MNRAS, volume 355, pages 44–50). In this paper, I finalized the criteria used to classify all of the radio sources and compiled the published version of the catalogue ('Table 2') which presented this information. I also analysed and presented the statistics of all radio background sources. The original Compact Array observations and reductions of the Small Magellanic Cloud (SMC) radio images are presented in Filipović et al. (2002). They analysed the sources with respect to location and flux density, providing an initial cross-identification and classification scheme. This preliminay work by W. Reid and T. Bohlsen was part of the final semester project of the Astronomy Internet Masters (AIM) course at the University of Western Sydney.

Chapter 4

The original version of Chapter 4 can be found in the MNRAS entitled, “An ATCA radio-continuum study of the Small Magellanic Cloud - III. Supernova remnants and their environments”, volume 364, pages 217–236. This work builds on the SMC data presented in Chapter 3. C. W. Danforth provided subtraction images using a relatively simple technique I could easily modify. W. Reid provided initial notes about known SNRs that I was able to condense in an appendix of the published version. The remainder of the analysis and presentation of statistics is mine, but in addition to my advisor, M. D. Filipović, John Dickel and P. A. Jones also provided extremely valuable suggestions which greatly enhanced the final draft of this work.

Chapter 5

The optical spectral observations, reduction and analysis presented in Chapter 5 are mine, based on previous work found in Dopita et al. (1984) and Smith et al. (1993). This chapter was originally published in the MNRAS, volume 376, pages 1793–1804. I thank the Australian National University Research School of Astronomy and Astrophysics for granting me time on the 2.3-meter Double Beam Spectrograph (DBS) at Siding Spring Observatory. Graeme White graciously assisted me with those observations. M. D. Filipović and I were granted observation time at the South African Astronomical Observatory (SAAO). Our travel to the SAAO was funded by Australian Government ANSTO (Australian Nuclear Science and Technology Organisation) grant number 05/06-O-11. Hα images used for these observations were from C. W. Danforth.

ACKNOWLEDGMENTS

Radio images used in this thesis were created by the Australia Telescope Compact Array (ATCA). This facility is part of the Australia Telescope, founded by the Commonwealth of Australia for operation as a National Facility managed by Australia's Commonwealth Scientific and Industrial Research Organisation (CSIRO).

I made use of the Karma and the Multi-Channel Image Reconstruction, Image Analysis and Display (MIRIAD) software packages developed by the Australia Telescope National Facility (ATNF). X-ray reduction and analysis was accomplished using the Science Analysis Software (SAS) package developed for *XMM-Newton*. X-ray spectral analysis required the use of XSPECT, a program found within the High Energy Astronomy Software (HEAsoft) package developed by the National Space and Aeronautics Administration (NASA).

Digitized Sky Survey 2-Red (DSS2-R) plates used are based on photographic data obtained using the UK Schmidt Telescope. The UK Schmidt Telescope was operated by the Royal Observatory Edinburgh, with funding from the UK Science and Engineering Research Council, until 1988 June, and thereafter by the Anglo-Australian Observatory. Original plate material is copyright (c) of the Royal Observatory Edinburgh and the Anglo-Australian Observatory. The plates were processed into the present compressed digital form with their permission. The DSS was produced at the Space Telescope Science Institute (STScI) under US Government grant NAG W-2166.

I used combined Hα (4×300 s) Cerro Tololo Inter-American Observatory (CTIO) 0.9-meter images to show spectral slit locations. These $\sim 0.4''$ images from Cheng et al. (1993) are described in greater detail in Chapter 5.

Optical spectra were reduced and analysed using Image Reduction and Analysis Facility (IRAF) software. IRAF is distributed by the National Optical Astronomy Observatories, which are operated by the Association of Universities for Research in Astronomy, Inc., under cooperative agreement with the National Science Foundation.

ABSTRACT

While observations and analysis of supernova remnants (SNRs) located within the Milky Way Galaxy have been extensive, severe limitations have been imposed by massive photoelectric absorption along the Galactic plane and significant uncertainties in distance. Alternatively, the study of extragalactic SNRs offers a unique opportunity to examine them at a relatively known distance without Galactic plane interference. Here, I present multi-frequency identification and analysis of radio SNRs and their local envirnments in the direction of NGC 300 and the Small Magellanic Cloud (SMC). Using both Australia Telescope Compact Array (ATCA) and Very Long Array observations, 18 radio SNRs (with 3 radio candidate SNRs and one microquasar candidate) were identified in NGC 300 based on selection criteria including spectral index and cross identification with optical and X-ray sources. X-ray co-identifications include those found in newly reduced data from the *XMM-Newton* archive and use of X-ray spectral models and hardness ratios. Five of these 18 radio remnants are associated with reported optical remnants, 3 have X-ray counterparts and 12 are found in archived [S II] images. The 1.374 GHz luminosity function suggests that only the brightest SNRs are seen and correlations with OB associations or H II regions suggest they originate within star forming regions. In the SMC, multi-wavelength identification criteria identified a total of 21 radio SNRs (16 known and 5 new candidates). Out of a total of 717 SMC radio sources found using the ATCA, 71 are classified as H II regions, 616 as background objects, 2 as microquasar candidates and 2 as planetary nebulae. Followup optical spectra also confirmed one of the radio candidates as an SNR. Statistics for SNRs, H II regions and background objects are presented for both galaxies; extensively for the SMC. These statistics suggest that for this mature population of remnants, radio brightness and density/abundance-sensitive optical spectral line intensities are not directly related to diameter, but rather reflect the local interstellar environment. An average of their 'metal' abundances ($10^{-4.1}$), based on these optical line intensities, agree with those previously reported for the SMC, obtained by other methods. Observations of extragalactic SNRs reflect both their nature (progenitor) and their nurture (environment) since in the evolution of their life cycle, the two cannot be separated.

TABLE OF CONTENTS

LIST OF TABLES

LIST OF FIGURES

PUBLISHED PAPERS NOT PART OF THIS THESIS

In addition to the work presented here, I have contributed significantly to the following papers during my Ph.D. training:

i. "Long-slit optical spectroscopy of Large Magellanic Cloud radio supernova remnants", published in the Monthly Notices of the Royal Astronomical Society (MNRAS), 2008, volume 383, pages 1175–1194. Authors include J. L. Payne, G. L. White and M. D. Filipović. Similar to Chapter 5 presented here, this work examines the optical spectra from a set of radio SNRs in the LMC. Abundance and density-sensitive line ratios are not felt to be related to individual SNR evolution; rather they reflect the local interstellar environment.

ii. "Multi-frequency study of the Large Magellanic Cloud supernova remnant (SNR) B0513-692 and new SNR candidate J051327-6911", published in MNRAS, 2007, volume 378, pages 1237–1247. Authors include I. S. Bojičić, M. D. Filipović, Q. A. Parker, J. L. Payne, P. A. Jones, W. Reid, A. Kawamura and Y. Fukui. This paper presents a multi-wavelength study of radio supernova remnant LMC B0513-692, an unrelated radio compact H II region (J051324-691049) located at its northwestern edge and a new SNR candidate, J051327-6911, located at its northeastern edge.

iii. "The super-soft source XMMU J052016.0-692505 in the LMC. A likely white dwarf Be/X-ray binary", published in Astronomy & Astrophysics, 2006, volume 458, pages 285–292. Authors include P. Kahabka, F. Haberl, J. L. Payne and M. D. Filipović. This paper reports the discovery of the super-soft X-ray source XMMU J052016.0-692505 using *XMM-Newton*.

iv. "Extragalactic Multi-frequency Searches for Supernova Remnants", a poster published in Supernovae: One Millennium After SN1006, 26th meeting of the IAU (2006IAUJD, discussion 9, number 45). Authors include J. L. Payne, M. D. Filipović and G. L. White. This poster reviews recent multi-frequency searches for SNRs in the Magellanic Clouds, NGC 300 and NGC 7793.

v. "An ATCA radio-continuum study of the Small Magellanic Cloud - IV. A multi-frequency analysis of the N66 region", published in MNRAS, 2006, volume 367, pages 1379–1393. Authors include W. A. Reid, J. L. Payne, M. D. Filipović, C. W. Danforth, P. A. Jones, G. L. White and L. Staveley-Smith. This paper uses optical spectroscopy, archived *Chandra* images and radio subtraction techniques to study the SMC N S66 H II region. This is divided into 10 components, composed separately of SNRs and H II regions.

vi. “A Radio-Continuum Study of the Supernova Remnant MSH 11-61A”, published in the Serbian Astronomical Journal, 2005, volume 170, pages 47–56. Authors include M. D. Filipović, J. L. Payne and P. A. Jones. This paper uses X-ray, radio-continuum and CO data to study the morphology and kinematics of MSH 11-61A.

vii. “Multi-Frequency Study of Supernova Remnants and H II Regions in NGC 300”, published electronically 2005, in “X-ray and Radio Connections” (eds. L. O. Sjouwerman and K. K. Dyer) by the National Radio Astronomy Observatory (NRAO), http://www.aoc.nrao.edu/events/xraydio . Authors include J. L. Payne, M. D. Filipović, T. G. Pannuti, P. A. Jones, N. Duric, G. L. White and S. Carpano. This was a preliminary version of Chapter 2.

CHAPTER 1

INTRODUCTION TO SUPERNOVA REMNANTS

Supernova Remnants (SNRs) are the result of some of most powerful events known to man. Under certain conditions, at the end of a star's life, a massive explosion releases 10^{53} ergs of energy in an event known as a supernova (SN). While ninety-nine percent of this energy is released as neutrinos, the remaining one percent (10^{51} ergs) propels the star's outer shell into the ambient medium by mechanical energy.

The study of SNRs have much to offer in our understanding of the mechanisms by which stars deposit the products of nuclear fusion to the interstellar medium (ISM). They are intimately tied to the evolution of a galaxy through recurring cycles of stellar evolution, from star birth to death. Extragalactic SNR research not only give information about the galaxies that are studied, but also our own Galactic SNRs whose research is impeded by light absorption, location and distance uncertainties.

Identification of extragalactic SNRs using multi-wavelength selection criteria is only one of the goals of this thesis. SNRs are connected to their local ISM environment, perhaps much more so than we normally think. The reason that we cannot separate these sources from their local ISM is because by the time we can detect them, they are mostly composed of local ISM. Thus, SNRs are really a combination of verb and noun; slightly dusty supernova kinetics combined with the local ISM.

With these ideas in mind, the goals of this thesis include:

1. identification of radio SNRs in NGC 300 and the SMC using multi-frequency selection criteria. This includes radio spectral index, location, extension and morphology with co-identifications in the optical and X-ray domains. I also examine the optical and X-ray spectra of their counterparts when possible.

2. use of luminosity function to determine completeness of each sample set.

3. determination of SNR environment by proximity to ISM dense regions such as OB associations and H II regions. This includes examination of radio subtraction images where Hα flux associated with thermal H II regions have been mathematically removed.

4. contrasting detection of SNRs in each electromagnetic domain with these local environments and likely progenitor type.

5. comparison of SNR properties such as diameter in different electromagnetic domains.

6. examination of statistics which attempt to map the evolution of SNRs according to diameter and brightness (e.g. $\Sigma \propto D$, $N(< D)$ relations and [N II]/Hα vs. λ6716/λ6731 ratio). Are these statistics related more to the local ISM as abundance calculations seem to imply.

7. identification and statistics of other interesting radio sources in the direction of target galaxies including H II regions, background sources, microquasars and planetary nebulae.

This chapter is a review of current research related to SNRs. Sections 1.1 through 1.4 define what SNRs are and how they originate. They also describe various classification schemes used to enhance the understanding of SNR origin and evolution. The classic model for SNR evolution is outlined in section 1.5.

The astrophysics of SNRs shocks are presented in section 1.6. These shocks are closely tied to radiative processes (section 1.7) as well as their suspected role in the production of cosmic rays. Radiative processes give rise to the electromagnetic radiation we measure here on Earth as described in section 1.8.

Many SNRs contain the remains of its stellar core, known as compact objects, which may have pulsar winds that create nebulae. The physics of these is discussed in section 1.9.

SNRs can be studied as a group through the examination and analysis of their statistics. Background information related to this is presented in section 1.10. Next, after a brief discussion of the difficulties of Galactic SNR research (section 1.11), subsection 1.11.3 outlines the contributions that the study of extragalactic SNRs can bring. The final section (1.12) in this chapter reviews the current 'state' of SNR observations in NGC 300 and the SMC. This will provide a transition to Chapter 2, which describes observations of SNRs in the southern galaxy, NGC 300.

1.1 What are SNRs and why are they important to astronomy?

SNRs are the remains of a star that ends its life with a massive explosion. The contents of a SNR may include the star's core, if present, in the form of a neutron star or black hole. SNRs contain elements formed during the explosion itself. By observing these remnants we can explore the astrophysical processes by which various wavelengths of light are emitted through their interaction with the environment. The magnetic field of the stellar progenitor and the ISM can also be studied. The evolution of SNRs allow us to study the circumstellar environment of the star before it exploded and the type of star that led to its formation.

1.2 What type of stars form SNRs?

A star that ends its life as a supernova is known as the progenitor star. Both low mass stars with less than 8 solar masses ($M_\odot$) of material and higher mass stars can become supernovae (SNe) leading to the formation of a SNR. However, the mechanism though which they become SNe is not the same.

Most stars have masses less than our Sun. These stars initially 'burn' hydrogen to helium via the process of fusion, releasing energy that prevent them from collapsing onto themselves under gravity. Through several additional fusion steps as the star evolves, their cores are converted to carbon. As described with the Hertzsprung-Russell diagram, these stars evolve through several stages to become red giants.

The maximum mass of the core[1] of evolved low mass stars is less than the Chandrasekhar limit of about 1.4 $M_\odot$ which allows electron degeneracy pressure to prevent it from collapsing further at the end of its life. This means that the remainder of the star's mass must be lost through stellar winds or gently lifted off at the end of its life forming a planetary nebulae.

In binary systems, the process of mass transfer from a less evolved star can cause a white dwarf to accumulate enough mass to cross the Chandrasekhar limit. Since the size of these objects is small and they are quite hot (10^4 K) with a nearly uniform temperature, these dead stars undergo a detonation event, completely destroying the white dwarf. This is believed to be the origin of Type Ia SNe.

Stars more massive than 8 $M_\odot$ have much more gravitational energy. This increased energy allows them to step through further exothermic nuclear reactions up to and including the production of iron. Beyond the iron group elements, all core reactions are endothermic, absorbing rather than generating energy. Thus, once the core is composed of iron, it no longer has a source of energy to support itself. This allows the star to collapse with most of the iron dissociating back into individual protons and neutrons until nuclear densities are reached. At this point the core becomes nearly rigid. The outer layers of the star falling inward rebound from the degenerate core, creating a core-collapse SNR in the wake of a massive supernova explosion.

1.3 Supernovae Classification

Although both high and low mass stars are associated with supernova events, the selection of an adequate taxonomy for these phenomena should fulfill the following criteria: mutual exclusion, exhaustiveness, non-ambiguity, repeatability and usefullness. Minkowski (1941) was the first to recognize that at least two main types of supernovae exist.

[1] The core is known as a white drawf.

Table 1.1 Properties of selected SNe types (expanded from Pannuti 2000 and Weiler & Sramek 1988). For clarity, Type IIb has been excluded since it is an intermediate between Types Ib/c and II (see text).

Property	Type Ia	Type Ib/c	Type II-P	Type II-L	Type II-n
Optical Spectrum	No H lines, deep 615.0 nm absorption	No H lines, no 615.0 nm absorption, He lines	H lines, complex spectra	H lines, complex spectra	H lines, narrow emission lines
Absolute Magnitude	−19	−17 to −17.5	≤ −17	≤ −17	≤ −17
Location	all galaxies	spirals and irregulars	spirals and irregulars	spirals and irregulars	spirals
Light Curve (B light)	sharp rise rapid decay	sharp rise rapid decay	sharp rise slow decay	sharp rise decay to plateau, slow decay	sharp rise very slow decay
Stellar Population	old	young	young	young	young
Example (Galaxy)	SN 1990N (NGC 4639)	SN 1983N (NGC 5236)	SN 1948B (NGC 6946)	SN 1979C (NGC 4321)	SN 1988Z (MCG+03-28-022)

Initially, the classification of SNe was based on observational information. Today, it is more based on the type of process leading to their formation (Turatto 2003). This is not to say that the present day classification is even close to satisfactory; schemes continue to evolve as we further understand each process involved.

Since the classification of SNe were initially based on visible light optical spectra and light curves, the outermost layer of these stars have been critical from the very beginning. Two main classes were identified on the basis of hydrogen lines in their spectra. Minkowski (1941) noted nine objects formed an "extremely homogenous group" he named "Type I". These had a considerably higher surface temperature than five other objects that he designated as "Type II". Type II SNe have hydrogen lines in their spectra and are thought to be formed from massive stars greater than 8 $M_{\odot}$.

In the mid-1980s, the presence of neutral helium (He I) in their light spectra allowed further classification of Type I SNe into those 'with' (Type Ib) and those 'without' (Type Ia) helium. Type Ib SNe were further divided (rather confusingly) into Type Ic ('without' both ionized silicon (Si II) and He I)[2], although the existence of these physically distinct types is currently in debate. Because of this controversy, they are usually grouped together as 'Type Ib/c'. Table 1.1, lists the most important SNe classes and their properties (Pannuti 2000).

It was not understood initially that Type Ia SNe were associated with a radically different process than

[2] It is the helium abundance, rather than absence, that distinguishes the two classes.

Type Ib/c or Type II SNe. Branch et al. (1995) notes that after a review of candidate progenitor binary systems of Type Ia SNe, these exploding stars were likely mass accreting carbon-oxygen white dwarfs. Type Ia SNe have a homogeneous spectroscopic and photometric behavior leading to their use as standard candles. They have recently been used by Turatto (2003) to determine the geometry of the universe.

SNe Ia are found in both elliptical and spiral galaxies, but not associated with the arms of spiral galaxies as frequently as other SNe types. Their spectra contain lines of calcium, oxygen, silicon and sulfur with a characteristic absence of hydrogen. In reality, each is not exactly homogeneous, but there is a correlation between their peak luminosity and light curve. In fact, there are several correlations which connect maximum luminosity with light curve shape, colour evolution, spectral appearance and host galaxy morphology (Leibundgut 2000). Their peak luminosity is associated with the amount of ^{56}Ni produced in the explosion (Turatto 2003), but at 150 days past maximum and beyond, all observed objects show the same decline rate and spectrum (Leibundgut 2000).

The explosion mechanism of Type Ia SN is an ongoing area of research. Paradigms currently under debate include models of pure deflagrations[3], delayed detonations, pulsating delayed detonations and sub-Chandrasekhar explosions (see Badenes et al. 2003 for a full explaination of these models). Badenes et al. (2003) note it is possible to identify the explosion mechanism from the spectra of young Type Ia SNRs if one takes the detailed ejecta structure into account. For example, comparison of models with observatons of the Tycho SNR suggests it's explosion mechanism was most likely a delayed detonation. In this model, the 'flame' propagates initially as a slow deflagration, but a transition to a detonation is induced at a prescribed flame density during the expansion of the white dwarf. This results in unburnt C-O processed partly into Fe-group and into intermediate-mass elements.

Type Ib and Ic SNe are seen only in spiral galaxies and are associated with massive stars; perhaps even more massive than Type II SNe progenitors. They show strong steep radio indices which are thought to arise from shock interactions with a dense circumstellar medium (CSM). Because of this, Type Ib/c SNe are thought to be associated with core-collapse events which have been stripped of their outer hydrogen (and possibly helium) envelope (Turatto 2003; Harkness et al. 1987). In the case of Type Ib, fast electrons accelerated by γ-rays from the decay of ^{56}Ni and ^{56}Co produce excited levels of helium (Lucy 1991).

Analysis of absorptions features of 11 SNe suggest that detached hydrogen maybe present in Type Ib. Since the optical depths of H and He are not very high, modest differences in the He I line optical depths may transform Type Ib into Type Ic objects (Branch et al. 2002).

[3]Subsonic combustion that propagates through thermal conductivity; detonation is a process of supersonic combustion.

Intermediate objects with both initial spectra similar to Type II and later spectra similar to Type Ib/c have been designated as Type IIb SNe. These include SN 1987M and perhaps the best studied SNe ever, SN 1993J located within M81 (Turatto 2003).

Type II SNe are characterized by the presence of hydrogen in their spectra, displaying a wide variety of properties in their light curves and spectra. Although 'normal' Type II SNe constitute the bulk of this class, four subclasses are commonly mentioned in the literature (IIb, II-P, II-L and IIn) along with a number of "peculiar" objects not fitting into any subclass. The added abbreviation "P" refers to plateau and the abbreviation "L" refers to linear, describing the shape of each subtype's optical light curve (Barbon et al. 1979) as shown in Fig. 1.1. An example of a SN with a plateau shaped light curve is SN 1987A located in the Large Magellanic Cloud (LMC). SN 1987A is associated with the B3 I progenitor star, Sk-69 202 (White et al. 1987).

In SNe II-P, it is believed that the light plateau continues during a recombination wave that moves through a massive hydrogen envelope releasing its internal energy. Although there are no other major spectral differences between SNe II-P and SNe II-L, there are a number of intermediate cases. After 150 days past maximum, the luminosity of both types settle into a steady exponential decline consistent with the constant trapping of energy released from the decay of ^{56}Co into ^{56}Fe (Turatto 2003).

Progenitors of SNe II-L are believed to have hydrogen envelopes 1-2 solar masses smaller than those of SNe II-P ($\sim$ 10 solar masses), presumably due to mass loss in the final phases of evolution. This loss of the hydrogen envelope may be due to varying degrees of stripping within binary systems. It has been suggested that Types II-P, II-L, IIb, Ib and Ic are ordered according to a decreasing hydrogen mass of their envelopes in such binary systems (Turatto 2003).

Type IIn SNe are associated with narrow emission lines. The spectra of these objects have a slow evolution and are dominated by strong Balmer emission lines with no broad absorptions. A classic example of this type of object is SN 1988Z, observed in the radio, optical and X-ray over a period of several years. It is believed that the spectra are the result of interactions between the ejecta and a dense circumstellar medium (CSM). The interaction of the fast ejecta with the slowly expanding CSM produces a forward shock in the CSM and a reverse shock in the ejecta. The radiation emitted is strongly dependent on the density of the CSM, ejecta and properties of the shock itself. If true, observations of these objects may give a history of mass loss in the late evolution of its associated progenitor stars (Turatto 2003). Dwarkadas (2004) noted that the collision of a highly wrinkled shock with various parts of the circumstellar shell of SNR 1987A may partly explain its strange appearing shock front.

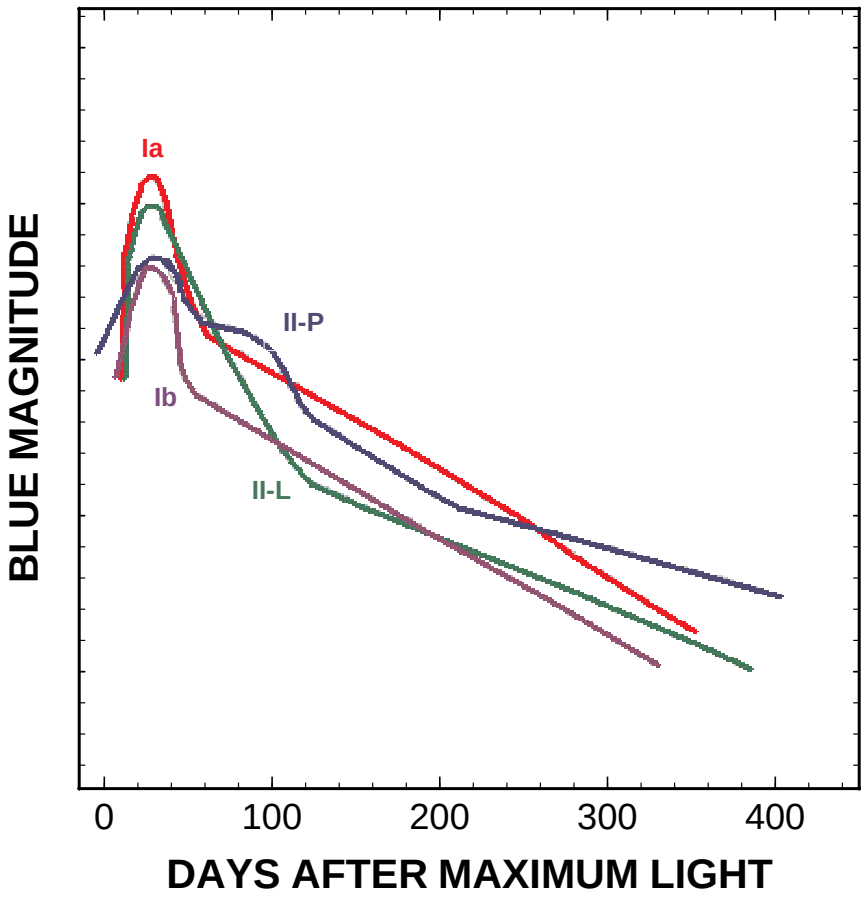

Figure 1.1 Lightcurves in blue light showing the differences in shape between Type Ia, Ib, II-L and II-P SNe.

Smith et al. (2007) reported the discovery of a peculiar Type IIn supernova, SN 2006gy located in NGC 1260. This bright object reached a peak visual magnitude of –22; possibly the most luminous supernova ever recorded. The mass of its progenitor was most likely greater than 40 $M_{\odot}$.

Several SNe do not fit the classification described above. These include hypernovae with proposed explosion (kinetic) energies as high as 10^{52} ergs and possibly associated with gamma ray bursts (GRBs) as discussed by Paczyński (1998). However, most "peculiar" SNe are probably core-collapse objects exploding under unusual conditions or mechanisms. Some may not be SNe, as evidenced by Fritz Zwicky's "Type V" SN 1961V. In this case, an 'exploding' star appears to have survived a giant eruption of material (Filippenko et al. 1995).

There is also a confusing terminology here that the reader must be aware of that has caused some inaccuracy in the literature. Chu & Kennicutt (1988) have classified SNRs in the Large Magellanic Clouds into Population I and II. This is not to be confused with Type I and II. Population I SNe arise from the explosion of massive stars (Type II and Ib, for example) while Population II SNe arise from the deflagration of carbon-oxygen white dwarfs in close binary systems (Type Ia). I have tried to avoid this horrible terminology when possible as it is designed to confuse novices.

Another way to classify SNe include observations of the event in the radio domain. Weiler et al. (2002) notes that over the past twenty years, papers about radio supernovae (RSNe) have established the radio evolution of about two dozen objects. This includes eight Type Ib/Ic SNe with the remainder Type II SNe[4]. Using models, these studies estimate the density and structure of the CSM and by inference, the evolution of the presupernova stellar wind. This is because the blastwave of the SNR passes 'through time' by traveling through the CMS at relatively fast speeds, i.e. 10,000 kms^{-1}, compared to pedestrian stellar wind speeds of 10 kms^{-1}.

Over the past four years, the afterglow of gamma-ray bursts have been detected in radio as well as other wavelengths. In particular, Weiler et al. (2002) note that an interesting and unusual gamma-ray burst GRB980425, thought to be related to SN1998bw, is a possible link between supernovae and gamma-ray bursters. Following the link through SN1998bw/GRB980425, they use the formalism for describing the radio emission from supernovae to model the gross properties of radio and optical/infrared emission from a half-dozen GRBs with extensive radio observations. From this, they conclude that at least some members of the "slow-soft" class of GRBs can be attributed to the explosion of a massive star in a dense, highly structured

[4]For a much larger list of more than 100 SNe that have low radio upper limits, see http://rsd-www.nrl.navy.mil/7214/weiler/kwdata/rsnhead.html .

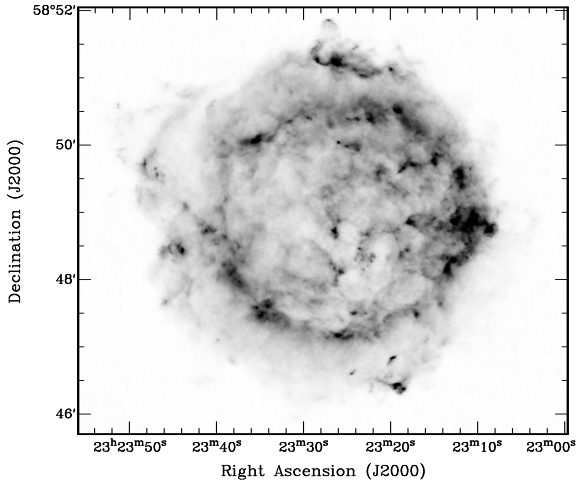

Figure 1.2 VLA (Very Large Array) 1.5 GHz continuum image (Wright et al. 1999) of the shell SNR Cas A. Most SNRs discovered in the Galaxy have this morphology.

circumstellar medium that was presumably established by the preexplosion stellar system.

1.4 SNR Classification

As the supernova explosion continues and material from the star expands out into space, SNRs are formed. There may be some overlap of a few years when, the object may be called both a SNR and a supernova. Ultimately, SNRs form which are classified based on their morphology and spectrum at different wavelengths. The purpose of such a scheme is to understand the underlying processes in their formation and evolution. Many of these objects were initially described based on their appearance in the radio domain. The three traditional types of radio SNRs include shell, plerionic and composite remnants. Green (2004) notes that of Galactic SNRs, 77% of remnants are classed as shell, 12% are composite and 4% are plerionic or filled-center. The remaining 7% have not yet been observed well enough to be sure or do not fit well into conventional types.

Shell SNRs (Fig. 1.2) are characterized by extended X-ray and radio emission in which their morphology takes the shape of a rough spherical shell. Of the 231 Galactic SNRs listed in D. A. Green's catalogue[5], more than 177 are radio shell type remnants. Their radio emission is from relativistic electrons produced by a mechanism known as diffusive shock acceleration (DSA).

The free expansion phase of shell evolution is characterized by expanding ejecta bounded by a forward shock as shown in Fig. 1.3. Because of deceleration, there is also a reverse shock which will eventually heat

[5]http://www.mrao.cam.ac.uk/surveys/snrs/snrs.info.html

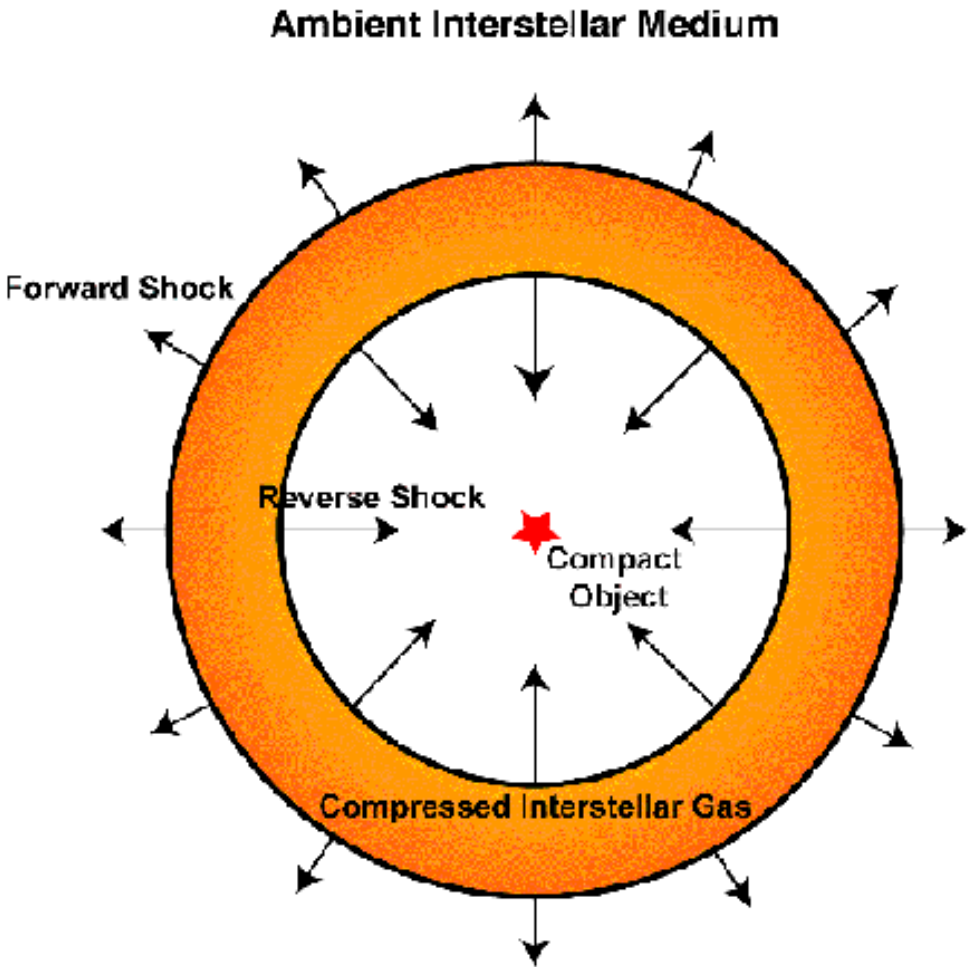

Figure 1.3 Drawing of hypothetical spherical SNR showing various regions. Taken from the High Energy Astrophysics Science Archive Research Center's (HEASARC) website: http://heasarc.gsfc.nasa.gov/docs/objects/snrs/cartoon.html .

the remnant interior giving rise to the 'Sedov-Taylor' phase (see section 1.5). The ISM's magnetic field is strong enough when the forward shock catches up to the star's wind bubble to allow the process of DSA to create radio emission. In contrast, the magnetic strength of the ejecta is not strong enough to allow DSA. This means that the reverse shock is not visible in the radio domain (van der Swaluw 2001).

For the most part, observed 'thermal' X-rays from shell supernova remnants are produced from the hot shocked gas inside the remnant between the forward and reverse shock at temperatures of 10^6 – 10^7 Kelvin (about 1 keV). Highly ionized atoms also produce spectral lines visible in X-ray spectra. Both ejected material and interstellar medium gas participate in this process. Young remnants have X-ray emission dominated by

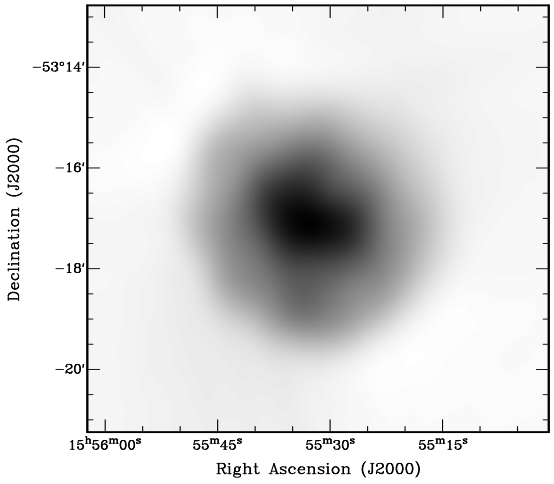

Figure 1.4 MOST 843 MHz continuum image (Whiteoak & Green 1996) of the plerion G328.4+0.2. Only 4 percent of Galactic SNRs fall into this catagory.

the shocked ejecta while older remnants are harder to detect at these energies. Some SNRs (e.g. SN 1006) also emit 'non-thermal' X-rays from the region of their forward shock in which low ambient density may play a role. This non-thermal X-ray radiation may offer clues to the acceleration of cosmic rays. It implies a very strong magnetic field and other yet-to-be-explained acceleration processes (Dickel 2005; Reynolds 2005).

A plerion is a center-filled remnant seen at both radio and X-ray energies. G328.4+0.2 is an example of a Galactic plerion as shown in Fig. 1.4 (843 MHz).

The central emission of radiation from these objects is believed to emanate from a pulsar that converts some of its spin-down energy into a relativistic wind. The wind's kinetic energy is converted to a hot plasma at a termination shock, resulting in a region of observed flux density known as a pulsar wind nebula (PWN). Energetic particles are injected which produce strong synchrotron radiation at radio through X-ray wavelengths (Dickel 2005). The plerionic component of these SNRs have a flatter synchrotron spectrum at radio frequencies than X-ray. These PWN are usually filled throughout and generally show very uniform magnetic fields. While the Crab Nebula is the best known of this class, there are at least 9 naked (without a shell) plerionic systems identified in our Galaxy (van der Swaluw 2001).

Only about 10 of the 32 known Galactic plerions contain any type of detectable pulsar. This is because the pulsar may have moved well away from the SNR, leaving residual emission from long lived radio synchrotron electrons. In contrast, since the lifetime of electrons at X-ray energies are much shorter, the brightest X-ray spot does point to the pulsar's position.

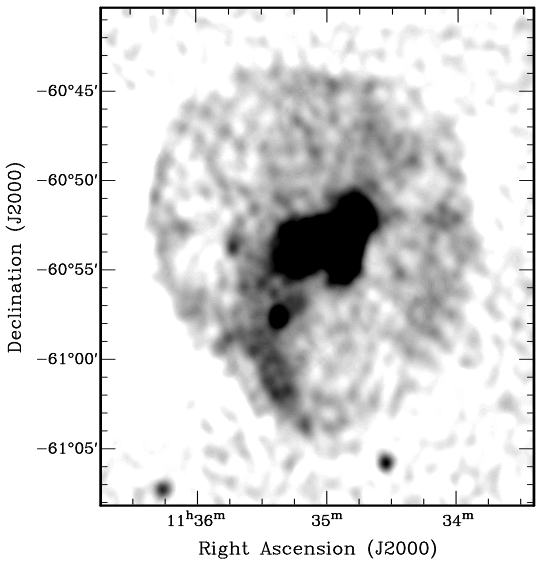

Figure 1.5 MOST 843 MHz continuum image (Whiteoak & Green 1996) of the composite G293.8+0.6. 12 percent of Galactic SNRs fall into this catagory.

Composite remnants have both a shell and plerionic component. There are at least 23 of these in the Milky Way. An example is G293.8+0.6 shown in Fig. 1.5. This Molonglo Observatory Synthesis Telescope (MOST) image shows the SNR at 843 MHz with a central plerionic emission surrounded by a faint shell.

In some composites, the pulsar wind seems to interact with the SNR's shell. An example is CTB80, in which it seems the pulsar wind is about to penetrate the shell of the SNR. The pulsar may also energize the shell through its active winds. A PWN may also be deformed and preceded by a bow shock if the pulsar catches up to the SNR's shell. This assumes that the pulsar moves at supersonic speeds when it crosses the rim of the SNR.

Some remnants do not fit into the conventional classes. For example, Rho & Petre (1998) have proposed a new "mixed-morphology" class based on remnants found to be center-filled at X-ray energies and shell-like at radio frequencies.

1.5 The Hydrodynamic Evolution of SNRs

SNRs introduce the material created during SNe into the interstellar medium. The traditional paradigm has been based on Woltjer's (1972) description, describing SNRs as spherical shells in one of four distinct phases of expansion into a uniform media. These include the free expansion phase, the Sedov-Taylor (adiabatic)

Table 1.2 SNR properties associated with SNe type (Chevalier 1977).

Property	Type I	Type II
Ejected Mass ($M_\odot$)	0.5	5
Mean velocity (km sec^{-1})	10,000	5,000
Kinetic energy (erg)	5 x 10^{50}	1 x 10^{51}
Visual radiated energy (ergs)	4 x 10^{49}	1 x 10^{49}

phase, the radiative snowplow phase and the dispersal phase. The physics is based on fluid-like behavior and hence known as the hydrodynamic evolution of SNRs.

These phases are only a rough guide to the actual processes that are occurring since SNRs are not exactly spherical and do not interact with a uniform media. Interactions associated with a SNR's pulsar or its PWN are also not included. Insertis & Rees (1991) studied the effect that strongly magnetized ISM has on SNR evolution and found that if the ratio of the initial ejecta speed to the Alfveń speed[6] is small, the magnetic field causes the SNR to have a short free expansion phase. The remnant adopts an elongated shape in the direction of the interstellar field and slowly cools. If the ratio of ejecta speed to the Alfveń speed is high the remnant undergoes an adiabatic deceleration. When the expansion speed drops to the Alfveń speed, expansion continues only in the direction of the interstellar field.

In any given SNR, many phases may be occurring at the same time and intermediate stages may last longer than the phases themselves. Some researchers (Truelove & McKee 1999; Blondin et al. 1998; Cioffi et al. 1988) focus exclusively on these transitional stages. Others wish to abandon the phases altogether and suggest age should be the primary consideration in SNR evolution (Jones et al. 1998).

The history of the progenitor star and the SNe explosion can also dictate the evolution of SNRs. In Table 1.2, Chevalier (1977) presents a rough estimate of the properties of SNRs based on SNe class.

Models of SNR evolution can be either analytical (e.g. an equation that gives the size of the remnant as a function of time) or numerical (e.g. computer simulations). There are few analytical models, since the equations governing the motion of the remnants ejecta are very complex and can't be solved without making limited assumptions (i.e. spherical geometry, constant energy, etc). Most of these solutions insist that the expansion obey a power law in time such that:

$$R_{\rm snr} \propto t^{\eta} \tag{1.1}$$

[6] A propagation speed of magnetic waves that depends on the magnetic field strength and density.

Table 1.3 Schematic evolution of an SNR from Woltjer (1972). This assumes an explosion energy of 10^{50} ergs, an initial ejecta velocity of 10,000 km/s, an ejecta mass of 0.1 $M_\odot$ and an interstellar hydrogen density of 1 cm^{-3}. The age *t*, radius *R*, velocity *V* and mass *M* are given at the transition points between the four evolutionary phases.

Phase	*t*(yr)	*R*(pc)	*V*(km/s)	*M*($M_\odot$)
I-II	90	0.9	10,000	0.2
II-III	22,000	11	200	180
III-IV	750,000	30	10	3600

where R_{snr} is the shock radius, t is the time after explosion and η is an exponent (Cioffi et al. 1988). An example of the use of such parameters is shown in Table 1.3 using a hypothetical SNR (Woltjer's 1972).

In numerical modeling, the evolution of the ejecta and ISM fit onto a computational grid and is followed over time using conservation equations of mass, momentum and energy. Because of computer limitations, models in the past have been one and two dimensional. This is rapidly changing to three dimensional models. Since these models can be very complex and are in a constant state of change, it is more useful to focus on analytical models here.

1.5.1 Free Expansion or Ejecta Dominated Phase

Supernova explosions generate a shock wave that propagates throughout the star's atmosphere. Free expansion begins with the interaction of ejecta and CSM or ISM (blast-wave shock) at the edge of the star's atmosphere.

In free expansion, the ejecta expansion velocity is much larger than the sound speed in the ambient gas. When this ambient medium is accelerated, compressed and heated by the shock it pushes back on the ejecta. In turn, the ejecta is decelerated, compressed and heated creating a reverse shock in which the shocked ambient medium expands back into the ejecta much faster than the sound speed of the ejecta.

A contact discontinuity separates into two shells; one containing dense, warm shocked ejecta and another containing hot, thin shocked ambient medium. The shocked ejecta is decelerated further by a pressure gradient between the reverse and blast-wave shocks (Truelove & McKee 1999). Unshocked ejecta continues to freely expand until it is met by the reverse shock. In this scenario, the reverse shock can be thought of as the agent that communicates the existence of the ambient medium to the ejecta.

This ejecta dominated phase lasts 100 to 1000 years and is easy to describe analytically (using simple

assumptions) since almost all of the mechanical energy of the SNR, E_0, is converted to kinetic energy. In free expansion, the ejecta mass is much larger compared to that swept-up from the ISM (van der Swaluw 2001). Equations which describe this include:

$$R_{\rm snr} = V_{\rm snr} t \tag{1.2}$$

and

$$V_{\rm snr} \approx \sqrt{\frac{2E_0}{M_{\rm ej}}} \tag{1.3}$$

where $R_{\rm snr}$ is the radius of the SNR, $V_{\rm snr}$ is the velocity of the shock, t is the time elapsed and $M_{\rm ej}$ is the ejecta mass. According to equation 1.1, free expansion is the case where $\eta = 1$.

In the early time limit of this stage, before the reverse shock has attained a significant velocity, the ejecta behaves like a spherical piston freely expanding into the ambient gas. In the late time limit of the next phase (Sedov-Taylor), after most ejecta energy has been transferred to the ambient gas, the shock is described as an adiabatic[7] blast-wave.

In free expansion, X-ray emission is dominated by the ejecta. In later stages, the X-ray emission is more dependent on the swept-up mass. In fact, as will be seen (equation 5.1), free expansion is the only stage where the ejecta has a significant influence on the measured properties of the shocked material.

There are several similar models in the literature based on these principles. For example, Truelove & McKee (1999) give detailed equations of SNR evolution and present their own set of self-similar[8] and non–self-similar solutions to describe the motions of the reverse shock and the blast-wave shock.

1.5.2 Sedov-Taylor Phase

The Sedov-Taylor adiabatic stage occurs when the swept-up mass of the ISM exceeds the mass of the ejecta. In this phase, the remnant is bounded by a strong blast wave and the interior of the remnant has been heated by the reverse shock. Radiative losses are negligible and hence energy is conserved (Woltjer's 1972). The analytic solution for SNR expansion in this situation is usually cited as:

$$R_{\rm snr}(t) \approx 1.15 \left(\frac{E_0 t^2}{\rho_0} \right)^{1/5} \tag{1.4}$$

[7] An adiabatic process is one where the thermodynamic quantity 'heat' is not lost.

[8] A basic definition of a 'self-similar' solution is that it looks the same on any scale.

and

$$V_{\mathrm{snr}}(t) = \frac{2}{5}\frac{R_{\mathrm{snr}}(t)}{t} \tag{1.5}$$

where ρ_0 represents the mass density of the ISM. This is also expressed in the literature (Cioffi et al. 1988) as:

$$R_{\mathrm{snr}} \propto t^{2/5} \tag{1.6}$$

where η is 2/5.

The interested reader can find a detailed derivation of this solution, first obtained by L. I. Sedov, in van der Swaluw (2001). Basically, this solution is the result of solving equations of fluid flow in a spherical symmetry, simplified assuming a similarity solution wherein fluid quantities depend on two independent variables (radius and time). Final steps involve mathematical conversion to a set of ordinary differential equations followed by integration of fluid energy density over volume while equating total energy to mechanical energy.

1.5.3 Pressure Driven Snowplow: Radiative Phase

The radiative or pressure-driven snowplow stage begins as the postshock fluid velocity approaches the shock velocity and lasts between 10,000 and 100,000 years. As reviewed by Cioffi et al. (1988), the first bit of shocked material to cool completely results in a thin shell that "snowplows" through the ISM, driven by the pressure of the hot, isobaric interior in addition to its own momentum (Cox 1972). McKee & Ostriker (1977) cites the standard analytic solution, assuming an absence of interior cooling, as:

$$R_{\mathrm{snr}} \propto t^{2/7} \tag{1.7}$$

with $\eta = 2/7$.

But, this solution is really too simplistic. In their numerically simulated examples, Cioffi et al. (1988) note that this phase begins less than one sound crossing time from the end of the free expansion stage. As a result, the interior of the blast wave never completely settles down to the Sedov-Taylor similarity solution. This 'memory of extra pressure' challenges the result given by McKee & Ostriker (1977) in equation 1.7. Cioffi et al. (1988) contended that the use of a simple "offset" power law is needed:

$$R_{\rm snr} \propto (t - t_{\rm offset})^{3/10} \tag{1.8}$$

where $t_{\rm offset}$ was a modification of time based on SNR stage. Cioffi et al. (1988) also felt that in reality the momentum-conserving snowplow phase (discussed below) is delayed beyond the merger of the remnant with the ISM, i.e., it never occurs!

1.5.4 Merging with the Interstellar Medium

The merging phase is basically a continuation of the previous stage. This phase occurs when the pressure in the interior of the remnant becomes comparable with the pressure of the ISM. Because there is no force acting on the SNR shell, momentum is conserved while the remnants shock continues to sweep up interstellar gas.

In this scenario, it is assumed that the velocity of expansion is inversely proportional to the volume of the remnant:

$$\frac{{\rm d}R_{\rm snr}}{{\rm d}t} \propto R_{\rm snr}^{-3} \tag{1.9}$$

which using a power law solution, $R_{\rm snr} \propto t^{\,\alpha}$, gives:

$$R_{\rm snr}(t) \propto t^{1/4}. \tag{1.10}$$

This phase has also been named the momentum-conserving snowplow; after which the SNR merges completely with the ISM $\sim 750,000$ years after the SN explosion (van der Swaluw 2001).

Matonick & Fesen (1997) discusses the largest size a single SNR can be while remaining optically bright enough to detect. This maximum size depends on the energy input of the SN, the mass of the ejecta, the ISM density and the amount of energy radiated by the SNR as it expands. They note that with a canonical explosion energy of 10^{51} ergs, an ejecta mass of 1 $M_\odot$, having a velocity of 10^4 km s^{-1} and ISM density of 1 cm^{-1}, at the lowest shock velocity which can be optically observed ($\sim$ 50 km s^{-1}), models indicate a maximum diameter of $\sim$ 100 pc.

1.5.5 The Radio Evolution of Older SNRs

Since SNRs emit radiation in the radio range, their radio evolution is important. Rohlfs & Wilson (2004) presented an semi-analytical evolution of radio SNRs with numerical models using principles of hydrodynamic evolution. Original ideas for this were first presented by J. S. Shklovsky in 1960.

If the radio emission of a SNR is composed of synchrotron radiation, the total flux density of an optically thin (transparent) source, S_ν, is:

$$S_\nu = KH\frac{V}{R^2}B^{n+1}\nu^{-n} \tag{1.11}$$

where V is the volume of the source, B the average magnetic flux density, ν the observing frequency and H a constant. K is another constant appearing in the distribution function of the differential number density of the relativistic electrons; $N(E)dE = KE^{-\delta}dE$. Our question is: how will S_ν evolve with time?

The constant K must depend on the total power output of the SN, i.e. the larger the power output, the larger K will be. But no specific relation between these two are known.

If the temperature in the SNR remains $> 10^4$ K throughout the whole evolution, the gas will be ionized and have a great amount of conductivity. Any magnetic field remains 'frozen' into the gas. If the gas expands, the magnetic field will decrease.

Considering the evolution of high energy electrons, they are confined in a volume V whose expansion is caused by their pressure. If the radiation losses are negligible, this expansion is adiabatic and the work done by the electrons is:

$$dW = -pdV \tag{1.12}$$

where

$$W = V\int E\ N(E)\ dE. \tag{1.13}$$

Using these ideas, it is possible to find the variables needed to solve equation 1.11. Under adiabatic conditions, it turns out that the relation is:

$$S_\nu(t) = S_\nu(t_0)\left(\frac{t}{t_0}\right)^{-4\delta/5} \tag{1.14}$$

This is the time evolution of an radio SNR. If we let the radio spectral index α be $(\delta - 1)/2$, this relation can be tested. Cas A with $\alpha = 0.77$, $\delta = 2.54$, and $t \approx 300$yrs, gives a predicted annual decrease $\frac{dS_\nu/dt}{S_\nu} = -0.7$ %. The observed decrease is -1.3 (± 0.1) % which is not too far off (Rohlfs & Wilson 2004).

1.6 SNR Shocks and Cosmic Rays

A shock is a pressure disturbance that moves through a compressible medium at a speed higher than the local speed of sound. The mechanisms by which SNRs emit radiation and accelerate particles are intimately tied to its shock. It is easy to understand how shocks could form after SNe explosions; a typical ejecta velocity in younger remnants may be 3,000 km s^{-1} while the warm surrounding ISM (at 10,000 K) may have a speed of sound of 10 km s^{-1} (Dyer 2001). The Mach number is the speed of a shock expressed in integral units of sound speed.

Radio emission of shell-type SNRs is modeled using DSA (Diffusive Shock Acceleration) as the main generator of radio emitting electrons. Electron acceleration is simulated from a thermal Maxwellian distribution[9] function and a test particle approximation (Asvarov 2003). DSA occurs when particles move back and forth across the shock, gaining energy from scattering off the incoming fluid.

In Fermi's (1949) theory for the acceleration of cosmic particles, charged ions interacted with magnetized clouds in a process where the energy gained ($\Delta E/E$) was proportional to $(V/c)^2$. In this scenario, V was the fluid (cloud) velocity and c the particle's speed. Because of the exponent, this was called a 'second order' Fermi shock acceleration. In a more efficient collisionless process, the energy gained is proportional to V/c. This is known as 'first order' Fermi shock acceleration. This collisionless shock has scattering centers provided by turbulence in the form of magnetohydrodynamic (MHD) waves embedded in the fluid (Dyer 2001). MHD is a powerful method of modeling shocks to approximate a collection of charged particles within a magnetic field.

It is believed that all hot gases in SNRs are heated by 'first order' collisionless shocks (Laming 2000). This is because collisional shocks, where particles dissipate energy by colliding with other particles in a Maxwellian distribution, are approximately one mean free path thick (Dyer 2001). In collisionless shocks, particles interact only by their magnetic fields and each particle responds individually to the magnetic field created by the entire plasma. In this case, the temperature distribution is not purely Maxwellian and the

[9]The distribution of speeds of molecules in thermal equilibrium as given by statistical mechanics based on a specific probability function.

length (or time) scale for these shocks is the thermal proton gyroradius (the radius of orbit about magnetic field lines). This is much smaller than the mean free path of collisional shocks.

Collisional shocks are not felt to be significant in SNRs because the particle collision length would need to be much larger than the size of the shock structure itself. Cas A, with a shock velocity of about 5,000 km s^{-1}, an ion density of 5 cm^{-3} and a relative proton energy of $\sim$ 8 keV, would have a deflection time scale of about 800 years (Vink 2004b). This is older than Cas A by at least 480 years.

The driving force for particle acceleration within SNR shocks may be connected to shock heating and temperature equilibration. Application of energy conservation laws, momentum and particle flux allow us to derive the shock jump conditions that give postshock temperatures, $T_{\rm i,e}$:

$$\mathrm{k}T_{\rm i,e} = \frac{2(\gamma-1)}{(\gamma+1)^2} m_{\rm i,e} v_{\rm s}^2 = \frac{3}{16} m_{\rm i,e} v_{\rm s}^2 \tag{1.15}$$

where the subscripts of the temperature and mass, i and e, refer to ions and electrons. We define $v_{\rm s}$ as the shock velocity, k is the Boltzmann's constant (1.38 x 10^{-23} joules per Kelvin) and γ is the specific heat ratio for a monatomic gas (5/3). This is known as the Hugoniot relation and it basically states that immediately following the shock transition, particles have temperatures proportional to their masses (Vink 2004b). Temperature equilibration by Coloumb collisions will ensue, but timescales for this may be greater than the SNR's age (Laming 2000).

Evidence for incomplete equilibration of electrons and ions behind SNR shocks can be found by examination of the Hα emission from non-radiative shocks. This technique examines narrow and broad spectroscopic components and were used by Ghavamian et al. (2001) to study nonradiative shocks from the Cygnus Loop, RCW 86 and Tycho[10]. They found $\sim 80-100$ percent equilibration in the Cygnus Loop, $40-50$ percent equilibration in RCW 86 and less than 20 percent equilibration in Tycho. Based on their models, they proposed an inverse relationship between equilibration and shock velocity. Younger SNRs have low equilibration while older ones have almost 100 percent temperature equilibration. Studies of SN 1006 by Vink (2004b) also support this idea which is also discussed in a review by Rakowski (2005) who presented a graph of observed

[10]The theory behind the broad and narrow Balmer line emission was pioneered by Chevalier et al. (1980). Directly behind a collisionless shock, a population of cold neutral ions not affected by the shock passage may emit Hα and Hβ Balmer lines if collisionally excited before being ionized. This narrow component of emission has a width that reflects the temperature of the pre-shock gas. The cold neutrals can interact with shock heated protons to result in a population of hot neutrals which gives rise to the broad component to the Balmer lines. This width represents the temperature of the post-shock protons.

electron to proton temperature ratios[11] as a function of shock velocity for seven SNRs.

This non-equilibration state may drive the process of first order Fermi acceleration. Every time the particle crosses the shock wave it picks up more energy until it eventually escapes as a cosmic ray. Under these conditions, the predicted power law index is:

$$p = \frac{(X+2)}{(X-1)} \tag{1.16}$$

corresponding to a $p = 2$ for a compression ratio[12] of 4.

Shocks may thus play a major role in the acceleration of cosmic rays. Attempts are being made to prove that SNRs are contributors of particle energies up to 10^{16} eV, a value known as the 'knee'. At this energy, the cosmic ray gyroradius becomes comparable with the typical size of a SNR (Laming 2000). Various models propose that both forward and reverse shocks play a major role.

SNR shocks may even account for particle energies as high as the 'ankle', 10^{18} eV. This is because SNRs are the only known Galactic sources that are able to provide enough energy to maintain an observed cosmic ray density of 10^{48} erg yr^{-1}. This assumes 10 percent of the average remnant kinetic energy is used for cosmic ray acceleration and that SNe occur at least every 50 to 100 years.

Radio synchrotron emission from SNRs do have spectral indexes implying a spectral energy slope of –2.2, consistent with the locally observed cosmic ray spectral index (Vink 2004b). This synchrotron emission only proves that electrons are being accelerated; the cosmic rays we observe are dominated by ions.

Observations of non-thermal synchrotron radiation from SNRs caused by relativistic electrons with energies in the MeV to GeV range constitute the earliest evidence of cosmic ray acceleration. Most shell SNRs have radio spectral indexes (α) of about –0.6 ($S_\nu \propto \nu^\alpha$). Cas A has a spectral index of –0.77, which is steeper than predicted by simple first order Fermi acceleration, i.e. $\alpha = -(p-1)/2 = -0.5$. It is felt that this steeper index may be the result of the back reaction of the cosmic ray pressure on the shock structure. Vink (2004b) found that SN 1006 has a X-ray spectral index of -3 which is steeper than expected from Fermi shock acceleration. This may indicate that these photons were emitted by electrons with energies close to the maximum electron cosmic ray energy.

The energy cut-off itself depends on the magnetic field. Given the average interstellar magnetic field strength in the μGauss range, even with magnetic field enhancement in the shock itself, the implied cut-off

[11] Ghavamian et al. (2001) modeled the broad and narrow emission including the temperature dependence of charge exchange and excitation of the fast and slow neutrals by electrons and protons to estimate the degree of equilibration between them.

[12] The compression ratio is defined as $X = \frac{\gamma+1}{\gamma-1}$, where, for the monatomic gas case, $X = 4$.

is around 50 TeV, which is not quite the 'knee'. Thus, much research is needed to further understand the magnetic fields within SNR shocks.

Reynolds & Keohane (1999) have suggested that our picture of cosmic ray origin may need alteration. Given the X-ray emission of 14 radio-bright shell remnants, they constrained the energy at which the electron energy distribution must steepen from its slope at radio-emitting energies. No object could reach the 1000 TeV necessary to consider shock acceleration a viable mechanism in the production of cosmic rays.

The ratio of hadronic to leptonic (electron) cosmic rays is about 100:1. Methods to study the origin of cosmic rays based on electron acceleration alone are not very useful. Telescopes (CANGAROO and HEGRA, for example) observing Cherenkov radiation to measure TeV γ-rays may become increasing important[13]. The idea here is that cosmic rays (ions) near the SNR collide with background ions producing pions which then decay (99 percent) into two 68 GeV photons. With a pion creation threshold of 290 MeV, the emerging γ-ray spectrum has a power law slope similar to the index of the particle spectrum. It may then be possible to observe γ-ray emission from SNRs giving more direct evidence for the production of cosmic rays.

There are currently few observations of TeV emission from shell-type SNRs. These include SN 1006, Cas A, Vela Z and RXJ 1713.7- 3946. *CGRO-EGRET* detected only a few of the known SNRs, most of which are older (e.g. IC 443 and γ-Cygni). To make matters worse, other processes such as inverse Compton scattering of background photons by ultra-relativistic electrons could be an alternative explanation for TeV γ-rays from young SNRs. However, as more observations are made, the picture may be rapidly improved (Vink 2004b).

The High Energy Stereoscopic System (HESS) consists of four 13-meter Cherenkov telescopes located in the Khomas Highland of Namibia. Images of the shell SNR RX J1713.7-3946 (G347.3-0.5) were presented by Aharonian et al. (2004) using only two telescopes in the array. They presented a TeV γ-ray image of the SNR showing a shell morphology similar to that seen in X-rays. Their energy spectrum indicated efficient acceleration of charged particles to energies beyond 100 TeV; most of the γ-rays detected are most likely created from the interaction of cosmic rays with dense molecular clouds near the remnant.

[13]Photons with energies of a hundred GeV or higher generate electromagnetic showers in the earth atmosphere. The secondary particles thus produced move faster than the phase velocity of electromagnetic light and therefore emit optical Cerenkov-light that can be measured with suitable telescopes. Existing imaging Cerenkov telescopes include the WHIPPLE, CAT, HEGRA, CANGAROO and TACTIC with energy thresholds between 300 GeV and 2 TeV. VERITAS (Very Energetic Radiation Imaging Telescope Array System) is a new major ground-based γ-ray observatory working in the 50 GeV to 50 TeV energy range. A sensitivity area of greater than 10^3 m^2 exists because the atmosphere is used as the interaction site (Pohl 2001).

Table 1.4 Radiation properties of SNRs (adapted from Pannuti 2000 and Weiler & Sramek 1988). The radio spectral index, α, is defined as $S_\nu \propto \nu^\alpha$, where S is flux density and ν is frequency.

	SHELL REMNANTS			PLERIONIC-COMPOSITE
Property	Balmer	Oxygen-Rich	Evolved	
Radio Emission	Full or partial shell, steep spectrum ($\alpha \leq -0.3$)	Full or partial shell, steep spectrum ($\alpha \leq -0.3$)	Partial shell, steep spectrum ($\alpha \leq -0.3$)	Filled center, flat spectrum plerion ($\alpha \geq -0.3$) and possible steep spectrum shell ($\alpha \leq -0.3$)
Optical Emission	Thermal line-emitting filaments of ISM; strong Balmer lines, weak in [O III] and [S II]	Thermal line-emitting filaments of processed material; strong [O III] high velocity dispersion	Thermal line-emitting filaments of ISM; [S II]/Hα > 0.7	Thermal line-emitting filaments and non-thermal continuum from plerion
X-ray Emission	Thermal emission	Thermal emission (luminous)	Thermal emission	non-thermal plerion emission, possible thermal shell emission
Location (spirals and irregular)	Interarm regions	Arms and H II regions	Interarm regions, arms and H II regions	Arms and H II regions
SNe Type	Ia	Ib/Ic	all types	II
Compact remains	none	+	+	+
Remnant Energy Source	Shock wave	Shock wave	Shock wave	Neutron star and possible shock wave
Example	Tycho (SN 1572)	Cas A	Cygnus Loop	Crab (SN 1054)

1.7 Radiative Processes in SNRs

Everything we know about SNRs is based on observations of the 'light' or electromagnetic radiation they emit. Electromagnetic radiation is an alternating disturbance in the local electric and magnetic fields. This disturbance is caused when a charged particle, such as an electron, is accelerated through spacetime. The character of the radiation emitted depends on several factors; particle distribution, local environment and, the initial and final charged particle states (e.g. bound-bound, free-bound). Radiation may be categorized in many ways that enhance our understanding of it and the processes that lead to its formation. Table 1.4 presents characteristics of this radiation observed from different types of SNRs.

In this section I discuss brightness, line spectra, each of the continuum processes important to the study of SNRs and the radiative transfer equation. Section 1.8 will then review the nature of SNR radiation in individual domains (i.e radio, X-ray) and its relationship to the type of astrophysical processes responsible.

1.7.1 Brightness

The energy received on Earth by SNRs is measured using the concept of brightness. In the second century AD, the perceived optical brightness of stars were divided into six classes by Ptolemy with the brightest ones described as 'first magnitude'. This was revised in the mid-nineteenth century to the more familiar mathematical formula for the apparent magnitude of a star with apparent brightness B:

$$M = -2.5 \log_{10} \left(\frac{B}{B_{1\ \mathrm{mag}}} \right) \tag{1.17}$$

where $B_{1\ \mathrm{mag}}$ is the apparent brightness of a standard 1 magnitude star. The absolute magnitude of a star is its apparent magnitude if observed from a reference distance of 10 pc. The SI units of brightness are watts per meter squared per hertz per steradian of sky. (A steradian is a square radian.)

The power received by radio telescopes from astronomical sources is extremely small. For convenience, the very small unit of radio flux density called the 'jansky' is used. Named after Karl Jansky, this unit is equal to 10^{-26} W m^{-2} Hz^{-1}. But since SNRs are extended objects that are easily resolved by radio telescopes, it is more useful to consider surface brightness, rather than total flux density. The surface brightness of an SNR is given by:

$$\Sigma = 1.5 \times 10^{-19} \frac{S/\mathrm{Jy}}{(\theta/\mathrm{arcmin})^2} \ \mathrm{W\ m^{-2}\ Hz^{-1}\ sr^{-1}} \tag{1.18}$$

where S is the flux density of the remnant in Jy and θ is its effective angular diameter[14] in arcmin. Surface brightness of SNRs is a quantity independent of distance and is often quoted at a reference frequency of 1 GHz.

Brightness temperature is the apparent temperature of radiation from a source that a black body[15] would have in order to radiate the same brightness. An optically thick astrophysical cloud with thermal emission would have a brightness temperature equal to its physical temperature. Brightness temperature is reduced if the same cloud is optically thin. Sources which emit synchrotron radiation can have very high brightness temperatures ($> 10^9$ K). Regardless of radiation mechanism, in the Rayleigh-Jeans approximation the brightness temperature T_b, is defined as:

$$T_\mathrm{b} = B\lambda^2/2\mathrm{k} \tag{1.19}$$

[14] The effective angular diameter of a circle with the same area as the SNR on the sky.

[15] A perfect radiator of energy.

where B is the brightness of the source, λ the observing wavelength, and k the Boltzmann constant. The Rayleigh-Jeans approximation is used for longer wavelengths such as radio and assumes that $h\nu << \mathrm{k}T_\mathrm{e}$ where h is the Plank constant, ν is frequency, k is the Boltzmann constant and T_e is the electron temperature. In the literature, 'electron' is used primarily because the population in question that is producing light are in fact usually electrons and not ions or protons.

The antenna temperature is the temperature of a black body that, if placed around a radio antenna, would produce the same power as measured when observing a real source. Although not the antenna's physical temperature, it is a measure of the strength of a signal from a radio source in terms of power per unit bandwidth.

High energy electromagnetic radiation is conceptualized and measured in a different way. This is due to its nature and the detectors that measure it. For example, X-rays are usually described in terms of the energy of their particle-like photons which are counted over time, rather than in terms of the wavelength or frequency of their wave-like nature. This is quoted in units of 'electronvolts' (eV) defined by the energy change when an electric charge of size of that carried on an electron moves through a potential difference of 1 volt (1 eV $\approx 1.6 \times 10^{-19}$ J). The energies of X-rays observed with satellite telescopes are typically several keV corresponding to astrophysical processes of many millions kelvin (Stephenson & Green 2002).

1.7.2 Line Spectra vs. Continuum Processes

Line emission measurements can reveal information about temperature, velocity, abundance and ionisation. Spectral lines are created from bound-bound transitions in which electrons move from a higher to a lower energy level or state releasing a photon of light dependent on differences in energy, $h\nu$. This can all become very complex and although a multi-electron atom can be described by a single wave function, it is more practical to describe it in individual-electron states by using four quantum numbers: n, l, m_l and m_s. These states help classify atomic energy levels in order to understand the process causing the emission[16].

The ionic state of an atom is usually denoted by the charge of the element written after its symbol. For example, neutral iron would be denoted Fe^0, singly ionized iron, Fe^+ and doubly ionized iron, Fe^{+2}. Another common practice is to indicate an element by a Roman numeral, such as Fe I for neutral iron, Fe II for singly ionized iron and so forth. Forbidden transitions are those with a lower probability than permitted ones and are given in brackets, such as '[S II]'. Some of the spectral lines important to the study of SNRs are listed in Table 1.5. More information can be found in the references cited therein.

[16] A full discussion of this is well beyond the scope of this paper.

Table 1.5 Incomplete list of SNR line spectra. Data adapted and condensed from (a) Dyer (2001), (b) Zombeck (1990) and (c) Fesen et al. (1996). Definitions of H-like and He-like are given in Section 1.8.2.

Decay	γ-ray (a) Energy (keV)	Half-life
^{26}Al $\longrightarrow$ ^{26}Mg	1809	7.5 x 10^5 yrs
^{60}Co $\longrightarrow$ ^{60}Ni	1332, 1173	5.3 yrs
^{56}Co $\longrightarrow$ ^{56}Fe	1238	77.3 days
^{44}Sc $\longrightarrow$ ^{44}Ca	1157,1150	5.7 hrs
^{44}Ti $\longrightarrow$ ^{44}Sc	67.85, 78.38	60 yrs
^{60}Fe $\longrightarrow$ ^{60}Co	59	1.5 x 10^6 yrs
Ion Notation	**X-ray (a) Energy (keV)**	**Comments**
Ni XXVII	7.806	He-like; $2p^1P \longrightarrow 1s^1S$
Fe XXV	6.700	He-like; $2p^1P \longrightarrow 1s^1S$
Ca XIX	3.902	He-like; $2p^1P \longrightarrow 1s^1S$
S XVI	2.60	H-like; S Ly α
Si XIV	2.00	H-like; Si Ly α
Mg XII	1.70	H-like; Mg Ly β
Ne X	1.20	H-like; Ne Ly β
Ne X	1.00	H-like; Ne Ly α
O VIII	0.77	H-like; O Ly β
Ion Notation	**Ultraviolet (c) Wavelength (Å)**	**Comments**
C III	977	
O VI	1032, 1038	SNR shocks
N V	1238, 1242	SNR shocks
C IV	1548, 1550	SNR shocks
Ion Notation	**Visible (c) Wavelength (Å)**	**Comments**
[O II]	3727	SNR shocks
Hδ	4102	$n = 6 \longrightarrow n = 2$
Hγ	4340	$n = 5 \longrightarrow n = 2$
[O III]	4363, 4959, 5007	SNR shocks
Hβ	4861	$n = 4 \longrightarrow n = 2$
[O I]	6300, 6364	SNR shocks
[N II]	6550, 6585	SNR shocks
Hα	6563	$n = 3 \longrightarrow n = 2$
[S II]	6716, 6731	SNR shocks
Ion Notation	**Infrared (c) Wavelength (Å)**	**Comments**
[S III]	9069, 9531	SNR shocks
[S II]	10287, 10321,10336, 10371	SNR shocks
Chemical Formula	**Radio (b) Frequency (GHz)**	**Comments**
OH	1.721	maser; SNR-molecular cloud interaction

Continuum processes important to SNRs include emission from free-bound transitions, bound-free transitions, bremsstrahlung, Compton, inverse-Compton and synchrotron mechanisms. I will discuss each of these in the subsections that follow.

The distribution of particles play a critical role of our understanding of “thermal” and “non-thermal” continuum processes since an observed spectrum reflects both emission mechanism and particle distribution. Thermal equilibrium occurs if particles have a Maxwellian distribution in energy. SNRs have thermal emission from bremsstrahlung mechanisms and from electron-ion impact excitation, ionisation and radiative capture of electrons by ions. This distribution can be described for electrons as:

$$N_{\mathrm{e}}(v) \propto \exp\left(-\frac{m_{\mathrm{e}}v^2}{2kT}\right) \tag{1.20}$$

where N_{e} is the number of electrons, m_{e} is the mass of an electron, v is the velocity of the electron, k is the Boltzmann constant and T is the temperature (kelvin).

A non-thermal spectrum draws from particle populations beyond the Maxwellian distribution and is created by various emission mechanisms. These populations exists in what is known as the non-thermal tail and can usually be described with a power law. Power law distributions may be placed in the form $N \propto E^{-p/2}$ and $N \propto E^{-p}$ in the nonrelativistic and relativistic case, respectively, where N is the number of particles and E is the energy. For example, synchrotron emission from an electron distribution $N \propto E^{-p}$, yields a spectral distribution $S(\nu) \propto \nu^{-(p-1)/2}$, where S is the flux density and ν is the frequency. If α is defined as $-(p-1)/2$, we see our familiar relation, $S_\nu \propto \nu^{\alpha}$ used to describe the spectrum of radio objects.

1.7.3 Radiative Recombination

A free-bound transition is known as radiative recombination, which occurs when an electron is captured by an atom causing a photon of light to be emitted. Bound-free transitions are the inverse of this event. The ‘cross section’ for capture depends on the velocity and therefore the energy of the electron. The wavelength of the resulting photon depends on the kinetic energy of the electron and the change in energy level (Dyer 2001). This can be expressed as:

$$h\nu = \frac{1}{2}\, m_{\mathrm{e}}v^2 + \Delta\, E_{\mathrm{n}} \tag{1.21}$$

where h is Planck’s constant, m_{e} is the mass of the electron, v is the velocity and E_{n} is the change in energy.

1.7.4 Bremsstrahlung

Bremsstrahlung (German for braking radiation) is an example of a free-free transition. This occurs when one particle, usually an electron, interacts with another, usually an ion or proton, slowing down in the process. It can be shown (see Longair 1992) that the thermal bremsstrahlung spectrum falls off at high energies and is characterized by the temperature, T (Charles & Seward 1995). The intensity, I, of the radiation at energy, E, is given by:

$$I(E,T) = AG(E,T)Z^2 n_e n_i (kT)^{-1/2} e^{-E/kT} \tag{1.22}$$

where k is the Boltzmann constant and G is the "Gaunt factor", a slowly varying function with value increasing as E decreases. Intensity is proportional to the square of the charge of the positive ions, Z. The product of the electron density, n_e and the positive ion density, n_i also enters into this equation. A is simply a constant. Non-thermal bremsstrahlung is similar to thermal bremsstrahlung, but draws from the electron population from beyond the Maxwellian distribution.

Apart from non-thermal emission, the plane of a galaxy is a source of significant radio emission with a thermal spectrum. This emission is from H II regions (and planetary nebulae in our own Galaxy) and is caused by bremsstrahlung emission.

1.7.5 Compton Scattering

Another emission mechanism, Compton scattering occurs when a high energy photon impacts a charged particle, transferring momentum to the particle. At low energies, this was first described as Thompson scattering. When a particle transfers momentum to the photon, we have the inverse situation known as inverse-Compton scattering. Longair (1992) describes this by a coordinate transformation of the Compton effect; this is the Compton effect in the rest frame of the particle. Equations describing inverse-Comptom scattering use a 'cross section', which is a mathematical way of describing the impact area. In high energy situations, this cross section is reduced in the 'Klein-Nishina' formula which I do not quote here but can be readily found in Longair (1992). In relativistic situations, the energy of the outgoing photon is boosted by γ^2, where γ is the Lorentz factor of the particle (usually electron):

$$\gamma = \left(1 - \frac{v^2}{c^2}\right)^{-1/2} \tag{1.23}$$

where v is velocity and c is the speed of light (Dyer 2001). Although some degree of inverse-Compton scattering occur in most astronomical objects, a further discussion related to SNRs is not warranted.

1.7.6 Synchrotron Radiation

Perhaps the most relevant radiative emission mechanism in the study of SNRs is synchrotron emission. Radiation is emitted when a charged particle in a magnetic field circles the magnetic field lines. At low energies, this produces cyclotron radiation at the gyrofrequency of the particle (electron). A relativistic electron produces a continuum of synchrotron radiation sometimes referred to as magnetobremsstrahlung. Most of the observed synchrotron radiation in SNRs is caused by the acceleration of particles at the shock interface with the compressed ambient magnetic field. Also, pulsars and their nebula (plerion) emit synchrotron radiation. Plerions has a much flatter spectra than synchrotron emission from a SNR shock ($\alpha = -0.1$; Dyer 2001).

A brief discription of the synchrotron emission mechanism may be summarized from Salter & Brown (1988) and Bhatnager (2001). If the angle (known as the pitch angle) between the velocity (**v**) and magnetic (**B**) vectors is θ and the total energy of the electron is $E = \gamma\, mc^2$, the frequency of gyration around the field lines is given by:

$$\nu_{\rm gyration} = \frac{e\mathbf{B}_{\perp}}{2\pi\, \gamma\, mc} = \frac{\nu_0}{\gamma} \tag{1.24}$$

where $\mathbf{B}_{\perp} = \mathbf{B} \sin\theta$ is the component of the magnetic field perpendicular to the electron path and ν_0 is the non-relativistic electron gyrofrequency. Relativistic effects will cause the radiation to be emitted in a narrow cone of half-angle of the order of $1/\gamma$.

A detector will detect pulses of radiation from such a system each time the cone of emission crosses its line of sight and the pulse shape is defined by a cut across the cone of emission. The frequency of the pulses as seen by the detector will be the Doppler shifted gyration frequency given by:

$$\nu^{'}_{\rm gyration} \sim \frac{\nu_{\rm gyration}}{\sin^2\theta} \tag{1.25}$$

while the pulse width is:

$$\Delta t \sim \frac{1}{2\pi\nu_{\rm gyration}\gamma^3} \tag{1.26}$$

Since the width of the individual pulses are narrow, most of the emitted energy is in harmonics of the fun-

damental frequency by $(2\pi\Delta\, t)^{-1} \sim \nu_{\rm gyration}\gamma^3$. For the ultra-relativistic electron, these harmonics are closely spaced and the resulting spectrum is for all intents a continuum. The critical emission, $\nu_{\rm c}$, at maximum is:

$$\nu_{\rm c} = \frac{3}{2}\gamma^2\nu_0 = 16.08 \times 10^6\, \mathbf{B}_\perp\, E^2 \text{ MHz} \tag{1.27}$$

where E is the electron energy in GeV and $\mathbf{B}_\perp$ is the magnetic field in gauss. The rate of energy loss by an electron due to synchrotron radiation is:

$$\frac{dE}{dt} = -119.7\, \mathbf{B}_\perp^2\, E^2 \text{ GeV/yr} \tag{1.28}$$

This equation states that the most energetic electrons lose energy at the fastest rate. With time, high energy electrons lose energy and radiate for longer times at lower energies. This produces observable changes in the properties of emission with time and is termed ‘aging’.

For a homogeneous and isotropic ensemble of electrons with energy density distribution $N(E)\, dE$, the total intensity, $I(\nu)$, is:

$$I(\nu) = \int_0^\infty N(E)\, P(\nu)\, dE \tag{1.29}$$

where $P(\nu)$ is the spectrum of the electron with energy in the range between E and $E + dE$. For a power law energy spectrum given by $N(E)\, dE = N_0\, E^{-p}\, dE$ in a limited range of energy, $E_1 < E < E_2$, the total intensity becomes:

$$I(\nu) = \frac{\sqrt{3}e^3 L}{8\pi mc^2} \left(\frac{3e}{4\pi m^3 c^5}\right)^{(p-1)/2} N_0\, \mathbf{B}_\perp^{(p+1)/2}\, \nu^{(1-p)/2}\, a(p) \tag{1.30}$$

where $a(p)$ is a slowly varying function of the power law index, p, and L is the spatial extent of the region with uniform magnetic field $\mathbf{B}$. For a power law distribution of initial energies, $I(\nu) \propto \nu^\alpha$ where α is the spectral index related to p as $\alpha = (1 - p)/2$. p in this formulation is usually greater than unity, so a negative spectral index can be observational evidence for synchrotron radiation.

Emission for a single electron will be elliptically polarised with the electric field vector perpendicular to the projected magnetic field vector. For an ensemble of electrons with a random distribution of pitch angles, the observed radiation will be partially linearly polarised with the degree of polarsation in a uniform magnetic field given by:

$$\Pi = \frac{p+1}{p+7/3} \tag{1.31}$$

Thus, two defining characteristics used to identify sources of synchrotron emission include linear polarisation and negative spectral index. Unfortunately, radiation can be measured as depolarised due to a variety of reasons. These include random orientations of the magnetic field vectors within the resolution element of the telescope, thermal material along the line of sight and perhaps even Faraday rotation in the Earth's ionosphere. Thus, while detection of linearly polarized emission is strong proof of synchrotron emission, a lack of it cannot rule it out. This is why a negative spectral index is most often used as a signature of synchrotron radiation.

The study of synchrotron radiation requires us to understand the origin of the involved relativistic electrons and magnetic field. A central pulsar is thought to be the source for both of these in Crab-like SNRs, while for shell SNRs, both come from the ambient ISM. The observed properties and evolution for Crab-like SNRs are believed to be dominated by rotational energy losses from the central pulsar (Bhatnager 2001).

Two classes of electron acceleration mechanism include turbulent acceleration at the unstable contact discontinuity and acceleration in the shock front itself. The first uses second order Fermi acceleration and the second uses the more efficient first order Fermi acceleration.

The inferred magnetic fields in SNRs, as measured from the rotation of background radio sources, X-ray observations and Zeeman splitting of OH maser lines, are two to three orders of magnitude higher than the ambient magnetic field. This suggests that magnetic field amplification is required.

The observed brightness of young shell SNRs is often more than can be explained by magnetic field amplification due to compression by the shock alone. For example, the observationally deduced magnetic field for Cas A is far too high to be explained by a factor of 4 shock compression. It is believed that for these shell type SNRs, a combination of particle acceleration in front of and behind the shock, along with magnetic field amplification, are responsible for the observed radio brightness.

Thus, mechanisms for magnetic field amplification are poorly understood. Compression alone does not explain it. The fact that observed magnetic fields are predominantly radial also argue against the idea that the amplified field is simply a 'swept-up' ambient field. Magnetic fields due to the deceleration of ejecta is an attractive idea and simulations show that such amplification is dependent on the orientation of the field and can produce barrel-shaped SNR morphologies.

1.7.7 The Equation of Radiative Transfer

In order to interpret radio observations quantitatively, it is necessary to understand how radiation travels through a medium. Consider loss and gain mechanisms in the direction of a observer without regard to the details of the atomic processes making up these mechanisms. It is assumed that all processes are stationary or in other words, that all parameters are time independent over the time scale of an observation.

With certain assumptions, I cite one of the most fundamental equations in astrophysics. This states that the radiation received by a (radio) telescope is the sum of (1) the attenuated background radiation, (2) the contribution from an object or nebula, and (3) the contribution of any foreground sources. Mathematically stated, the observed intensity from an emitting region of linear size L with a foreground radiation intensity of $I_{\rm fg}$ and background intensity of $I_{\rm bg}$ is given by:

$$I = I_{\rm bg} e^{-\tau} + \int^{\tau} \frac{j}{\kappa} e^{-t} dt + I_{\rm fg} \tag{1.32}$$

where j and κ are the emission and absorption coefficients and τ is the optical depth. This relates the physical processes in a medium, as described by κ and j, to the radiation intensity measured by the telescope. One must evaluate κ and j in order to understand their effects on the observed radiation field.

In the case of bremsstrahlung radiation, when a charged particle moves in the electric field of another charged particle, it undergoes an acceleration resulting in the emission of electromagnetic radiation. In realistic situations, there is a distribution of particle velocities and the total radiation is determined by integrating the emission during one interaction over the velocity distribution. It is assumed that the electric field in which the particle is moving is effective only over a finite distance, the radiated energy is small compared to the kinetic energy of the moving particle and the period of the emitted wave is small compared to the duration of the encounter (Bhatnager 2001).

Using these assumptions, an expression for the free-free absorption coefficient in the radio domain is:

$$\kappa_\nu = \left(\frac{N_{\rm e} N_{\rm i}}{\nu^2}\right)\left(\frac{8 Z^2 e^6}{3\sqrt{3} m^3 c}\right)\left(\frac{\pi^{1/2}}{2}\right)\left(\frac{m^{3/2}}{kT}\right) G \tag{1.33}$$

where $N_{\rm e}$ and $N_{\rm i}$ are the number densities of electrons and ions, ν the wave frequency, Z the ion charge, m the electronic mass, c the speed of light, k Boltzmann's constant, T the kinetic temperature and G the Gaunt factor averaged over a Maxwellian velocity. All units are CGS. The Gaunt factor is different for temperatures above and below 892,000 K which is the division between classical and quantum-mechanical regimes.

An approximation to equation 1.33 used in the analysis of radio observations of H II regions is:

$$\kappa_c \approx \frac{0.08235 N_e N_i}{\nu^{2.1} T_e^{1.35}} \tag{1.34}$$

where ν is in units of GHz, N is in units of cm^{-3} and κ_c is in pc^{-1} (κ_c is used to distinguish this approximation from κ_ν above).

For a Maxwellian velocity distribution, $j(\nu)/\kappa(\nu) = B_\nu(T_e)$ where in the Rayleigh-Jeans approximation used at radio frequencies, $B_\nu \approx 2kT_e/\lambda^2$. For a source of homogeneous density and temperature with $I_{fg} = 0$, equation 1.32 can be written as:

$$I = I_{bg} e^{-\tau} + \frac{2kT_e\nu^2}{c^2}(1 - e^{-\tau}) \tag{1.35}$$

where optical depth, $\tau = \int \kappa_c dx$[17].

At low frequencies, the frequency dependence of the free-free absorption coefficient given by equation 1.34 causes τ to become greater than one which after equation 1.35 is translated to brightness temperature, T, gives:

$$T(x) \approx T(0)e^{-\tau} + T_e. \tag{1.36}$$

In this scenario, $T(0)$ is the brightness temperature at the back of the source and $T(x)$ is the brightness temperature toward the observer. At high frequencies, the $\nu^{-2.1}$ dependence makes $\tau < 1$ and the result is:

$$T(x) \approx T(0) + T_e\tau. \tag{1.37}$$

Unlike the previous case with low frequencies, the antenna temperature increases as the beam is scanned over a source such as an H II region.

The flux density S at a frequency ν is:

$$S = \int_{source} I_\nu d\Omega \approx \frac{2k\nu^2}{c^2} \int T_{source} d\Omega \tag{1.38}$$

where Ω is the angular extent of the source and T_{source} is the source electron temperature. From equation 1.35, assuming $I_{bg} = 0$:

[17] Remembering that $\kappa_c \propto \nu^{-2.1}$ from equation 1.34.

$$S_\nu = S(1 - e^{-\tau}) \tag{1.39}$$

In the high frequency, optically thin regime ($\tau << 1$), $S_\nu \approx S\tau$ and since $\tau \propto \nu^{-2.1}$ and $S \propto \nu^2$, $S_\nu \propto \nu^{-0.1}$. Spectra at high frequencies is a weak function of the frequency. In the optically thick regime of low frequencies, $S_\nu = S \propto \nu^2$. This means that the spectral indices for this thermal radiation above and below a critical turnover frequency (1 – 2 GHz) are markedly different (–0.1 vs. 2).

The important point from the perspective of radio SNRs is that thermal emission progressively diminishes at frequencies below 1 GHz while non-thermal emission progressively becomes stronger in this range of frequencies. Strong emission from H II regions has been observed all along the Galactic plane. High frequency observations above 1 GHz are more sensitive to thermal emission and not well suited to the study of SNRs. At lower frequencies, thermal emission is diminished while non-thermal emission from SNRs grows progressively stronger.

1.8 Multi-Wavelength Observations of SNRs

Morphologies of SNRs change based on the wavelength one observes. An example is the "mixed-morphology" class discussed above. Classification schemes are therefore based on what one sees at a particular electromagnetic domain.

1.8.1 Gamma-Ray

Stellar processes and supernova explosions create radioactive elements which decay, producing γ-ray line spectra. M. Burbidge, G. Burbidge, W. Fowler and F. Hoyle developed the idea that the exponential decrease in the light output observed after the first 100 days following a Type I SNe is due to nuclear energy released by the spontaneous fission of ^{254}Cf (Clayton & Craddock 1965). Elements with relatively long half-lives are used to determine abundances in the initial explosion, date the explosion and calibrate nucleosynthesis models. For example, ^{44}Ti decays into ^{44}Sc with a half life of about 60 years emitting lines at 67.85 and 78.38 keV. Motizuki & Kumagai (2004) have investigated the decay sequence of ^{44}Ti of the young SNRs Cas A and SN 1987A. For SN 1987A, they reported an initial ^{44}Ti mass between 0.82–2.3 x $10^{-4} M_\odot$ using Monte-Carlo simulations.

^{44}Ti is produced in different amounts by different types of SNe. This ranges from $\sim 7 \times 10^{-5} M_\odot$ by Type

Ia, $10^{-4}M_{\odot}$ for Types II and Ib and as much as $3.9 \times 10^{-3}M_{\odot}$ for rare helium white-dwarf detonations. Iyudin et al. (1998) reported a previously unknown young SNR (GRO J0852-4642), found by the Imaging Compton Telescope (*COMPTEL*) based on the discovery of a ^{44}Ti emission line. This observation was located in the direction of the Vela SNR at an estimated distance of $\sim$ 200 pc and age of about $\sim$ 680 yrs. This represents a powerful new method to find nearby young SNR missed by radio and optical surveys.

An excellent review of γ-ray emission from radioactive isotopes in stars and galaxies can be found in Diehl & Timmes (1998). Decay lines from ^{56}Co, ^{60}Co, ^{44}Sc, ^{56}Ni, ^{60}Fe, ^{44}Ti, ^{26}Al and ^{56}Ni have all been detected in SNe and SNRs.

1.8.2 X-Ray

Many of the line transitions observed in SNRs at X-ray energies (0.1–10.0 keV) are from elements stripped of all but one or two electrons. A way to simplify the understanding of these complex transitions is to treat them as if they were variations of a simpler hydrogen or helium system. These ions are referred to as 'helium-like' or 'hydrogen-like'. Hydrogen is a simple and well known atom in which the energy of a photon is described by:

$$\Delta E = 13.6\, Z^2 \left(\frac{1}{{n_{\rm i}}^2} - \frac{1}{{n_{\rm f}}^2} \right) \text{eV} \tag{1.40}$$

where Z is the atomic number and $n_{\rm i}$ and $n_{\rm f}$ are the initial and final atomic levels. This equation can provide a useful approximation for understanding and describing X-ray line emission.

Complex transitions can be understood by an entire nomenclature based on these ideas. For example, it is well known that emission lines arising from electron transitions ending in the ground state of a hydrogen atom are called Lyman (Ly) lines. When created by an electron initially one level above, this is known as Lyα. In a similar fashion, electrons which originated two levels above the ground state are called Lyβ. Thus, a hydrogen-like X-ray line for Si might be Si Lyα, which means that a Si ion, Si XIV, has a transition in which an electron moves from the second to the first energy level (more precisely 2p to 1s).

Multiple electron atoms can also be thought of in the above terms, but the transitions show multiple lines which are often smeared. Downward transitions to the ground state (n = 1) are called K-shell transitions. In similar fashion, downward transition to the second level (n = 2) are called L-shell transitions and to the third level (n = 3), M-shell transitions.

Common X-ray line blends from multi-electron ions observed in SNRs include: Ni Kα, Fe Kα, Ca Kα,

S Kβ, S Kα, Si Kγ, Si Kβ and Si Kα. These lines are produced by electron impacts on these ions, exciting electrons to a higher state which produce photons when they promptly decay to the ground state.

Most of the shock heated material in SNRs is visible in X-rays, having temperatures between 10^6 – 10^7 K. Emission mechanisms have been previously thought to consist of mainly bremsstrahlung and line radiation, but a number of remnants are now known to emit X-ray synchrotron radiation from ultra-relativistic electrons. This was already known for pulsar wind dominated or Crab-like nebulae, but shell-type remnants such as SN 1006 have recently been suspected of emitting synchrotron radiation from electrons accelerated by the blast wave (Vink 2004a).

Non-thermal emission can dominate much of a SNR such as the case with SN 1006, G266.2-1.2 (RX J0852.0-4622), G347.3-0.5 and RX J1843.8-0352. Alternatively, a SNR can have signatures of non-thermal emission along with X-ray lines. Examples of this include RCW 86, Cas A and Tycho. As noted by Dyer et al. (2004), non-thermal emission may be common among most young SNRs. Ballet (2005) noted that the synchrotron emission arises in a very thin shell (few arcsec) at the blast wave. The thinness of that shell implies that the high energy electrons cool down quickly behind the shock; this implies a magnetic field there of more than 100 μG.

Dyer et al. (2004) performed a spatially resolved spectral analysis of SN 1006 using *ASCA* (Advanced Satellite for Cosmology and Astrophysics) observations. Using XSPEC, they find that their synchrotron electron escape models fit the brightened northeast and southwest limbs of this SNR accounting for about 46–47 % of the X-ray flux. The remainder of the remnant's X-ray emission is thermal. Bamba et al. (2004) used *Chandra* to resolve non-thermal filaments from thermal emission in the northeastern shell of SN 1006. The non-thermal filaments seem to occur in thin sheets; this may imply that the magnetic field is perpendicular to the flow of charged particles instead of parallel as previous DSA models have suggested.

The traditional modeling and interpretation of X-ray thermal spectra from SNRs assume that shocks do not place a significant fraction of their energies into the formation of cosmic rays. Decourchelle & Ellison (2001), however, do believe that shocks accelerate electrons to TeV energies and that there is support for efficient proton acceleration. This implies that these effects should be included in the modeling of thermal X-ray emission. They suggest such modeling may serve as a tracer of cosmic ray acceleration.

Abundance patterns and circumstantial evidence, such as proximity to an OB association, may provide clues about the type of progenitor star that led to formation of a SNR. Younger oxygen rich (O-rich) SNRs thought to be remnants of the most massive stars (Type Ib/c) are important to a more complete understanding of nucleosynthesis yields (Vink 2004a). Among these are the SNRs Cas A, G292.0+1.8 (MSH 11-54) and

E0102-7219. Their identification as O-rich was originally based on optical line data, but X-ray spectroscopy confirms this idea.

While core-collapse SNe create SNRs rich in heavier elements, detonation Type Ia SNRs show more Fe lines in their spectra. Carbon-oxygen white drawfs require over 0.5 $M_{\odot}$ of C-O to be fused into ^{56}Ni in order to be disrupted and eject material at high velocity. Therefore, young Type Ia SNRs should emit copious Fe-L in the energy range of 0.8 to 1.2 keV or Fe-K in the range of 6.4 to 7.0 keV. However, Type Ia SNRs Tycho (SN 1572) and SN 1006 both lack any prominent Fe-L emission.

The age of the remnant may be critical in this regard, and in order to see all of the Fe transitions, one has to observe older remnants in which the reverse shock has heated almost all of the ejecta. An example of this is DEM L71 in which *Chandra* observations show that most of the O VII/VIII emission comes from a narrow shell while Fe-L line emission is seen in the center of the remnant. Assuming the plasma inside is pure iron, the calculated mass (~ 0.8 $M_{\odot}$) is consistent with Type Ia nucleosynthesis models. These older remnants are less suitable for obtaining the overall ejecta abundances since the outer C-O and Si layers have most likely mixed with the ISM (Vink 2004a).

Regional information about the nature of X-ray emission is also critical to the understanding of a SNR's environment and origin. Pannuti et al. (2003) recently used *RXTE*, *ROSAT* and *ASCA* observations of the Galactic shell-type remnant G347.3-05 to model X-ray emission from specific regions, including its interior and three of its rims. While modeling the interior of the remnant yielded results consistent with thermal emission, the non-thermal rims appear to be expanding into low ambient densities ($0.05 - 0.07$ cm^{-3}). Comparison with two other predominately non-thermal young, X-ray luminous but radio weak SNRs (SN 1006 and G266.2-1.2) reveal that they too are expanding into a low density ambient region. This suggests that the local environment at least partially dictates the nature of a SNR's X-ray spectrum. Newer X-ray telescopes, such as *XMM-Newton* and *Chandra* with their increased sensitivity and resolution ($< 1''$), will enrich this aspect of observations even further.

1.8.3 Ultraviolet and Visible

Ultraviolet line emission from SNRs originate from dense shocked ambient material. However, observations have been limited primarily to late-stage radiative remnants such as the Cygnus Loop and Crab. This is because atmospheric absorption require space based observations and local extinction from interstellar dust limit what can be done.

It is in the radiative phase that the shocks in SNRs cool, giving off line radiation in the visible spectrum. Common lines include Hα, He I, [O I], [O II], [O III], [N II], [Ne III] and [S II]. The optical line ratio, [S II]/Hα is used to distinguish SNRs from H II regions when the remnants cannot be identified through appearance. This technique was pioneered by Mathewson & Clarke (1973a) who used it to find nine SNRs in the LMC using radio and optical techniques. They noted that the combined strength of the [S II] lines $\lambda\lambda$6716–6731 from SNR shells are about equal to Hα. In radiatively excited H II regions, the [S II] emission is generally an order of magnitude weaker than Hα. SNRs have much stronger shock fronts than H II regions and these shocks heat and ionize the gas which recombine over a period of time. As a result, SNRs have the spectrum of a recombining plasma with strong forbidden line emission arising from a wide range of ionisation states including S^+ (Blair & Long 1997). Mathewson & Clarke (1973a) used a ratio ([S II] to Hα + [N II][18]) cutoff of 0.5 to identify SNRs.

However, this line ratio criterion has drawbacks, as will be discussed in more detail later. Here I mention that there is an overlap between H II regions and planetary nebulae having high ratios and SNRs having low ratios, which creates an 'ambiguous' zone between 0.40 and 0.67 (Fesen et al. 1985). In these cases, one looks for other forbidden lines as distinguishing criteria. Although the line ratio [O III] (λ4959 + λ5007)/λ4363 is always observed in SNRs and never seen for even the hottest H II regions and planetary nebulae, the λ4363 line is usually too weak and the sky Hg I λ4358 too strong to permit its use. Using a Galactic sample of evolved remnants, Fesen et al. (1985) have suggested the best optical discriminator of candidate SNRs may be use of the [S II]/Hα ratio in combination with the presence of [O I] and [O II] lines.

The use of line spectra in the visible and ultraviolet can also lead to some very insightful studies of the environments of SNRs (see Fig. 1.6). Danforth et al. (2003) used *Far-Ultraviolet Spectroscopic Explorer (FUSE)* O VI and C III emission spectra to describe the environment of SNR 0057-724[19] located within the N S66 region of the Small Magellanic Cloud (SMC).

Ratios of spectral line intensities are useful to determine information about SNRs and their environments, including temperature and electron density, as discussed in Section 5.5.2. Line ratios of [N II]($\lambda\lambda$6550 + 6585)/Hα and λ6731/Hα are also used to determine estimates of the local interstellar abundance as discussed

[18]This is a contaminant of Hα which requires the cutoff ratio to be lower in order to detect all SNRs.

[19]The rectangular shaped SMC SNR 0057-724 (IKT 18) was also studied by van der Heyden (2004) using data from *XMM-Newton*. This high mass (196 $M_\odot$) source has low SMC-like abundances and an age estimate of 11,000 years consistent with an evolved SNR with swept-up ISM material. These low abundances prevent determination of progenitor type. Yee (1991) has suggested that giant H II regions, in this case N S66, are often associated with SNRs. His conclusion is based on the 'scaled' subtraction of an Hα map from high resolution low-frequency (e.g. 843 MHz) radio images which allows IKT 18 and its environment to be visualized.

in Section 5.5.3.

1.8.4 Infrared

Dwek & Rice (1987) note that *Infrared Astronomical Satellite* (*IRAS*) observations of Galactic SNRs reveal that infrared emission from collisionally heated dust is the dominant cooling mechanism during much of their lifetimes. Infrared observations are less affected by interstellar extinction than optical and ultraviolet ones but are mostly limited to the Galaxy. Infrared lines from SNRs are usually ground-state fine structure lines of C to Ni and low to moderately ionized states at temperatures of several hundred degrees include: O I, O II, O IV, Ne II, Ne III, S I, S III, S IV, Ar II, Ar III, and Ar IV (Dyer 2001).

Although not true blackbodies due to poor absorption of longer wavelengths, many SNRs are known as 'greybody' emitters in the infrared. The dust is not necessarily from the ambient medium as evidenced by Meikle et al. (1993) who found infrared evidence for dust condensation in SN 1987A at day 350. This is far too early for the 'swept-up' ambient medium to play much of a role. Dust may also be magnetically aligned allowing polarization studies to give information on the alignment and strength (lower limit) of the magnetic fields on the largest scales near the SNR and in the line of sight (Dyer 2001).

Saken et al. (1992) found clear infrared emission from 35 out of 161 Galactic SNRs examined, based on *IRAS* data. They found that younger SNRs (Tycho, Kepler, Cas A and the Crab) had significant 12 and 25 μm flux densities while older remnants (Cygnus Loop and Vela) are brightest at 60 and 100 μm. Most SNRs tended to have their brightest emission at 60 μm (Saken et al. 1992).

Infrared lines are useful in the study of SNRs within dense environments. This is because infrared fine-structure lines are produced by dense gas expected behind radiative shocks and trace the ground-state populations of all of the abundant elements. Rho & Reach (2003) reviewed recent *Infrared Space Observatory* (*ISO*) and near-infrared observations of SNRs interacting with molecular clouds. They note that pre-shock densities as high as $\sim 10^4$ cm^{-3} are required to explain detected atomic fine-structure lines. Far-infrared emission of H_2O, OH and CO is also detected from shock excited regions, consistent with the presence of a warm dense gas. These regions are heated into dense clumps by supernova shocks and cool primarily by emission of infrared [O I] 63 μm and [Si II] 34.8 μm lines. The authors note that star formation may be induced by these interactions with molecular clouds.

Reach et al. (2006) used *Spitzer Space Telescope* Infrared Array Camera (IRAC) images to study Galactic SNRs at 3.6, 4.5, 5.8 and 8 μm. They note that infrared emission from SNRs may originate from synchrotron

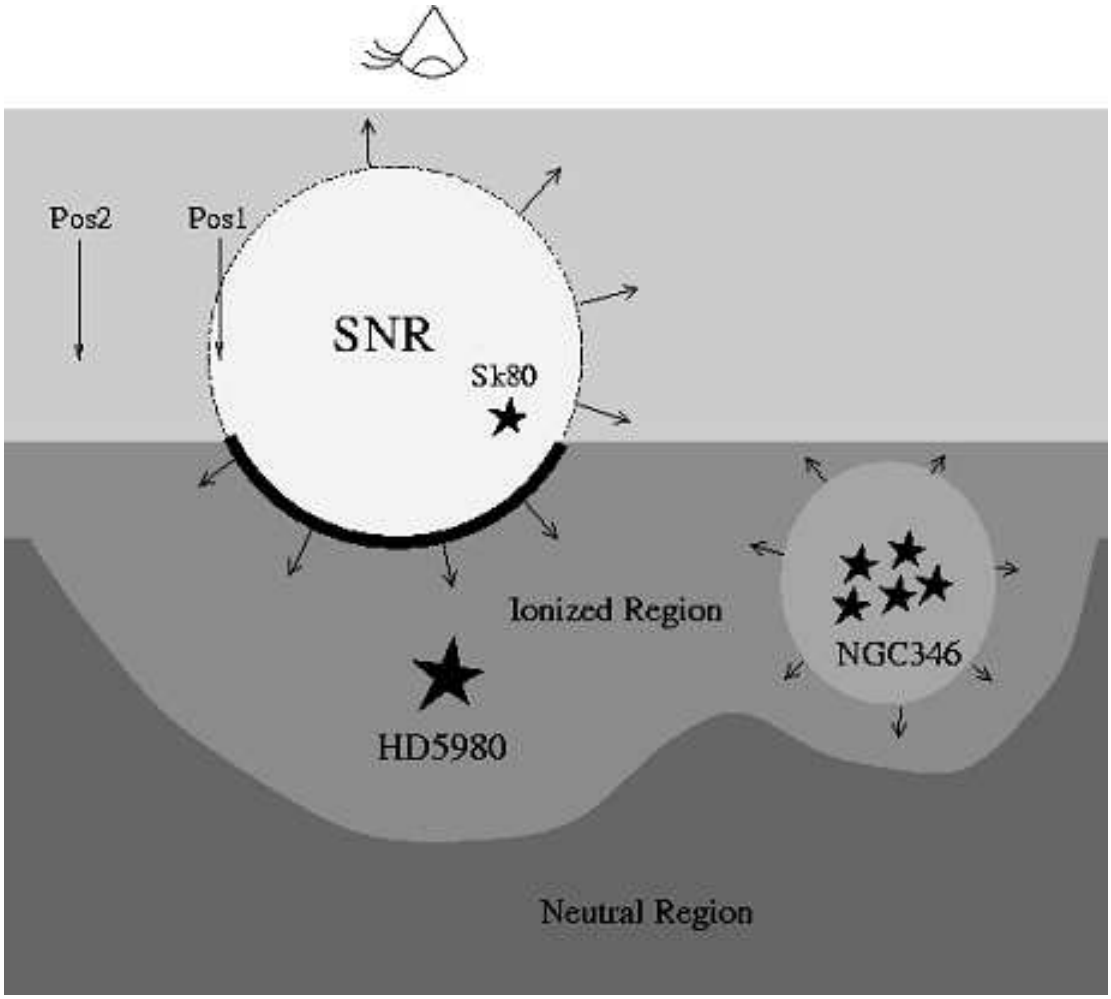

Figure 1.6 Danforth et al. (2003) created this model of SNR 0057-724 and N S66 using line spectra in the ultraviolet and optical to measure radial velocities at position 1 (Pos1). Since position 2 (Pos2) lies outside the remnant, no line emission is measured there. SNR 0057-724 is located on the near side of N S66 and is interacting with the denser, ionized gas on the rear side. Fuse O VI and C III as well as X-ray emission forms from this shock interaction. The approaching side of the shock is traveling through a less dense medium and is therefore harder to detect. HD 5980, an eclipsing binary system, is located behind the SNR, while Sk 80, an O7 Ia star, is either within or in front of the SNR. The massive stars in the field have ionized a layer of nebular material and are felt to keep the swept-up gas behind the shock wave from recombining completely. A slowly expanding bubble around NGC 346 is powered by stellar winds and thermal pressure. Fantastic studies of this nature greatly enhance our understanding of SNRs and their environments.

emission, shock-heated dust, atomic fine-structure lines and molecular lines. While most SNRs could have significant infrared emission, many are located in regions of the Milky Way too confused with bright H II regions and atomic or molecular clouds along the line of sight.

They were able to find 18 infrared counterparts from a list of 95 known SNRs and analyse them based on infrared colours from the wavelengths above. These infrared colours suggested emission from molecular lines (9), fine-structure lines (3), polycyclic aromatic hydrocarbons (4), or a combination thereof. None were dominated by synchrotron radiation at mid-infrared wavelengths. This detected sample emphasized remnants interacting with relatively dense gas, most with molecular or ionic lines due to shock cooling in the mid-infrared. *Spitzer Space Telescope* observations of LMC SNRs (Williams et al. 2006) (N11L, N44, N206, N63A and N157B) suggest infrared line emission is a significant contributor.

1.8.5 Radio

Molecular emission can occur in the infrared and radio range due to rotation, vibrations and electronic transitions. Under certain conditions, masers (Microwave Amplification by Stimulated emission of Radiation) occur in SNRs which indicate very specific environments in terms of energy and density. Maser emission is observed both outside and within SNR shocks despite the once held belief that these shocks should dissociate molecules.

As noted by Yusef-Zadeh et al. (2003), OH masers at 1720 MHz have provided powerful signatures of SNR-molecular cloud interaction sites. Radio surveys have uncovered 19 SNRs in the Galaxy accompanied by OH maser emission located behind the shock front from the expansion of a SNR encountering a molecular cloud. Yusef-Zadeh et al. (2003) presents a model of this interaction in which X-ray emission from the remnant enhances the production of OH molecules. They also note a strong association between maser emitting SNRs and mixed-morphology or thermal composite SNRs.

Radio-continuum surveys continue to be the main source for the identification of new SNRs. Morphology, linear polarization and non-thermal spectral indices are the classical tools used to identify new SNRs. Another technique compares radio maps from the Effelsberg survey with *IRAS* 60 or 100 μm surveys since they have similar angular resolutions. This method is based on the fact that the ratio of infrared to radio flux density for H II regions is about an order of magnitude stronger than that for SNRs (Reich 2002).

The majority of radio identified SNRs have a shell morphology. These shells are strong emitters of synchrotron radiation and their spectra is described by a simple power law:

$$S_\nu \propto \nu^\alpha \tag{1.41}$$

with S_ν the observed flux density at the observing frequency, α the spectral index and ν the observing frequency.

Most SNRs are in their adiabatic phase and have spectral indices near –0.5 which is expected for a strong shock and a compression factor of 4. Magnetic fields are tangential for the majority while young SNRs show steeper spectra (–0.6 to –0.8) and radially directed magnetic fields (Reich 2002). Radio detections can occur as early as four days after a SN event (SN1993J, Type IIb in M8). Young SNRs are identified by measurement of short lived isotopes such as ^{44}Ti which has a mean lifetime of 60 years.

SNRs in the adiabatic phase show a number of effects from their interaction with the ISM. Their bi-symmetric morphology and tangential magnetic field in the shell have been used to derive the orientation of the interstellar magnetic field. OH maser emission studies of adiabatic SNRs indicate small condensations within the shell where the magnetic field strength ranges up to about 0.5×10^{-3} Gauss (Reich 2002).

In the radiative phase, SNRs shells are highly compressed while the interior remains hot and therefore still detectable by X-ray observations. The shells also have a filamentary radio morphology also seen optically with a perfect correspondence between the two domains.

Even if the pulsar from a SNR cannot be detected, its wind may become pressure-confined forming a isotropically radiating nebula, which classifies the remnant as a core-collapse event. These objects have cores with a flat radio spectrum within a steep non-thermal shell[20] requiring low and high frequency observations in order to separate both components (Reich 2002).

Dulk & Slee (1975) reported spectral turnovers in several SNRs in the Galactic plane at low frequencies. This has been confirmed by Kassim (1989) using measurements at 30.9 and 57.5 MHz. The spectral index above $\sim$ 100 MHz is negative and typical of most SNRs. Although there is evidence that the emitting regions of SNRs continue producing a similar spectral index at lower frequencies, the spectral indices we observe 'turns over' below 100 MHz because of absorption by low density ionized gas in the intervening ISM (Kassim 1989). It is possible to constrain the physical properties of the ionized gas responsible for the absorption, and three accepted ionized components of the ISM which absorb low frequency radio emission include: H II regions, extended H II region envelopes and warm ionized mediums. Lacey et al. (2001) also attributes the spectral turnover found on the western side of Galactic SNR W49B to extrinsic free-free absorption by an

[20] Plerions including the Crab Nebula do not have an obvious shell.

intervening H II cloud. For more information the reader is referred to Kassim (1989) and Bhatnager (2001).

1.9 Compact Objects and Pulsar Wind Nebulae in SNRs

For many years, with the exception of the Crab and Vela pulsar, the study of compact objects in SNRs have been plagued by lack of evidence. Stars greater than 8 $M_\odot$ are thought to end with a collapse of their cores forming either black holes or neutron stars. There may also be a limiting mass of a 100 $M_\odot$, above which oxygen burning leads to the complete destruction of the star. With the maximum mass of a neutron star in the range of 1.5 – 2.0 $M_\odot$, more massive stars may form black holes directly. However, the generation of a supernova shock requires the initial formation of a neutron star, otherwise the star would remain bound to the black hole and be accreted by it. An example of the latter may be the massive black hole Cygnus X-1 (Chevalier 1996).

The time required to create a supernova shock may be of the order of one second. After this amount of time, there may be other ways to form a black hole. One idea is that reverse shock waves causes matter to fall back into the core. As much as 0.1 $M_\odot$ could fall back into the core of the star within hours after the explosion (Chevalier 1996). This may be a low estimate, and if so, there may be an initial core mass range whereby a detonation could occur from the addition of mass originally ejected. Another way that Chevalier (1996) cites to achieve a black hole after SN is the formation of a hot neutron star than remains stable long enough to create a shock wave, then cools with an ensuing collapse.

These objects would be difficult to observe since most of the radiation field becomes trapped in the inflow. The low radiative output of black holes has led to the suggestion that SNRs that should have a central compact object, such as SN 1987A and Cas A, may be harboring a black hole.

Observations of SNe have not yielded any information about the nature of central compact objects, and there is a general lack of observed pulsars within shell SNRs. Some suggest that either these SNRs do not contain a pulsar or they are unusually weak (Chevalier 1996).

Newly born pulsars have very short periods in the range of 10–100 ms with a rotational energy approaching the 10^{51} ergs of kinetic energy released by the surrounding SN explosion. These young pulsars are observed to ‘spin-down’, increasing their periods and presumably releasing kinetic energy into its surroundings. For the youngest sources, the spin-down luminosity is about 10^{35} – 10^{39} erg s^{-1} (Gaensler 2003). This energy dissipation is possibly due to torques produced by extreme electromagnetic fields near the surface of a neutron star. Away from the star, the torques pump energy into a relativistic magnetized wind so that the star

ultimately deposits its rotational energy into its surroundings. If this wind is subjected to external pressure, this source becomes directly observable as the pulsar wind nebulae (PWN).

Chevalier (1998) notes that the evolution of these nebulae can be divided into six observational phases. Most synchrotron radiation is absorbed by the surrounding SNR in phase I (0 to 100 yrs); free-free absorption plays a role in radio emission and photoabsorption for X-rays. The pulsar provides almost constant power during phase II (100 to 1000 yrs) in which the SNR is optically thin. The nebula expands with little acceleration at the outer edge. Power input from the pulsar drops steeply during phase III (1000 to 10,000 yrs) allowing adiabatic expansion approaching free expansion within the SNR. These nebulae are also called 'bubble PWNe', a description of their expansion. Phase IV (10,000 to 100,000 yrs) marks the point where the SNR's reverse shock slows the edge of the nebula. This occurs during the SNR's Sedov-Taylor phase. If the pulsar has been moving with a velocity of hundreds of km s^{-1}, a bow shock may form as it approaches the edge of the SNR shell. Known as phase V (100,000 yrs), this is a brief stage in which the pulsar wind interacts with the shell of the radiative SNR. These nebulae are also called 'bow shock PWNe'. Phase VI occurs if the pulsar leaves the SNR and interacts with the ISM yielding potential information about it.

Classic bubble PWNe (phase III), such as the Crab Nebula for which a shell has yet to be found, can be studied by making use of the difference in synchrotron lifetimes of emitting particles at radio and X-ray energies. While the much longer radio lifetime can trace the history of the pulsar's spin down since birth, the shorter X-ray lifetime traces the pulsar's current behavior (Gaensler 2003).

Bubble PWN structure can be divided into three zones. In the inner region, a relativistic cold particle wind may be launched from the pulsar, but this is yet to be observed. At a distance, a termination shock forms from the balancing of the outflowing wind pressure with gas and magnetic pressure from the surrounding region. At this shock, particles are thermalized and accelerated to X-ray emitting energies. Observable synchrotron emission is seen downstream as the flow continues to decelerate.

Termination shocks have been observed by *Chandra*, confirming that this model has validity (Gaensler 2003). *Chandra* observations have found a toroidal, rather than a spherical geometry to the termination shocks of these PWNe, sometimes with collimated 'jets' oriented along the symmetry axis defined by the shocks. It is hoped that future observations of PWNe will give information about the properties of neutron stars including spin axis orientations, magnetic fields, birth histories and pulsar emission mechanisms.

Bow shock PWNe (phase V) are also divided into zones. These include a freely flowing wind zone, a shocked wind zone, a shocked ISM zone and a ambient undisturbed material zone. Two separate emission mechanisms are thought to be observable. Hα emission is generated from collisional excitation of ambient

neutrals at the outer shock. The second mechanism produces X-ray and radio synchrotron emission from an internally shocked pulsar wind. Both of these have been detected in B1957+20 (Stappers 2003).

The shape and brightness of bow shocks may prove to be a valuable probe of the ISM. Observations of the time evolution of Hα bow shocks over timescales of 5 to 10 years may provide a unique probe of density fluctuations in the ISM on scales of a 1000 AU (Gaensler 2003).

1.10 Statistics of SNRs

Statistics of SNRs can be very useful in the study of both Galactic and extragalactic populations of SNRs. They can help determine the sample completeness, evolutionary stage, age, formation rate and distance.

A paper by Xu et al. (2005) gives an excellent review of methods used to find parameters associated with SNRs. For example, they note that there are five current methods to detect the age of a remnant:

1. If associated with a neutron star, age can be approximated by the pulsar's characteristic age as a ratio of rotation period and twice the rate of change of that period ($t = P/2\dot{P}$).

2. If the total explosion energy of the progenitor and the energy loss rate of the remnant is known, this ratio can also give an age of the remnant ($t = E/\dot{E}$).

3. The ratio of the remnant's linear radius (R) and expanding velocity (v_s) is proportional to its dynamical age by a constant, C ($t = CR/v_s$). This constant depends on the phase and type of remnant.

4. SNRs with a known radius and thermal temperature (T) measured by X-ray observations can also be dated ($t = 3.8 \times 10^2 R_{pc}(kT)_{\rm keV}^{-1/2}$yr).

5. If the remnant has a known spectral turnover or break due to synchrotron losses and its magnetic field, B is known, age can also be approximated ($t \approx 40\,000 B^{-1.5} v_b^{-0.5}$yr).

Sadly, the necessary parameters to complete these equations are difficult to obtain even for Galactic remnants, much less those at greater distances in other galaxies. Uncertainties are as large as a magnitude with most.

Distances to SNRs are attempted by observations of extinction, X-ray emission, supernova magnitude, use of background star, SNR kinematics and H I absorption. The latter may be especially useful in deducing the distance to Galactic remnants, but is in no way precise.

Given what we now understand about the evolution of SNRs, it is a fairly trivial assumption (and observation) that small SNRs are bright while large ones are faint. As they age, SNRs both expand and fade.

Thus, one might attempt to study the evolution of these objects by plotting their luminosity versus diameter relation. But it is even safer, given uncertainties in distance to plot the average surface brightness (Σ, total flux density divided by solid angle) versus their mean diameter, D. This reduces distance related uncertainties to one power.

The idea that the $\Sigma - D$ relation may be useful originated in theoretical discussions by Shklovskii (1960). D. K. Milne appears to have been the first to produce an observational $\Sigma - D$ plot, although one such plot can also be found in a study of 25 SNRs by Poveda & Woltjer (1968). The first theoretical $\Sigma - D$ relation was in the form of:

$$\Sigma_\nu = \mathrm{A}\ D^{-\beta} \tag{1.42}$$

where A is a constant and β is the slope of the log–log plot. The subscript ν for frequency is also very important as this relation changes for the same group of SNRs at different frequencies.

It was hoped that this relation would allow distance determinations to SNRs, but there are several problems with this idea. Guseinov et al. (2003) points out that some parts of SNRs have low intensity so that the entire shell cannot be observed. Flux density and angular size measurement problems may occur if the SNR is projected onto a H II region. One must also account for a SN's explosion energy, the density of the interstellar medium and the central neutron star or pulsar (Guseinov et al. 2003). These selection effects limit the use of this relation.

Study of extragalactic SNRs have led to some excitement with respect to the $\Sigma - D$ relation in recent years, since they are at a known distance. As noted in Urošević (2002) and Urošević (2003), this may eliminate what is known as the Malmquist bias; a selection effect dependent on distance where only the brightest objects can be seen. But this concept has been oversimplified in the literature and certainly selection effects also plague these studies due to limitations in the sensitivity and resolution of current telescope technology.

Mathewson et al. (1983b) presented the relation between radio surface brightness at 408 MHz and optical diameter for 27 SNRs in the MC's. They limit their evaluation to Type II SNRs, finding:

$$\Sigma_{408\mathrm{MHz}} = 1.5 \times 10^{-16} D^{-2.6} \mathrm{Wm^{-2}Hz^{-1}sr^{-1}}. \tag{1.43}$$

Using *Einstein* observations, they also found the X-ray surface brightness as a function of linear optical diameter for confirmed SNRs in the LMC and SMC to be:

$$\Sigma_{\rm X-ray} = 1.1 D_{\rm pc}^{-3.3} {\rm ergs\ cm^{-2} s^{-1} sr^{-1}}. \quad (1.44)$$

Remnant types were not separated for the latter equation.

Urošević (2002) and Arbutina et al. (2004) have recently written interesting papers concerning the $\Sigma - D$ relation. Urošević (2002) reviews the empirical Galactic and extragalactic $\Sigma - D$ relations (including M31, M33, M82, SMC and LMC) for SNRs while searching for a connection to Galactic radio loops (Loop I, II, III and IV). These loops are thought by some to have a SNR origin. Except for the starburst galaxy, M82 thought to be composed of young small diameter bright SNRs[21], he finds a fairly persistent slope (β) that approaches 2. Consideration of Galactic radio loops tend to push the population of slopes ever closer to this value. For M82, the Σ_ν = A $D^{-\beta}$ relation was found to have a β value approaching 3.6 at 8.4 GHz. At 1 GHz, they found β to be 4.08 ± 0.39.

Arbutina et al. (2004) discuss the so-called trivial relation of $\Sigma - D$. This basically states that $\Sigma_\nu \propto D^{-2}$. Even if the flux density S_ν (or luminosity $L_\nu \propto \Sigma_\nu\, d^2$; where d is distance) is random, i.e. there is no relation at all, we can still get $\Sigma_\nu \propto D^{-2}$ simply because the inverse square dependence on D is implied by the definition of surface brightness.

There may be a dependence on ISM density as noted in Arbutina & Urošević (2005). They compared the $\Sigma - D$ relation of a group of oxygen-rich SNRs assumed to have evolved in a denser medium than a population of Balmer-dominated SNRs. Although they found no difference in the slope of these relations, oxygen rich remnants were brighter as a group. Their conclusions are not definitive at this time and will require larger samples than currently available.

The $\Sigma - D$ relation is likely to remain controversial for some time. Over the past 40 years, it has gone completely out of favor to return once again. Throughout this paper, I will quote its value without much comment, but the reader should beware of accepting any value as gospel.

Another diagnostic of SNR evolution is the integral number-diameter relation; $N(< D)$. The number of remnants less than a given diameter should be constrained by the time a remnant takes to evolve to its diameter times the local SN formation rate. Another way of saying this is, if all SNRs evolve similarly, the number of remnants with diameter up to a given D is simply the age, t, of the remnant at the limiting diameter divided by the average time between remnant producing supernovae. For remnants in the free expansion

[21] Green (2004) points out that selection effects, especially sensitivity, limit the usefulness of the $\Sigma - D$ relation in the case of M82. However, these criticisms were successfully refuted by Urošević et al. (2005) using Monte Carlo simulations.

phase, $D \propto t$, so $N(< D) \propto D$. In the adiabatic Sedov-Taylor phase, $D \propto t^{2/5}$, so $N(< D) \propto D^{5/2}$ and so forth (Green 1988).

For Galactic remnants, Clark & Caswell (1976) find that the $N(< D)$ relation obeys $N = 8 \times 10^{-3} D^{5/2}$, consistent with most SNRs being in the adiabatic phase of evolution. However, these measurements were felt to be plagued with uncertainties and distance recalibrations by B. Y. Mills led to a $N \propto D^{1.15}$ relation (Reynolds 1988). Although a similar relation was discovered for M31, the LMC and M33 both have a $N \propto D^1$ relation. This discrepancy could be due to selection effects or different phases of SNR evolution as a population.

In fact, Berkhuijsen (1987) pointed out that the observed exponent of + 1 of cumulative $N(\leq D) \propto D$ relations could result from a random distribution of diameters possibly ascribed to variations in ambient density. After corrections to an ambient density $n_0 = 1\text{cm}^{-3}$ for different groups of SNRs in the LMC, SMC and Galaxy, Berkhuijsen (1987) finds the exponents increase to the +2 to +3 range, yet the exponent of +1 still cannot be statistically ruled out.

Finally, another relation that is rather interesting is a plot of SNR diameter versus Galactic height. Xu et al. (2005) plotted the linear diameter of 190 Galactic SNRs to the Galaxy's height finding that those at lower heights tend to be smaller. This is understandable if one considers that the distribution of the ISM is such that it is much denser near the Galactic plane and exponentially decreases as one moves away from it. Of course, one also assumes that SNRs expand more rapidly in a low density environment.

1.11 Galactic SNRs

Although the optical Crab Nebula was identified with the historical SN AD 1054, it was the development of radio astronomy in the 1950s that led to the identification of many more SNRs in the Galaxy (Stephenson & Green 2002). R. Hanbury Brown and C. Hazard identified radio emission from Tycho's SN of AD 1572 which was later associated with a faint optical nebulosity. Other radio sources including IC443 and the Cygnus Loop, both associated with optical nebulosities, were soon identified as SNRs. Subsequent observations, principally at radio wavelengths, have led to the identification of most of the known Galactic SNRs.

Galactic SNRs range in angular size from a few arcmin to several degrees, most between $10'$ and 1°. This correlates to a diameter between a few and 100 pc. Most SNRs are named based on the centroid of their radio emission expressed in Galactic coordinates, although the better known, brighter remnants have individual names (e.g. the 'Crab Nebula'), or other names based on earlier catalogues.

Examples of Galactic shell remnants include Tycho's and Kepler's SNe of AD 1572 and 1604, respectively, G120.1-1.4 and G4.5+6.8. G327.6+14.6 is also a shell remnant associated with the supernova event in 1006 AD. Older shell SNRs include IC443 (G189.1+30) and the Cygnus Loop (G74.0-8.5). These older shell SNRs are often far from circular and have considerable asymmetry in the brightness of the emission from their rims, since the local ISM has varying density.

Typical flux densities from Galactic shell SNRs give a spectral index near –0.5 while younger ones tend to be steeper. Their radio emission tend to be polarised, enhancing the idea of a synchrotron process. There is also thermal emission associated with these shells at optical and X-ray wavelengths. As I have noted, a few shell SNRs show a harder, non-thermal component to their X-ray emission at higher energies.

The filled-center 'Crab Nebulae' (G184.6-5.8) is unusual in the sense that it is clearly powered by a central pulsar. Galactic plerions typically have a radio spectral index of about –0.1, similar to that from H II regions, except that the underlying emission is non-thermal. Examples of Galactic plerions also show optical emission, both thermal and non-thermal in the case of the Crab Nebula, and non-thermal X-ray emission.

Plerions are the hardest to identify because of their diffuse structure and similarity of its spectrum to H II regions. It also seems certain that some of these remnant classifications will change because of higher sensitivity observations. For example, G21.5-0.9, originally classified as a plerion from radio observations is now recognised as a composite remnant after a faint X-ray shell was reported in 2000. MSH 15-56 (G326.3-1.8) is another example of a composite Galactic SNR.

Stephenson & Green (2002) notes that the optical emission from some Galactic shell SNRs show 'Balmer dominated' spectra that have strong hydrogen lines with both narrow and broad components. These lines are modeled in terms of a non-radiative shock in a partly neutral medium; the narrow component coming from collisionally excited hydrogen and the broad component from charge exchange producing fast moving hydrogen. The term non-radiative here is used as the timescale for recombination. Radiation behind the shock is then long compared with the dynamical timescale.

Anyone who studies Galactic SNRs and has a computer is familiar with D. A. Green's Catalogue of SNRs at http://www.mrao.cam.ac.uk/surveys/snrs/ . This site not only gives summary listings for all known Galactic SNRs but also detailed information for each, including current references.

1.11.1 Selection Effects

The dominant selection effects in the study of SNRs are most applicable at radio wavelengths. Green (2004) notes that simplistically, two selection effects apply to the identification of Galactic SNRs. These include difficulty in identifying faint (low surface brightness) remnants and small angular size remnants. Since the Galactic background varies with position, the first of these is not a uniform effect and the surface brightness limit (1 GHz) for completeness of the current Green Galactic SNR catalogue is $\sim 10^{-20}$ W m^{-2} Hz^{-1} sr^{-1}. However only 64 of 217 Galactic SNRs are above this limit and remnants have been detected down to 2×10^{-22} W m^{-2} Hz^{-1} sr^{-1} at 1 GHz in the Effelsberg Survey and 5×10^{-22} W m^{-2} Hz^{-1} sr^{-1} in the MOST Survey.

Since the beamwidths of radio surveys vary greatly, it is also hard to pin down an angular size limit to Galactic SNRs. Based on the MOST survey, this limit is currently near 2 arcmin. This effect selects against young but distant Galactic remnants.

SNRs in external galaxies have different selection effects as more reliable distances are available for these. For unresolved sources, in most radio studies the dominant selection effect is a flux density limit, which corresponds to a fixed luminosity limit for a particular galaxy (Green 2004).

1.11.2 Spectral Index

Trushkin (1998) presented radio-continuum spectra for 200 Galactic SNRs using both their measurements of flux density of 120 SNRs with the RATAN-600 radio telescope and data found in the literature including Green's catalog (Green 1998). They found the sample mean spectral indices at 0.4 and 4.0 GHz to be -0.41 ± 0.34 and -0.50 ± 0.21, respectively. The distributions at each frequency had no significant difference although the number of SNRs between $-0.8 < \alpha_{4\ \mathrm{GHz}} < -0.6$ was slightly higher. They also note it is unlikely compact and young SNRs have spectral indices that are steeper than extended 'adult' ones. Attempts by such authors as Weiler (1983) have been made to relate different mean spectral indices to classes including shell, plerions and composite SNRs. However, given the diversity of individual SNRs, this really doesn't seem feasible.

It is possible to study different spectral fits for Galactic SNRs at the CATS database found at http://cats.sao.ru/ . This site points to catalogues containing SNR flux density measurements.

Trushkin (1998) also found that 70 out of 190 SNR spectra (37%) had clear low frequency turnovers caused by absorption in the thermal background of the Galaxy[22]. The distribution of the flux maximum frequency shows that 50 to 150 MHz is most common.

[22] SNRs G74.1-1.2, G41.1-0.3 and G180.0-1.7 had high frequency turnovers.

Of 16 SNRs with active neutron stars, the spectra of 15 have no low frequency turnover. This may be due to the contribution of pulsars inside the remnants that contribute energy in the 20 – 50 MHz range. In fact, the Trushkin (1998) spectral catalogue contain 10 SNRs with a clear turn up at low frequencies; 5 of these contain radio pulsars.

1.11.3 Benefits of Extragalactic SNR Observations

Assuming that the Cygnus Loop is 18,000 years old and the supernova rate is 5 per century within the Galaxy, there should be about 900 SNRs younger than the Cygnus Loop. D. A. Green's list contains only 231 SNRs and some of these are older than the Cygnus Loop.

Of 182 known Galactic SNRs reported in 1994, all had been detected in radio, 70 in X-ray using *ROSAT* and 40 in the optical domain (Magnier et al. 1995). Galactic SNRs are found in the longer wavelength radio domain (Long 1996) but not as readily in optical or X-ray domains because they have a diffuse low-surface brightness and are embedded within the Galactic plane. This is where gas and dust strongly absorb X-ray and optical radiation. New Galactic radio and X-ray studies continually identify unknown SNRs missed in previous surveys because of interference by absorption.

The distances to Galactic SNRs are not very precise. Few reliable techniques exist for measuring Galactic SNR distance. Among the best are proper motion of expansion measurements, but these are useful only for bright, young nearby SNRs (Magnier et al. 1995). Other less reliable methods include SNR placement within the Galactic rotation curve, identification of intervening H I clouds and the $\Sigma - D$ relation. Because of diameter variations, the $\Sigma - D$ relation is believed to give distance uncertainties to at least a factor of three (Berkhuijsen 1986). Distances are relatively better known for SNRs located within nearby spiral galaxies. This is because the distances to these galaxies can be measured independently.

SNRs located within these galaxies can be studied as a group, giving a better understanding of their radial distribution, associations with spiral arms and progenitor populations. The latter may include OB associations and stars within H II regions. Large samples of extragalactic SNRs, unavailable from Galactic observations, also give important information about a galaxy's supernova formation rate. Since the distances to all of the SNRs in a study sample are nearly identical, a better understanding of the $\Sigma - D$ and $N(< D)$ relation may also be possible.

There is less extinction or confusion when face-on spirals are observed, allowing the true shape of these SNRs to be determined. Of course, there is a trade-off. Although small angular sizes make total flux density

estimates easier, they also make accurate determination of SNR diameters difficult to obtain (Long 1996).

1.12 Sculptor Group Galaxy NGC 300 and the SMC

I conclude this chapter with a summary of current SNR research in NGC 300 and the SMC. This is obviously relevant to the chapters that follow. Appendix B at the end gives a summary of research in other nearby galaxies. This may be useful to other researchers in the field.

1.12.1 Sculptor Group Galaxies

The Sculptor (a.k.a. South Polar) group of galaxies include its edge-on centerpiece, NGC 253, and the spirals NGC 300 and NGC 7793. NGC 300 and NGC 7793 have been the subject of numerous SNR studies at radio, X-ray and optical wavelengths. Since they have been studied together on several occasions, the current discussion may be relevant to both galaxies. NGC 300 is an Sc galaxy with an inclination[23] of 42 deg. Although it has a spiral pattern, its spiral arms are not well-defined. At a distance of about 2 Mpc, one arcsecond corresponds to $\sim$ 9.8 pc.

D'Odorico et al. (1980) searched NGC 300, finding seven candidate SNRs. Two, DDB 2 and DDB 5, were later confirmed by optical spectroscopy in 1983. Blair & Long (1997) searched eight fields in NGC 300 and two fields in NGC 7793 using interference filters and CCD imaging at the Cassegrain focus of the 2.5-meter du Pont Telescope at Las Campanas Observatory. They identified nebulae bright in [S II] relative to Hα creating a list of 28 candidates for each galaxy. Optical (480–690 nm) long-slit CCD spectra confirmed that selected SNR candidates had [S II]/Hα ratios greater than 0.4. They note that their Hα images were contaminated by [N II] decreasing the [S II]/Hα ratios of the CCD images.

While the canonical value of 0.4 in the ratio of [S II] to Hα has worked well in the Milky Way and Local Group galaxies to separate shock-heated nebulae from photoionized gas, the exact value of this cutoff has not been important because there is a gap in the distribution. Photoionized H II regions tend to show a ratio of $\sim$ 0.2 or below. The dividing line between the [S II]:Hα ratios appropriate for photoionized and shock-heated nebulae appears to be much less distinct in these Sculptor Group galaxies, causing some confusion and incompleteness in the samples. This confusion effect is especially pronounced in the case of NGC 7793, where the observed [S II] to Hα ratio in a few of the most diffuse photoionized H II regions rises well above 0.4.

[23] Defined here as the angle between the plane of the sky and the major axis of the galaxy.

Blair & Long (1997) also determined the optical diameter for their sources, noting that the majority of the objects were reasonably well resolved. They based their measurements on the earlier distance value of 2.1 Mpc, noting that the smallest SNRs in NGC 300 are at the seeing disk value of 1.5 ″. These apparent diameters should be considered upper limits. They found the majority of SNRs in both of these galaxies to have apparent diameters in the 25–75 pc range. This reflected a well-evolved ISM-dominated population for which their search technique worked best. However, Blair & Long (1997) reported 16 (12 in NGC 7793 alone) objects with diameters in the 75–260 pc range for which there were no Galactic counterparts; a trend also seen in other galaxies (e.g. M33). These objects may represent superbubbles which are remnants formed from more than one supernova explosion whose ejecta mixes with stellar winds found in a group of massive stars. Dunne et al. (2001) have studied X-rays from superbubbles of about the same size located within the LMC and found that this emission is brighter than that theoretically expected for a wind-blown bubble alone, again suggesting that X-ray emission has been enhanced by interactions with SNRs.

Read & Pietsch (2001) conducted an analysis of *ROSAT* PSPC and HRI observations of NGC 300, presenting a source list classifying each on the basis of their temporal, spectral (using hardness ratios) and multi-wavelength characteristics. NGC 300 had been observed by *ROSAT* five times between 1991 and 1997, resulting in two PSPC exposures totaling $\sim$ 46 ks and three HRI exposures totaling $\sim$ 40 ks. At X-ray energies between 0.1–2.4 keV, Read & Pietsch (2001) found 26 PSPC and 10 HRI sources within the optical D_{25} disk (defined by de Vaucouleurs et al. 1991) of NGC 300. Three of their X-ray sources were coincident with Blair & Long (1997) SNRs and another suspicious SNR candidate was associated with the Blair & Long (1997) H II region, BL97-H13. Two additional SNR candidates were found based on X-ray spectrum and non-variability.

Carpano et al. (2004) recently presented X-ray properties of 73 point sources in NGC 300 using a maximum likelihood threshold[24] of 100; a threshold high enough to exclude fictitious objects from the final list. Work is in progress to characterize these sources further which include searches for optical counterparts.

Working on the assumption that radio SNRs could be found within H II regions, Pannuti et al. (2000) searched NGC 300 using VLA 6 cm and 20 cm observations. They used previously published optical results (e.g. H II regions reported by Deharveng et al. 1988), their own Hα optical images and archived *ROSAT* X-ray data to find a total of 17 SNR candidates. Three candidates were known from optically selected SNRs and 14 were new; overlooked by the [S II]/Hα criterion of $\geq$ 0.4. Four radio selected candidates possessed some

[24]Probablities, P, are related to maximum likelihood values, L, by the relation $P = 1 - e^{-L}$. A likelihood of 10 corresponds to a Gaussian significance of 4.0 σ.

detectable X-ray emission while their analysis of *ROSAT* X-ray data (including spectral fits from Read et al. 1997) yielded an X-ray selected sample of six soft spectrum sources coincident with regions of Hα emission. Two of these were common to both radio and optically selected SNRs.

Pannuti et al. (2000) added 16 (14 radio and 2 X-ray) new SNR candidates to those found by Blair & Long (1997) suggesting that optical surveys have a possible selection effect. SNRs identified through optical methods represent those located in regions with low confusion from Hα emission, away from star forming regions. Hard spectrum X-ray (kT > 1 keV) SNRs with no optical counterparts are also selected against. On the other hand, radio selection can only identify candidates that are associated with H II regions. Thus, this sample is biased toward star forming regions. The conclusion is that, to find all of the SNRs in a galaxy, both approaches are needed and compliment each other.

1.12.2 Small Magellanic Cloud

According to Dickel (2005), we are approaching 50 SNRs in the Magellanic Clouds that have been studied in both radio and X-ray. Thus, they provide a good sample of remnants all at a known distance for use in statistical and comparative studies.

The SMC is an irregular galaxy in our Local Group seen in the southern hemisphere. According to Westerlund (1997), the most likely value for the distance moduli of the SMC is $\sim 18.90 \pm 0.10$. This translates to approximately 60.2 kpc. Feast (1999) reports a slightly further distance of $\sim$ 65 kpc. Current observations support the conclusion that the SMC is seen nearly edge on. Cepheid depth estimates for it are between 15 and 20 kpc but may extend as far as 23 kpc (Feast 1991).

Many different criteria have been used in the past to identify SNRs in the MCs. For example, Westerlund (1997) lists his criteria for the identification of SNRs in the Clouds as:

1. the source has an optical emission with a [S II] to (Hα + [N II]) ratio greater than or equal to 0.6, a looped or filamentary structure in Hα and a Hα flux density different from one expected from the radio flux density for a thermal source;

2. the source must be a non-thermal radio source; and,

3. the source should be an extended soft X-ray source.

Of course, each source is an entity in itself and must be considered based on all information available.

SNRs identifications occurred first in the LMC, but the SMC was not far behind. Studies by Mathewson & Clarke (1972, 1973b) used the Mills Cross of the Molonglo Radio Observatory at 408 MHz and narrow-band image tube photography (with the 102-cm reflector at Siding Spring Observatory) to identify 2 SNRs in the SMC.

In 1986, an international collaboration studied both the LMC and SMC at several radio frequencies using the Parkes 64-meter telescope. Up to six frequencies ranging from 1.4 and 8.55 GHz were used to find a total of 483 sources towards the LMC and 224 towards the SMC (Filipović et al. 1998b).

In this study, from a list of 19 SMC SNRs and SNR candidates obtained by Ye (1988), 10 were confirmed as certain SNRs. Six well-known SNRs and three SNR candidates could not be detected in any of the Parkes radio surveys due to flux density limits. Filipović et al. (1998b) reported two candidate SNRs and felt that more SNRs existed in the MCs, confused with H II regions.

Selection criteria used by Filipović et al. (1998b) to identify sources included first separating them into three groups based on radio spectrum. These were pioneered by McGee & Newton (1972) and include:

1. background sources with $-1.8 < \alpha < -0.6$;
2. SNRs with, $-0.8 < \alpha < -0.2$; and,
3. H II regions with a flat spectrum, $\alpha > -0.2$.

Their criteria (see Section 4.1 in Filipović et al. 1998b) then made use of comparisons with all other multi-wavelength studies available. In addition, they visually inspected sources for position, extension and structure as part of their criteria.

Seward & Mitchell (1981) used the *Einstein* Observatory to study a 40 square degree region centered on the SMC. Of the twenty eight sources listed in their Table 2, one previously unknown SNR was discovered (the second brightest source observed) and four soft X-ray sources were suspected. These were later confirmed as SNRs.

Haberl et al. (2000) used pointed *ROSAT* PSPC observations to verify 17 SMC X-ray SNRs, all previously reported as remnants. They also found two additional extended sources that they suggest as SNR candidates. Their criteria were based on Haberl & Pietsch (1999).

van der Heyden (2004) presented a detailed *XMM-Newton* spectral analysis of 13 of the 16 previously known SNRs in the SMC with detailed X-ray images of individual SNRs revealing a range of different morphological features. Based on their model, they find eight sources (DEM S 32, IKT 2, HFPK 419, IKT

6, IKT 16, IKT 18 AND IKT 23) consistent with SNRs in the Sedov-Taylor phase. Two (IKT 6 and IKT 23) have a shell morphology with oxygen-rich X-ray emission from their centers. Although each remnant had its own individual abundance profile, enhanced oxygen, nitrogen and magnesium in their spectra were felt to indicate a core-collapse origin. Based on heavy metal abundances, all of these sources are most likely the result of core-collapse progenitors.

They found four remnants (KT4, IKT 5, DEM S 128 and IKT 25) in or at the beginning their radiative cooling stage. The X-ray emission from these four SNRs are most likely from the ejecta remains of Type Ia SNe. This was because they had similar spectral features including a broad spectral hump around the Fe-L complex ($\sim$ 0.9 keV). It was the excess emission around 0.9 keV and high Fe abundances that strongly suggested their origin.

Comparison of abundance estimates (van der Heyden 2004) for different SNRs reveal that larger remnants have lower values while smaller ones have higher values. This implies that the older remnants have swept-up so much ISM that their abundances approach ISM values. SNR observations indicate the mean SMC ISM hydrogen density derived from Sedov-Taylor model fits is $\sim 0.32 \times 10^6$ m^{-3}. This is a magnitude lower than the hydrogen density derived from Sedov-Taylor fits of LMC remnants ($\sim 1.8 \times 10^6$ m^{-3}). Since X-ray emission scales with density squared, this may explain why SMC SNR luminosities are lower compared to those in the LMC. Lower densities also have implications for the evolution of SNRs; SMC remnants may take 2.5 times longer to reach the radiative cooling stage compared to LMC remnants.

X-ray data can also be used to estimate SNe rates in a galaxy. van der Heyden (2004) divided the number of SMC SNRs by the age of the oldest remnant. They obtained a core-collapse SNe rate of one per 2400 years, much lower than the estimate given by Filipović et al. (1998a) of one SNR per 350 years based on radio data. van der Heyden (2004) also estimated the Type Ia SNe rate to be one every 4,800 years.

SNR 0101-7226, has a radio shell but no X-ray emission. This puts the upper limit to the SNR's X-ray emission one hundred times fainter than a typical SNR, while the radio surface brightness is average for Galactic remnants. This lack of coincindence is quite typical in other galaxies. Pannuti et al. (2002) have examined several galaxies in the local group and usually find an overlap of less than 20% between radio and X-ray candidates. Selection effects may explain some of this as most SNRs in the SMC have some X-ray emission (see Chapter 4). However, there may also be a missing key factor in these types of comparisons.

CHAPTER 2

SCULPTOR GROUP SD GALAXY NGC 300

2.1 Original Abstract

We present a multi-frequency study of supernova remnants (SNRs) and H II regions in the nearby Sculptor Group Sd galaxy NGC 300[1], based on new ATCA observations at the wavelengths of 13 and 20 cm, *XMM-Newton* observations, newly-processed *ROSAT* (PSPC/HRI; Read & Pietsch 2001) and VLA (20/6 cm) images of this galaxy. We have investigated the physical properties at the X-ray and radio wavelengths of the 28 optical SNRs found by Blair & Long (1997) and have expanded on the multi-wavelength work by Pannuti et al. (2000) on this same galaxy. From a total of 54 radio sources and 11 X-ray sources, we report 18 SNRs and three (3) SNR candidates (classified by spectral index alone) in NGC 300. Five of these 18 SNRs are associated with reported optical SNRs and three have X-ray counterparts. An additional 12 radio SNRs are seen in the Blair & Long (1997) [S II] images. We also investigate the luminosity function of our SNRs. Three background radio sources are confirmed and 12 other sources could represent additional background objects. Twenty two radio correlations with OB associations within NGC 300 correspond to either H II regions or SNRs making them a good tracer of SNRs near star-forming regions. Additionally, two radio sources coincide with potential globular clusters of NGC 300 reported by Kim et al. (2002).

2.2 Introduction

Supernova remnants (SNRs) are associated with many crucial processes within galaxies, but a complete understanding of these sources remains elusive. While many SNRs located within the Milky Way Galaxy have been extensively studied (see for example, the recent multi-wavelength study of the Galactic SNR 3C 397; Dyer & Reynolds 1999), such work has been hampered by factors such as massive photoelectric absorption along the plane of the Galaxy at short wavelengths, as well as significant uncertainties in distances to SNRs (and corresponding diameter uncertainties). In addition, the position of the Sun within the Galactic disk and toward its edge makes it difficult to completely sample all of the Galactic SNRs.

To address these difficulties and to garner more insights into the nature of SNRs, observers have searched for SNRs in nearby galaxies such as the Large Magellanic Cloud (LMC; Filipović et al., in preparation;

[1] This article was published in Astronomy and Astrophysics, volume 425, pages 443–456 (2004). Co-authors include M. D. Filipović, T. G. Pannuti, P. A. Jones, N. Duric, G. L. White and S. Carpano; see 'Contribution of Others' section for more information.

Williams et al. 1999), the Small Magellanic Cloud (SMC; Filipović et al., in preparation), M31 (Braun & Walterbos 1993), M33 (Gordon et al. 1998), and the Sculptor Group galaxies NGC 300 and NGC 7793 (Blair & Long 1997, hereafter referred to as BL97; and Pannuti et al. 2002). Most of these surveys have concentrated on optical methods to detect SNRs and have met with considerable success in revealing a large number of new sources. However, such optical observations need to be complemented by observations at other wavelengths associated with emission from SNRs (such as X-ray and radio) to both detect a maximum number of SNRs in a galaxy of interest and to locate SNRs at all stages of their evolution.

As pointed out in Lacey & Duric (2001), there may be a selection effect inherent in optical surveys, which are more sensitive to detecting SNRs away from H II regions. Such SNRs may be weak emitters in the X-ray and radio because of their location within low density environments which are not conducive to high X-ray and radio luminosities. In contrast, SNRs that are powerful sources of X-ray and radio emission are often located within H II regions. It is precisely because of their location in H II regions that they may be missed by optical surveys.

Although there are certainly exceptions, it can be thought that SNRs located in regions of low density were parented by low-mass white dwarf progenitor stars as Type Ia supernovae, while in contrast SNRs that are found in regions of high density were created by high-mass progenitor stars such as Type Ib/Ic/II supernovae. Thus, multi-wavelength studies also give a more complete picture of a galaxy's star formation history (Pannuti et al. 2002).

In this chapter, we present results of a multi-wavelength search for SNRs in NGC 300 using new radio and X-ray data. Table 2.1 lists some of the more important properties of this galaxy. In Section 2.3, we describe our observations and data analysis. We discuss and explain the method used to identify SNRs, H II regions and background sources in Section 2.4. Position and flux density analysis is presented in Section 2.5, and a description of individual sources is given in Section 2.6. Finally, Section 2.7 is a summary and concluding discussion.

2.3 Observations and Data Analysis

2.3.1 Radio-Continuum Data

Radio-continuum observations of NGC 300 were made on 28 February 2000 with the Australia Telescope Compact Array (ATCA). The array was in the 6C antenna configuration, with baselines ranging between 153 and 6000 m. All observations were made simultaneously at 1374 and 2496 MHz (λ=20 and 13 cm). Using

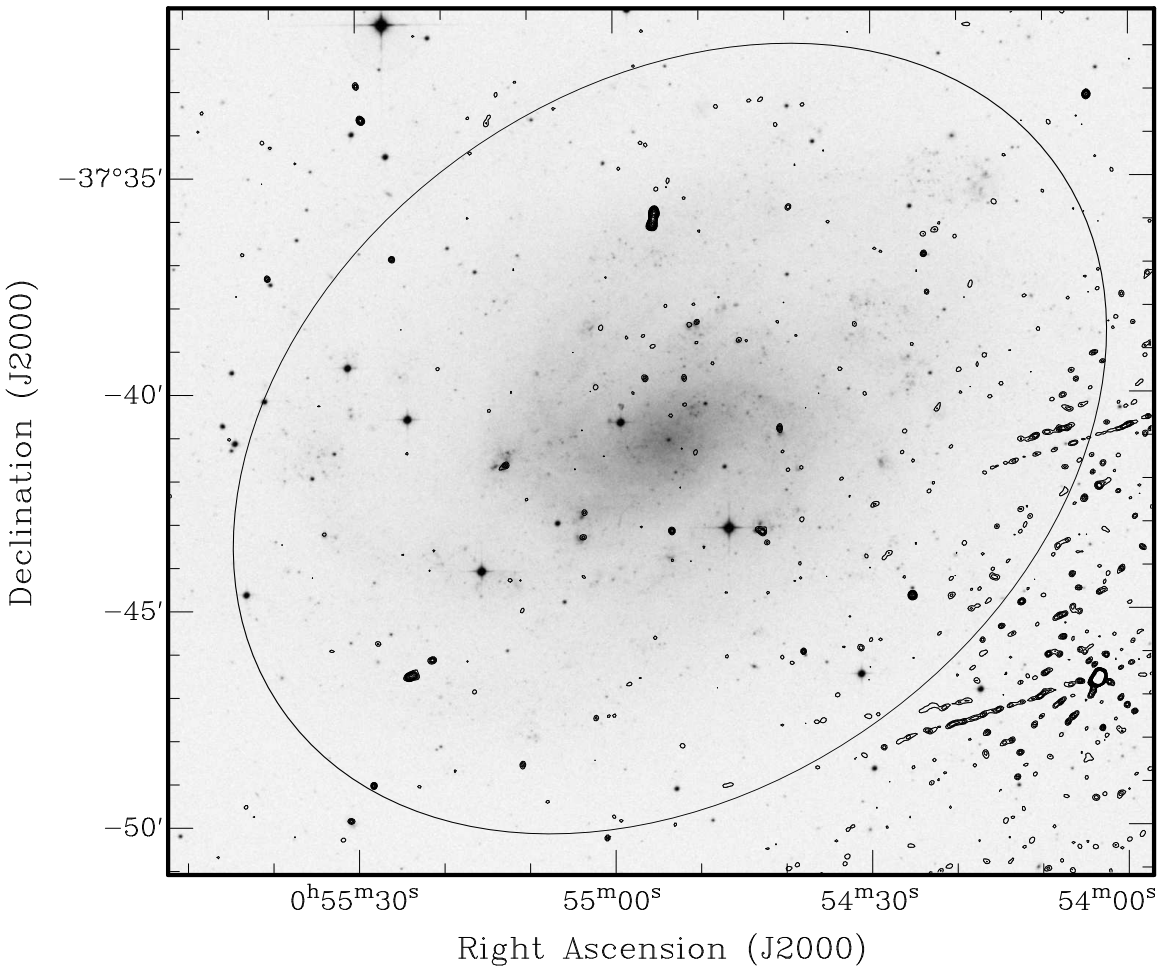

Figure 2.1 ATCA 1374 MHz contours overlaying an DSS2-Red (R) image (grey scale) of NGC 300. An ellipse (21.9′×15.5′) overlay centered on the galaxy at RA(J2000)=$00^h54^m53.48^s$ Dec(J2000)=−37°41′3.8″ provides a visual boundary. Flux from two nearby contaminating sources, NVSS J005403-374636 and NVSS J005353-374020, can be seen in the bottom right-hand corner of the image. Contours are: 0.2, 0.3, 0.4, 0.5, 0.7, 1, 1.5, 2, 3, 4 and 5 mJy beam^{-1}. This image has a 1 σ noise value of 0.058 mJy beam^{-1}.

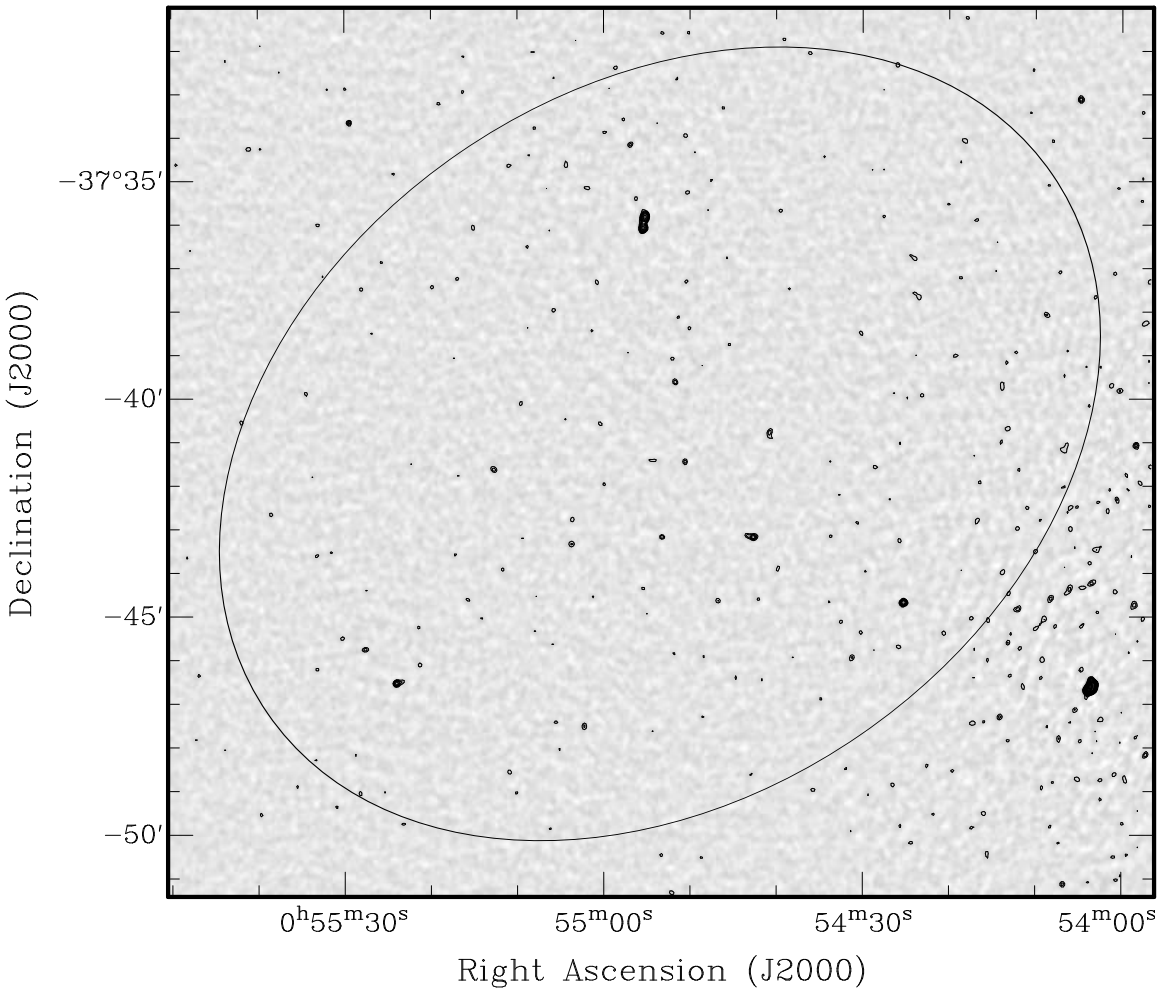

Figure 2.2 The ATCA 2496 MHz image of NGC 300 bounded by our ellipse with its contours. Flux from two nearby contaminating sources, NVSS J005403-374636 and NVSS J005353-374020, can be seen in the bottom right-hand corner of the image. Contours are: 0.2, 0.3, 0.4, 0.5, 0.7, 1, 1.5, 2, 3, 4 and 5 mJy beam^{-1}. This image has a 1 σ noise value of 0.062 mJy beam^{-1}.

Table 2.1 Important properties of NGC 300. (NED=NASA/IPAC Extragalactic Database)

Property	Value (Reference)
Hubble Type	SA(s)d (Tully 1988)
R.A. (J2000.0)	$00^h54^m53.48^s$ (NED)
Dec. (J2000.0)	$-37°41'3.8''$ (NED)
Inclination	46 degrees (Tully 1988)
Distance	2.02 Mpc (Freedman et al. 2001)
Linear Conversion	1 arcsec = 9.8 pc
Observed Diameter D_{25}	20.2 arcmin (Tully 1988)
Mass (H I)	$2.4 \times 10^9 M_\odot$ (Tully 1988)
N_H Column Density	2.97×10^{20} cm^{-2} (Read et al. 1997)
SNRs with Optical Flux	28 (Blair & Long 1997)
SNRs with Radio Flux	17 (Pannuti et al. 2000)
SNRs with X-ray Flux	6 (Read & Pietsch 2001)

Table 2.2 Summary of radio-continuum observations of the region of NGC 300.

Radio Telescope	Freq. (MHz)	Beam Size	rms Noise (mJy/b.a.)	Obs. Date
ATCA	1374	$6''\times6''$	0.058	28 Feb 2000
ATCA	2496	$6''\times6''$	0.062	28 Feb 2000
VLA	1465	$4.70''\times3.76''$	0.066	13 June 1998
VLA	4885	$8.63''\times4.22''$	0.037	22 May 1993

this baseline configuration, we achieved a resolution of $6''$ for each frequency (Table 2.2). This was considered as the best angular resolution with which to study NGC 300 in detail, ensuring at the same time sufficient sensitivity to detect any extended emission component. Primary flux density calibration was achieved using PKS 1934-638 and for phase calibration we used the secondary calibrator J0048-427. Data reductions were performed using the Multi-channel Image Reconstruction, Image Analysis and Display (MIRIAD) software package (Sault & Killeen 2003). Radio-continuum images of these observations are shown in Figs. 2.1 and 2.2.

NGC 300 was also observed by Pannuti et al. (2000) (hereafter referred to as PDL) using the Very Large Array (VLA) of the National Radio Astronomy Observatory (NRAO) at a wavelength of 6 cm in the hybrid CnB configuration (northern arm in the B array) on 22 May 1993 and at a wavelength of 20 cm in the BnA configuration on 13 June 1998 (Table 2.2). To minimize bandwidth smearing, which limits the field of view when observing in normal continuum mode, the VLA observed NGC 300 in multi-channel line mode with seven channels per IF and a channel width of 3.125 MHz, thereby synthesizing a total band of 37.5 MHz

after dropping the first of the seven channels. The effective observing frequencies for the images made from the remaining six channels were 4860 MHz (6 cm) and 1448 MHz (20 cm). Data reduction were performed using the Astronomical Image Processing System (AIPS) software package (Greisen 2003).

The VLA images were corrected for primary beam attenuation and then converted to MIRIAD format before undertaking flux density measurements using the MIRIAD package. A summary of all radio observations is given in Table 2.2.

2.3.2 X-Ray Data

XMM-Newton

XMM-Newton observations on NGC 300 occurred December of 2000 and January of 2001 during revolutions 192 ($\sim$ 37 ks) and 195 ($\sim$ 47 ks), respectively. Data was collected using the EPIC MOS 1, MOS 2 and PN detectors utilizing a medium filter (Ehle et al. 2003). *XMM-Newton*'s 5σ sensitivity limit is estimated at $\sim 1.4 \times 10^{36}$ ergs s^{-1} (1 erg s^{-1} = 10^{-7} Watts).

After processing each dataset (using Science Analysis Software, SAS; Loiseau 2003), an X-ray image of NGC 300 was created (see Fig. 2.3). To do this, filtered MOS 1 event files from revolution 192 and 195 were first merged. In similar fashion, merged MOS 2 and PN event files from both observations were created. MOS 1 and MOS 2 merged event files were next combined and finally a single event file containing all events from both observations created the image. Editing provided "good time interval" (gti) files by removing times associated with contamination from flaring particles.

Source detection (SAS's edetect chain) was accomplished using the combined (both observations) filtered event lists from MOS 1, MOS 2 and PN separately. During source detection, lists were generated using a minimum likelihood threshold of 15 (which corresponds to a Gaussian significance of $\sim 5.1\sigma$). These were then combined to produce a source list. This allowed determination of the coordinates of preliminary X-ray sources. We found a total of 533 X-ray sources but further analysis is in preparation by one of us (S. Carpano). Ten (10) coinciding sources were chosen visually by comparing overlapping contours from the *XMM-Newton* and all four radio images using the KARMA software package.

For each of the *XMM-Newton* point-like sources that coincided with radio sources, count rates were determined from each individual detector by first extracting its filtered spectrum and background. Backscale calibration was automatically applied to these files. Response and auxiliary matrix files were created to calibrate the data to the instrumental response of the telescope. It is noted that occasionally sources fell very

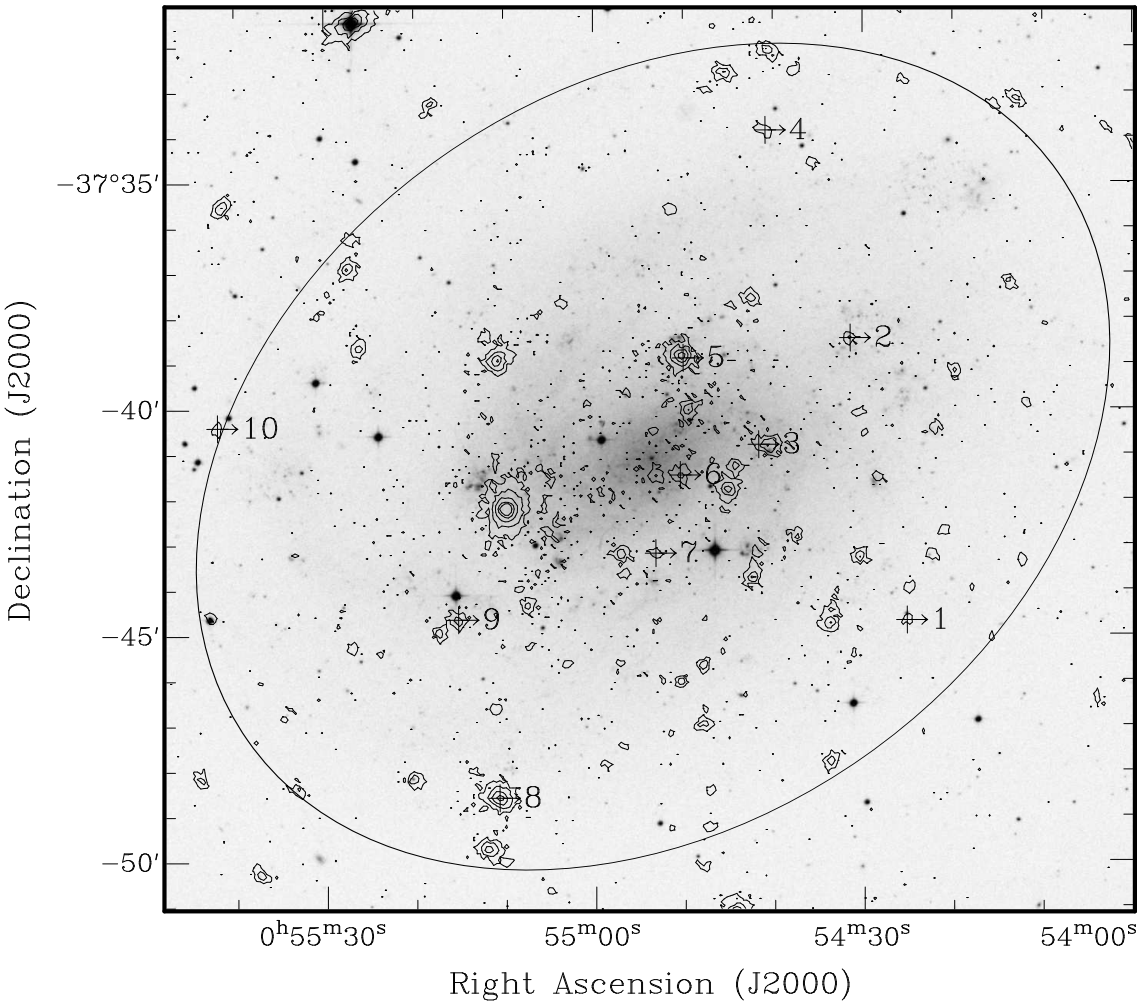

Figure 2.3 *XMM-Newton* (energy range 0.3–6.0 keV) image (contours) of NGC 300 bounded by our ellipse overlaid on DSS2-Red (R) image (gray scale). Radio identifications are marked and X-ray contours are: 1.9, 5.8, 17.3, 52.2 and 104.3 in units of 10^{-2} cnts s^{-1} $arcmin^{-2}$. The resolution of the X-ray image is 4″.

Table 2.3 Summary of X-ray observations of the region of NGC 300.

X-ray Obs. Date	Instrument	RA (J2000) h m s	Dec (J2000) ° ′ ″	Exp (sec)
28-11-1991	PSPC	00 54 52	–37 41 24	9324
26-05-1992	PSPC	00 54 52	–37 41 24	36693
08-06-1994	HRI	00 54 52	–37 41 24	15224
27-05-1995	HRI	00 54 52	–37 41 24	19138
02-06-1997	HRI	00 54 52	–37 41 24	5619
27-12-2000	XMM–rev 192	00 54 56	–37 41 09	36909
02-01-2001	XMM–rev 195	00 54 56	–37 41 10	46711

near to the detectors grid; this may have affected a source's hardness ratio somewhat, but not as greatly as the count rate itself.

The total counts and net count rates for each source were found with the High Energy Astrophysics Science Archive Research Center's (HEAsoft's) XSPEC package in the full (0.3–6.0 keV), soft (0.3–1.0 keV), medium (1.0–2.0 keV) and hard (2.0–6.0 keV) energy bands.

ROSAT

The *ROSAT* archive contains several pointed PSPC and HRI observations centered close to the field of NGC 300. More details on the *ROSAT* mission can be found in Trümper (1983). The two nearest *ROSAT* PSPC (energy range 0.1–2.4 keV) observations which have the best angular resolution were used in this study. For more details of the PSPC observations see Table 2.3.

In Fig. 2.4 we show the *ROSAT* PSPC image ("hard" energy range 0.52–2.01 keV) of the NGC 300 region. It was obtained from combining the two PSPC observations and binned to 5″ pixels. Several *ROSAT* HRI observations were performed within the field of NGC 300 but lower exposure times (total of ~ 40 ks) did not allow a deeper quantitative study than was obtained from the PSPC observations (total of ~ 46 ks). For more details on the PSPC and HRI observations, see Read & Pietsch (2001).

2.4 Source Analysis

We conducted the multi-frequency analysis of ATCA (1374 and 2496 MHz) and VLA (1448 and 4860 MHz) sources by identifying source positions with data from previous catalogues and our *XMM-Newton* data. These catalogues include optical observations by BL97, Soffner et al. (1996), Kim et al. (2002), Pietrzyński et al.

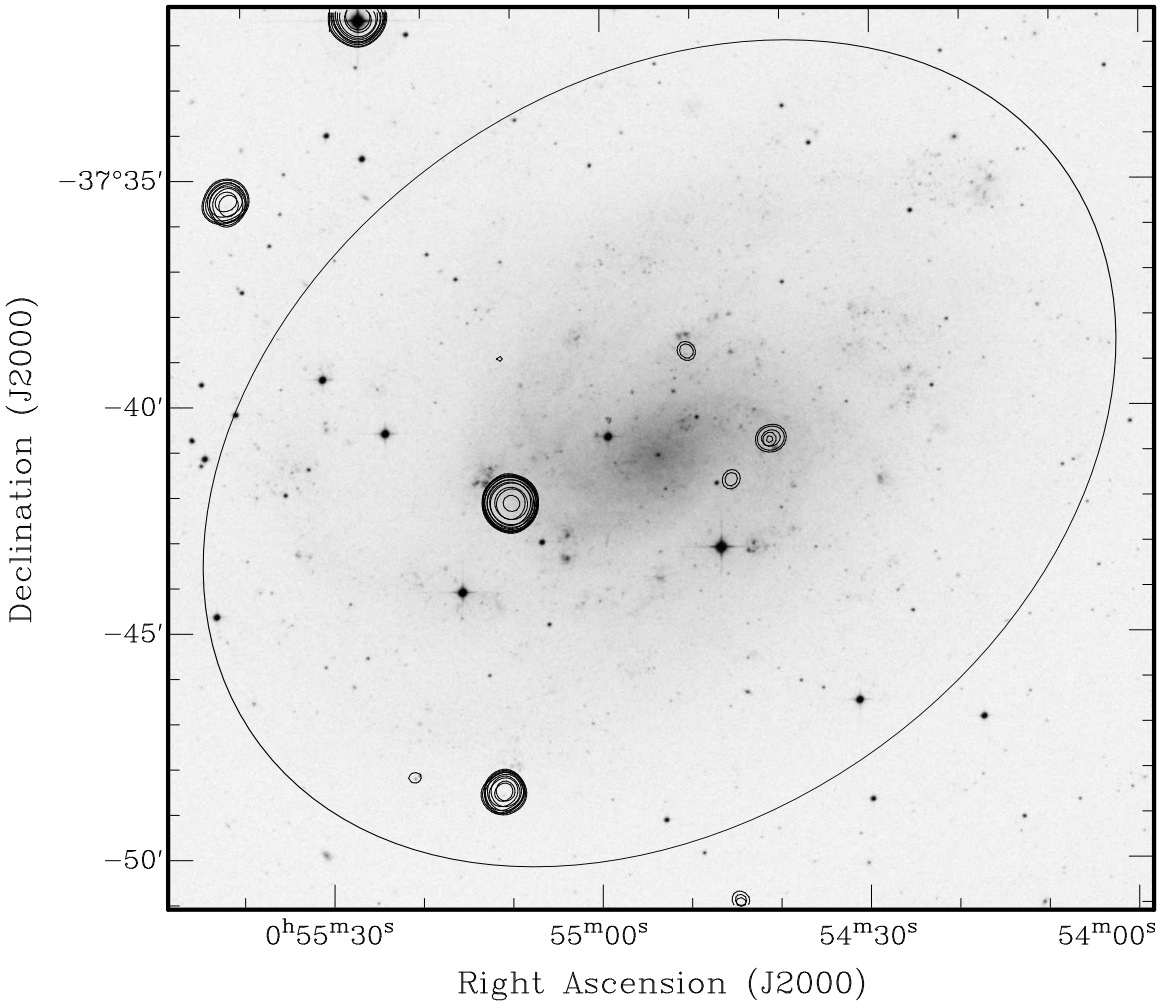

Figure 2.4 *ROSAT* PSPC (energy range 0.52–2.01 keV, 46 ks) image (contours) of NGC 300 bounded by our ellipse overlaid on DSS2-Red (R) image (gray scale). Contours are: 1.4, 1.6, 2.0, 2.7, 3.8, 6.9, 12.8, 24.9, 48.9, 97.0 and 193.2 in units of 10^{-3} cnts s^{-1} $arcmin^{-2}$. The resolution of the X-ray image is 5″.

(2001) and Deharveng et al. (1988); radio analysis by PDL and X-ray data from Read & Pietsch (2001).

Initially, we assume all radio images have a positional accuracy of less than 1″. Then, utilizing the viewer in the Karma software package (Gooch 1996), sources were selected using multi-frequency contour levels and catalogue annotation files overlaying a DSS2-Red (R) [2] image of the galaxy. A elliptical visual boundary to NGC 300 of 21.9′×15.5′, centered on RA(J2000)=$00^h54^m53.48^s$ Dec(J2000)=−37°41′03.8″, is provided by the NASA/IPAC Extragalactic Database (Jet Propulsion Laboratory, California Institute of Technology and National Aeronautics and Space Administration). A grid annotation file allowed systematic visualisation of each source field such that no region would be missed.

2.4.1 Radio Sources

After converting VLA images to MIRIAD format, task IMSTAT was used to determine the rms sensitivity of all datasets individually by averaging several large quiet regions. We found sensitivity values of 0.058, 0.062, 0.066 and 0.037 mJy beam^{-1} for frequencies of 1374, 2496, 1465 and 4885 MHz, respectively. Assuming a distance of 2.02 Mpc (Freedman et al. 2001), this corresponds to luminosity limits of 2.83×10^{16}, 3.03×10^{16}, 3.22×10^{16} and 1.81×10^{16} W Hz^{-1}. In our visual selection of radio sources in this galaxy, we were also required to account for poorly cleaned sidelobes from two nearby radio sources, NVSS J005403-374636 and NVSS J005353-374020.

The position and flux density for each source at a given radio frequency were determined using the two-dimensional point-fitting algorithms in the MIRIAD software package with primary beam corrected images. This involved creating a region using task CGCURS, containing only the selected source, and analyzing this region with task IMFIT to find the source's flux density (with errors) and position. Since 20% of our sources are extended beyond image resolution, a gaussian fitting process must include integration over the entire area of the object.

Estimates of the spectral index (α) of each radio feature/source were made based on flux densities obtained from corresponding radio-frequencies. (The spectral index α is defined by the relation $S_\nu \propto \nu^\alpha$, where S_ν is the integrated flux density and ν is frequency.) This process was accomplished using a standard line of best fit algorithm. Errors ($\Delta\alpha$) were deduced given the scatter in flux density and errors in individual flux density estimates.

We list in Table 2.4, for each of 54 detected radio objects; source number (col. 1), position (RA and Dec,

[2] This all sky survey is composed of digitized 15 μm scans from Schmidt Plates which cover almost the entire sky. More information about this survey and its data can be found at http://arch-http.hq.eso.org/dss/eso-dss.html .

cols. 2 and 3), integrated flux densities (1374 MHz, col. 4; 1448 MHz, col. 5; 2496 MHz, col. 6 and 4860 MHz, col. 7) and corresponding errors, spectral index and error (col. 8), source type (col. 9), comparisons to BL97 images (col. 10) and identifications (col. 11) with sources at other wavelengths.

2.4.2 X-Ray Sources

Using the methods described above we found ten *XMM-Newton* X-ray sources in the area of NGC 300 having radio-continuum counterparts within an estimated *XMM-Newton* positional error of $\sim 4''$. We present a contour image of *XMM-Newton* observations of NGC 300 in Fig. 2.3 and Table 2.6 lists the X-ray sources that match our radio sources.

For point like sources with more than 200 counts per observation, we were able to fit simple spectral models to the combined data for each observation using XSPEC after grouping the data to a minimum of 25 counts. Using this technique it was possible to fit a spectrum to two X-ray sources, XMMU J005450.0-373853 and XMMU J005510.7-374835 (our XMM5 and XMM8, respectively). As Table 2.5 shows, we find the best spectral fit for XMM5 to be the photoelectric absorption with bremsstrahlung model although the photoelectric absorption with power law model was a nearly as good. For XMM8, the best fit was clearly the photoelectric absorption with power law model.

Spectral fitting was more difficult for sources having few counts (< 200). For these sources, we used hardness ratios to give some indication of their X-ray spectra. Using our energy bands: soft (0.3–1.0 keV), medium (1.0–2.0 keV) and hard (2.0–6.0 keV); HR1 was defined as the ratio of the difference of medium and soft counts to their sum ((med–soft)/(med+soft)). In similar fashion, HR2 was defined as the ratio of the differences of hard and soft counts to their sum ((hard–soft)/(hard+soft)). Table 2.6 shows the results of these calculations for data obtained from the PN detector for each observation.

Fig. 2.5 shows a colour-colour diagram of HR1 vs HR2 for each source and observation. Numerous authors including Haberl et al. (2000) have created similar diagrams to establish a relation between various types of sources including supersoft sources, foreground stars, X-ray binaries and SNRs, utilizing *ROSAT* observations of the Magellanic Clouds. The definitions of HR1 and HR2 vary with different X-ray telescopes and so it is not possible to use *ROSAT* source type criteria with *XMM-Newton* data.

Kong & Di Stefano (2003, and reference therein) have created *XMM-Newton* colour-colour diagrams in their analysis of IC 342 with energy bands and hardness ratios similar to ours. Superimposed models in their Fig. 4 colour-colour diagram shows that power law spectra tend to occupy the top right section while

Table 2.4 Measured radio-continuum properties of objects within NGC 300. Listed positions (RA and Dec) are from 1374 MHz observations where possible. In Col. 10, visual comparisons are made to BL97 [S II] versus Hα (with some contamination from [N II]) images; 0=no flux, VF=very faint flux, F=faint flux, M=medium flux and S=strong flux. Prefixes to source numbers used in Col. 11: H=HRI (Read & Pietsch 2001), P=PSPC (Read & Pietsch 2001), D=Deharveng et al. (1988), S=Soffner et al. (1996), DSS2-Red(f/m)=STScI Digitized Sky Survey (1993,1994), BL=Blair & Long (1997), RPS97=Read et al. (1997), PSNR=Pannuti et al. (2000), GC=Kim et al. (2002), AS_=Pietrzyński et al. (2001) and XMM=Here. Source type abbreviations are: SNR=supernova remnant, HII=H II region, BKG=background object and xrb=X-ray binary (capital letters denote higher confidence). †– denotes snr candidates.

1 ATCA Source Number	2 RA (J2000) h m s	3 Dec (J2000) ° ′ ″	4 $S_{1374\,MHz}$ (mJy)	5 $S_{1448\,MHz}$ (mJy)	6 $S_{2496\,MHz}$ (mJy)	7 $S_{4860\,MHz}$ (mJy)	8 $\alpha \pm \Delta\alpha$	9 Source Type	10 [S II]/Hα (BL)	11 Identifications
J005408.6-373804	00 54 08.69	–37 38 04.7			0.61±0.01					DSS2-Red(f)
J005422.5-373615	00 54 22.53	–37 36 15.1	1.37±0.04						0/VF	
J005423.4-373741	00 54 23.48	–37 37 41.4	0.41±0.02	0.38±0.06	0.40±0.06		+0.0±0.1	hii/bkg	0/0	
J005423.8-373648	00 54 23.84	–37 36 48.4	0.64±0.02	0.58±0.06	0.40±0.04		–0.7±0.1	snr†	0/0	
J005423.8-373621	00 54 23.88	–37 36 21.1	0.33±0.01						0/0	
J005425.2-374441	00 54 25.25	–37 44 41.9	2.44±0.10	2.55±0.10	2.02±0.09	0.23±0.03	–1.8±0.5	BKG		XMM1
J005431.2-374554	00 54 31.28	–37 45 54.6	0.41±0.03	0.33±0.04	0.44±0.03		+0.3±0.4	hii/bkg		
J005431.9-373825	00 54 31.91	–37 38 25.9	0.30±0.02					SNR	F/F	P29(HR2=0.15), BL-S6([S II]/Hα=0.60), XMM2,AS_18
J005437.9-374559	00 54 37.99	–37 45 59.5	0.65±0.03	0.66±0.06	0.27±0.02		–1.5±0.2	bkg	0/0	
J005438.1-374144	00 54 38.16	–37 41 44.2	0.27±0.02	0.34±0.06		0.11±0.01	–0.8±0.2	SNR/HII	F/S	S(west)31, D39,DSS2-Red(f),PSNR2(R1),AS_25
J005438.4-374240	00 54 38.49	–37 42 40.5		0.33±0.02				snr/HII	F/F	D40,PSNR3(R2), RPS97(no. 2),AS_26a
J005439.6-373543	00 54 39.61	–37 35 43.4	0.42±0.02	0.43±0.10	0.33±0.02		–0.4±0.1	snr†	0/0	
J005440.6-374049	00 54 40.68	–37 40 49.7	0.56±0.03	0.30±0.05	0.38±0.06	0.21±0.01	–0.5±0.3	SNR/HII	M/M	P38(HR2=-0.33), BL-S10([S II]/Hα=0.67), XMM3,H11,S(west)22,DSS2-Red(f),AS_29
J005441.0-373348	00 54 41.05	–37 33 48.9	0.29±0.02	0.33±0.05				bkg/snr	0/0	XMM4
J005442.7-374313	00 54 42.70	–37 43 13.3	0.63±0.07	0.69±0.06	0.65±0.04	0.21±0.02	–0.9±0.3	SNR/HII	M/S	D53B,DSS2-Red(m), BL-S11([S II]/Hα=0.53),AS_34
J005443.1-374311	00 54 43.11	–37 43 11.0	0.59±0.08	0.75±0.05	0.43±0.03	0.32±0.03	–0.6±0.2	SNR/HII	M/S	D53A,PSNR4(R3),DSS2-Red(s),AS_34
J005445.3-373842	00 54 45.31	–37 38 42.8				0.17±0.03		HII	0/0	D62,AS_45
J005445.3-373847	00 54 45.39	–37 38 47.1	0.30±0.03		0.25±0.01		–0.3±0.1	SNR/HII	F/S	D61,DSS2-Red(m),AS_45
J005448.0-373323	00 54 48.01	–37 33 23.7	0.31±0.03	0.37±0.07					0/0	DSS2-Red(f)
J005450.2-374030	00 54 50.28	–37 40 30.0		0.73±0.09		0.39±0.01	–0.5±0.2	SNR/HII	M/S	D76A,PSNR7(R6),DSS2-Red(m),AS_56
J005450.3-373822	00 54 50.30	–37 38 22.4	0.36±0.05	0.23±0.01	0.25±0.01	0.23±0.03	–0.2±0.2	SNR/HII	M/S	D77,DSS2-Red(m),AS_52a
J005450.3-373850	00 54 50.35	–37 38 50.9	0.24±0.02					xrb	M/F	DSS2-Red(f)P32(HR2=0.75),H10, XMM5,AS_52
J005450.5-374123	00 54 50.52	–37 41 23.0	0.28±0.02	0.30±0.03	0.37±0.02		+0.4±0.1	hii/bkg	0/0	XMM6
J005450.7-374022	00 54 50.73	–37 40 22.2	0.19±0.01			0.13±0.01	–0.3±0.1	SNR/HII	F/F	DSS2-Red(f),D76B,AS_56b
J005450.8-374015	00 54 50.82	–37 40 15.1				0.14±0.02		HII	VF/VF	D76B,AS_56b
J005451.1-373826	00 54 51.16	–37 38 26.1	0.95±0.05	0.33±0.01		0.14±0.02	–1.2±0.7	SNR/HII	M/S	D79,DSS2-Red(m),AS_52d
J005451.3-374621	00 54 51.34	–37 46 21.9		0.24±0.02				HII	VF/S	PSNR10(R9),D82,DSS2-Red(f)
J005451.7-373939	00 54 51.79	–37 39 39.6	0.35±0.03	0.46±0.03	0.40±0.02	0.33±0.04	–0.1±0.2	SNR/HII	M/S	DSS2-Red(s),D84, PSNR11(R10),GC6,AS_57
J005453.3-374311	00 54 53.30	–37 43 11.9	0.69±0.04	0.66±0.06	0.43±0.03	0.12±0.01	–1.4±0.2	BKG	M/F	DSS2-Red(m),XMM7,GC7
J005455.3-373557	00 54 55.32	–37 35 57.5	17.88±1.31	16.78±1.06	10.18±0.83	2.01±0.13	–1.7±0.3	bkg	0/0	
J005456.3-373940	00 54 56.36	–37 39 40.0	0.39±0.04	0.68±0.06				HII	M/F	DSS2-Red(m),D99
J005456.7-373413	00 54 56.77	–37 34 13.8	0.28±0.03	0.31±0.06	0.49±0.04		+0.9±0.1	hii/bkg	0/0	
J005500.5-374037	00 55 00.58	–37 40 37.4	0.20±0.01		0.25±0.01	0.12±0.01	–0.4±0.4	SNR/HII	F/S	DSS2-Red(m),D109,S(east)20,AS_76
J005500.7-374143	00 55 00.73	–37 41 43.5	0.20±0.01					HII	VF/S	DSS2-Red(f),S(east)19,D111
J005500.9-373720	00 55 00.93	–37 37 20.1	0.22±0.01	0.29±0.04	0.30±0.01		+0.3±0.4	hii/bkg	0/0	
J005501.4-373829	00 55 01.49	–37 38 29.9	0.84±0.02		0.48±0.06		–0.9±0.1	SNR	0/0	AS_82
J005502.1-373952	00 55 02.13	–37 39 52.4	0.89±0.04						0/0	
J005502.2-374731	00 55 02.25	–37 47 31.0	0.36±0.03	0.26±0.02	0.44±0.02		+0.6±0.5	hii/bkg	0/0	
J005503.5-374246	00 55 03.50	–37 42 46.0	0.34±0.02	0.41±0.03	0.31±0.01	0.24±0.03	–0.4±0.1	SNR/HII	F/S	DSS2-Red(m), D118A,PSNR12(R11),AS_84
J005503.6-374320	00 55 03.66	–37 43 20.1	0.33±0.03	0.32±0.04	0.34±0.02	0.13±0.02	–0.7±0.3	SNR/HII	M/S	D119A,DSS2-Red(m), PSNR13(R12),AS_86
J005507.3-374106	00 55 07.30	–37 41 06.1				0.14±0.01		HII	VF/M	DSS2-Red(f),D126,S(east)4,AS_94
J005510.8-374835	00 55 10.85	–37 48 35.3	0.52±0.04	0.30±0.05	0.45±0.01		+0.2±0.9	AGN		DSS2-Red(f),P58(HR2=0.01), H16,XMM8
J005512.3-373908	00 55 12.37	–37 39 08.5			0.26±0.01			HII	0/F	DSS2-Red(f),D136
J005512.7-374140	00 55 12.70	–37 41 40.3	0.49±0.04	0.55±0.01	0.41±0.03	0.21±0.02	–0.7±0.1	SNR/HII	M/S	DSS2-Red(m), PSNR14(R13),D137A,AS_102b
J005515.4-374439	00 55 15.40	–37 44 39.2	0.20±0.01	0.22±0.02				SNR/HII	S/S	D141,P49(HR2=-0.16),XMM9, BL-S26([S II]/Hα=0.57),DSS2-Red(f), AS_107
J005516.4-374653	00 55 16.45	–37 46 53.7	0.34±0.02						VF/VF	
J005521.3-374609	00 55 21.35	–37 46 09.6	0.67±0.03	0.76±0.11	0.41±0.02		–1.0±0.3	bkg/snr	0/0	
J005523.9-374632	00 55 23.95	–37 46 32.4	2.23±0.17	2.10±0.29	1.33±0.22		–0.9±0.1	bkg/snr	0/0	
J005525.8-373653	00 55 25.82	–37 36 53.8	0.63±0.05	0.55±0.05	0.33±0.02		–1.0±0.1	bkg/snr		
J005527.6-374546	00 55 27.66	–37 45 46.4	0.36±0.03	0.30±0.01	0.60±0.02		+1.0±0.4	hii/bkg		
J005528.2-374903	00 55 28.25	–37 49 03.3	0.96±0.05	0.77±0.06	0.61±0.03		–0.6±0.3	snr†		
J005533.6-374147	00 55 33.65	–37 41 47.8			0.39±0.02			HII	0/F	D158,DSS2-Red(f)
J005533.8-374314	00 55 33.87	–37 43 14.6	0.27±0.01					SNR/HII	M/S	D159,BL-S28([S II]/Hα=0.61), DSS2-Red(f),AS_113
J005541.9-374033	00 55 41.94	–37 40 33.5			1.24±0.04			snr	0/0	P36(HR2=-0.26),XMM10

Table 2.5 *XMM-Newton* photoelectric absorption model fits to radio counterparts in NGC 300 (1σ confidence interval using MOS 1, MOS 2 and PN data). Source XMM5 was also found to closely fit a power law spectrum. The corresponding values for this model are shown in parentheses.

Spectral Fits					
		Bremsstrahlung		Power Law	
Source Number	Revolution Number	Column (10^{20}cm^{-2})	Temperature (keV)	Column (10^{20}cm^{-2})	Index
XMM5	192	$22.6^{+4.1}_{-3.1}$	$5.0^{+1.2}_{-0.9}$	(30.4)	(1.9)
XMM8	192			$9.1^{+4.5}_{-3.1}$	$2.8^{+0.4}_{-0.2}$
XMM5	195	$28.1^{+4.1}_{-3.2}$	$5.2^{+1.0}_{-1.0}$	(37.4)	(1.9)
XMM8	195			$10.3^{+2.5}_{-2.0}$	$2.8^{+0.1}_{-0.1}$

Table 2.6 *XMM-Newton* sources found to match our radio sources showing PN detector hardness ratios and count rates. A complete catalogue of *XMM-Newton* sources can be found in Carpano (in prep.). Col. 4 abbreviation Pe represents the estimated positional error.

(1)	(2)	(3)	(4)	(5)			(6)		
Source Number	RA (J2000)	Dec (J2000)	Pe	Revolution 192			Revolution 195		
(XMMU)	h m s	° ′ ″	(″)	Tot (cnt/ks)	HR1	HR2	Tot (cnt/ks)	HR1	HR2
XMM1 / J005425.2-374441	00 54 25.20	–37 44 41.1	0.9	1.13	–0.26	–1.00	1.47	–0.13	–0.25
XMM2 / J005431.4-373827	00 54 31.45	–37 38 27.0	0.7	0.62	–0.01	–0.60	1.76	+0.04	–0.19
XMM3 / J005441.6-374048	00 54 41.69	–37 40 48.0	1.5	1.27	–0.63	–0.99	1.63	–0.58	–1.00
XMM4 / J005440.8-373351	00 54 40.85	–37 33 51.3	0.8	1.39	+0.84	+0.94	0.72	+0.31	+0.62
XMM5 / J005450.0-373853	00 54 50.08	–37 38 53.2	0.1	28.39	+0.31	+0.11	20.62	+0.35	+0.19
XMM6 / J005450.4-374128	00 54 50.45	–37 41 28.4	0.6	2.02	–0.48	–0.92	2.23	–0.64	–1.00
XMM7 / J005453.2-374311	00 54 53.21	–37 43 11.8	0.8	0.88	–0.34	+0.79	1.27	–0.35	+0.02
XMM8 / J005510.7-374835	00 55 10.75	–37 48 35.8	0.3	27.16	–0.37	–0.75	29.83	–0.43	–0.73
XMM9 / J005515.2-374439	00 55 15.27	–37 44 39.6	0.4	5.36	–0.69	–0.95	0.93	–1.00	–0.98
XMM10 / J005542.0-374025	00 55 42.04	–37 40 25.6	0.7	2.35	–0.76	–0.88	1.08	–0.88	–0.93

soft thermal models occupy the lower left. For each of their models, the column density increases from left to right. We used XSPEC's "fakeit" command to create our own simulated simple model spectra for our colour-colour diagram shown in Fig. 2.5.

Our hardness ratios primarily add insight to previously selected SNRs as the colours of the X-ray sources are not reliable enough to identify source type alone. It must be remembered that this exercise tells us only about the spectrum of these objects. Recent observations of Galactic SNRs such as RX J1713.7-3946 and SN 1006 (Koyama et al. 1997) have shown that they can have non-thermal as well as thermal properties in X-ray.

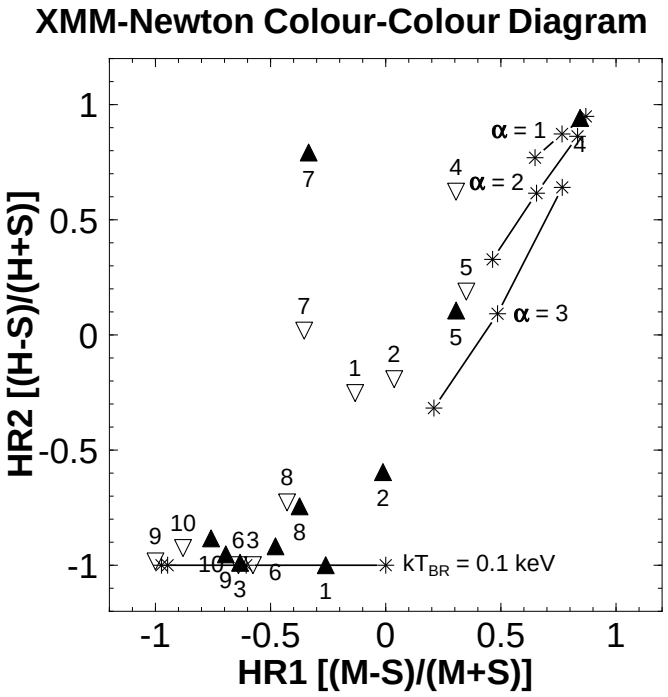

Figure 2.5 Colour-colour diagram for all correlated *XMM-Newton* sources using PN hardness ratios. Each source is numbered while filled triangles indicate sources from revolution 192 and open triangles represent those from revolution 195. The estimated hardness ratios from different models are shown as lines connected to 'fake' data points (stars). Power law models tend to have hardness ratios in the upper right of the diagram while thermal models have ratios in the lower left of the diagram.

Table 2.7 Results of multi-frequency source comparison. Numbers represent sources in common to two surveys. *XMM-Newton* sources are in "()" if not confirmed. Abbreviations used are: *ROSAT*=Read & Pietsch (2001); D=Deharveng et al. (1988); S=Soffner et al. (1996), DSS2-Red(f/m)=STScI Digitized Sky Survey (1993,1994), BL=Blair & Long (1997), *XMM-Newton*=Here, K=Kim et al. (2002) and P=Pietrzyński et al. (2001).

	ATCA 20cm	VLA 20cm	ATCA 13cm	VLA 6cm	*XMM-Newton*	*ROSAT*-PSPC	*ROSAT*-HRI	BL	D	S	K	P	DSS2-Red(f/m)
ATCA 20cm	44	32	29	15	9	5	3	5	16	4	2	18	21
VLA 20cm	32	35	26	14	7	3	2	3	14	2	2	13	17
ATCA 13cm	29	26	33	12	6	3	2	2	11	2	2	11	15
VLA 6cm	15	14	12	19	3	1	1	2	15	4	2	16	15
XMM-Newton	9	7	6	3	(533)	(25)	(7)	(6)	(4)	(6)	(1)	(11)	–

2.4.3 Identifications

Table 2.7 lists the number of sources in common with our data and other (optical and X-ray) catalogues. This information was compiled from both visual inspection of our data and annotation files (created from the literature) using KARMA's kview.

Positional identifications with published sources in the optical and X-ray domains were considered high if they fell within the positional limits of these surveys ($\sim$ 4″). An exception was the *ROSAT* catalogue created by Read & Pietsch (2001) who cite positional errors for each of their X-ray sources individually. Annotation circles were created for this catalogue with a radius corresponding to these errors in order to find each corresponding radio source. Next, each individual source identification was carefully reexamined using contour levels from different wavelengths before being added to our list.

Using this process, an interesting systematic error is suspected with respect to data presented by Soffner et al. (1996) and Deharveng et al. (1988). When a correction of δDec=–3.9″ was applied to each of these datasets, the respective positions of their sources matched the DSS2-Red (R) plate almost exactly. It seems reasonable that errors of this magnitude occur in the literature presumably due to registration of their optical image on the sky astrometric frame.

As a matter of background, we now discuss catalogues of NGC 300 found in the literature in more detail. BL97 detected 28 SNRs candidates through CCD imagery with interference filters to isolate emission from Hα + [N II], [S II] and a continuum near 610 nm, to identify nebulae bright in [S II] relative to Hα. Optical long-slit CCD spectra of these candidates confirmed that these sources met the usual criteria of a flux ratio ([S II]/Hα) of 0.4 or greater. (All five BL97 SNRs which match our radio sources have ratios exceeding 0.57.) As noted in Gordon et al. (1999), the physical basis for this is that in photoionized regions, most sulfur is in the doubly ionized state. By contrast, in shock-heated nebulae, the cooling time is short so that many ionisation states occur, including S^+. This causes us to observe higher [S II]/Hα ratios in SNRs than in H II regions. In this study we use BL97 1500s images transferred from tape to help characterize our sources.

BL97 also determined the optical diameter for their sources, noting that the majority of the objects were reasonably well resolved. They based their measurements on the earlier distance value of 2.1 Mpc, noting that the smallest SNRs in NGC 300 are at the seeing disk value of 1.5 ″ (1″ = 10.2 pc). These apparent diameters should be considered upper limits. The majority of BL97 SNRs have apparent diameters in the 25–75 pc range, which they felt reflected a well-evolved ISM-dominated population for which their search technique worked best. However, BL97 reported four (4) large SNRs in NGC 300 with diameters in the 75–200 pc

range for which there are no Galactic counterparts; a trend also seen in other galaxies (e.g. M33). These objects may represent superbubbles; remnants formed from more than one supernova explosion along with stellar winds found in a group of massive stars. Dunne et al. (2001) have studied X-rays from superbubbles of about the same size located within the Large Magellanic Clouds and found that the X-ray emission is brighter than that theoretically expected for a wind-blown bubble alone, suggesting that the X-ray emission has been enhanced by interactions with several SNRs of similar age.

Hα images were used to determine H II regions in NGC 300 by Deharveng et al. (1988) and Soffner et al. (1996). Deharveng et al. (1988) cataloged 176 H II regions within NGC 300 while Soffner et al. (1996) report finding 90. In addition, Soffner et al. (1996) show 31 counterpart regions reported in Deharveng et al. (1988).

Related to these H II regions, OB associations composed of groups of young, massive, gravitationally unbound stars formed from molecular clouds within NGC 300 were studied by Pietrzyński et al. (2001). Using the Path Linkage Criterion (PLC), they found 117 such associations. These OB associations were reported to overlap with at least 60% of the H II regions found by Deharveng et al. (1988). Pietrzyński et al. (2001) note that these associations are well suited as tracers of recent or ongoing star formation. In our analysis, we find (Table 2.4) 22 OB associations that correspond to either H II regions or SNRs.

We are mindful to distinguish these H II regions and OB associations from other objects near NGC 300. Kim et al. (2002) found 17 globular cluster candidates in NGC 300 using *U BV I* CCD photometry. Their search used photometric information, morphological parameters and visual inspection, and they note that the globular clusters were barely resolved in their images.

Results from *ROSAT* PSPC and HRI X-ray observations of NGC 300 have been presented by Read & Pietsch (2001). A summary of X-ray sources and their properties from the *ROSAT* PSPC image (Fig. 2.4) is presented in their Table 2.

2.4.4 Multi-Wavelength Selection Criteria

Multi-frequency analysis enhances our understanding of the nature of discrete sources in NGC 300. We assume that this galaxy is essentially transparent to radio emission, and, radio and X-ray catalogues contain not only sources located within NGC 300, but also background sources lying behind it. We use a similar classification to that used by Filipović et al. (1998) to divide the radio sources into two major groups:

1. non-thermal sources, such as:

Table 2.8 Selection Criteria for Radio Source Type. Note use of logical AND and OR for this table.

Source Type	Selection Criteria	
SNR	a) $\alpha \leq -0.2$ AND H II / OB Association	OR
	b) Known Optical SNR	
snr	a) $-0.8 \leq \alpha \leq -0.2$ ("radio snr candidate")	OR
	b) X-ray Source	
HII	a) Known From Optical (Deharveng / Soffner)	
hii	a) $\alpha \geq -0.2$	
BKG	a) $\alpha \leq -0.8$ AND X-ray	OR
	b) Known From X-ray / Radio Study	
bkg	a) X-ray Source	OR
	b) $\alpha \geq -0.2$	OR
	c) $\alpha \leq -0.8$	

a) background quasars and galaxies

b) SNRs within NGC 300

2. thermal sources, such as H II regions within NGC 300.

With this in mind, we used the spectral index obtained from our ATCA and VLA radio data to aid in the classification of each source into the above categories using the following criteria based on McGee & Newton (1972):

(i) Background sources with $\alpha \leq -0.8$,

(ii) SNRs with a steep spectrum $-0.8 \leq \alpha \leq -0.2$, and

(iii) H II regions with a flat spectrum, $\alpha \geq -0.2$, although background radio sources can also have a flat spectrum.

Sources cannot be classified by radio spectral index alone due to large overlaps between various source types and spectral index errors. H II regions and SNRs are often associated since the latter may be embedded in or near the former. Further, PDL requires that a radio source be associated with a region of Hα emission in order to differentiate background radio sources from those intrinsic to NGC 300.

Therefore, we use our *XMM-Newton* data, identifications from six other catalogues, DSS2-Red (R) images, original BL97 images and radio spectral index to create our classification. Because of the distance to NGC 300 (2.02 Mpc), we are unable to use source extension and morphology as part of our criteria.

Specifically, we used the following classification scheme (Table 2.8) to classify each source within the area of NGC 300 defined by our ellipse:

(i) **For Background Sources:** If a source with a very steep spectral index ($\alpha \leq -0.8$) was found to have an identification in the X-ray domain, it was designated as a background source or "BKG". If no spectral index could be calculated because the source was too faint at other radio wavelengths, then catalogue identifications were used to determine if the source *could* be a background object. If no resolution using this information was possible, these sources were not designated. Sources with a steep radio spectral index but no other identifications were designated as "bkg" as were those sources with a flat spectral index (due to the possible variability of background sources in general). We adopted the estimate given by PDL that approximately five background sources should have been observed in random directions through the disk of NGC 300 in the 20 cm image at a 3 σ level of 0.2 mJy beam^{-1} or greater. (They based their estimate on work by Mitchell & Condon (1985) for the number density of background sources.)

(ii) **For H II Regions:** Sources described in other catalogues as H II regions were designated as "HII". Sources with a flat radio spectral index that did not have identifications at other wavelengths or catalog descriptions were listed as "hii/bkg". The "hii" designation was required because DSS2-Red (R) or Hα images may not have been sensitive enough to show these potential H II regions. The "bkg" designation was included since these radio sources *could* be intrinsically variable with flat indices. Sources with a steeper (or borderline steeper) spectral index which were described as both H II regions (and possibly supernova remnants) in other catalogues were designated as "SNR/HII" since these most likely represent areas where a supernova remnant was embedded within or associated with an H II region. Most of these sources could be visually seen in BL97 [S II] images as discussed below although this alone did not classify the objects.

(iii) **For Supernova Remnants:** In addition to SNRs embedded within H II regions, a source known to be a supernova remnant from other catalogues was designated as "SNR" in Table 2.4. Our classification of a radio SNR candidate, "snr†" was based on spectral index when no identifications were found and did not include those sources that could have been a supernova remnant while just as likely another type of source, such as a background object. For example, ATCA J005525.8-373653 could be either a background source or SNR and was designated as "snr/bkg". This source was not included in our count of SNR candidates. Any source that had radio and X-ray emission unexplained otherwise has "snr"

Table 2.9 Comparisons of positions including 95 percent confidence intervals (CI) and standard deviations. D=Deharveng et al. (1988).

Comparison	$\Delta\,\alpha$ ±CI (arcsec)	$\Delta\,\delta$ ±CI (arcsec)	s.d. α (arcsec)	s.d. δ (arcsec)	Notes
1374 MHz - 1448 MHz	–0.0±0.4	+0.3±0.7	1.1	2.0	32 matches
1374 MHz - 2496 MHz	–0.0±0.5	+0.0±0.7	1.4	1.8	30 matches
1374 MHz - 4860 MHz	–0.0±0.8	+0.6±1.5	1.4	2.6	15 matches
1374 MHz - H II	–0.7±0.7	–0.5±0.8	1.3	1.5	16 matches; D
1374 MHz - *XMM-Newton*	+0.5±3.8	–1.1±1.6	4.9	2.1	9 matches

(possible supernova remnant) as one of its designations.

2.5 Calibration Procedures

2.5.1 Position Calibration

The accuracy of the positions of all of our radio sources found by methods described in Section 2.4.1 is limited by the pointing accuracy and beam size of the ATCA and VLA telescopes. Since our criteria for radio source cross-identifications are based initially on a radius of less than 1″ and radio source cross-identifications with optical catalogues on less than 4″, we expect a small amount of scatter in position differences if there is true positional agreement.

We have compared the positions of 16 H II regions cited in Deharveng et al. (1988) (systematically corrected as discussed Section. 2.4.1) to their ATCA counterparts at 1374 MHz and have found no significant positional bias between our radio positions and the published optical positions. At the 95 percent confidence level (using the student-t with n-1 degrees of freedom), the positional differences in right ascension and declination ($\Delta\,\alpha$ and $\Delta\,\delta$, respectively) are $\Delta\,\alpha = -0.7'' \pm 0.7$, $\Delta\,\delta = -0.5'' \pm 0.8$. Comparisons of 1374 MHz positions with positions at the other radio frequencies and *XMM-Newton* show the radio catalogues to be self-consistent (Table 2.9).

2.5.2 Radio-Continuum Uncertainties in Flux Densities

In Fig. 2.6 we compare ATCA (1374 MHz) to VLA (1448 MHz) flux densities. We find the line of best fit for this data to be S_{1448} = (–0.0155±0.017) + (0.979±0.04)S_{1374}. There is no evidence for systematic differences in the flux densities from the ATCA and the VLA.

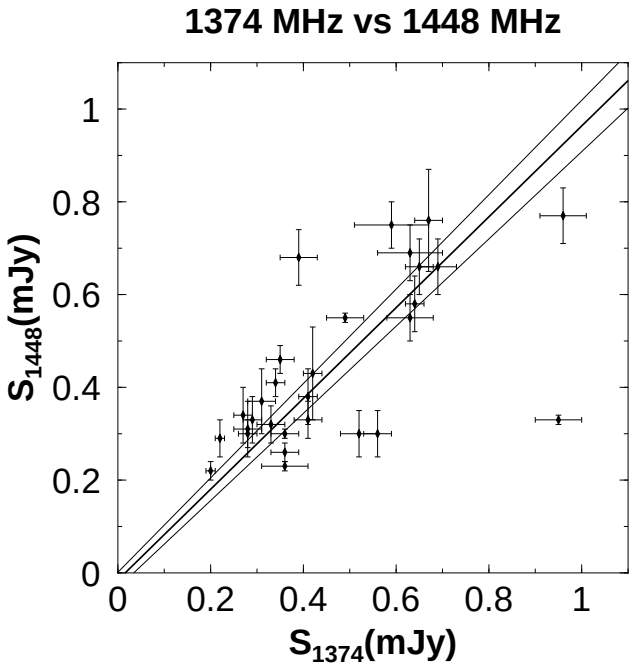

Figure 2.6 Comparisons of flux density between ATCA (1374 MHz) and VLA (1448 MHz) sources with individual flux density error bars plotted on a linear scale. A weighted line of best fit within a 1σ confidence interval is $(-0.0155\pm0.017) + (0.979\pm0.04)S_{1374}$. This graph shows all except the three strongest sources but all sources were used in statistical calculations.

2.6 Sources

2.6.1 Supernova Remnants

Luminosity Function of SNRs

Because of the relative certainty of the SNRs distance, the luminosity function is directly proportional to our observed flux densities. The luminosity of each radio source at a specific frequency, ν, is given in W Hz^{-1} and is defined by the relation:

$$L_\nu = 4\pi D^2 S_\nu \tag{2.1}$$

where D is the distance to NGC 300 of 2.02 Mpc (Freedman et al. 2001) and S_ν is the flux density at a given radio frequency. In our case, the source flux density at 1374 MHz was used to estimate the luminosity of each SNR source. The 5σ completeness level at this frequency is 0.29 mJy with a corresponding level in luminosity of 1.4×10^{17} W Hz^{-1}.

In Fig. 2.7 we show a histogram of 17 SNRs (ATCA J005450.2-374030 does not have a flux density at 1374 MHz). The mean luminosity of the SNRs is $2.05{\times}10^{17}$ W Hz^{-1} with standard deviation 1.09 $\times 10^{17}$ W Hz^{-1}. Here, we are seeing only selected high luminosity sources just above the completeness level. Deeper studies are required for a complete sampling of SNRs in NGC 300.

Optically Selected SNRs

Of the five BL97 SNRs identified with our sources, two (BL-S10 and BL-S11, Fig. 2.8) have radio spectral indices consistent with SNRs. We cannot determine a spectral index for the remaining sources: BL-S6, BL-S26 and BL-S28 (Fig. 2.8). Additionally, three of these BL97 sources (BL-S6, BL-S10 and BL-26) have corresponding X-ray emission. As noted by Chen & Chu (1998), only a small number of optically identified extragalactic SNRs can be confirmed at radio and X-ray wavelengths with these being among the most luminous remnants.

ATCA J005431.9-373825 corresponds to BL-S6 with a [S II]/Hα ratio of 0.60. This SNR coincides with an OB association and is seen both in *ROSAT* and *XMM-Newton* observations. Our colour-colour diagram is not helpful in determining the X-ray spectrum of this source and it contains too few counts for model fitting.

BL97's S10 identifies with ATCA J005440.6-374049 and is associated with an H II region and an OB

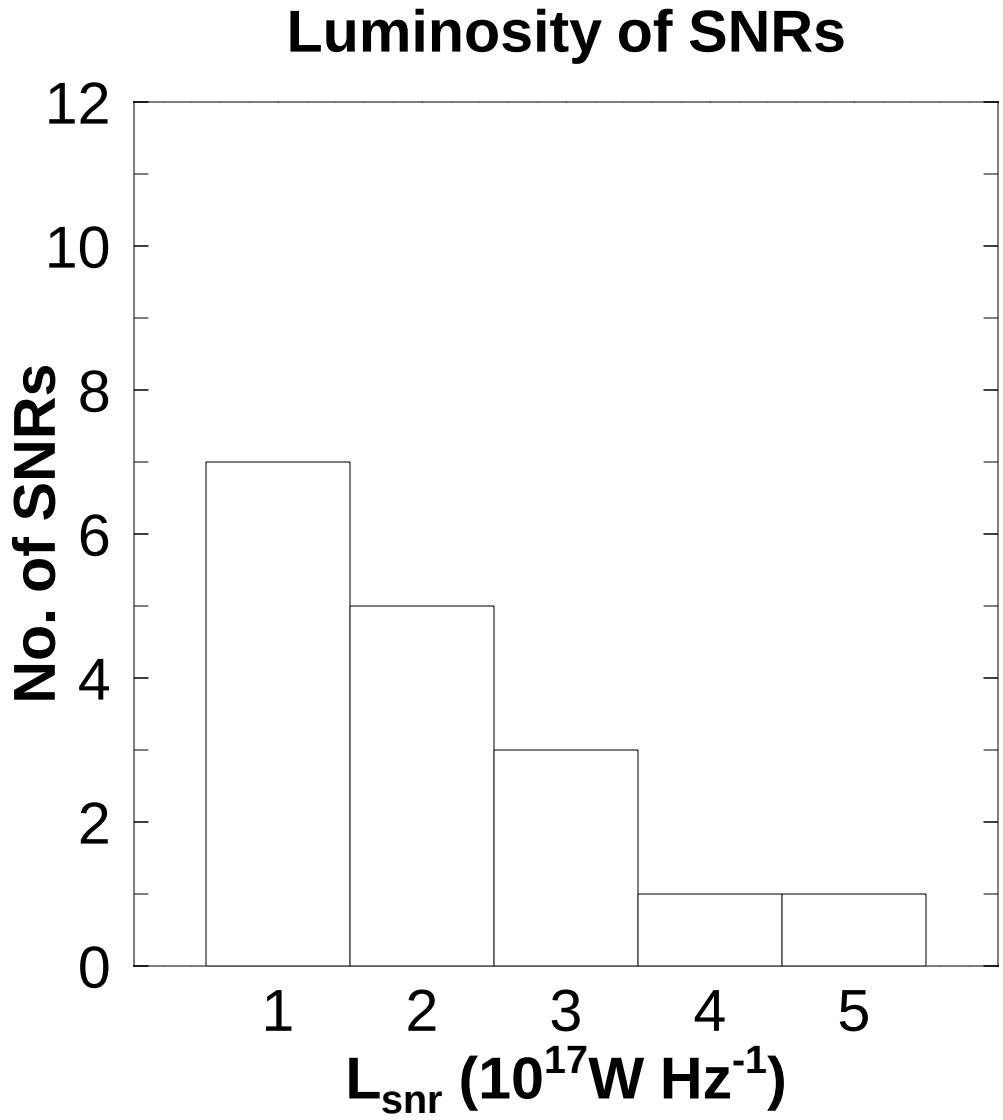

Figure 2.7 Luminosity function of SNRs in NGC 300.

association. Read & Pietsch (2001) suggest that it is a soft source and our *XMM-Newton* data implies that it has a thermal spectrum. Our calculated radio spectral index of –0.5 is also consistent with an SNR.

ATCA J005515.4-374439 (BL-S26) also has a thermal spectrum by inspection of its *XMM-Newton* X-ray colour diagram (Fig. 2.5, XMM9) and is also labeled P49 in *ROSAT* observations (see Fig. 2.8). Its radio spectral index cannot be reliably found since we only have flux densities for two very near frequencies (1374 and 1448 MHz).

In Table 2.7, we note a total of six (6) *XMM-Newton* sources with an existence likelihood of 15 which appear to be valid sources on visual inspection that match BL97 SNRs within a 4″ positional radius. Thus, possibly as many as three BL97 optical SNRs have X-ray emission but no radio detection. We also find four (4) and six (6) X-ray cross-matches within H II regions from Deharveng et al. (1988) and Soffner et al. (1996), respectively. Four BL97 SNRs with X-ray emission are associated with H II regions and only two of these have radio emission.

BL97 notes that while the canonical value of 0.4 in the ratio of [S II] to Hα has worked well in the Milky Way and Local Group galaxies to separate shock-heated nebulae from photoionized gas, the exact value of this cutoff has not been important since there is a gap in the distribution. Photoionized regions tend to show ratios of $\sim$ 0.2 or below. In Col. 10 of Table 2.4 we show the results of a visual inspection of original 1500s plates from BL97. [S II] plates were also used to create optical backgrounds for our radio and X-ray contours shown in Fig. 2.8. Although not quantitative, we see [S II] emission from 12 sources other than the SNRs reported by them. H II regions without an SNR identification tend to show little or no [S II] emission.

Some of the more interesting objects in Fig. 2.8 not reported in BL97 include ATCA J005438.1-374144, in which the typical spherical shape of a SNR can be seen. Radio emission (with a resolution of about 6″ compared to an optical resolution of 1.5″) with a spectral index of –0.8 is seen from the most intense area at ‘4 o’clock’, highlighting that non-thermal radio emission from SNRs is formed at the shock. In fact, the expanding shell of a SNR may be undergoing different processes at the same time causing some areas to emit non-thermal radio radiation while other regions do not (also see the same process shown in Fig. 2.8(u) for BL-S28). This may also be the case with sources ATCA J005450.2-374030 and ATCA J005450.7-374022. BL97 noted that there appeared to be 4 large SNRs in their data that measured up to 200 pc (20″). With these two sources, we may be detecting radio emission from one large SNR or superbubble.

Radio emission from what appears to be a shell shock front is also seen in J005451.1-373826 and J005500.5-374037 (Fig. 2.8), with the latter having a more complete shell appearance.

ATCA J005443.1-374311, J005445.3-373847, J005450.3-373822,
J005451.7-373939, J005503.5-374246 and J005512.7-374140 have less defined shells.
ATCA J005503.6-374320 may show only a half shell in [S II], but this would put the diameter of the remnant at about 100 pc and its shape is not well defined.

We cannot determine [S II]:Hα ratios of the above sources from existing BL97 observations. We feel that optical long-slit CCD spectra from these SNRs initially found in our radio data and now suspected from visual inspection of BL97's [S II] images, would be helpful in their final determination as SNRs. This information might also fine tune the [S II]:Hα ratio cutoff between H II regions and SNRs.

Radio Selected SNRs

We found thirteen additional SNRs than reported by BL97 based on radio spectral index and identification with H II regions or OB associations (Table 2.4). Although most of them have some optical emission as discussed above, there is a general lack of X-ray emission from this group of objects. This emphasizes that radio wavelengths are especially important for the detection these objects.

SNR ATCA J005451.7-373939 has a positional identification with both a globular cluster (GC6) and an OB association. It seems likely in this case, that the radio emission is associated with the OB association and the globular cluster is simply superimposed, since cluster SNRs most likely dissipated into the interstellar medium long ago.

2.6.2 Other Interesting Sources

We find three background sources based on positional identifications and spectral index. Although most of these sources represent distant galaxies, one of these, ATCA J005453.3-374311, is coincident with a globular cluster as reported by Kim et al. (2002). Its X-ray colour (XMM7 in Fig. 2.5) and radio spectral index is consistent with a power law spectrum.

ATCA J005425.2-374441 also has a very steep spectral index of –1.8, but its X-ray colour (XMM1) is a bit softer. Still, it is certainly possible that this object also has a X-ray power law spectrum as evidenced by its X-ray colour proximity to ATCA J005510.8-374835 (Fig. 2.9) which clearly corresponds to an AGN (XMM8, P58) as reported by Read & Pietsch (2001). Using *XMM-Newton* data, we were able to fit a photoelectric absorption power law model to the latter as shown in Fig. 2.10 and Table 2.5.

Based on spectral index alone, there are at least two other probable background sources. It is not possible

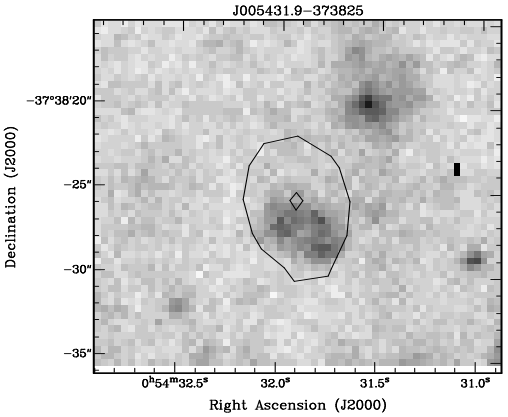

(a) ATCA J005431.9-373825 at 1374 MHz. (BL-S6)

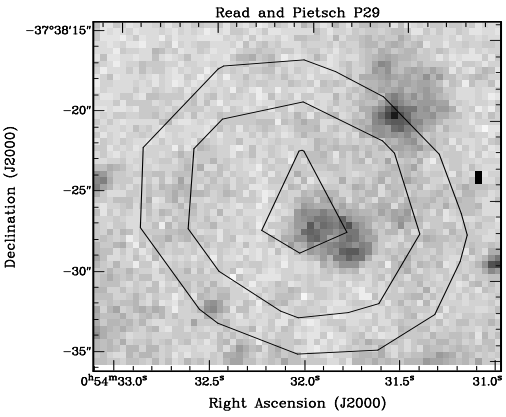

(b) *ROSAT* (P29) image contours: 2.2, 2.3 and 2.4 in units of 10^{-3} cnts s^{-1} $arcmin^{-2}$.

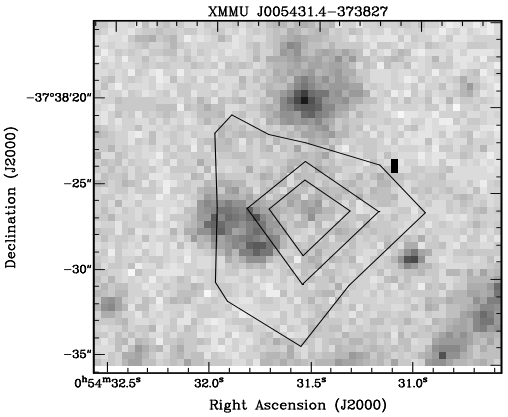

(c) *XMM-Newton* (XMM2) image contours: 2.7, 4.1 and 5.5 in units of 10^{-2} cnts s^{-1} $arcmin^{-2}$.

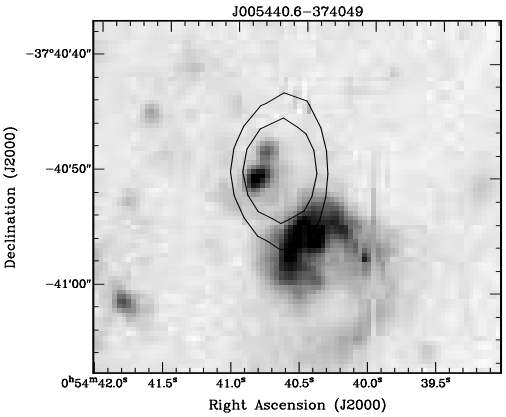

(d) ATCA J005440.6-374049 at 1374 MHz. (BL-S10)

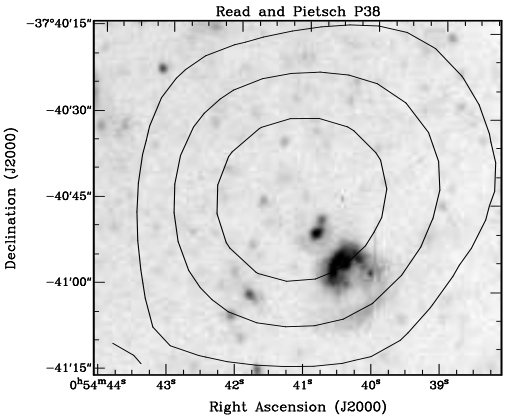

(e) *ROSAT* (P38) image contours: 2.0, 2.7 and 3.8 in units of 10^{-3} cnts s^{-1} $arcmin^{-2}$.

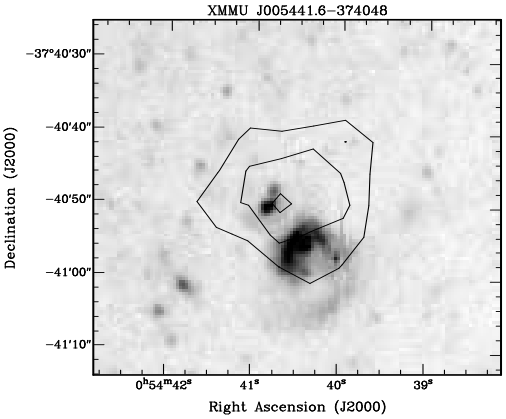

(f) *XMM-Newton* (XMM3) image contours: 4.1, 8.2 and 16.5 in units of 10^{-2} cnts s^{-1} $arcmin^{-2}$.

Figure 2.8 SNRs with radio and X-ray contours in NGC 300 overlaying BL97 1500s [S II] images. Radio contours are ∼ 3 and 5 sigma values (0.174 and 0.291 mJy $beam^{-1}$ for 1374 MHz; 0.198 and 0.330 mJy $beam^{-1}$ for 1448 MHz; 0.186 and 0.311 mJy $beam^{-1}$ for 2496 MHz).

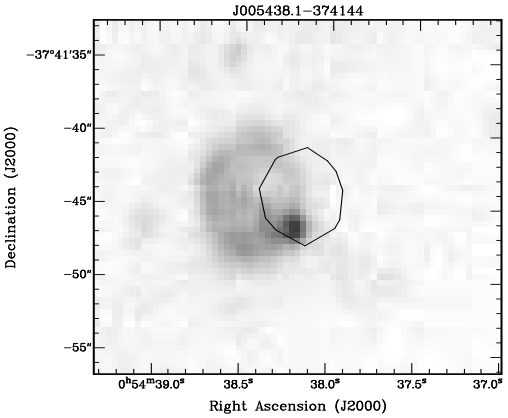

(g) ATCA J005438.1-374144 at 1374 MHz.

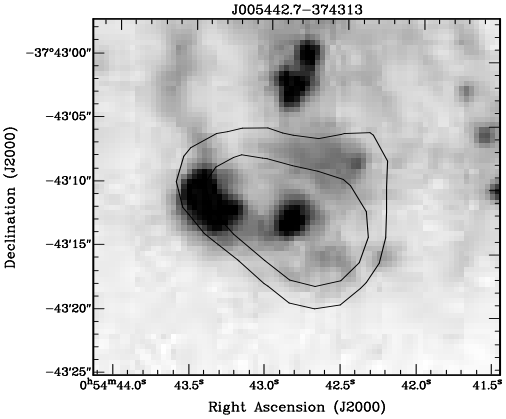

(h) ATCA J005442.7–374313 at 1448 MHz. (BL-S11)

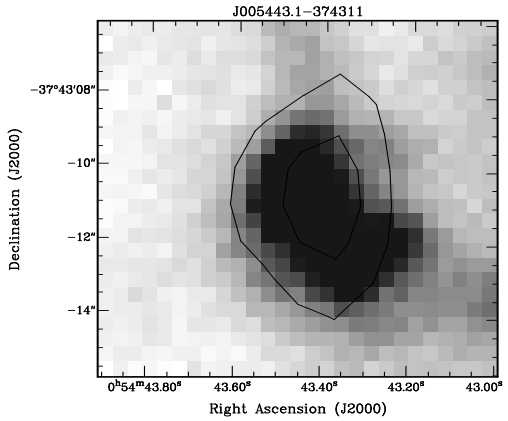

(i) ATCA J005443.1-374311 at 1448 MHz.

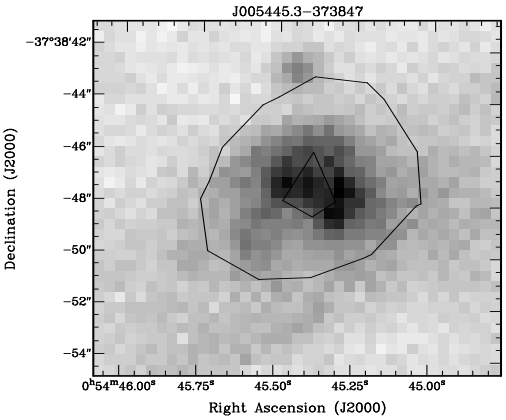

(j) ATCA J005445.3-373847 at 1374 MHz.

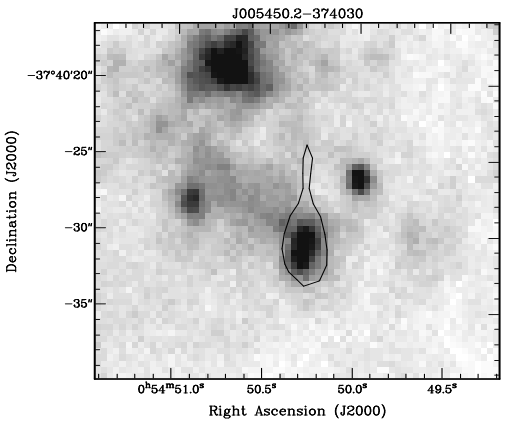

(k) ATCA J005450.2-374030 at 1448 MHz.

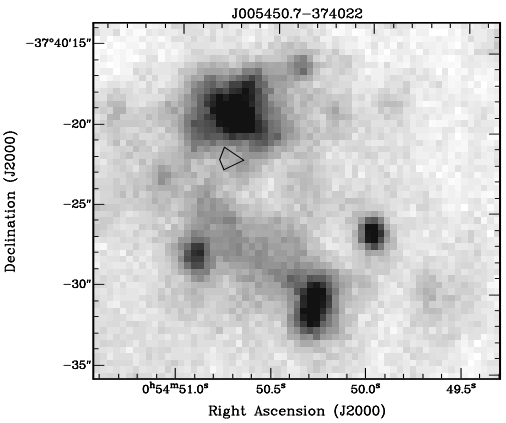

(l) ATCA J005450.7-374022 at 1374 MHz.

Figure 2.8 (Cont.) SNRs with radio and X-ray contours in NGC 300 overlaying BL97 1500s [S II] images. Radio contours are ~ 3 and 5 sigma values (0.174 and 0.291 mJy beam^{-1} for 1374 MHz; 0.198 and 0.330 mJy beam^{-1} for 1448 MHz; 0.186 and 0.311 mJy beam^{-1} for 2496 MHz).

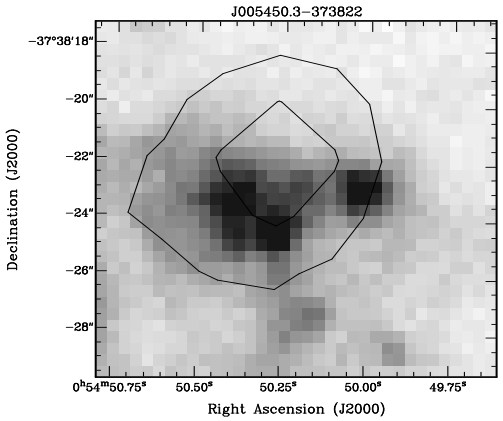

(m) ATCA J005450.3-373822 at 1374 MHz.

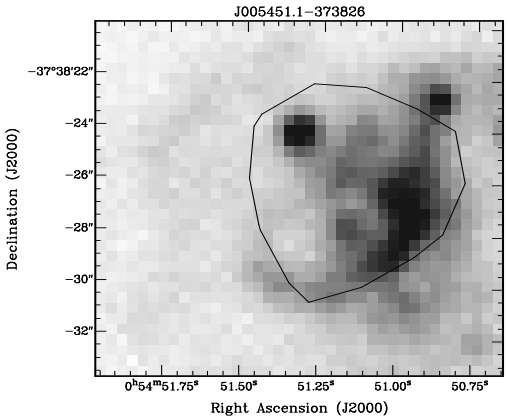

(n) ATCA J005451.1-373826 at 1374 MHz.

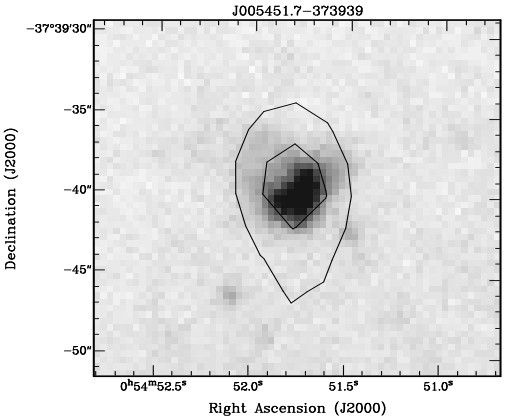

(o) ATCA J005451.7-373939 at 1374 MHz.

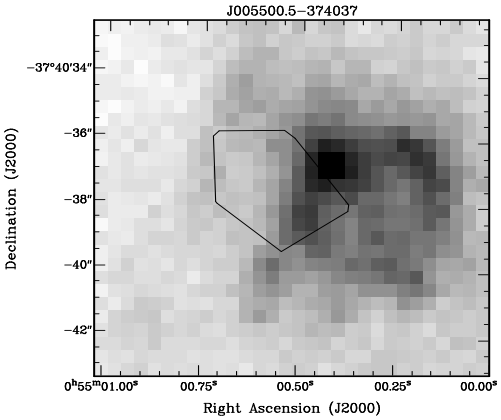

(p) ATCA J005500.5–374037 at 1374 MHz.

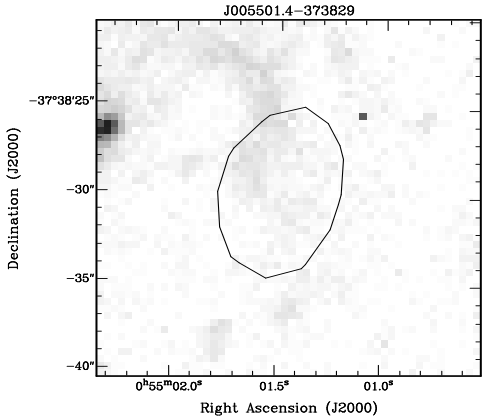

(q) ATCA J005501.4-373829 at 1374 MHz.

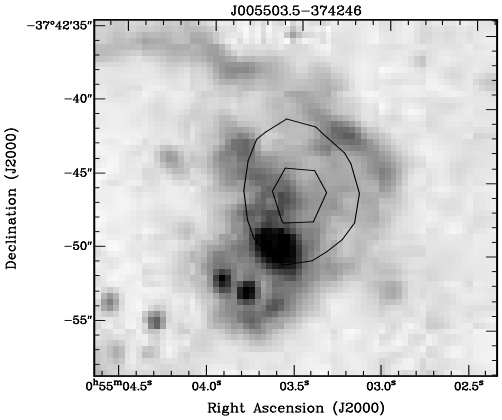

(r) ATCA J005503.5-374246 at 1374 MHz.

Figure 2.8 (Cont.) SNRs with radio and X-ray contours in NGC 300 overlaying BL97 1500s [S II] images. Radio contours are ∼ 3 and 5 sigma values (0.174 and 0.291 mJy beam^{-1} for 1374 MHz; 0.198 and 0.330 mJy beam^{-1} for 1448 MHz; 0.186 and 0.311 mJy beam^{-1} for 2496 MHz).

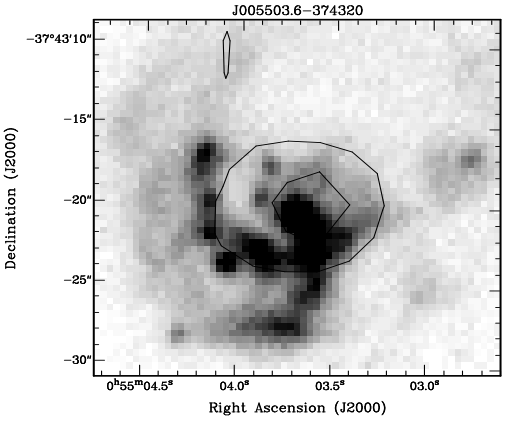

(s) ATCA J005503.6-374320 at 1374 MHz.

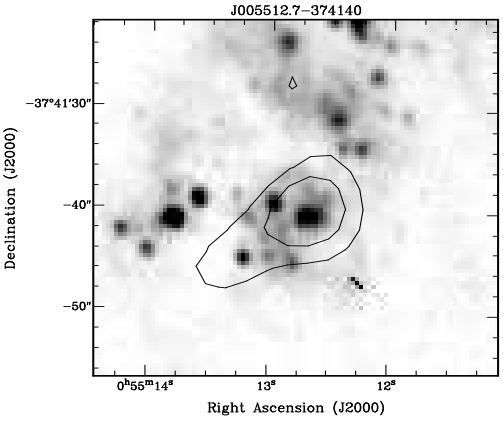

(t) ATCA J005512.7-374140 at 1374 MHz.

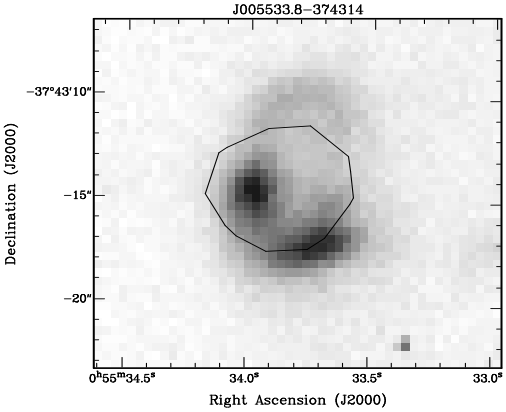

(u) ATCA J005533.8-374314 at 1374 MHz. (BL-S28)

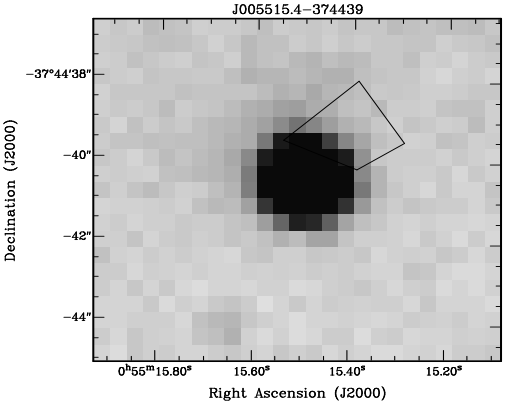

(v) ATCA J005515.4-374439 at 1374 MHz. (BL-S26)

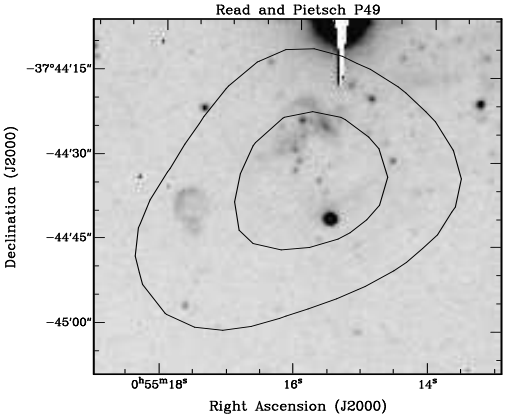

(w) *ROSAT* (P49) image contours: 2.0 and 2.7 in units of 10^{-3} cnts s^{-1} $arcmin^{-2}$.

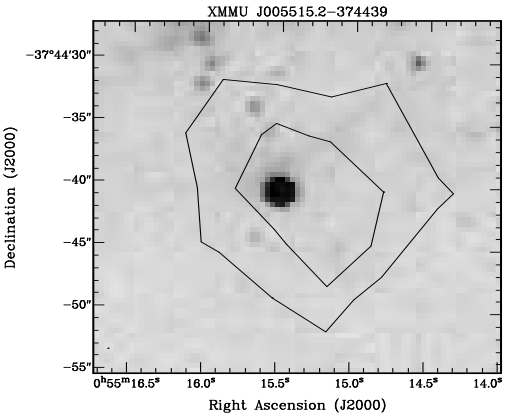

(x) *XMM-Newton* (XMM9) image contours: 2.7 and 5.5 in units of 10^{-2} cnts s^{-1} $arcmin^{-2}$.

Figure 2.8 (Cont.) SNRs with radio and X-ray contours in NGC 300 overlaying BL97 1500s [S II] images. Radio contours are ~ 3 and 5 sigma values (0.174 and 0.291 mJy $beam^{-1}$ for 1374 MHz; 0.198 and 0.330 mJy $beam^{-1}$ for 1448 MHz; 0.186 and 0.311 mJy $beam^{-1}$ for 2496 MHz).

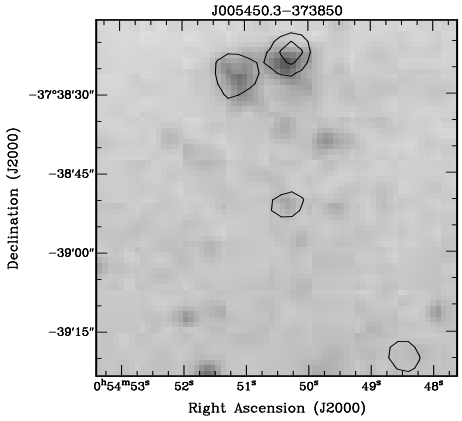

(a) ATCA J005450.3-373850 at 1374 MHz. (X-ray binary)

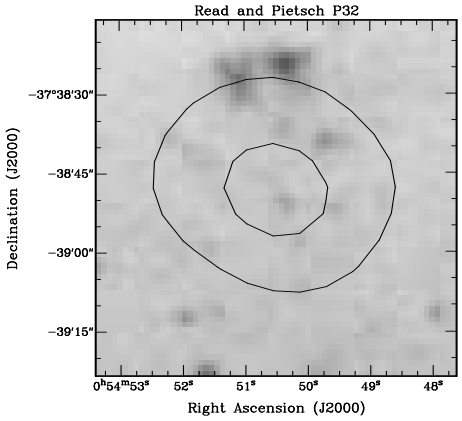

(b) *ROSAT* (P32) image contours: 2.0 and 2.7 in units of 10^{-3} cnts s^{-1} $arcmin^{-2}$.

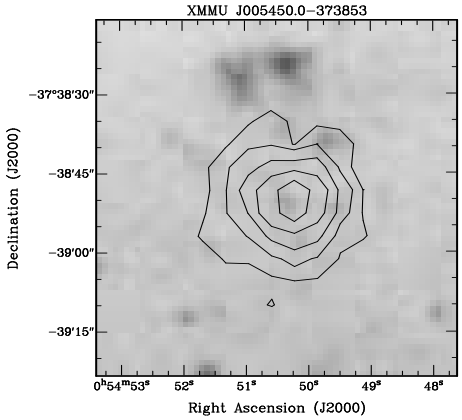

(c) *XMM-Newton* (XMM5) image contours: 4.1, 8.2, 16.5, 32.9 and 65.9 in units of 10^{-2} cnts s^{-1} $arcmin^{-2}$.

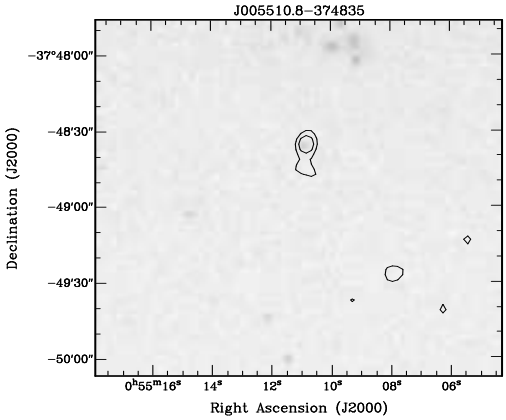

(d) ATCA J005510.8-374835 at 1374 MHz. (AGN)

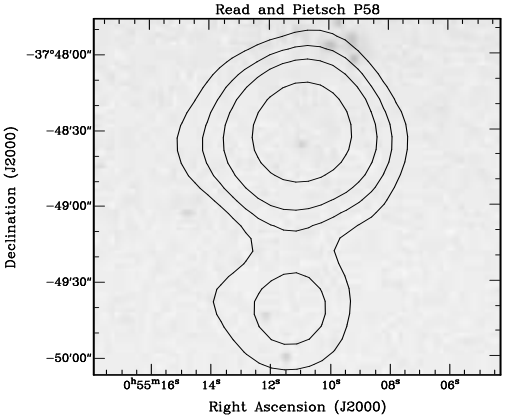

(e) *ROSAT* (P58) image contours: 2.0, 2.7, 3.8 and 6.9 in units of 10^{-3} cnts s^{-1} $arcmin^{-2}$.

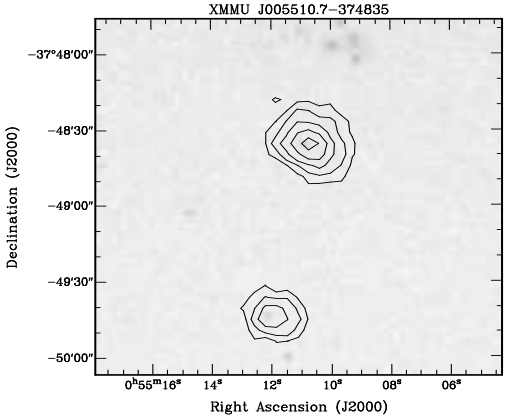

(f) *XMM-Newton* (XMM8) image contours: 4.1, 8.2, 16.5, 32.9 and 65.9 in units of 10^{-2} cnts s^{-1} $arcmin^{-2}$.

Figure 2.9 Other interesting objects in NGC 300 with radio and X-ray contours overlaying the DSS2-Red (R) image. 1374 MHz contours are 0.174 and 0.291 mJy $beam^{-1}$.

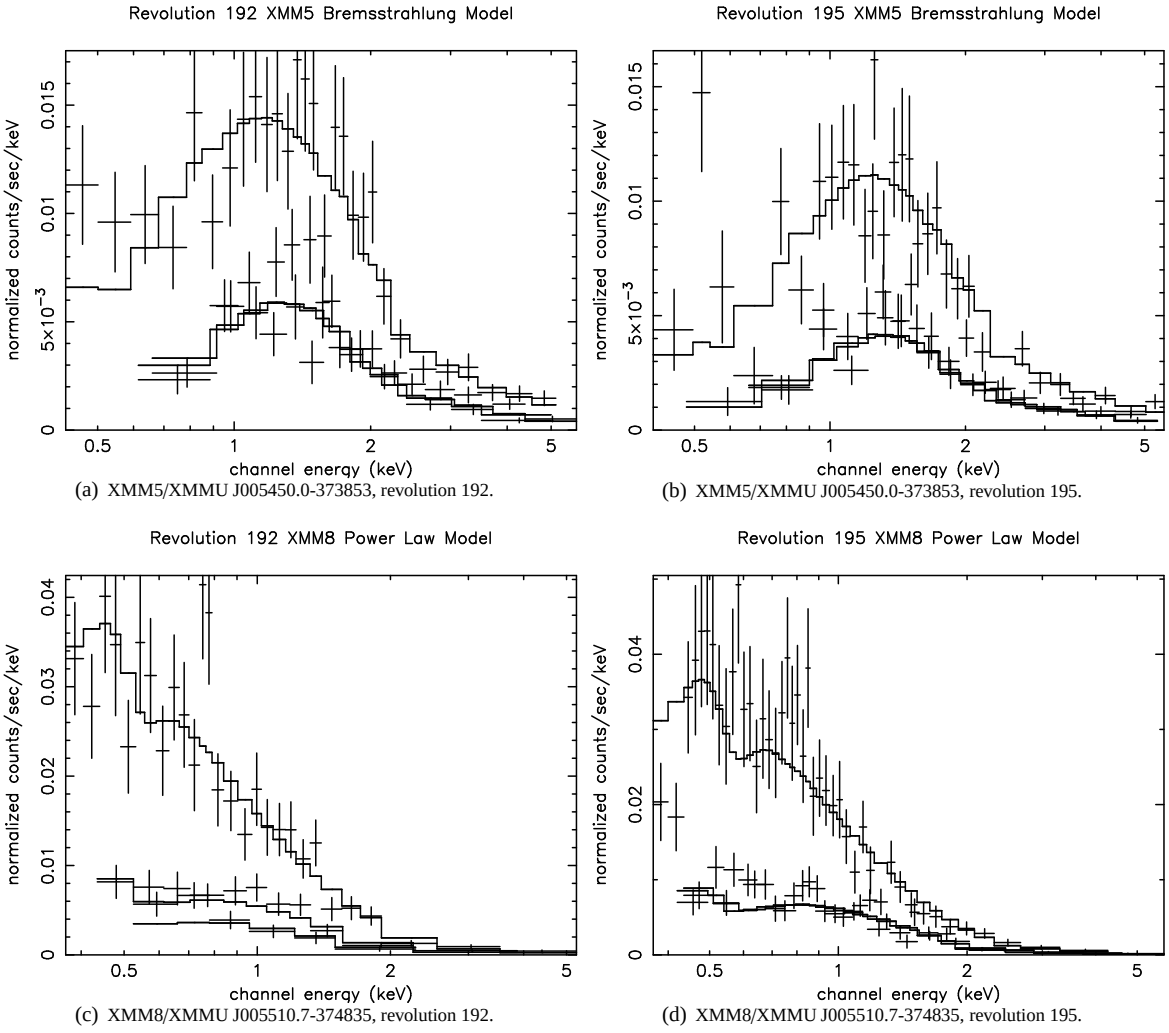

(a) XMM5/XMMU J005450.0-373853, revolution 192.

(b) XMM5/XMMU J005450.0-373853, revolution 195.

(c) XMM8/XMMU J005510.7-374835, revolution 192.

(d) XMM8/XMMU J005510.7-374835, revolution 195.

Figure 2.10 Spectrum fits for our *XMM-Newton* sources 5 and 8. In each diagram, grouped spectral data show model fits from PN data (top) with MOS 1 and MOS 2 data below (x-axis shows energy range, 0.3 keV to ~ 6.0 keV; y-axis shows counts per second per keV). The best simple fit for source 5 is the photoelectric absorption bremsstrahlung model while that for source 8 is the photoelectric absorption power law model.

to tell if the remaining 10 "bkg" objects are really background objects as they could represent a different source type.

ATCA J005450.3-373850 (Fig. 2.9) is possibly associated with an X-ray binary[3] (XMM5, P32) as reported by Read & Pietsch (2001) which they base on its distance of 30″ from the nearest SNR and its HR2 value of 0.75. Using HRI data, they also found a 41% probability that the X-ray source is variable. We have labeled this source "xrb" since the spectrum we found is also consistent with their conclusion. Our X-ray

[3] X-ray emission from accretion onto a compact star from a normal star in a binary system.

model fit shows the object to have a photoelectric absorption bremsstrahlung spectrum (Fig. 2.10). However, the photoelectric absorption power law fit is also very good (see XMM5 in Table 2.5). Perhaps this object has both thermal and power law properties. Its radio emission may be the result of synchrotron emission from jets, making this a rare example of a microquasar. Only one other suspected extragalactic microquasar has been reported by Dubus (2003) in the nucleus of M33. We expect this type of source to be rarely found in extragalactic studies since detection of the relatively faint radio emission is unlikely at far distances.

2.7 Chapter Summary

PDL could place only limits on the radio spectral indices from eight of their 14 radio sources because they had only one flux density (λ=20 cm) for each of them. One of the goals of the present study is to expand on those observations using new ATCA and *XMM-Newton* data. Our findings do support the six SNRs identifications that they made for radio sources having VLA flux densities at both 6 and 20 cm wavelengths and we pick up a 6 cm flux density for their R1 allowing us to agree with a total of seven of their sources. We also name their R2 as a possible 'snr' only, since its association with Read & Pietsch (2001) P44 has been called into doubt by those authors (see page 980 of Pannuti et al. 2002). While we disagree with six of PDL's SNRs, with the addition of ATCA flux densities in the 13 and 20 cm wavelength range, we find an additional six radio SNRs. Updating Fig. 9 in Pannuti et al. (2002) we present a Venn diagram depicting the intersection of sets of SNRs within NGC 300 in Fig. 2.11. The diagrams are very similar except that we do not include "possible" X-ray sources and although the number of radio sources is almost identical, they do not represent the same sources between the two studies. The optical and radio numbers in parentheses represent the number of SNRs in these categories if our additional BL97 identifications with radio sources are included.

In summary, out of a total of 54 radio sources, we have found and described 18 SNRs in NGC 300; 13 in addition to those found in the optical by BL97. Three of the five SNRs identified by BL97 that have radio counterparts also have X-ray counterparts. We find evidence for [S II] emission from an additional 12 of our radio sources, implying that a total of 17 SNRs have some optical component.

There are three additional SNR candidates in NGC 300 which will await further studies for verification. These sources do not appear to have any optical component, although ATCA J005528.2-374903 is not within the boundary of the BL97 images.

All identifications with *ROSAT* sources are included in our *XMM-Newton* X-ray identifications with radio sources except source number 2 (coincident with PDL's R2 discussed above) reported in Read et al. (1997).

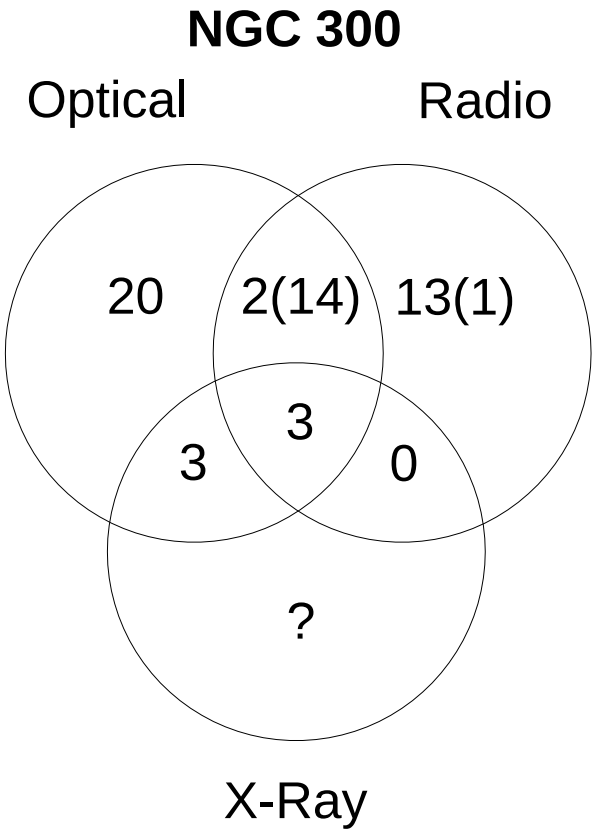

Figure 2.11 Venn diagram showing the intersection of selected sets of SNRs for NGC 300. Optical refers to the objects listed in BL97. Parenthesis show the total number of SNRs in each category if our additional [S II] optical identifications are added to those reported by BL97. The '?' denotes that at this time, we do not know the total number of X-ray SNRs within this galaxy. That information is being prepared by S. Carpano for later independent publication.

Although this source could be a supernova remnant also, we do not have a radio spectral index to prove it.

We have investigated the luminosity functions of our SNRs and find that conclusions about them as a group cannot be made since we are selecting for only the most luminous SNRs.

While it has been understood that many SNRs lie embedded within H II regions, we also note a strong correlation of our radio sources with OB associations within this galaxy. This is another good place to look for SNRs from massive progenitor stars.

We also find the expected number of background sources within the region covered by NGC 300. We note that other objects, for example, globular clusters near NGC 300, may lie in the same direction, thus adding some confusion with identification of sources. An additional seven *XMM-Newton* X-ray sources match our radio sources other than the SNRs mentioned above. Three are identified with background objects and one is associated with a likely X-ray binary as discussed above. Also, two X-ray sources could be background objects while one identifies with another X-ray supernova candidate (P36) discussed in Read & Pietsch (2001). The latter's counterpart, XMM10, shows hardness ratios consistent with a thermal spectrum but we have no additional information to prove it as a SNR.

CHAPTER 3

A CATALOGUE OF DISCRETE RADIO SOURCES DETECTED TOWARD THE SMALL MAGELLANIC CLOUD

3.1 Original Abstract

We present the classification of radio-continuum sources from the Australia Telescope Compact Array (ATCA) Catalogue of the Small Magellanic Cloud (SMC)[1]. This increases the number of discrete radio sources from 224 (Parkes Catalogue; Filipović et al. 1997) to 717. These sources have been categorised into one of three groups: supernova remnants (SNRs), H II regions and background sources. In total, we name 71 sources as H II regions (or candidates) and 21 sources as SNRs (or candidates) within the SMC. Six sources are named as either H II regions or background sources. Two sources are candidate radio planetary nebulae and one additional source is coincident with an X-ray binary, all also located within the SMC. We classify 616 objects as background sources and present their statistics.

3.2 Introduction

The SMC is one of our nearest galactic neighbours at a distance of $\sim$ 65 kpc (Feast 1999). Radio-continuum observations of this galaxy have been carried out since the early 1960s, partly because its known distance can allow more accurate estimates of physical properties such as luminosity (Filipović et al. 1998). This has resulted in an increased number of SNR detections and new catalogues.

In this chapter, we attempt to classify and study sources detected as part of an ATCA radio-continuum study of the SMC at 1.42 GHz (λ = 21 cm) and 2.37 GHz (λ = 12.7 cm). Further observations were made in selected areas of the SMC at 4.80 GHz (λ = 6.25 cm) and 8.64 GHz (λ = 3.5 cm).

One-sigma flux uncertainties of these images include 1.8 mJy beam^{-1} at 1.42 GHz, 0.4 mJy beam^{-1} at 2.37 GHz, 0.8 mJy beam^{-1} at 4.80 GHz and 0.4 mJy beam^{-1} at 8.64 GHz. The resolution of the images were as follow: 1.42 GHz at 98″, 2.37 GHz at 40″, 4.80 GHz at 30″and 8.64 GHz at 15″. The threshold of detection was set at 5-σ for one or more frequencies. More information, including observational and analytical details can be found in Staveley-Smith et al. (1997) and Filipović et al. (2002) (hereafter Paper I).

[1]This article was published in Monthly Notices of the Royal Astronomical Society, volume 355, pages 44–50 (2004). Co-authors include M. D. Filipović, W. Reid, P. A. Jones, L. Staveley-Smith and G. L. White; see 'Contribution of Others' section for more information.

Section 3.3 of this chapter outlines the classification criteria used here. Results are given in section 3.4 with a more through discussion of background objects in section 3.4.1. A summary is given in section 3.5. The following chapter will discuss SNRs and H II regions in greater detail and present their statistics.

3.3 Multi-Frequency Analysis of ATCA Sources

The SMC is essentially transparent to radio emission and all catalogues of SMC sources contain not only sources located within the SMC but also background sources seen through the SMC. In order to classify sources found in the ATCA surveys presented in Paper I, we use multiple criteria including: identification with previously known sources, source extension and morphology, source position within or outside of the SMC proper, and radio spectral index.

3.3.1 Catalogue Identification of Sources

During the last few decades, the SMC has been investigated over almost all of the electromagnetic spectrum (including Hα, optical, infra-red, radio, CO and X-ray) resulting in a number of catalogues. We list those used in our analysis in Table 3.1.

Positions of our ATCA sources were matched to within approximately 10″ for point sources and 20″ for extended sources. The selection of these limits were somewhat arbitrary based on the positional errors and resolution of our images. Cross-identification of each catalogue source was based on the catalogue's search radius assumptions listed in Table 3.1. We also visually examined the shape and structure of each radio source to verify identifications.

A large number of sources are common to our ATCA catalogue and those noted in Table 3.1. Most of these represent identifications of the same source at different wavelengths although a few may represent source confusion between nearby sources or objects within sources (e.g. an SNR located within an H II region). Comparison of the number of ATCA sources matched (Table 3.1, Col. 4) with the number of *times* each catalogue is matched (Table 3.1, Col. 5) gives an indication of the amount of confusion present. For example, a single Henize (1956) source may match multiple ATCA sources since these H II regions are relatively extended and may even overlap. On the other hand, SUMSS sources are not very extended; hence we see a one to one relationship between the number of *times* this catalogue is matched and the number of ATCA sources with SUMSS identifications.

For our list of SNRs we find an average of 7.2 matching identifications per source (for more details see

Table 3.1 Summary of the results of the cross-referencing analysis.

(1) Name	(2) Frequency	(3) No. of Catalogue Sources in Field	(4) No. of ATCA Matches	(5) No. of Times Catalogue is Matched	(6) Reference	(7) Search Radius Assumption
N	Hα	120	67	109	Henize (1956), with 'Nail' sources by McKibben Nail et al. (1953)	20″ plus source ext.
DEM S	Hα	167	106	107	Davies et al. (1976)	25″ plus source ext.
JD	λ = 5007	59	2	2	Jacoby & DeMarco (2002)	10″
M (MA)	Optical (UKST)	62	1	1	Morgan (1995)	10″; see their summary, Table 3
NGC (IC)	Optical	101	16	18	Sinnott (1988)	25″
H&S	Optical	30	9	9	Hodge & Snow (1975)	25″
LI-SMC	IR (IRAS)	249	27	27	Schwering & Israel (1990)	25″
PKS	Radio	24	6	6	Otrupcek & Wright (1991)	source specific pos. error
SMC	Radio	224	63	87	Filipović et al. (1997)	25″ doubled for ext. sources
MOST	Radio	338	289	289	Ye (1988)	15″
SUMSS	Radio	738	509	509	Bock et al. (1999)	source specific ext.
PMN	4.85 GHz	194	54	54	Wright et al. (1994)	25″ plus 50 percent of source ext.
S	5.00/8.80 GHz	27	18	18	McGee et al. (1976)	25″
MC4	408 MHz	63	56	59	Clarke et al. (1976)	source specific pos. error
MRC	408 MHz	22	6	8	Large et al. (1981)	10″ doubled for ext. sources
IJL	CO (SEST)	42	22	24	Israel et al. (1993)	45″
1E	X-ray (Einstein)	28	18	18	Seward & Mitchell (1981)	2′
IKT	X-ray (Einstein)	25	18	18	Inoue et al. (1983)	2′
WW	X-ray (Einstein)	70	23	23	Wang & Wu (1992)	40″
BKGS	X-ray (Einstein)	35	17	17	Bruhweiler et al. (1987)	1′
RX-J	X-ray (ROSAT)	248	61	63	Kahabka et al. (1999)	source specific pos. error & ext.
RX-J_2	X-ray (ROSAT)	517	109	117	Haberl et al. (2000)	1′
HRI	X-ray (ROSAT)	121	19	19	Sasaki et al. (2000)	source specific pos. error & ext.
MCRX	Radio	7	4	4	Dickel et al. (2001)	10″
YIT	Radio 843 MHz	39	39	41	Ye et al. (1998) (2004 priv communication)	10″

Chapter 4; Tables 4.2 and 4.3, Col. 8) and for H II regions we find an average of 4.3 identifications per source. Background sources have 1.9 matchings per source. A total of 79 ATCA sources had no match in any of the 25 cross-referencing catalogues; most of these have been classified as background sources[2].

Of 338 background sources in the MOST survey, 289 have corresponding ATCA sources. We find 738 background sources in the SUMSS survey within our observation region
(RA (J2000)=$01^h18^m11^s$ to $00^h42^m17^s$; DEC (J2000)=$-71^0 31' 12''$ to $-73^0 46' 38''$). These are
matched to 509 ATCA sources. We also identify 56 ATCA sources in the MC4 catalogue (with a total of 63 sources in our defined region).

Wavelength identifications play an important function in source classification, although each must be evaluated on a case by case basis. For example, X-ray coincidence with a radio source tends to support identification as a SNR. A coincidence with an infrared source, on the other hand, might suggest the object is a H II region. Other features of the object in question such as extension also play a role. An extended source within the SMC suggests a SNR or H II region, unless its extension and location is typical of a radio galaxy or quasar. We expect that most sources not coincident with the SMC proper represent background sources (see later discussion of expected background objects based on Wall 1994 in section 3.4.1).

There are limitations to our method of cross-identification. For example, the resolution of our data ranges from 15″ to 98″; much lower than the 0.7″ resolution of optical studies such as the SuperCOSMOS Sky Survey. Despite our positional accuracy of $< 1''$, one of our sources may identify with up to 15 optical sources, making use of this sort of information useless. We avoid use of these identifications.

3.3.2 The Radio-Continuum Spectral Index

The spectral index α is defined by the relation $S_\nu \propto \nu^\alpha$, where S_ν is the integrated flux density and ν is frequency. For each source, we used available flux densities found at ATCA 1.42 GHz, 2.37 GHz, 4.8 GHz and 8.64 GHz. In addition, flux densities from the MOST (Ye 1988) catalogue at 843 MHz, SUMSS (Bock et al. 1999) catalogue at 843 MHz and MC4 (Clarke et al. 1976) catalogue at 408 MHz were used. 96 sources had only one flux density available for which no spectral index could be calculated.

Uncertainties in observed flux densities lead to uncertainties in calculated spectral index. In the present study, we re-examined our ATCA flux densities reported in Paper I and fitted those in question again using the MIRIAD task IMFIT at the same 3σ cutoff used previously for extended sources.

[2]Background sources include foreground stars as well. For example, ATCA J005307-743904 appears to be associated with the eclipsing RS CVn binary CF Tuc (Budding et al. 1999).

Errors in flux density occur because sources become further resolved at higher frequencies. This has complicated spectral index comparisons with previous surveys since we resolve older catalogued sources into multiple ones and estimate a flux density for each component.

We employed a standard line of best fit algorithm to determine each source's spectral index and standard error. As a rough guide to source type by spectral index, we employed McGee & Newton's (1972) suggested classification of Magellanic Clouds radio sources into three main groups[3] based on their radio spectra:

1. Background sources with $-1.8 < \alpha < -0.6$
2. SNRs with a steep spectrum $-0.8 < \alpha < -0.2$
3. H II regions with a flat spectrum, $\alpha > -0.2$

There are large overlaps in spectral index between various source types (Rosado et al. 1993; Filipović et al. 1998). SNRs and background sources have similar spectra resulting from synchrotron emission. However, background sources are often variable at radio-continuum frequencies and therefore spectral index can be flat or even inverted. H II regions and SNRs are often associated by location; a number of SNRs in the MCs are embedded in or near to H II regions (Filipović et al. 1998).

3.3.3 Classification Criteria

Based on the discussion above, our criteria for source identification was as follows:

1. **Background Sources:**

   Sources were examined with respect to their previous catalogue identifications, comments, extension, position (RA (J2000)=$01^h18^m11^s$ to $00^h42^m17^s$;
   DEC (J2000)=$-71^0 31' 12''$ to $-73^0 46' 38''$) and spectral index. Background objects were designated as either 'BKG' or 'bkg' based on our confidence of their true nature.

   Sources known from at least one of our reference catalogues (Table 3.1) with an appropriate spectral index were designated with a capital 'BKG'. Using this method, we name 409 sources as 'BKG' and 207 as 'bkg'. We were not able to calculate spectral indices for 82 'bkg' sources.

2. **For HII regions:**

[3] Note that this is similar but not exactly the same as that presented in Chapter 2.

Sources previously catalogued as H II regions and found to have consistent extension, location and spectral index are designated as 'HII'. Potential H II regions were also compared with *IRAS* 12 and 25μm SMC images to identify any association with thermal regions. 46 sources with no (13) or inappropriate spectral indices (33) were designated as 'hii'.

Six of our sources appear to be equally described as H II regions and background sources. These are designated 'B/H' (background source or H II region). For example, two sources could have been classified as H II regions based on spectral index alone. However, they were included in our 'B/H' list because their positions and previous catalog descriptions suggest they are background sources.

3. **For SNRs:**

   Each source known to be a SNR from two or more other catalogues was examined. If its position, spectral index and morphology were appropriate, it was designated as 'SNR'. Available names, diameters, luminosities, comments and references were also listed.

   H II regions with steeper indices were checked for radio extension and position. If they had not been classified elsewhere, they were designated SNR candidates ('snr'). Using this method, five candidates were found. These are linked with other catalogues describing them at least once and up to three times, as possible SNRs. We have listed SNR candidates separately in Chapter 4.

   There are also three additional sources we discuss in Chapter 4 that show some SNR characteristics. These three sources lack sufficient evidence to be classified as SNR candidates.

3.4 Results

Using the above criteria, a catalogue of 717 source identifications was created. We show a sample of this catalogue in Table 3.2, the complete version can be found electronically at the CDS via **http://vizier.cfa.harvard.edu/viz-bin/VizieR?-source=J/MNRAS/355/44** . Appendix A (Table 1) is a partial table that lists all sources and columns 1–15.

Table 3.2 includes the following columns:

Column 1 – Our ATCA source number.

Column 2 – The group name; separate sources individually defined at one frequency but linked in a lower one.

Column 3 – The ATCA name based on Right Ascension and Declination; hours, minutes, seconds and de-

Table 3.2 Catalogue of the ATCA SMC sources (sample).

1	2	3	4		5	6	7	8	9	10	11	12	13	14	15	16	17
ATCA	Group	ATCA	J2000		S_{408MHz} MC4	S_{843MHz} SUMSS	S_{843MHz} MOST	$S_{1.42GHz}$ ATCA	$S_{2.37GHz}$ ATCA	$S_{4.8GHz}$ ATCA	$S_{8.64GHz}$ ATCA	X-ray Luminosity	$\alpha \pm \Delta\alpha$	S_{1GHz} est.	Type (previous	Other Names	Comments
No.	Name	Name	R.A.	Dec	(Jy)	(Jy)	(Jy)	(Jy)	(Jy)	(Jy)	(Jy)	(ergs s^{-1})		(Jy)	vs. here)		
1		J002907-735348	00 29 07.33	–73 53 48.2		0.1222	0.1260	0.0571	0.0060				–2.80 0.37	0.088	BKG BKG	MOST J002906-735344; SMC B0027-7409; SUMSS J002907-735350	
2		J003025-731813	00 30 25.00	–73 18 13.1		0.0569	0.0567		0.0030				–2.85 0.00	0.035	BKG BKG	MOST J003025-731809; SMC B0028-7336; SUMSS J003025-731814	
3		J003036-735148	00 30 36.62	–73 51 48.4		0.0481	0.0417		0.0029				–2.65 0.07	0.028	BKG BKG	MOST J003035-735137; WW 11; SUMSS J003036-735143	
4		J003006-740011	00 30 06.35	–74 00 11.0		0.1048	0.0768	0.0763	0.0177				–1.45 0.35	0.079	BKG BKG	MOST J003007-740004; SMC B0028-7416; PMN J0030-7400; SUMSS J003006-740009	
5		J003034-742914	00 30 34.83	–74 29 14.3	0.33	0.1766	0.1250	0.1134	0.0514				–1.00 0.11	0.133	BKG BKG	MC4 B0028-747; MOST J003034-742904; SUMSS J003032-742902	
6		J003131-743032	00 31 31.52	–74 30 32.3		0.0465	0.0489	0.0233	0.0187				–0.95 0.12	0.039	BKG BKG	MOST J003131-743024; SUMSS J003129-743025	
7		J003140-743448	00 31 40.41	–74 34 48.0		0.0940	0.0715	0.0555	0.0422				–0.65 0.12	0.073	BKG BKG	MOST J003141-743440; PMN J0031-7434; SUMSS J003137-743440	
8		J003255-714549	00 32 55.29	–71 45 49.5		0.1039		0.0379	0.0084				–2.43 0.17	0.075	BKG BKG	SMC B0030-7202; PMN J0032-7145; SUMSS J003254-714547	
9		J003252-722933	00 32 52.50	–72 29 33.7		0.0474	0.0485	0.0785	0.0368				–0.14 0.31	0.052	BKG bkg	MOST J003252-722927; SMC B0030-7246; PMN J0032-7229; SUMSS J003251-722934	
.	...	...	...	...	...	...	...	...	...	...	...	...	...	...	...	...	...
.	...	...	...	...	...	...	...	...	...	...	...	...	...	...	...	...	...
.	...	...	...	...	...	...	...	...	...	...	...	...	...	...	...	...	...
39		J003647-713609	00 36 47.34	–71 36 09.2		0.0319		0.0193	0.0125				–0.91 0.02	0.027	BKG BKG	SUMSS J003647-713614	
40		J003659-713813	00 36 59.25	–71 38 13.6		0.0087		0.0262	0.0087				0.01 0.71	0.013	BKG bkg	SMC B0034-7155; RX-J 19; RX-J_2 52; SUMSS J003659-713803	: AGN?
41		J003625-714637	00 36 25.94	–71 46 37.5		0.0208		0.0125	0.0040				–1.59 0.21	0.018	BKG BKG	RX-J_2 67; SUMSS J003627-714638	
42		J003636-715126	00 36 36.64	–71 51 26.3		0.0083			0.0026				–1.12 0.14	0.007	BKG BKG	RX-J_2 75; SUMSS J003636-715129	
43		J003633-715143	00 36 33.78	–71 51 43.3				0.0548							BKG bkg		
44	0036-7209	J003624-720853	00 36 24.45	–72 08 53.7		0.0358			0.0049				–1.92 0.14	0.026	BKG BKG	RX-J_2 144; SUMSS J003623-720900	: For spectral index, S1.42 GHz halved with #45.
45	0036-7209	J003619-720951	00 36 19.24	–72 09 51.5		0.0501	0.0668	0.0585	0.0190				–0.97 0.31	0.054	BKG BKG	MOST; SMC B0034-7225; RX-J_2 144; SUMSS J003619-720950	: For spectral index, S1.42 GHz halved with #44.
.	...	...	...	...	...	...	...	...	...	...	...	...	...	...	...	...	...
.	...	...	...	...	...	...	...	...	...	...	...	...	...	...	...	...	...
.	...	...	...	...	...	...	...	...	...	...	...	...	...	...	...	...	...
177		J004728-730601	00:47:28.58	–73:06:01.5			0.0360	0.1381	0.0284	0.0368	0.0244	0.6	–0.36 0.29	0.059	SNR SNR	part of N 19; RX-J 59; SNR SMC B0045-733; RX-J_2 401; IKT J004753-730459	: diffuse, knot, nucleus and envelope, disk and filament, irregular, emission nebulae, AGN
178		J004716-730811	00:47:16.61	–73:08:11.5	0.70		0.4600	0.4576	0.3410	0.2881	0.0891	5.8	–0.57 0.11	0.478	SNR SNR	N 19; S 9; MC4 B0045-734; NGC 261; DEM S 32; IKT 2; LI-SMC 43; WW 16; BKGS 1A; RX-J 61; SMC B0045-7324; MRCXJ0047.2-7308	: nucleus and envelope, diffuse, disk and filament, emission nebulae, SNRs/ext. structures
.	...	...	...	...	...	...	...	...	...	...	...	...	...	...	...	...	...
.	...	...	...	...	...	...	...	...	...	...	...	...	...	...	...	...	...
.	...	...	...	...	...	...	...	...	...	...	...	...	...	...	...	...	...
716		J013328-743636	01:33:28.81	-74:36:36.8		0.0378		0.0273	0.0121				–1.10 0.16	0.034	BKG BKG	SUMSS J013327-743633	
717		J013342-744610	01:33:42.37	-74:46:10.0		0.0590		0.0440	0.0073				–2.02 0.49	0.054	BKG BKG	SUMSS J013340-744610	

grees, minutes, seconds.

Column 4 – The J2000 positions.

Column 5 – Flux density at 408 MHz; from the MC4 (Clarke et al. 1976) catalogue.

Column 6 – Flux density at 843 MHz; from the SUMSS (Bock et al. 1999) catalogue.

Column 7 – Flux density at 843 MHz; from the MOST (Ye 1988) catalogue.

Column 8 – Flux density at 1.42 GHz; ATCA, this work.

Column 9 – Flux density at 2.37 GHz; ATCA, this work.

Column 10 – Flux density at 4.8 GHz; ATCA, this work.

Column 11 – Flux density at 8.64 GHz; ATCA, this work.

Column 12 – 0.1 – 4.0 keV X-ray luminosities in units of ergs s^{-1}; from X-ray catalogues listed in Table 3.1.

Column 13 – Spectral index and standard error.

Column 14 – Estimated flux density at 1 GHz based on spectral index.

Column 15 – Source type according to past work and here.

Column 16 – Names of cross-identified sources listed in previous catalogues.

Column 17 – Comments from other catalogues.

3.4.1 Background Sources

Of the 717 ATCA objects (Table 3.2), 616 or 86% have been classified as background sources (BKG or bkg). All SUMSS (Bock et al. 1999) and 280 MOST (Ye 1988) sources are included in this list.

In Fig. 3.1 we show the spectral index distribution of background sources between –3.4 and +1.2. Many of our background sources have flat spectra while others give a misleading steep result. Forty four of our sources have a spectral index less than –1.8 while all are greater than –3.4. All but four of these sources lie outside of the SMC which reflects selection of background sources based on location outside of this galaxy. Forty seven background sources have spectral indices greater than –0.2 of which 20 lie within the SMC. It is possible that their flux densities were contaminated by thermal regions within the SMC or that they are really compact H II regions that have yet to be identified.

We found no sources with spectral indices less than –1.8 to have a previous identification with an X-ray source, a known galaxy or AGN. Nine background sources with spectral indices greater than –0.2 are associated with either a previously identified AGN or background galaxy.

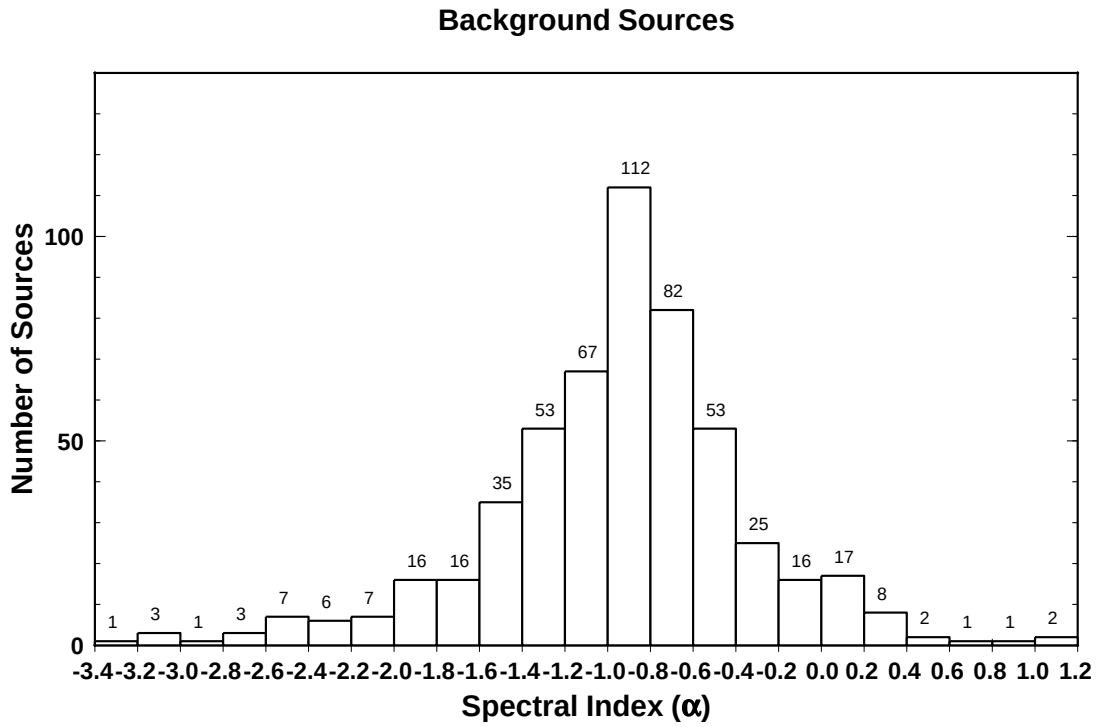

Figure 3.1 The distributions of radio spectral index between –3.4 and +1.2 for background sources.

The most likely reason for our wide distribution of spectral indices is increased resolution of sources at higher wavelengths. This is why we could not use spectral index as our primary selector of source type. On average, we find our background sources have a spectral index and standard deviation of $\alpha_{mean} \pm \sigma$ = –0.95±0.61. The mean spectral index for all of our sources towards the SMC is –0.87±0.69, which is slightly steeper than that found by Filipović et al. (1998) (–0.73±0.61).

In Fig. 3.2 we show the distribution of background sources over the observed SMC field. A faint radio image (ATCA/PKS 2.37 GHz) superimposed on the background source markers makes it apparent that the SMC is transparent to background sources, and that they are evenly distributed.

The expected background integral source count at 1.42 GHz was obtained by interpolating polynominial fits (Log N – Log S) given by Wall (1994). These fits give the predicted number of background sources in the observed field. Our other frequencies were excluded because of incomplete sky coverage (4.80 and 8.64 GHz) or limitations of Wall's fit to low flux densities given our 5σ cut-off of 2 mJy (2.37 GHz). For 1.42

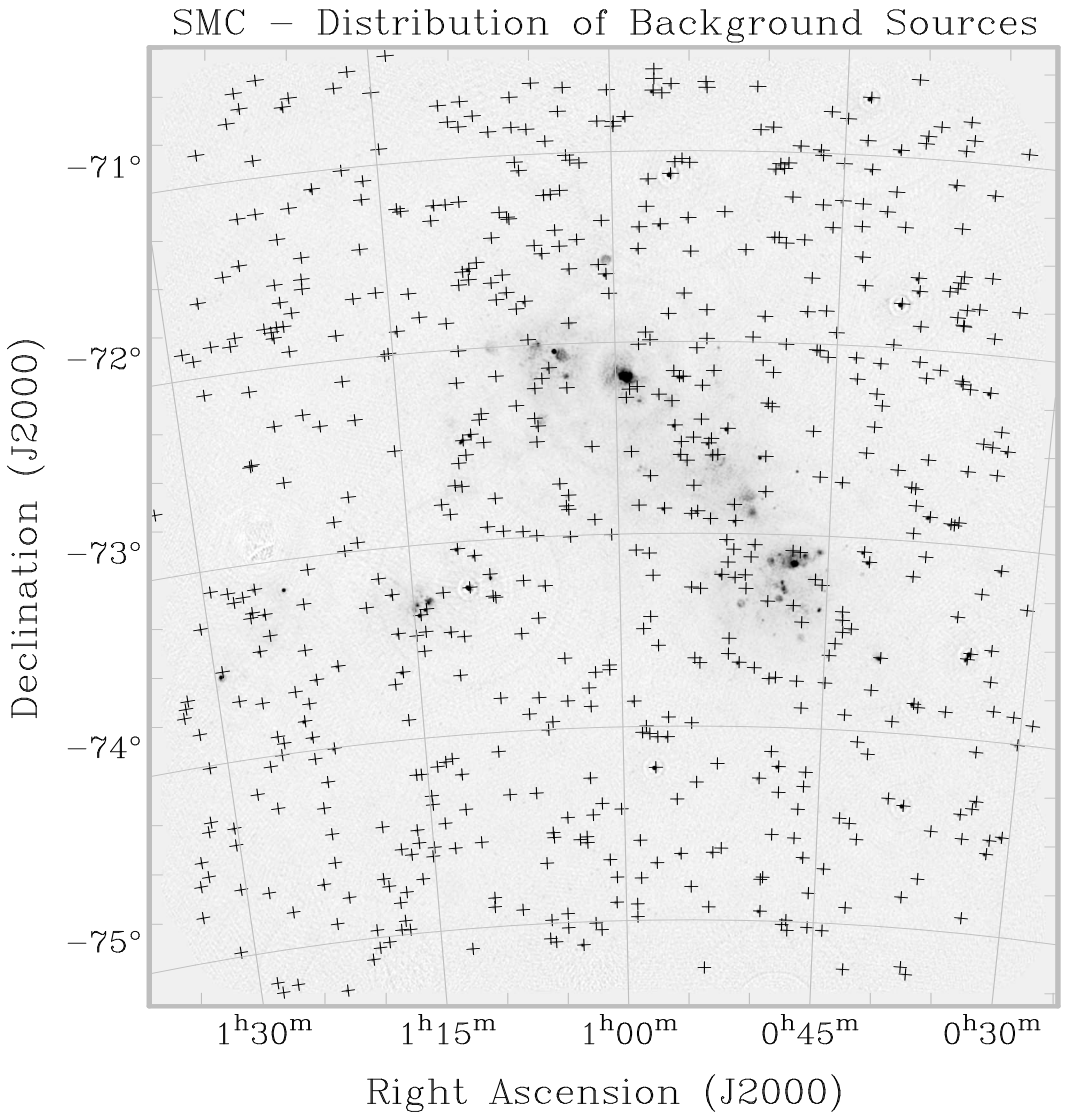

Figure 3.2 The Distribution of background sources (crosses) over the observed SMC field (ATCA/PKS 2.37 GHz image).

GHz, given a 5σ cut-off of 9 mJy and a sky coverage of $\sim$ 20 square degrees, we expect from Wall (1994) to find 426 ± 43 background sources. We find a total of 427 sources above the 5σ cut-off at 1.42 GHz, with 347 of them named as background sources. Although still useful, the estimates given by Wall (1994) are in some statistical disrepute by his own admission and their calculation omit surveys at 0.61, 0.84 and 8.4 GHz. Thus, the agreement of numbers, at 81%, is as close as one can expect.

Our catalogue of background sources behind the SMC may be useful as a finding list to guide future studies of H I 21 cm-line absorption within the cloud. Using the ATCA, Marx et al. (1997) has created such a list of compact radio sources in and behind the Large Magellanic Cloud (LMC) complete to 6 mJy peak flux density at 1.4 GHz and 3 mJy at 2.4 GHz (Our completeness flux densities are similar; 9 mJy at 1.4 GHz and 2 mJy at 2.4 GHz). Using the LMC source list to direct further observations, Marx-Zimmer (2000) report identification of 20 absorption features toward nine of 20 sources in the direction of the 30 Doradus region, finding 'cool' H I clouds more abundant or cooler than those typical within the Milky Way.

3.4.2 SNRs and H II Regions

The ATCA Mosaic survey of the SMC detected 16 confirmed SNRs (Chapter 4; Table 4.1) and five SNR candidates (Chapter 4; Table 4.2). This selection should result in the most complete sample of large and intermediate sized remnants in the external galaxies. They are the subject of the next chapter. We have also classified a total of 71 sources as H II regions (listed in Table 4.5) and six (6) as 'H II or BKG' regions.

3.4.3 Planetary Nebulae, Pulsars and Binary Objects

Since our survey covers a relatively large portion of the sky in the direction of the SMC, we searched for other source types including planetary nebulae, pulsars and binary objects.

Planetary nebulae (PNe) within the SMC would not have measurable emission much above our ATCA sensitivities. For example, Zijlstra et al. (1994) has reported a radio [WC]-type planetary nebula in the LMC named SMP 58 (Sanduleak et al. 1978). This PN has a flux density of 0.8 mJy at both 3 and 6 cm wavelengths. If located within the SMC at 65 kpc, its flux density would only be 0.47 mJy; the low end of our sensitivity range (0.4 to 1.8 mJy beam^{-1}).

Although the primary emission mechanism of PN is considered thermal, Dgani & Soker (1998) presented a radio emission model after the discovery of A30, a PN dominated by non-thermal emission. Their model suggests that the amount of flux density from this mechanism would be exceedingly low at the distance of

the SMC (less than 1 μJy).

We searched our radio-continuum sources for possible co-identifications with PNs using lists given by Morgan (1995) (Table 3) and Jacoby & DeMarco (2002) (Table 4). These two surveys list 139 PNs in the SMC. Two of our sources, J004336–730223 and J005729–723220, do match in position (less than 7″) to PNs 4 and 26 as listed in Table 4 of Jacoby & DeMarco (2002). These faint sources are designated 'PN' in Table 3.2 with J005729–723220 having the stronger flux density of 25.6 mJy at 1.42 GHz. These are potentially rare radio detections of extragalactic planetary nebulae. H II region J011447-732007 also identifies with Meyssonnier & Azzopardi (1993) source MA 1796 referenced in Morgan (1995), however visual inspection at 2.37 GHz shows it hopelessly confused with other sources within the region.

Studies by Lorimer et al. (1995) of 280 radio pulsars have indicated that they have an average spectral index of $\alpha = -1.6$ with a range down to $\alpha = -3.4$. If our sample contained a large number of these objects, this could explain our steep spectral index distribution. However, only three known radio pulsars have been reported in the SMC (Crawford et al. 2001). None of these match any of our sources.

Six of our background sources are located within the positional errors of X-ray binaries reported in previous catalogues. However, only one, J004718–723947 with a spectral index of $+0.93 \pm 0.46$, appears to be reasonably coincidental to X-ray binary RX-J 57 on visual inspection (less than 9″). This source has been marked 'XRB' in Table 3.2. If this source really is a microquasar, it would be a rare find at distances outside the Milky Way. Only two other suspected extragalactic microquasars have been reported[4]. A microquasar would also be expected to emit radio synchrotron energy which our spectral index doesn't support. We cannot say that any other of our sources are definitely binaries within the SMC. Certainly binary objects do not explain our spectral distribution.

3.5 Chapter Summary

All detected ATCA radio-continuum sources listed in Paper I have been classified according to our criteria which include position, morphology, extent, previous identifications and spectral index. From a total of 717 radio sources, we identify 71 H II regions, 16 SNRs, five (5) candidate SNRs, two (2) candidate radio planetary nebulae and one X-ray binary within the SMC. We identify 616 background sources and calculate individual spectral indices for several sources that were blended in past surveys.

[4]This includes one found in the nucleus of M 33 as reported by Dubus (2003) and J005450.3-373850 reported in Chapter 2.

CHAPTER 4

THE SMALL MAGELLANIC CLOUD – SNR STATISTICS

4.1 Original Abstract

A total of 717 sources from the Australia Telescope Compact Array (ATCA) Catalogue of the Small Magellanic Cloud (SMC) were classified as discussed in the last chapter (also Payne et al. 2004a)[1]. Here, we present a statistical analysis of all 16 confirmed supernova remnants (SNRs) and five (5) new candidate remnants. Included is a detailed discussion of the latter and three (3) other sources that have some SNR characteristics. We have also found a new microquasar candidate (ATCA J005523-721055) in addition to ATCA J004718-723947 reported in Chapter 3. Source diameter comparisons suggest that SNRs as a group are of similar size in radio, optical and X-ray with surface brightness values in the range of Galactic remnants. Remnant spectral indices, α [Defined as $S_\nu \propto \nu^\alpha$, with S_ν (flux density) and ν (frequency)], have a mean of –0.63 (s.d.=0.43) and *ROSAT* X-ray hardness ratios confirm them to be soft X-ray sources compared to background objects. We could not find any meaningful correlation between SNR surface brightness and diameter; we also discuss the number-diameter relation. A Venn-diagram summarizes that most SNRs emit radiation in all three of the radio, optical and X-ray domains. H II region diameter comparisons between radio and optical sources show them to be a very diverse group that defy any simple relationship, preventing any meaningful calculation of flux density or spectral index. To better understand environments containing SNRs, we have scaled Hα images of four SMC regions and subtracted their flux from the ATCA 2.37 GHz radio image. These 2.37 GHz – Hα subtraction (or difference) images reveal some new sources with predominantly non-thermal emission, exposing SNRs confused with H II regions.

4.2 Introduction

Located at a distance of $\sim$ 65 kpc (Feast 1999), the SMC is a prime target for the astrophysical research of objects including SNRs and H II regions. Here, we present results using ATCA radio-continuum observations at 1.42 GHz (λ = 21 cm) and 2.37 GHz (λ = 12.7 cm) centered on RA (J2000) = 00^h55^m and Dec (J2000) = –72°50′ covering a $\sim$ 20 square degree field of the sky. Parkes data were added to these to

[1]The present chapter was published in Monthly Notices of the Royal Astronomical Society, volume 364, pages 217–236 (2005). Co-authors include M. D. Filipović, W. Reid, C. W. Danforth, L. Staveley-Smith, P. A. Jones and G. L. White; see 'Contribution of Others' section for more information.

provide missing short-spacing as outlined in Stanimirović et al. (1999). Further observations were made in selected regions of the SMC at 4.80 GHz (λ = 6.25 cm) and 8.64 GHz (λ = 3.5 cm) in 1997 and 1998.

Flux uncertainties of these images include 1.8 mJy beam^{-1} at 1.42 GHz, 0.4 mJy beam^{-1} at 2.37 GHz, 0.8 mJy beam^{-1} at 4.80 GHz and 0.4 mJy beam^{-1} at 8.64 GHz. The resolution of the images were as follow: 1.42 GHz at 98″, 2.37 GHz at 40″, 4.80 GHz at 30″and 8.64 GHz at 15″. More details and the resulting catalogue can be found in Staveley-Smith et al. (1997) and Filipović et al. (2002) (hereafter known as Paper I).

Initial classification of sources were presented in Chapter 3 (Payne et al. 2004a) of this series. For that study, we used criteria including identification with previously known sources, source extension and morphology, position and radio spectral index. Table 3.2 is a sample of the complete source list which can be found in Appendix A (Table 1). It is also available in a machine-readable format from CDS (**http://vizier.cfa.harvard.edu/viz-bin/VizieR?-source=J/MNRAS/355/44**).

Positional identification with previously known sources at other wavelengths is one of the most important tools for the classification of astronomical sources. For example, X-ray data catalogues show good alignment, matching all 16 known SNR radio sources; three of five candidates SNRs have at least one listing in an X-ray catalogue. In addition, recent *XMM-Newton* X-ray spectral analysis (van der Heyden et al. 2004) classified ten (10) SMC SNRs by progenitor type. This type of information greatly enhances the understanding of these sources. Thus, X-ray source identifications are very efficient for confirming SNRs, despite a rapid reduction of apparent X-ray luminosity with increasing size (Long 1983).

This chapter is organized as follows: Section 4.3 gives a list of SNRs and candidate SNRs within the SMC. Images from four separate areas of the SMC in which scaled Hα flux corresponding to H II regions have been subtracted are presented in section 4.4. A detailed discussion of individual candidate SNRs can be found in section 4.5 and a discussion of the new microquasar candidate in section 4.6. Statistics of SNRs and H II regions are presented in section 4.7. Section 4.8 was originally an appendix to the published paper which gives supplemental information about the confirmed radio SNRs. Section 4.9 summarizes the results of this chapter.

4.3 SNR and Candidate SNR Tables

Tables 4.1, 4.2 and 4.3 contain a detailed list of individual SNRs, candidate SNRs and other sources having some SNR attributes. We describe Table 4.1 below; Tables 4.2 and 4.3 are similar except that there are no previously reported spectral indices or progenitor types for these sources, but source catalogue names from

Table 4.1 SMC Confirmed Supernova Remnants. For diameter measurements, note that the resolution at 2.37 GHz is 40″. The Progenitor Type in Column 9 is taken from van der Heyden et al. (2004). For notes and images of these sources, refer to Section 4.8. References for previously reported spectral indices taken from (a) Dickel et al. (2001), (b) Mathewson & Clarke (1972), (c) Mathewson et al. (1983), (d) Ye et al. (1995), (e) Amy & Ball (1993), (f) Filipović (2000) and (g) Mills et al. (1984).

(1) ATCA No.	(2) ATCA SNR Name	(3) R.A. (J2000)	(4) Dec (J2000)	(5) $\alpha \pm \triangle\alpha$	(6) Previous α	(7) Diameter 2.37 GHz (″)	(8) Luminosity ($\times 10^{15}$ W Hz^{-1})	(9) Progenitor Type	(10) Other Names
158	J004637-730823	00 46 37.6	–73 08 23.3	–0.61±0.55	–0.6 [a]	111	10.7	II	B0044-734
177	J004728-730601	00 47 28.6	–73 06 01.5	–0.36±0.29		165	14.4		B0045-733
178	J004716-730811	00 47 16.6	–73 08 11.5	–0.57±0.11	–0.5 [b]	114	173.0	II	B0045-734
199	J004821-731931	00 48 21.2	–73 19 31.6	–1.06±0.11	–0.9 [a]	111	56.8	Ia	B0046-735
222	J004907-731402	00 49 07.8	–73 14 02.0	–0.62±1.52		121	9.8	Ia	B0047-735
249	J005110-732212	00 51 08.7	–73 21 21.4	–0.66±0.04	–0.4 [c]	175	39.9	II	B0049-736
258	J005240-723820	00 52 42.5	–72 37 12.9	–1.03±0.05		302	55.5		B0050-728
345	J005800-721101	00 58 00.0	–72 11 01.4	0.02±0.18		114	26.8		B0056-724
347	J005817-721814	00 58 18.4	–72 17 22.7	–0.74±0.10		210	29.9	II	B0056-725
366	J005927-721010	00 59 27.7	–72 10 33.6	–0.81±0.27		181	166.0		B0057-724
378	J010023-713322	01 00 23.9	–71 33 21.1	–0.78±0.06		137	63.2		B0058-718
419	J010313-720958	01 03 15.4	–72 09 57.4	–0.47±0.09	–0.5 [d]	86	43.5		B0101-724
430	J010402-720149	01 04 01.2	–72 01 52.3	–0.65±0.02	–0.7 [e]	60	113.0	II	B0102-723
447	J010524-720923	01 05 24.2	–72 09 23.4	–0.47±0.02	–0.48[f]	149	20.5	Ia	B0104-722
451	J010505-722319	01 05 08.9	–72 23 16.7	–0.68±0.05	–0.5 [g]	194	32.9	II	B0103-726
468	J010619-720527	01 06 20.0	–72 05 28.1	0.19±0.28		79	9.2	Ia	B0104-723

our cross-referencing analysis are included.

4.3.1 Description of Table 4.1

Information contained in Table 4.1 is given in the following columns:

Column 1 – The ATCA source number (No.) from Chapter 3.

Column 2 – ATCA catalogue name.

Column 3 – Central position right ascension (J2000).

Column 4 – Central position declination (J2000).

Column 5 – Spectral index, α, and error, $\Delta\alpha$.

Column 6 – Previously reported spectral index.

Column 7 – Radio diameter (arcsec) at 2.37 GHz.

Column 8 – Luminosity (W Hz^{-1}) at 2.37 GHz.

Column 9 – Progenitor type (from van der Heyden et al. 2004).

Column 10 – Other names.

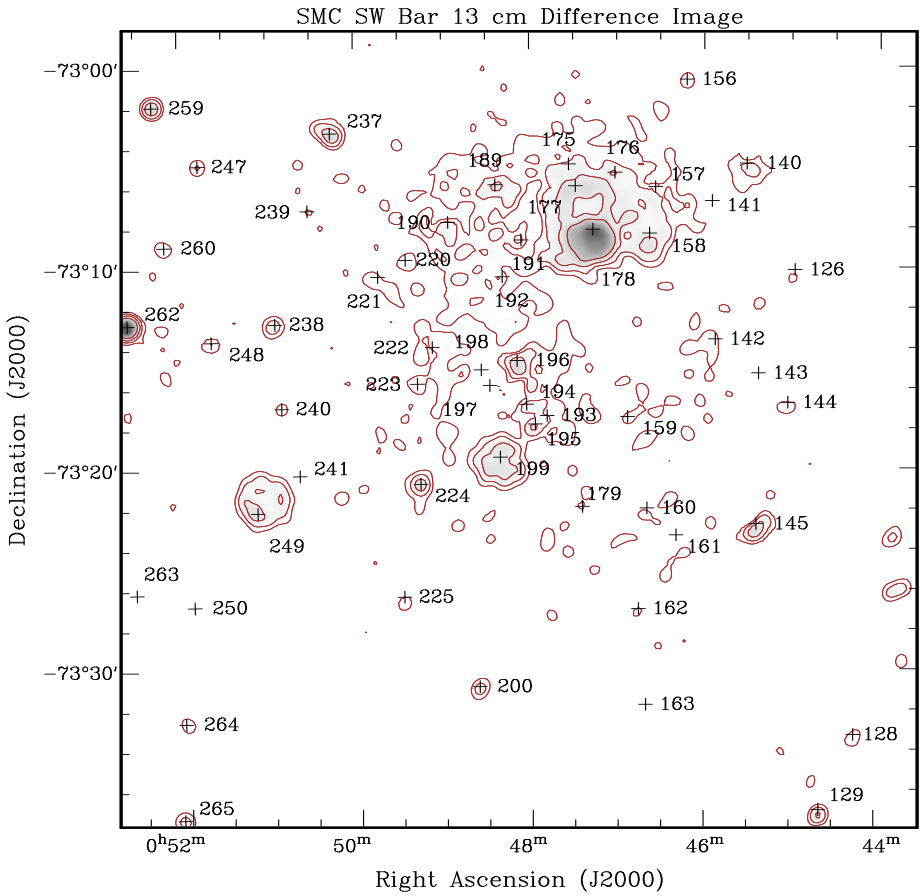

Figure 4.1 Subtraction image (2.37 GHz – Hα) of the SMC southwest Bar region. ATCA SMC source numbers 158 (J004637-730823), 177 (J004728-730601), 178 (J004716-730811), 199 (J004821-731931), 222 (J004907-731402) and 249 (J005110-732212) are SNRs (Table 4.1). ATCA SMC 191 (J004806-730842) and 193 (J004748-731727) are candidate SNRs (Table 4.2) and sources ATCA SMC 126, 140, 141, 144, 145, 155 – 157, 159, 160, 161, 163, 189, 190, 192, 194 – 198, 200, 220, 221, 223, 225, 241 and 250 are classified as H II regions. Remaining sources are background sources. Image sensitivity (rms) is 0.002 and contours are 0.008, 0.016, 0.032 and 0.064 mJy pixel^{-1}. Note that this process is far from perfect; H II regions ATCA SMC 145, 195 and 196 are as bright as as the rim of ATCA SMC 249 (SNR J005110-732212).

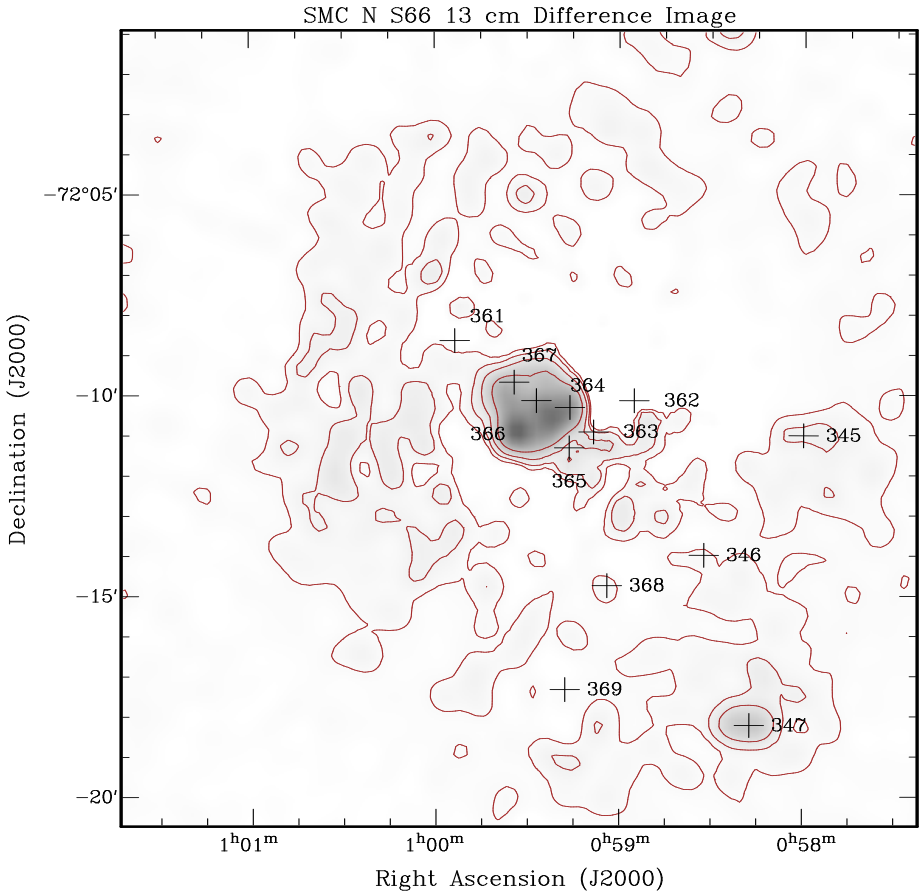

Figure 4.2 Subtraction image (2.37 GHz – Hα) of the SMC N S66 region showing extensive sidelobes to the east. ATCA SMC source numbers 345 (J005800-721101), 347 (J005817-721814) and 366 (J005927-721010) are known SNRs (Table 4.1) while sources ATCA SMC 361, 362, 363, 364, 365 and 367 are H II regions. The remainder are background sources. Image sensitivity (rms) is 0.002 and contours are 0.008, 0.016, 0.032 and 0.064 mJy pixel^{-1}.

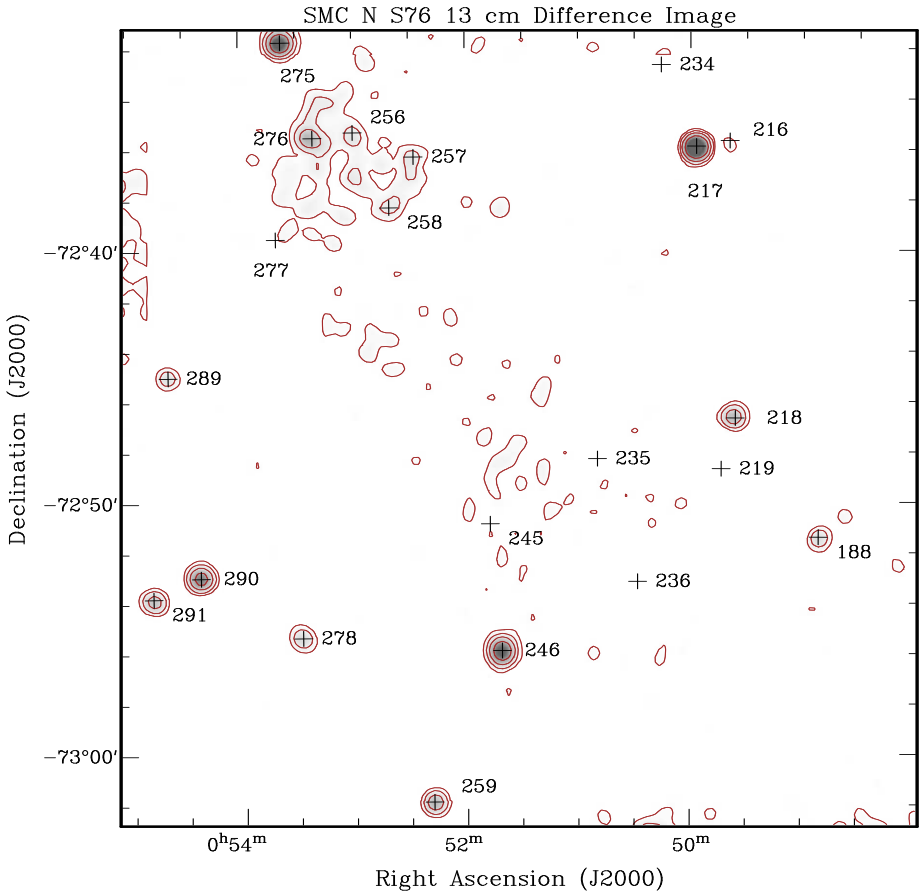

Figure 4.3 Subtraction image (2.37 GHz – Hα) of the SMC N S76 region. ATCA SMC source number 258 (J005240-723820) is a known SNR (Table 4.1) and sources ATCA SMC 219, 234, 235, 236, 257 and 277 are H II regions. ATCA SMC sources 188 and 217 could not be classified as either a background source or H II region with certainty. The remainder are classified as background sources. Image sensitivity (rms) is 0.002 and contours are 0.009, 0.018, 0.036 and 0.072 mJy pixel^{-1}.

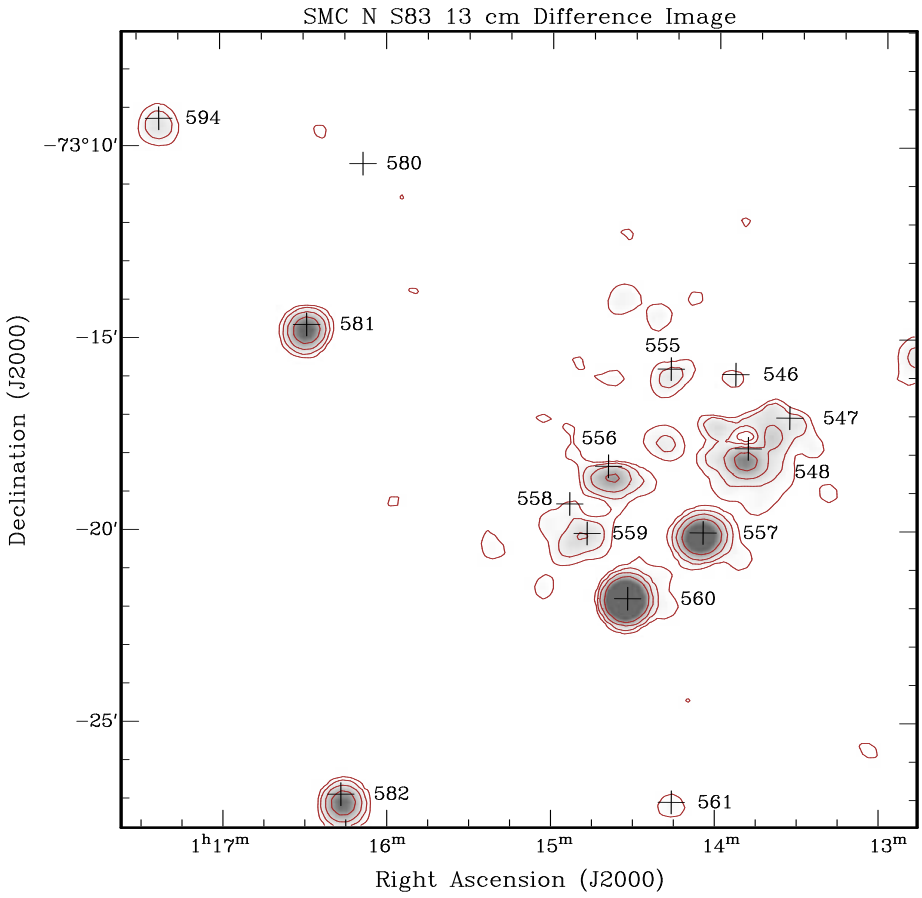

Figure 4.4 Subtraction image (2.37 GHz – Hα) of the SMC N S83 region. ATCA SMC source number 547 (J011333-731704) is a candidate SNR (Table 4.2) while sources ATCA SMC 546, 548, 555, 556, 558, 559 and 580 are H II regions. The remaining are considered background sources. Image sensitivity (rms) is 0.002 and contours are 0.008, 0.016, 0.032 and 0.064 mJy pixel^{-1}.

Table 4.2 SMC Candidate Supernova Remnants.

(1) ATCA No.	(2) ATCA SNR Name	(3) R.A. (J2000)	(4) Dec (J2000)	(5) $\alpha \pm \triangle\alpha$	(6) Diameter 2.37 GHz ($''$)	(7) Luminosity ($\times 10^{15}$ W Hz^{-1})	(8) Other Names
87	J004100-733648	00 41 00.1	–73 36 48.6	–0.94± 0.14	102	23.0	DEM S5; LI-SMC 10; RX-J 34; SMC B0039-7353; RX-J_2 530; MOST J004048-733653
191	J004806-730842	00 48 06.1	–73 08 42.7	–0.28±0.20	79	53.0	BKGS 1A; IJL J004730-730820; N S19; S 9
193	J004748-731727	00 47 48.6	–73 17 27.4	–0.58±0.04	76	13.5	N S21; N S23
445	J010539-720341	01 05 39.2	–72 03 41.7	–1.89±0.44	79	20.0	N S78C; DEM S130
547	J011333-731704	01 13 33.8	–73 17 04.4	–0.17±0.17	76	35.5	N S83(A,C); DEM S147; RX-J 227; SMC B0112-7333; RX-J_2 448; S 26; PKS BO113-735; MC4 B0112-736; PMN J0114-7318; NGC 456; Nail 148

Table 4.3 Sources with SNR Attributes. DEM S142 was not included in the ATCA source list as it has only faint radio emission at 1.42 GHz and is below the sensitivity at all other survey frequencies.

(1) ATCA No.	(2) ATCA SNR Name	(3) R.A. (J2000)	(4) Dec (J2000)	(5) $\alpha \pm \triangle\alpha$	(6) Diameter 2.37 GHz ($''$)	(7) Luminosity ($\times 10^{15}$ W Hz^{-1})	(8) Other Names
163	J004640-733150	00 46 40.6	–73 31 50.9	–0.47± 0.12	135	22.8	IJL J004643-733112; NGC 265; LI-SMC 38; N 17; DEM S 25
–		01 11 16.0	–72 09 30.0				DEM S142
487	J010819-715956	01 08 19.6	–71 59 56.6	–0.73±0.05	240	48.8	IJL J010831-715946; SMC B0106-7215; PMN J0108-7200; N 80 (80A); S 23; DEM S 135; LI-SMC 184

4.4 Subtraction Images

Ye et al. (1991) demonstrated that the 'scaled subtraction' of a Hα map from a high resolution radio image was an efficient method of searching for SNRs in H II regions, especially those in the dust-deficient Magellanic Clouds. This technique also allows an estimate of a remnant's boundary when otherwise it would be impossible. The latter may be used to estimate the flux density of an SNR.

Wide-field optical CCD images were obtained at the Curtis Schmidt Telescope at Cerro Tololo Inter-American Observatory (CTIO) in 1999 November covering the entire central SMC with 2048×2048 pixel images at $\sim 3''$ resolution through Hα (λ_c = 6563 Å, $\Delta\lambda$ = 30 Å) and red continuum (λ_c = 6850 Å, $\Delta\lambda$ = 95 Å) filters. The images were reduced and aligned using standard procedures in IRAF; they are described in detail in Danforth et al. (2002). We use these images for the subtraction process, diameter measurements, morphology characterization and co-identifications throughout this chapter.

To compare the Hα emission-line data with radio-continuum emission data, we performed the following steps: First, the red continuum image was carefully subtracted from the Hα image adjusting the relative scaling as necessary to produce a continuum-subtracted image. The data are not flux-calibrated so arbitrary scaling was necessary to minimize stellar residuals. Second, the continuum-subtracted Hα image was

smoothed to the same resolution as the radio data using a simple Gaussian smoothing kernel. If the continuum subtraction in the first step was not perfect, the smoothing kernel was usually broad enough that stellar residuals contributed negligible flux to the smoothed image[2]. Finally, the smoothed image was aligned, scaled and subtracted from the radio data. Scaling was determined such that the minimum flux over large portions of the difference image was close to zero but not negative. The resulting difference image should show only the non-thermal component of the radio-continuum emission.

The subsections below describe 2.37 GHz – Hα difference images of N S66, N S76, N S83 and the southwest Bar, labeled with sources that were classified in Payne et al. (2004a). We use these methods to identify SNRs within their environments and note their relative positions with respect to background objects.

It is stressed, however, that radio H II regions cannot be perfectly scaled by the Hα image. In Fig. 4.2, for example, the SNR, ATCA SMC 345 (J005800-721101) has fainter emission than the H II regions forming the N S66 complex. In some cases, the remaining thermal radio emission from an H II region is strong enough to overcome flux from a nearby SNR. An example of this is shown in Fig. 4.3 with SNR ATCA SMC 258 (J005240-723820) and H II region ATCA SMC 257 (J005227-723619).

If the Hα image scaling to H II regions is too aggressive, all of the non-thermal emission may be completely removed. Thus, radio – Hα subtraction techniques can only augment what is already known about these remnants. The goal simply cannot be to exclusively remove all of the surrounding H II region from the remnant.

4.4.1 Southwest Bar

The SMC 'Bar' is a diverse region consisting of OB associations, young clusters, supergiants, H II regions, cepheids, supergiant shells and SNRs (Westerlund 1997a). The entire Bar is about $2.5^\circ \times 1^\circ$ in size while Fig. 4.1 covers only the southwest region. This image contain six SNRs and two candidate SNRs surrounded by 27 H II regions. Information concerning these objects may be found in section 4.5 and Tables 4.1 and 4.2.

4.4.2 N S66

The large H II region, N S66 is approximately 115×130 pc in size located in the northern part of the SMC Bar and ionized by the young association NGC 346 (Fig. 4.2). Its age is about $\sim$ 2.5 Myr and it contains at least 800 stars (Westerlund 1997b). The centerpiece of the N S66 region is SNR J005927-721010 (B0057-724),

[2]Kernel FWHM for the 2.37 GHz image was 40″.

detected in the radio by Ye et al. (1991) who found that the difference map revealed a shell structure with the X-ray source IKT 18 (Inoue et al. 1983) at its center. This is surrounded by ATCA SMC sources 361 – 365 and 367 which represent the large H II regions of the N S66 complex (Henize 1956). Source ATCA SMC 363 is the central H II region known as N S66.

Danforth et al. (2003) studied this region using data from the *Far-Ultraviolet Spectroscopic Explorer* (*FUSE*) to propose a physical relationship between SNR J005927-721010 (B0057-724) and N S66. In this model (see Fig. 1.6), the SNR is located on the near side of N S66, interacting with the denser, ionized gas on the far side creating OVI, CIII and X-ray emission from shock interactions. The approaching side of the shock is propagating through a more diffuse medium and therefore harder to detect. The stars in this system also include the massive WN (nitrogen dominant Wolf-Rayet) + OB system HD 5980 behind and Sk 80 possibly within the SNR. About two arcminutes to the west of the SNR is the star cluster NGC 346. The N S66 system also contains SNR J005800-721101 (B0056-724) to the west and SNR J005817-721814 (B0056-725) to the southwest of SNR J005927-721010.

4.4.3 N S76

The northeast region of N S76 (Fig. 4.3) contains SNR J005240-723820 (ATCA SMC 258) which is located just south of the H II region, J005227-723619 (ATCA SMC 257). Five other ATCA SMC sources classified as H II regions (219, 234, 235, 236 and 277) can be seen in Fig. 4.3. This image also demonstrates the characteristic appearance of radio background objects as relatively intense discrete point-like sources.

4.4.4 N S83

Within the N S83/N S84 regions of the SMC (Fig. 4.4), Testor & Lortet (1987) noted a high degree of fragmentation contained within one sheet of stars. Bolatto et al. (2003) reported unusually high CO line ratios $(2 \rightarrow 1)/(1 \rightarrow 0)$ and describe the N S83 region as a relatively active star-forming region comprised of several CO clouds, H II regions and various early-type stars.

N S83 has an expanding shell coincident with both the NGC 456 stellar association and the candidate SNR J011333-731704 (ATCA SMC 547). This expanding shell has a CO line ratio greater than 2 and appears to be interacting with the nearby molecular cloud, sweeping and compressing $\sim 10^4$ $M_\odot$ of molecular hydrogen, perhaps stimulating a second generation of star formation. Bolatto et al. (2003) proposed this shell was likely wind-driven from a massive 2.3 million year old star. We found a spectral index of -0.17 ± 0.17,

not steep enough to confirm this object as a SNR. A remnant here may be similar to SNR N 49 within the LMC which also appears to be interacting directly with a molecular cloud. If later confirmed as a SNR, this region would represent a rare opportunity to study molecular cloud interactions with a SNR in a metal-poor environment.

4.5 Candidate SNRs

We have identified five (5) new candidate SNRs and three (3) other new sources with some SNR characteristics.

Candidate SNR J004100-733648: (Fig. 4.5(a); Ye 1988; Filipović et al. 1998b; Filipović et al. 1998a) This candidate is faintly seen in the Hα image shown in Fig. 4.5(a). Its optical diameter is 52 ± 8 pc compared to a smaller 2.37 GHz diameter of 32 ± 8 pc. Small shell-like northward extensions are also seen at radio frequencies suggesting that only the southern shock emits enough energy to be detected at these frequencies. This object is very near the background object J004050-733657 at 4.8 and 8.64 GHz. Its spectral index (-0.94 ± 0.14) is rather steep, but it is seen in *ROSAT* observations. Its Hα shell morphology, multi-wavelength diameter and luminosity are also consistent with its identification as a candidate remnant.

Candidate SNR J004748-731727: (Figs. 4.1, 4.5) This radio candidate (ATCA SMC 193) is associated with H II region J004802-731653 (ATCA SMC 194) shown in Fig. 4.1. It is otherwise known as DEM S37, N S21 to N S23 and includes NGC 267. Morphology of the discrete source at 2.37 and 4.8 GHz reveal a typical SNR structure, but the brightness of the surrounding thermal emission required special procedures to accurately determine the flux density at 1.42 GHz. To do this, we found an overall flux density which included the H II region and then reduced the result in proportion to the area covered by its 2.37 GHz image. Since all three frequencies with flux densities were equally affected by the thermal emission from nearby H II , the calculated spectral index of -0.58 ± 0.04 is reasonable.

Candidate SNR J004806-730842: (Figs. 4.1 and 4.5(c); Dickel et al. 2001) As seen in Fig. 4.5(c), the radio emission from this remnant may represent only the southwestern portion of the shock although there is a large amount of contamination from the surrounding H II region, N S19. It has eight (8) identifications in the literature as a likely SNR.

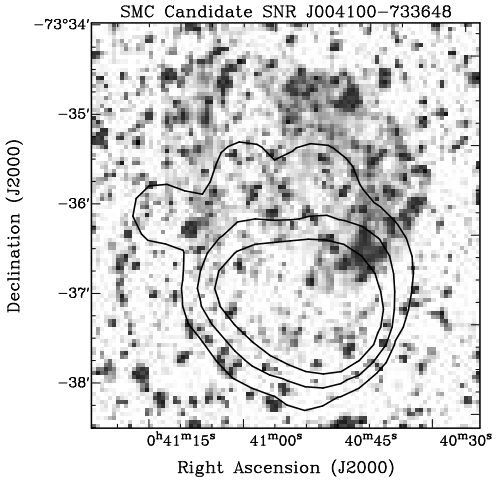

(a) Candidate SNR J004100-733648 Hα image and 2.37 GHz contours at 2, 4 and 8 mJy beam^{-1}. Radio emission is seen from the southern shock of the remnant.

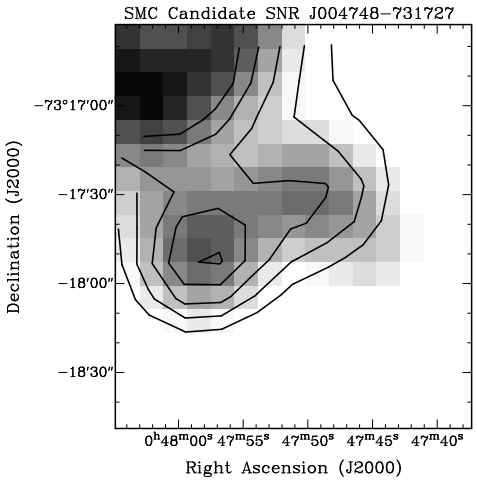

(b) Candidate SNR J004748-731727 (image center) 4.8 GHz image with 2.37 GHz contours (8, 10, 12, 14 and 16 mJy beam^{-1}). Note the association with H II regions ATCA SMC 194 and 195.

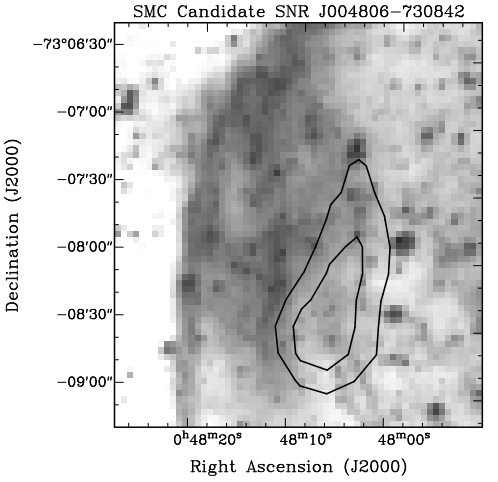

(c) Candidate SNR J004806-730842 Hα image and 2.37 GHz contours at 12 and 14 mJy beam^{-1}. Radio emission is noted from the southwest edge of the remnant.

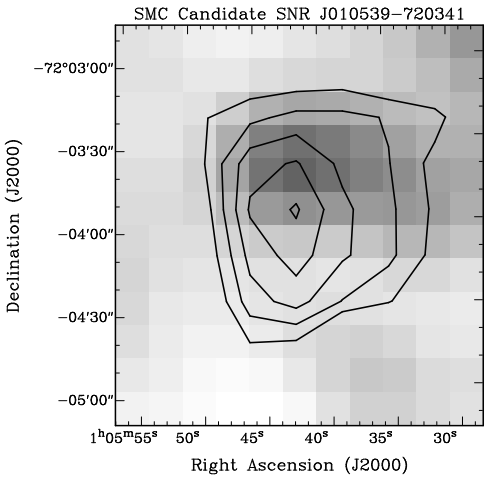

(d) 2.37 GHz image with MOST 843 MHz contours (4, 5, 6, 7 and 8 mJy beam^{-1}) of candidate SNR J010539-720341.

Figure 4.5 Selected new candidate SNRs and sources with SNR attributes. ATCA beam sizes for 1.42, 2.37, 4.80 and 8.64 GHz are 98″, 40″, 30″and 15″, respectively. Sensitivities are 1.8, 0.4, 0.8 and 0.4 mJy beam^{-1}, respectively.

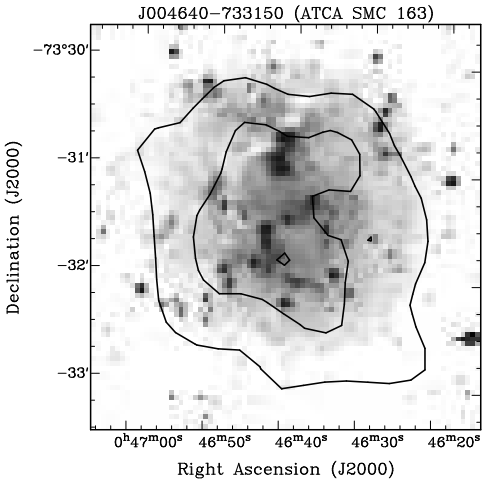

(e) Hα image of ATCA SMC 163 with 2.37 GHz contours (2, 4, and 6 mJy beam^{-1}). Note that the Hα emission appears 'torn' in various directions from center giving it a 'shell-like' structure.

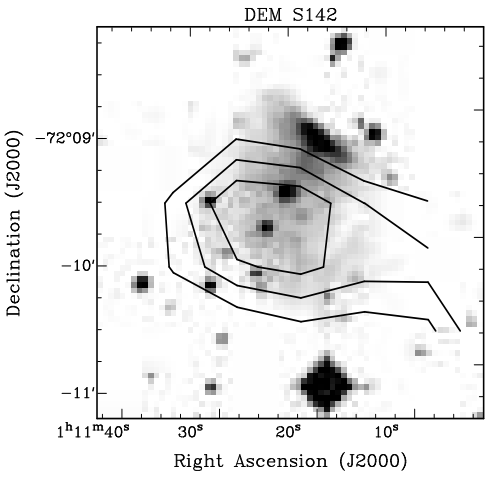

(f) Hα image of DEM S142 with 1.42 GHz contours (7, 8 and 9 mJy beam^{-1}). This object is not seen at the other radio frequencies.

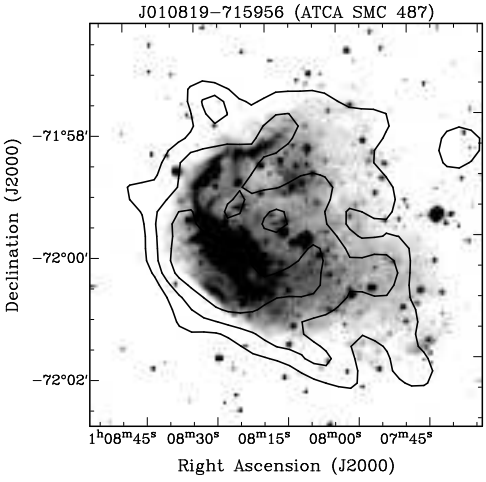

(g) Hα image of ATCA SMC 487 with 2.37 GHz contours (1.5, 2.5 and 4 mJy beam^{-1}). This object has a radio structure suggestive of a SNR and a 'shell-like' shape in Hα.

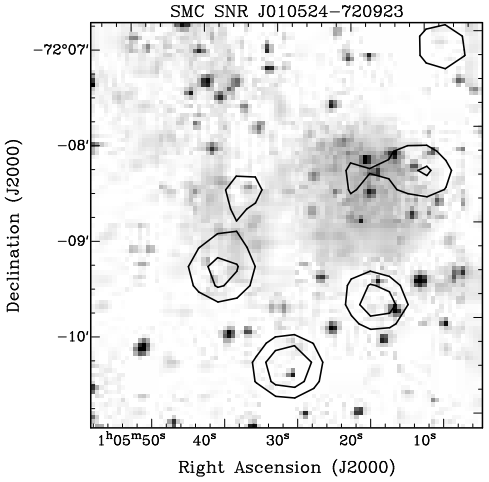

(h) SNR J010524-720923 Hα image and 2.37 GHz contours at 4 and 5 mJy beam^{-1}. Points of radio emission create a ring that encircles the optical remnant.

Figure 4.5 (Cont.) Selected candidate SNRs and sources with SNR attributes. ATCA beam sizes for 1.42, 2.37, 4.80 and 8.64 GHz are 98″, 40″, 30″and 15″, respectively. Sensitivities are 1.8, 0.4, 0.8 and 0.4 mJy beam^{-1}, respectively.

Candidate SNR J010539-720341: (Fig. 4.5) This candidate has a 2.37 GHz diameter of 25 ± 8 pc and displays a circular disk and shell. It is part of the H II region J010505-715936 (ATCA SMC 444). Its fitted radio spectrum is steep at -1.87 ± 0.44, although affected by thermal emission. This is mostly the result of a poor flux density measurement at 8.64 GHz. If this value is removed, the spectral index is a more reasonable -0.82 ($r^2 = 0.97$).

Candidate SNR J011333-731704: (Fig. 4.4; Filipović 2000; Caplan et al. 1996) This candidate is embedded in the H II region N S83 and has been catalogued as an emission nebula or H II region five times. It has two X-ray identifications as a possible SNR. Examination of the radio images reveal only a hint of diffuse radio structure typical of a SNR (also see section 4.4.4).

Additional sources show some SNR characteristics, but each lack sufficient evidence to be classified even as a SNR candidate.

I.) **ATCA SMC 163** shown in Fig. 4.5(e) is located at $\alpha = 00^h46^m40.6^s$ and $\delta = -73°31'50.9''$ (J2000). This source is listed as a H II region in Appendix A, Table 1, but its radio diameter ($\sim$ 47 pc) and circular morphology is suggestive of a SNR. In Hα, the object is extended in various directions suggestive of a 'shell-like' SNR structure. Its spectral index is -0.47 ± 0.12. X-ray co-identification and further optical and radio observations could confirm it.

II.) **DEM S142** shown in Fig. 4.5(f) is located at $\alpha = 01^h11^m16.0^s$ and $\delta = -72°09'30''$ (J2000). Despite faint radio contours at 1.42 GHz, this source was not included in this survey since its emission is below radio sensitivities at all other frequencies. The source has a strong triangular shaped Hα emission feature with faint extensions approximately 30″ north of the radio center.

III.) **ATCA SMC 487** shown in Fig. 4.5(g) is located at $\alpha = 01^h08^m19.6^s$ and $\delta = -71°59'56.6''$ (J2000), and listed as an H II region in Appendix A, Table 1. At 2.37 GHz, the structure of this source is suggestive of a SNR. Its Hα image reveals a 'shell-like' SNR shape. It has a steep spectral index (-0.73 ± 0.05)

and no observed X-ray emission.

4.6 Microquasar Candidate ATCA J005523-721055 (ATCA SMC 303/304)

We note the first discovery in the radio of a new microquasar candidate in the SMC coincident with an X-ray pulsar; in addition to the microquasar candidate ATCA J004718-723947 (ATCA SMC 174) noted in Chapter 3. The new candidate is one of three detected High Mass X-ray Binaries (HMXB) listed by Edge et al. (2004) and named

CXOU J005527.9-721058. Timing analysis revealed a period of 34.08 ± 0.03 s with a confidence greater than 98%. The pulsar's position of $\alpha = 00^h55^m27.7^s$ and $\delta = -72°10'59''$ (J2000), is located within 12″ of J005523-721055 (ATCA SMC 303) at $\alpha = 00^h55^m23.5^s$ and $\delta = -72°10'55.2''$ (J2000) and near ATCA J005539-721055 (ATCA SMC 304) at

$\alpha = 00^h55^m39.21^s$ and $\delta = -72°10'55.5''$ (J2000) (Fig. 4.6).

They note this HMXB is within 3″ of *ROSAT* 2RXP J005527.1-721100 (HR2=0.36 ± 0.05), an object coincident with a V=16.8 magnitude optical source with a $B - V$ colour index of –0.116. This value would be expected for the optical companion in a Be X-ray binary system. J005523-721055 and J005539-721055 have radio spectral indices of -0.45 ± 0.23 and -0.18 ± 0.49, respectively, possibly the result of non-thermal radio jets/lobes emanating from the X-ray source. As noted in Chapter 3, these objects are rare in extragalactic radio surveys and their confirmation requires more than coincidence.

4.7 Statistics of Sources Towards the Small Magellanic Cloud

4.7.1 Multi-Frequency Diameter Comparisons

We compare the mean diameters of the radio SNRs at 2.37 GHz to Hα and X-ray diameters as well as values given in the literature in Table 4.4. Estimates were accomplished using KPVSLICE from the KARMA software package, paying attention to the intensity decreases of 50% near the edges of each SNR. This is an imperfect process since SNRs are often just shells; they certainly are not perfect spheres in most cases.

Matonick & Fesen (1997) noted that 11 optical remnants in the SMC have been reported in the literature (citing papers from Mathewson & Clarke 1972; Mathewson & Clarke 1973; Mathewson et al. 1983; Mathewson et al. 1984 and Chu & Kennicutt 1988). We were able to confirm 10 of these SNRs in Hα and add mean

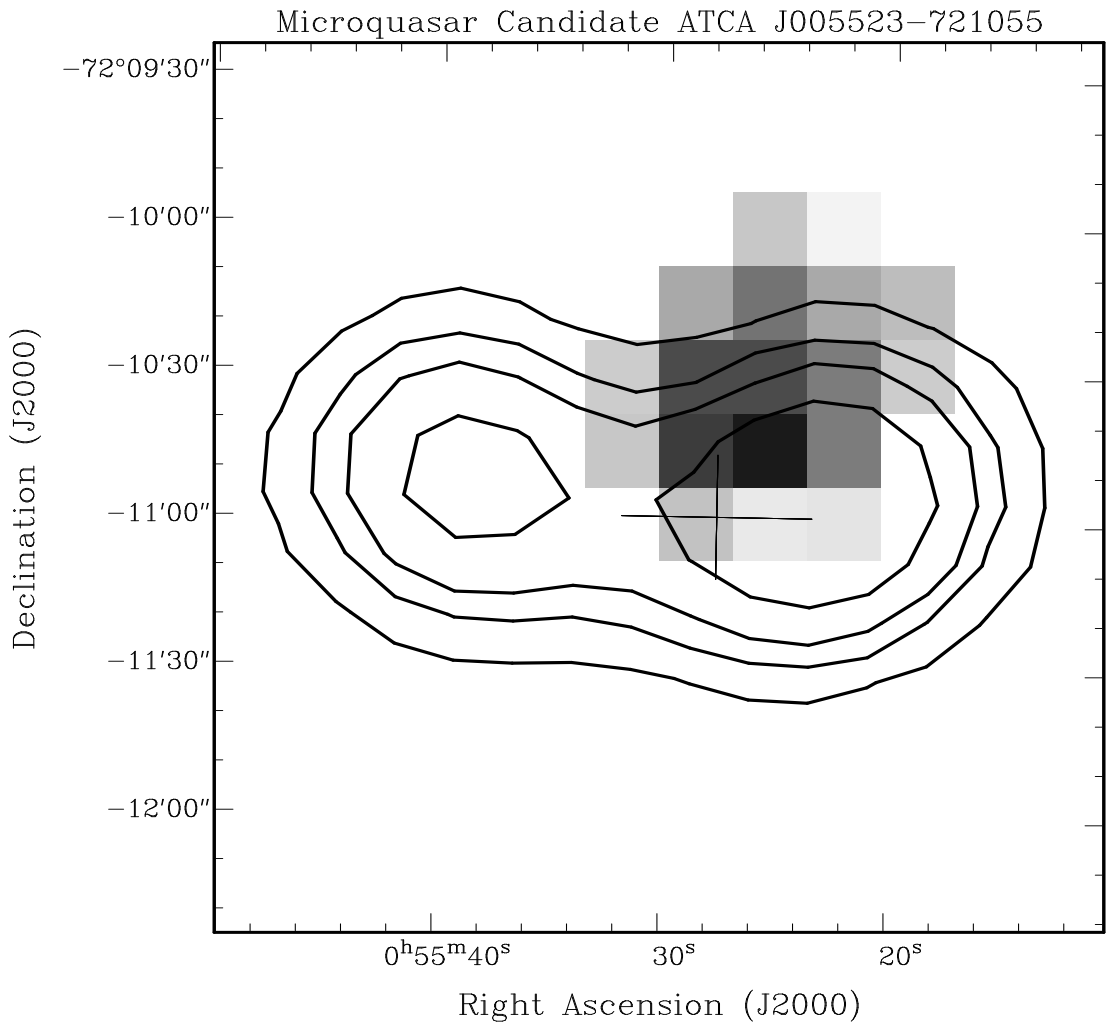

Figure 4.6 *ROSAT* hard image (Haberl et al. 2000) with 2.37 GHz contours (5, 10, 15 and 25 mJy beam^{-1}) of microquasar candidate ATCA SMC 303 (and possibly ATCA SMC 304) and CXOU J005527.9-721058 (cross). It is suspected that rare radio jets/lobes are seen emanating from this HMXB.

Table 4.4 Comparisons of SNR diameters in radio (2.37 GHz), optical and X-ray. Optical measurements utilized Hα images and X-ray measurements were made from a *ROSAT* hard spectrum image (Haberl et al. 2000). Measurements reported in the literature are in parenthesis; a or b indicates that X-ray or optical emission, respectively, have been detected in the literature but no diameter measurements have been made.

ATCA No.	SNR Name	Radio Diameter ± error (pc)	Optical Diameter ± error (pc)	X-ray Diameter ± error (pc)	Optical and X-ray references and comments
158	J004637-730823	35 ± 4	–	43 ± 6 (43)	no optical present; van der Heyden et al. 2004
177	J004728-730601	52 ± 4	–	57 ± 6	no optical present
178	J004716-730811	36 ± 4	36 ± 2 × 26 ± 2 (26)	35 ± 4 (21)	Mathewson et al. 1983; van der Heyden et al. 2004
199	J004821-731931	35 ± 4	32 ± 8 (31)	32 ± 6 (27)	Mathewson et al. 1983; van der Heyden et al. 2004
222	J004907-731402	38 ± 4	52 ± 4 (51)	38 ± 4 (37)	Mathewson et al. 1984; van der Heyden et al. 2004
249	J005110-732212	55 ± 4	52 ± 4 (48)	57 ± 12 (47)	Mathewson et al. 1984; van der Heyden et al. 2004
258	J005240-723820	95 ± 4	(58)	95 ± 8	no clear boundary in Hα; Mathewson et al. 1984
345	J005800-721101	36 ± 4	–	38 ± 8	no optical present
347	J005817-721814	66 ± 8	62 ± 8 (56)	69 ± 4 (63)	Mathewson et al. 1984; van der Heyden et al. 2004
366	J005927-721010	57 ± 4	b	52 ± 4 (50)	optical confused within H II region; van der Heyden et al. 2004
378	J010023-713322	43 ± 8	56 ± 8 (62)	47 ± 4	Mathewson et al. 1984
419	J010313-720958	27 ± 4	28 ± 2 (25)	32 ± 4 (20)	Mathewson et al. 1983; van der Heyden et al. 2004
430	J010402-720149	19 ± 5	15 ± 2 (7)	19 ± 4 (15, 14)	Mathewson et al. 1983; van der Heyden et al. 2004; Gaetz et al. 2000
447	J010524-720923	47 ± 4	44 ± 4	47 ± 4 (39)	van der Heyden et al. 2004
481	J010505-722319	61 ± 4	66 ± 8 (57)	57 ± 8 (62, 54)	Mathewson et al. 1983; van der Heyden et al. 2004; Park et al. 2003
468	J010619-720527	25 ± 4	33 ± 4 (29)	28 ± 4 (35)	Mathewson et al. 1984; van der Heyden et al. 2004
87	J004100-733648	32 ± 8	52 ± 8	30 ± 8	radio and X-ray at southern shock
191	J004806-730842	25 ± 4	46 ± 2 × 25 ± 2	a	radio and X-ray at southwestern shock
193	J004748-731727	24 ± 4	–	–	no optical or X-ray emission present
445	J010539-720341	25 ± 8	17 ± 2	–	no X-ray emission present
547	J011333-731704	24 ± 4	b	a	optical confused within H II region

diameter measurements for J010524-720923 and three candidate SNRs (J004100-733648, J004806-730842 and J010539-720341).

For X-ray, few references in the literature are made for diameter measurements in the SMC. We were able to make use of hard spectrum *ROSAT* images from Haberl et al. (2000) to measure all of the radio SNRs and one candidate (J004100-733648). We were also able to compare a few to those given in the literature by van der Heyden et al. (2004) (*XMM*), Park et al. (2003) (*Chandra*) and Gaetz et al. (2000) (*Chandra*).

While radio to optical and X-ray diameters comparisons are straight forward for some remnants such as J010313-720958 and J010619-720527, they are not for many others. This may be because emission at one domain from some remnants may only be detected from an active portion of the shock front and not the entire remnant. Fig. 4.5(h) shows what appears to be only scattered patches of radio emission from SNR J010524-720923, creating a ring around the optical remnant. In Fig. 4.5(a), the southern portion of the shock from candidate SNR J004100-733648 appears to emit more non-thermal radio emission.

In the standard SNR model, it is believed that non-thermal radio energy emanates from the forward shock front while thermal X-ray radiation from the reverse shock, implying that X-ray diameters should be less than radio ones. Such generalizations are always dangerous, reports of non-thermal X-ray radiation from SNRs

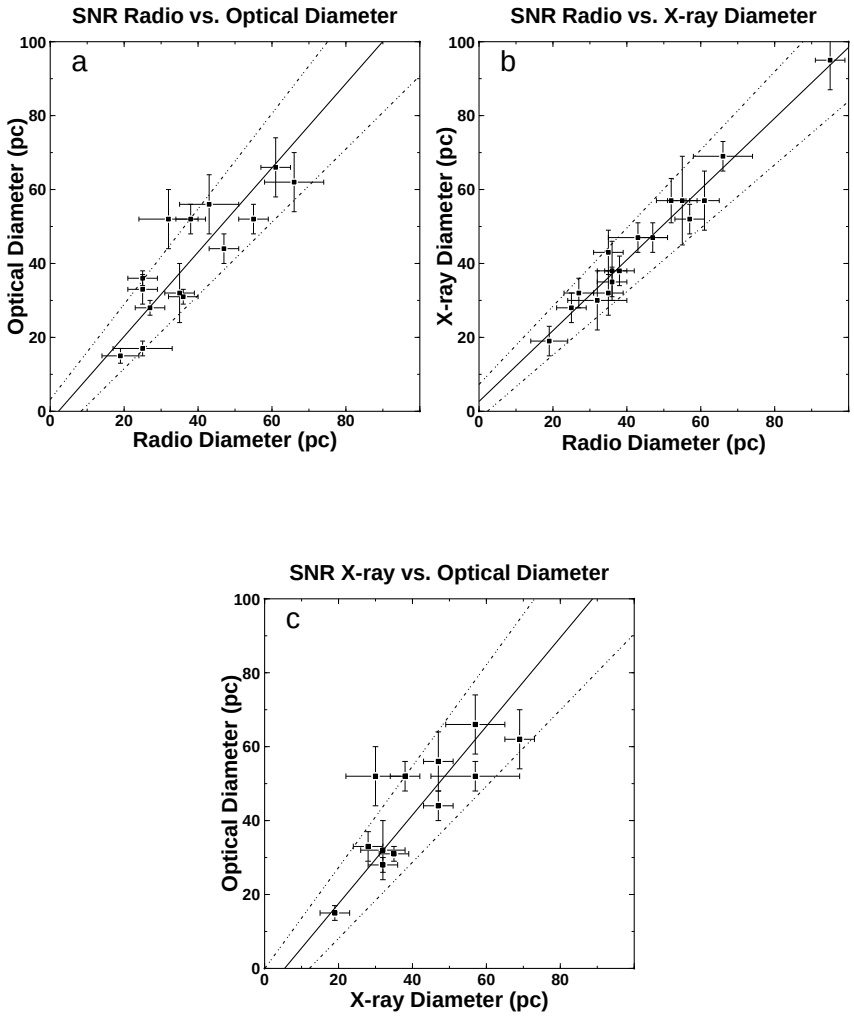

Figure 4.7 Graphic comparisons of radio, optical and X-ray SNR diameters. A weighted regression line of best fit with 1σ confidence intervals is shown for each graph; (a) $D_{Optical} = -2.54\pm5.7 + (1.14\pm0.15)D_{Radio}$, (b) $D_{X-ray} = 2.66\pm4.6 + (0.958\pm0.10)D_{Radio}$ and (c) $D_{Optical} = -6.49\pm6.4 + (1.20\pm0.17)D_{X-ray}$.

are becoming commonplace (for example Vela Z; Aschenbach 1998). As Fig. 4.7 shows, given measurement errors and a weighted regression line of best fit, it is not possible to show more than a one-to-one relationship between radio, optical and X-ray diameters.

We also compare radio and optical H II region diameters in Table 4.5, using the Davies et al. (1976) (DEM) catalogue for optical measurements. Estimates from the 2.37 GHz radio map using KVPSLICE were made with edges estimated by noting where a falloff of about 50% occurred. Such estimates of each H II region's major and minor axis are plagued with many problems. Although radio observations are free from dust obscuration, they have lower resolution and sensitivity. Major and minor axes measured at 2.37 GHz cannot be exactly matched to the corresponding DEM Hα ones. And, H II regions are certainly not perfect sphere or rectangles.

Fig. 4.8 (a) shows the comparison of 47 of the 71 radio H II regions (or candidates), highlighting some interesting features. Smaller optical H II regions have radio diameters which are very similar, while larger optical H II regions have radio diameters which are very near the resolution of the radio image (12.6 pc). Radio observations may only detect the central Strömgren sphere of the cluster of stars that form the H II region while optical observations detect extending filaments of dust and gas from the center, making them appear extended in that domain. This limitation prevents accurate determination of flux densities for the H II regions listed in Appendix A, Table 1, simply because their boundaries are uncertain. Without accurate flux densities, spectral index calculation is therefore unreliable. Fig. 4.8 graph (b) includes only H II regions with reasonable spectral indices ($\alpha \geq -0.2$). This sub-population have diameters near the radio resolution.

4.7.2 Spectral Index Distribution

Appendix A, Table 1 contain the spectral indices used in the process of our source classification. In the last chapter, we also presented a histogram of the source spectral index distribution for background sources. We reproduce this in Fig. 4.9 with a histogram for the distribution of SNRs and candidate SNRs (also see Table 4.6). Candidate SNRs (ATCA SMC 87, 445 and 547) account for three of the values outside the expected range of $-0.8 < \alpha < -0.2$ (McGee & Newton 1972). We find SNRs and candidate SNRs have a mean spectral index of -0.63 (s.d.=0.43) while background sources have a mean of -0.95 (s.d.=0.61).

The mean spectral index for all sources towards the SMC is -0.87 (s.d.=0.69), which is slightly steeper when compared to -0.73 (s.d.=0.61) found by Filipović et al. (1998a) (Parkes survey). Table 4.6 provides a detailed comparison between our findings and theirs. The higher sensitivity of the ATCA data contributes to

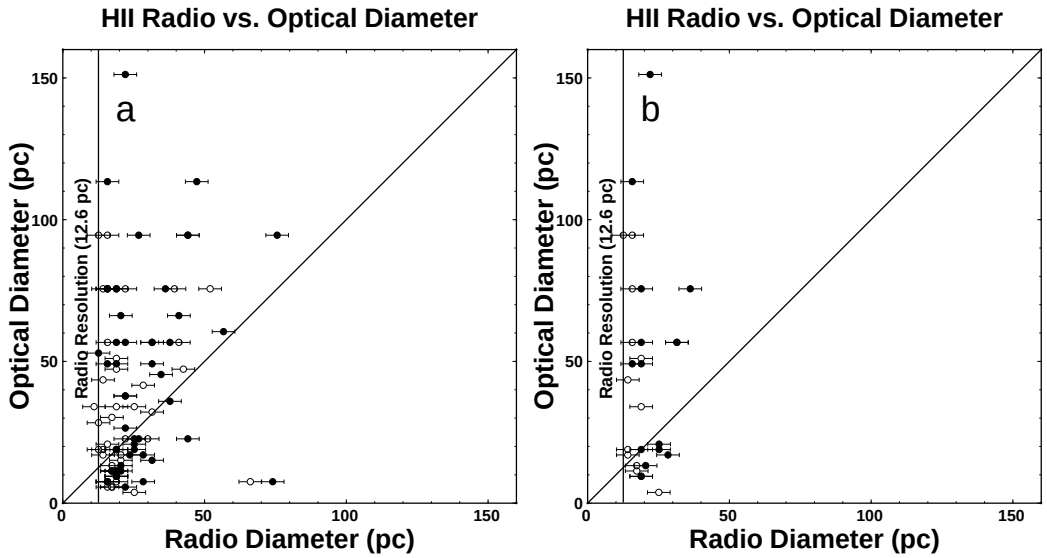

Figure 4.8 Graphic comparison of 2.37 GHz radio vs. Hα diameters of H II regions plotted on a linear scale. For easier comparison, ATCA SMC 363 (J005908-721056 or N S66; the largest H II region in the SMC), has been excluded. Filled circles represent major axis and open circles represent minor axis, both in parsec. The vertical line at 12.6 pc represents the resolution of the radio image (optical resolution using the 48-inch SRC Schmidt camera is presumed to be less than 1 pc and therefore cannot be practically shown as a horizontal line). (a) All H II regions for which comparison can be made. Although there is some correlation between small optical H II regions and radio, this correlation is lost as the optical diameter increases. (b) Comparison for H II regions which have reasonable spectral index ($\alpha \geq -0.2$). This sub-population tends to be near the radio resolution.

Table 4.5 Radio (2.37 GHz) and optical (Hα) diameter comparisons of H II regions. Confusion with surrounding H II regions in N 66 prevented a diameter measurement of J005934-720942. Several radio H II regions have no corresponding entry in Davies et al. (1976). Radio measurements have an estimated error of ±4 pc; none were given by Davies et al. (1976).

H II Region	2.37 GHz Diameter (pc) Major vs. Minor Axis	Hα Diameter (pc) Major vs. Minor Axis
J004216-725910	19×13	19×19
J004457-731010	22×16	
J004530-730453	28×25	
J004554-730645	38×17	57×30
J004501-731647	16×16	8×8
J004523-732250	22×16	26×21
J004620-724514	14×14	
J004611-730043	19×16	
J004633-730604	32×28	49×42
J004652-731731	19×19	
J004639-732204	38×25	36×34
J004619-732324	22×22	57×38
J004640-733150	41×41	66×57
J004823-730557	32×20	15×15
J004856-730748	57×43	60×47
J004819-731032	19×19	9×9
J004802-731653	35×32	45×32
J004756-731752	38×16	
J004809-731442	27×19	23×19
J004828-731556	41×22	
J004834-731509	32×19	57×51
J004943-724843	19×19	9×9
J004925-730940	22×22	
J004944-731030	16×16	76×76
J004918-731551	15×15	
J005015-723241	25×25	21×4
J005049-724819	47×44	113×95
J005028-725311	44×39	95×76
J005040-732022	25×14	19×19
J005153-721650	22×11	38×34
J005155-732650	25×20	
J005206-721615	19×19	
J005227-723619	38×20	
J005258-731144	16×14	
J005235-732610	24×20	17×17
J005300-721238	35×20	
J005341-723934	17×17	11×6
J005338-731221	22×16	151×95
J005544-721608	28×19	8×8
J005616-721732	44×30	23×23
J005604-721931	27×22	95×76
J005816-723852	19×19	11×11
J005824-723955	20×17	13×13
J005756-723932	28×22	
J005953-720840	57×20	
J005855-721010	25×22	
J005908-721056	28×28	265×208
J005916-721020	27×22	
J005916-721120	11×9	
J005934-720942		
J005914-722423	28×14	17×17
J010125-715054	25×22	23×23
J010216-715140	19×17	19×11
J010248-715312	22×17	6×6
J010203-722450	19×16	57×57
J010326-720308	74×66	8×8
J010432-720508	22×19	
J010505-715936	20×19	66×47
J010538-720643	14×14	
J010819-715956	76×52	95×76
J010913-731140	16×13	113×95
J011115-722247	19×16	76×76
J011353-731557	16×16	8×6
J011348-731753	36×32	76×57
J011416-731549	20×17	11×11
J011439-731821	19×19	49×34
J011453-731921	16×16	
J011447-732007	22×14	
J011608-731029	16×14	49×43
J012408-730905	13×13	53×28
J012930-733313	19×14	76×76

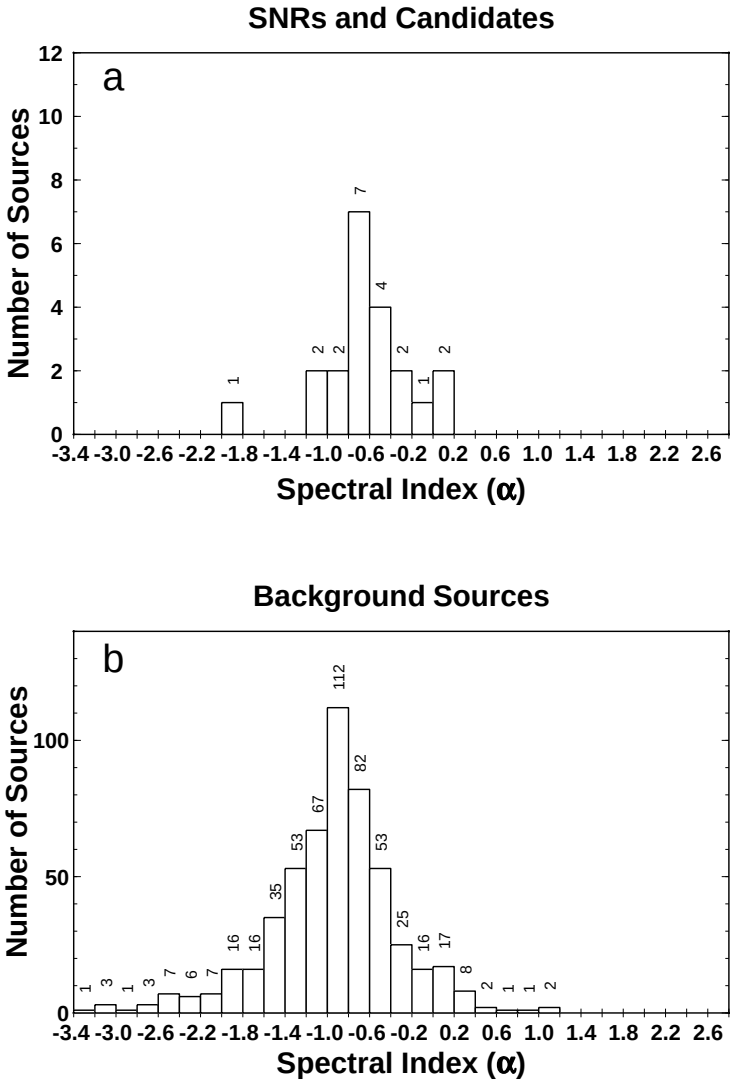

Figure 4.9 The distributions of radio spectral index for (a) all SNRs, including candidate SNRs, and (b) 534 background sources with calculated values.

Table 4.6 Spectral index distribution by source type. FHW98 in column 5 stands for Filipović et al. (1998a).

Source Type	No. of Sources	Mean α	s.d.	FHW98 No/α/s.d.
Known SNRs	16	–0.58	0.33	—
Candidate SNRs	5	–0.77	0.69	—
All SNRs	21	–0.63	0.43	12/–0.22/0.25
Background	534	–0.95	0.61	63/–0.45/0.48
Total SMC	621	–0.87	0.69	164/–0.73/0.61

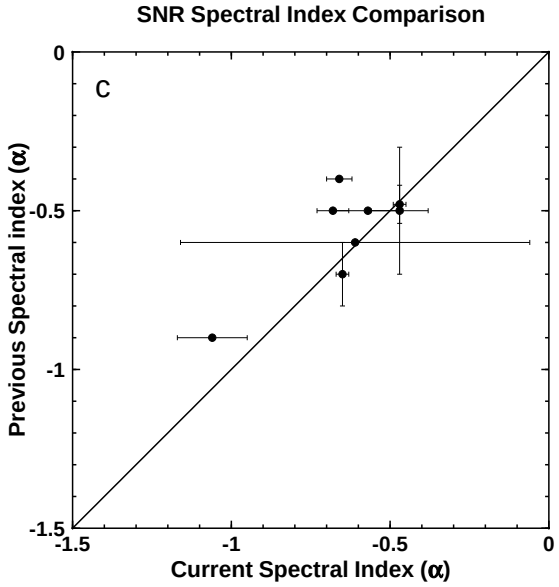

Figure 4.10 Comparison of SNRs with previously reported spectral indices and errors, if known.

this; we have a sample of 616 background sources compared to only 63 in the Parkes survey. Of 49 sources that have steep spectral indices less than −1.8, 43 (87.7%) have flux densities less than 10 mJy.

We do not report the spectral index distribution of H II regions here for many reasons, including the problem of ill defined boundaries mentioned at the end of section 4.7.1. Other effects can make flux density and spectral index calculation of any source inaccurate. One is so called 'physical mixing' of still unresolved sources which are embedded in another. H II regions often have SNRs embedded in them and may also be superimposed with background sources. Improved resolution at higher frequencies can cause a measured flux density lower than expected when two sources resolve out. Uncertainty can also occur when sources have low source flux densities near the sensitivity limit of the image. Lack of short-spacing data added to the 1.42 and 2.37 GHz images but not to the 4.80 and 8.64 GHz data may also contribute to spectral index error in the case of larger objects.

It must be stressed that the issue with flux density measurement and resulting spectral indices of H II regions compared to SNRs is not one of size or surface brightness, but rather of uncertain boundaries and heterogeneity between these two types of objects. Fig. 4.8 (b) in section 4.7.1 shows that the sub-population of H II regions that have reasonable spectral indices ($\alpha \geq -0.2$) do tend to be nearer the radio resolution in diameter than other regions, but this does not imply that all smaller H II regions will have reasonable spectral values. They are composed of different types of sources whereas SNRs are but a single type of object.

Our distribution of SNR spectral index does seem reasonable given an analysis of 200 Galactic known SNRs by Trushkin (1998) showing mean spectral indices at 0.4 and 4.0 GHz of −0.41 (s.d.=0.34) and −0.50 (s.d.=0.21), respectively. The number of SNRs with an index between $-0.8 < \alpha_{4\ \mathrm{GHz}} < -0.6$ in that study was slightly in excess. Comparison of (8) SNR spectral indices to ones found in the literature (see Table 4.1 and Fig. 4.10) also imply that our values are reasonable.

4.7.3 Distribution of Radio Spectral Index and X-Ray Hardness

In Fig. 4.11 we compare radio spectral index to X-ray hardness in order to characterize source types. This plot utilizes radio spectral index values and HR2 values from Kahabka et al. (1999) and Haberl et al. (2000) using *ROSAT* data. They performed their X-ray analysis in five energy channel ranges including; soft (channel 11–41, 0.1–0.4 keV), hard (channel 52–201, 0.5–2.0 keV), hard1 (channel 52–90, 0.5–0.9 keV), hard2 (channel 91–201, 0.9–2.0 keV) and broad (0.1–2.4 keV). In this scheme, HR2 is defined as the ratio of the difference between hard2 and hard1 to their sum (HR2 = [hard2 – hard1]/[hard1 + hard2]). Obviously, if hard1 or

hard2 energy ranges have undetectable counts, the ratio approaches +1 or –1, respectively. As noted in Payne et al. (2004b, and references therein), sources with more positive HR2 values tend to have power law spectra whereas those sources with negative HR2 values are softer and include objects such as SNRs. The latter tend to have thermal spectra.

Open circles in Fig. 4.11 represent background sources from Appendix A, Table 1. These objects tend to have a negative radio spectral index (64/70) and positive HR2 values (61/70). SNRs are denoted by asterisks and tend to have negative spectral indices with softer X-ray spectra. *ROSAT* HR2 values are not available for 620 of the 717 sources, including SNR J005800-721101 and candidate SNRs J004806-730842, J004748-731727 and J010539-720341. One, J004806-730842, was identified by *Einstein* observations.

4.7.4 Luminosity and Surface Brightness Functions

The luminosity distribution of SNRs adds to the understanding of the physical nature and evolution of these sources. They are part of the SMC at a known distance, thus their luminosity is directly related to the observed flux. The luminosity function can therefore be obtained more directly than for sources in the Galaxy. The luminosity of each radio source is given in W Hz^{-1} and defined by the relation:

$$L_\nu = 4\pi D^2 S_\nu, \tag{4.1}$$

where D is distance to the SMC and S_ν is the flux density at a given radio frequency. We used flux densities at 2.37 GHz to estimate the luminosity of each source in Tables 4.1, 4.2 and 4.3. The completeness level at this frequency is 2 mJy (the 5σ level) with a corresponding completeness luminosity of 10^{15}W Hz^{-1}.

In Fig. 4.12 we show luminosity (a) and surface brightness (b) histograms of SNRs (and candidate SNRs). The mean luminosity is 4.8×10^{16}W Hz^{-1} with a standard deviation 4.7×10^{16}W Hz^{-1} and the mean surface brightness is 4.86×10^{-21} $Wm^{-2}Hz^{-1}sr^{-1}$ (s.d.=7.31×10^{-21}).

Green (2004) pointed out that for the Galaxy, low luminosity SNRs are difficult to distinguish due to confusion with bright H II regions. The Effelsberg Galactic survey (2.7 GHz) detected new SNRs down to a surface brightness corresponding to 2×10^{-22} $Wm^{-2}Hz^{-1}sr^{-1}$ at 1 GHz. The MOST survey detected SNRs down to a similar value of 5×10^{-22} $Wm^{-2}Hz^{-1}sr^{-1}$ at 1 GHz. Our surface brightness completeness level of 6.8×10^{-22} $Wm^{-2}Hz^{-1}sr^{-1}$ at 2.37 GHz is very near this limit.

Setting a surface brightness for completeness is difficult. For example, the current version of the Galactic SNR Catalog (Green 2004) has a 1 GHz completeness level set at 10^{-20} $Wm^{-2}Hz^{-1}sr^{-1}$. However, of 217

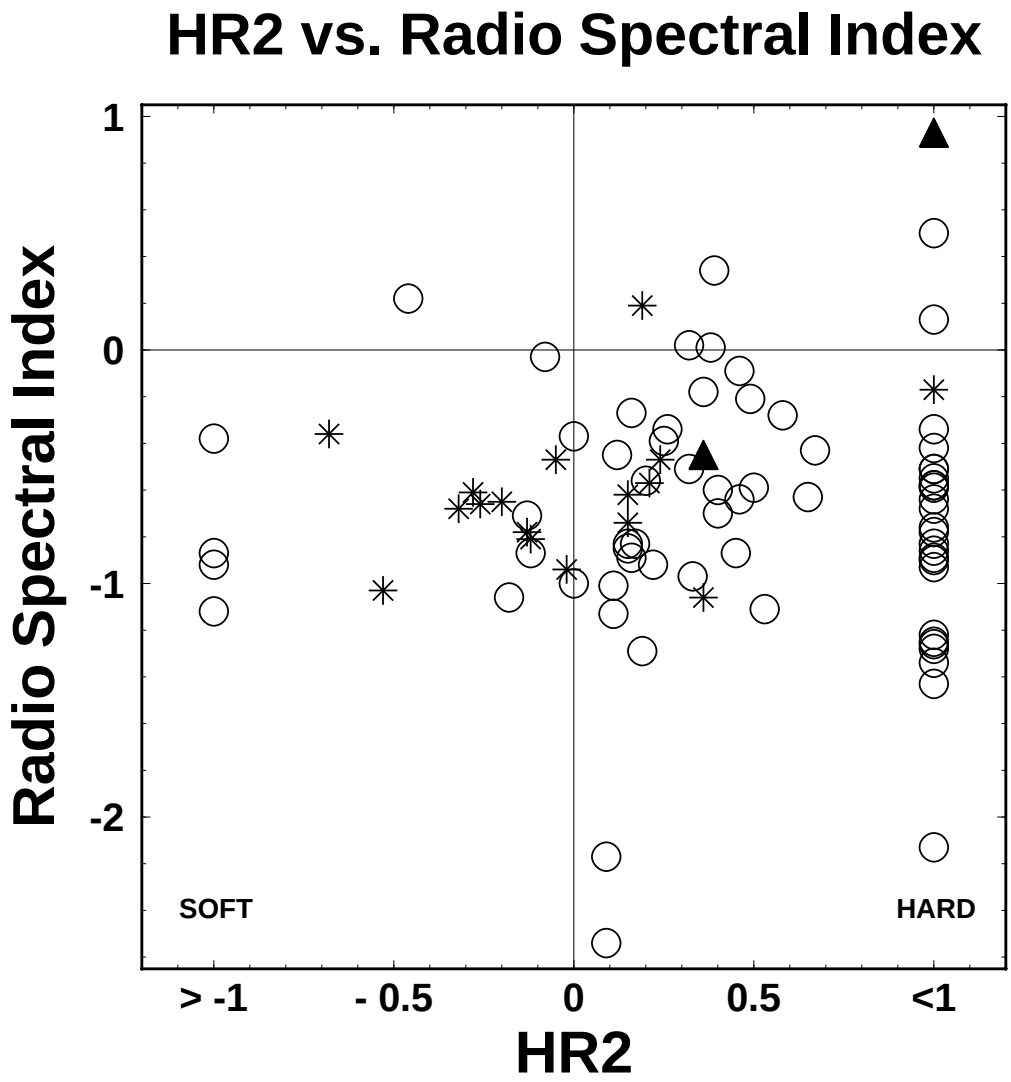

Figure 4.11 The distribution of radio spectral index (α) and X-ray hardness (HR2) for different classes of sources towards the SMC. Asterisks represent – SNRs; open circles – background sources and filled triangles – X-ray binary candidates. HR2 and α are defined in the text.

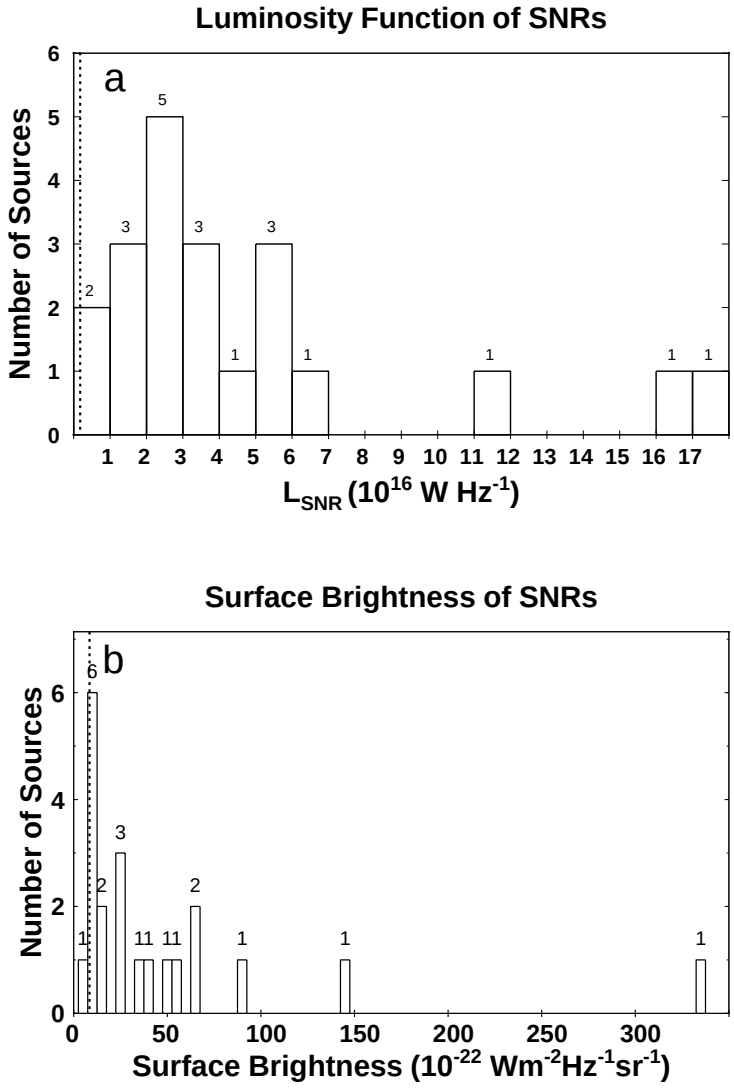

Figure 4.12 2.37 GHz luminosity histograms (a) and surface brightness (b) of SNRs (and candidates) in the SMC. Vertical lines represent the approximate completeness level assuming the $S_{2.37}$ flux densities to be complete down to $\sim$ 2 mJy. For luminosity this is 0.1×10^{16}W Hz^{-1} and for surface brightness, 6.8×10^{-22} Wm^{-2}Hz^{-1}sr^{-1}. Surface brightness units are divided in bins of 5×10^{-22} units.

Galactic SNRs, only 64 are above this nominal surface brightness limit.

We also plot the $\Sigma_{1\ \mathrm{GHz}}-D$ plot for SNRs and candidate SNRs in Fig. 4.13. Ideally, pulsar-driven remnants should be excluded, since their presumed energy source is not the kinetic energy from a supernova explosion. Identification of these objects have been hampered by limitations in spatial resolution; the only extragalactic Pulsar Wind Nebulae (PWNe) reported are SNR B0453-685 and N 157B, both in the LMC (Gaensler et al. 2003). We are very limited in the number of SNRs in our SMC sample and we assume none are PWNe.

We find that the relation yields a slope of -1.4 ± 0.5. There is a large degree of scatter in this graph and we find that r^2 is only 0.317[3]. Arbutina et al. (2004) discusses the concept of the 'trivial' relation between surface brightness and diameter. This basically states that $\Sigma_\nu \propto D^{-2}$. Even if the flux density or luminosity ($L_\nu \propto \Sigma_\nu \times d^2$ using d as distance) is random and there really is no relation, we can still obtain $\Sigma_\nu \propto D^{-2}$ simply because the inverse square dependence on D is implied by the definition of surface brightness. We include Fig. 4.13 for completeness and do not feel it reveals anything useful.

4.7.5 SNR Integral Number-Diameter Relation

A more straight forward diagnostic of SNR evolution is the integral number-diameter relation, $N(\leq D) \propto D$. The relation holds true for Galactic SNR which are heterogeneous and plagued with distance uncertainties. If the observed sample is complete, $N(\leq D) \propto D$ would be expected if most SNRs are in the free expansion phase, while, $N(\leq D) \propto D^{2.5}$ may signify that most remnants are in the adiabatic phase (Berkhuijsen 1987).

After calibrating distances, Mills (1983) obtains a Galactic $N(\leq D) \propto D^{1.15}$. In the Magellanic Clouds and M 33, the relation has the form $N(\leq D) \propto D$ (for example, Type II SNRs with $D < 50$ pc in the LMC according to Mathewson et al. 1983), suggesting a different phase evolution (possibly free expansion) for these SNRs compared to Galactic SNRs.

Unfortunately, as pointed out by Berkhuijsen (1987), the observed exponent of +1 of cumulative $N(\leq D) \propto D$ relations could also result from a random distribution of diameters possibly ascribed to variations in ambient density. After corrections to an ambient density $n_0 = 1$ cm^{-3} for different groups of SNRs in the LMC, SMC and Galaxy, Berkhuijsen (1987) finds the exponents increase to the +2 to +3 range, yet the exponent of +1 still cannot be statistically ruled out. In Fig. 4.14 we plot this relation for the SMC SNRs and candidate SNRs finding a slightly higher slope than +1; $N(\leq D) = 0.02D^{+1.7\pm0.2}$, $r^2 = 0.77$.

Fig. 4.14 shows the slope of the single line may be the combination of two separate populations of SNRs.

[3] r^2 is known as the coefficient of multiple determination. It represents the fraction of the dependent variable explained by the regression.

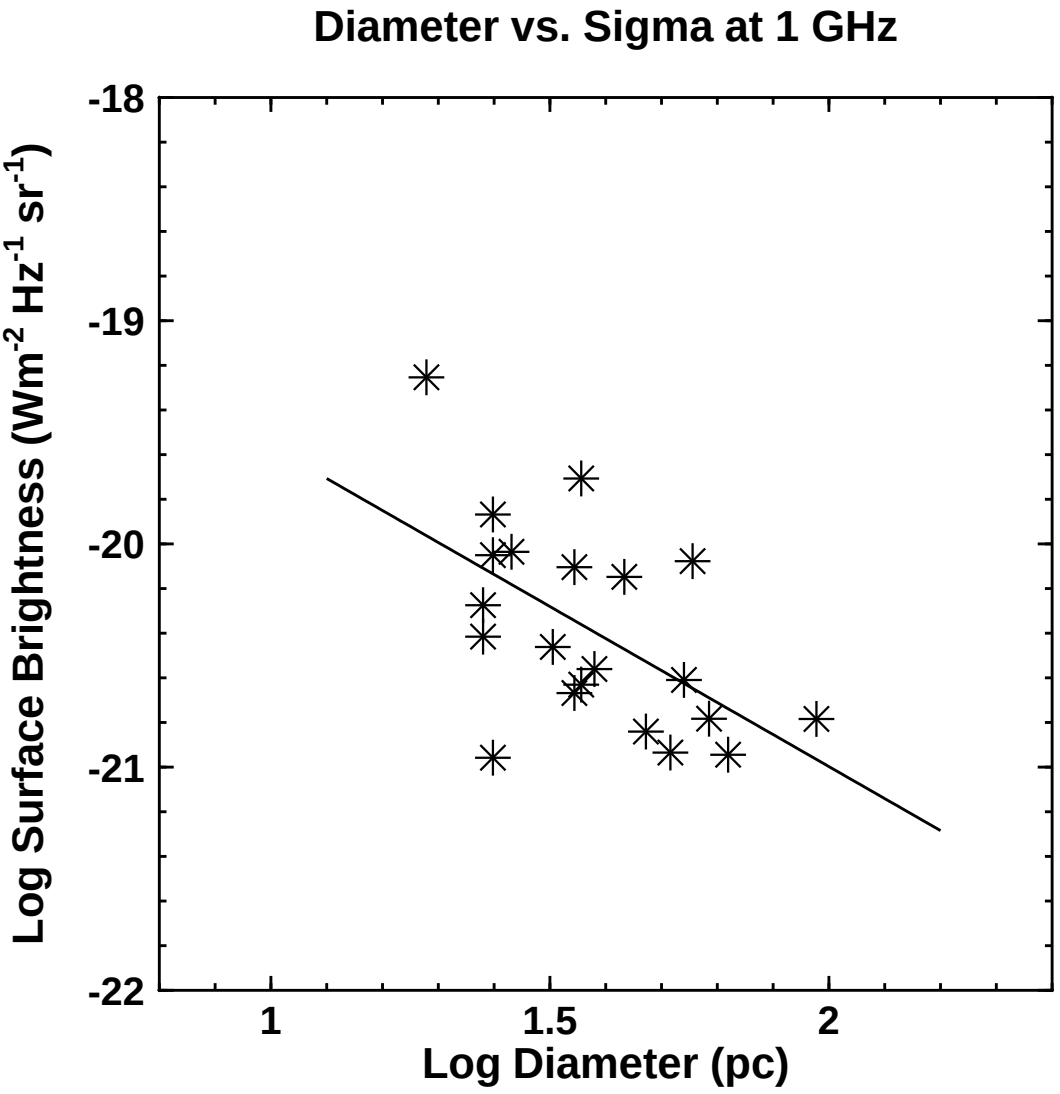

Figure 4.13 Surface brightness (1GHz) versus diameter for SNRs and candidates shown with asterisks. The solid regression line is $\Sigma \propto D^{-1.4\pm0.5}$, $r^2 = 0.317$. Given the amount of scatter in the data, there appears to be a doubtful relation.

The dotted and dashed lines are a better fit: smaller (younger) SNRs with $N(\leq D) = 0.00003D^{+3.6\pm0.7}$; $r^2 = 0.86$ and larger (older) SNRs with $N(\leq D) = 0.63D^{+0.8\pm0.0}$; $r^2 = 0.99$. This would imply that the number of smaller remnants ($\leq$ 35 pc) increase faster than the number of larger remnants ($>$ 35 pc); members of the larger group are lost to selection effects as they become fainter and mix into the environment. Putting all this into perspective, a hypothetical SNR model by Woltjer (1972) suggested that a remnant in its expansion phase might be about 1.8 pc in diameter while one in its adiabatic phase about 22 pc. The diameter of our smallest SNR is $\sim$ 19 pc, implying that we are seeing the steeper accumulation of remnants in their adiabatic phase followed by an incomplete sample of remnants in their snowplow or mixing phase. The shape and transition (near 30 pc) of the cumulative number diameter diagram for LMC and Galactic SNRs, published in Milne, Caswell & Haynes (1980) (see their Fig. 7) is remarkably similar.

In Fig. 4.15 we show the distribution of SNR number vs. diameter. From this graph it can be seen that most have a diameter of about 30 pc. Remnants of this size are believed to be in their adiabatic phase of evolution.

4.7.6 H II Region Number-Diameter Relation

According to Ye (1992, and references therein), the large-diameter end of the integral frequency distributions of H II regions can be represented by:

$$N(> D) = N_0 e^{-D/D_0}, \tag{4.2}$$

where $N(> D)$ is the number of H II regions with diameters larger than D.

These fits were done by eye using a log-linear plot or a maximum likelihood method as explained by Ye (1992). Giant H II regions are excluded from this process using criteria such as $S_{5\mathrm{GHz}}d^2 \geq 400$ Jy kpc^2. These giant regions are simply ones ionized by clusters of massive stars in which their Strömgren spheres overlap.

Ye (1992) attempts to give a meaningful theoretical explanation for this relation by testing two models of H II region evolution. The 'classical' model consists of an initial phase is known as *formation* followed by *isothermal expansion*. In the other model, stars with strong winds may participate in a 'bubble' evolution consisting of *free expansion* evolving to a *adiabatic expansion* followed by a *snowplow* phase, reminiscent of SNR evolution. His models fail to differentiate any trend using data from several galaxies including the Magellanic Clouds.

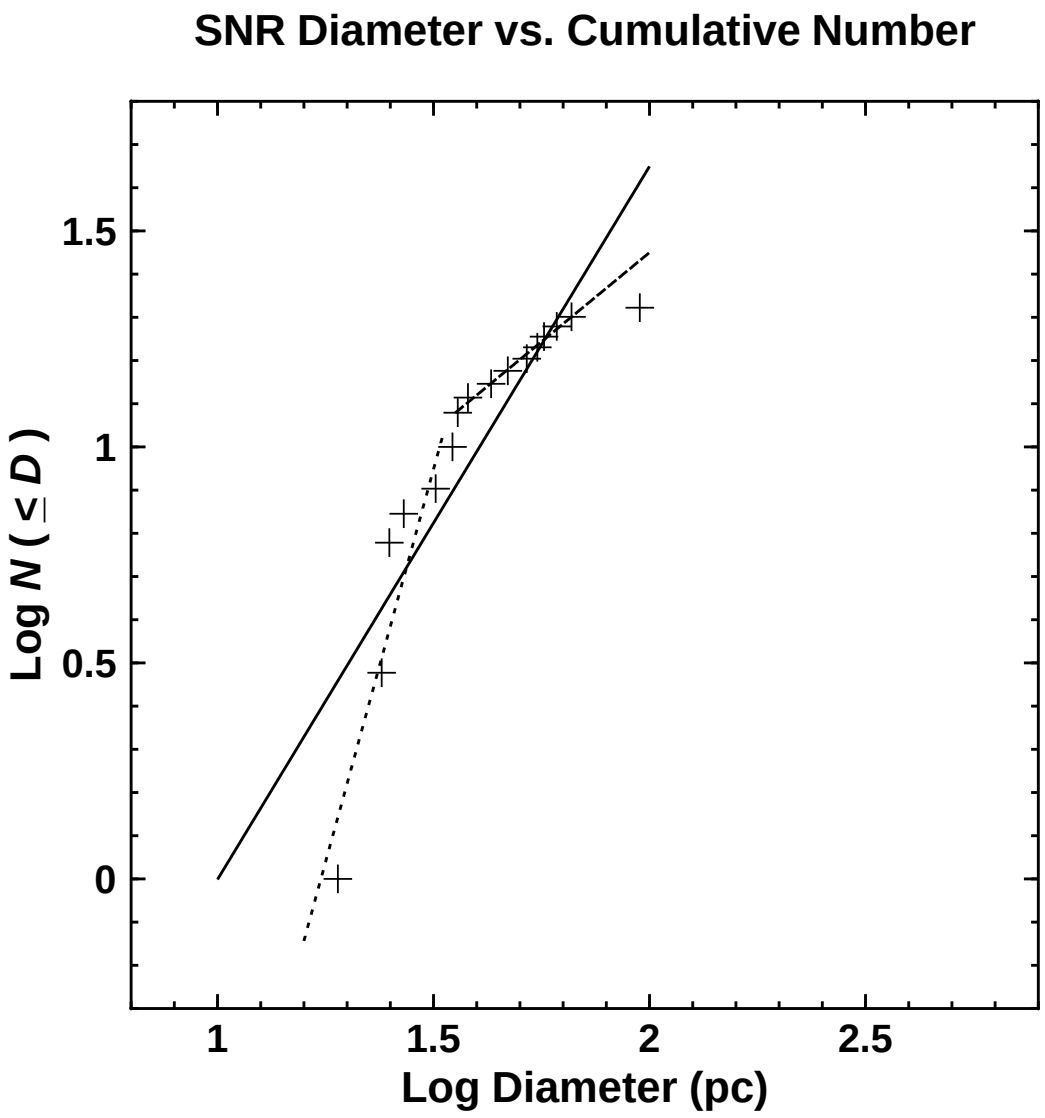

Figure 4.14 Log diameter vs. log cumulative number of SNRs (and candidates) in the SMC. The relation is found to be $N(\leq D) = 0.02D^{+1.7\pm0.2}$ with $r^2 = 0.77$. The relation can also be fitted to two lines: smaller (younger) SNRs with $N(\leq D) = 0.00003D^{+3.6\pm0.7}$; $r^2 = 0.86$ (dotted line) and larger (older) SNRs with $N(\leq D) = 0.63D^{+0.8\pm0.0}$; $r^2 = 0.99$ (dashed line).

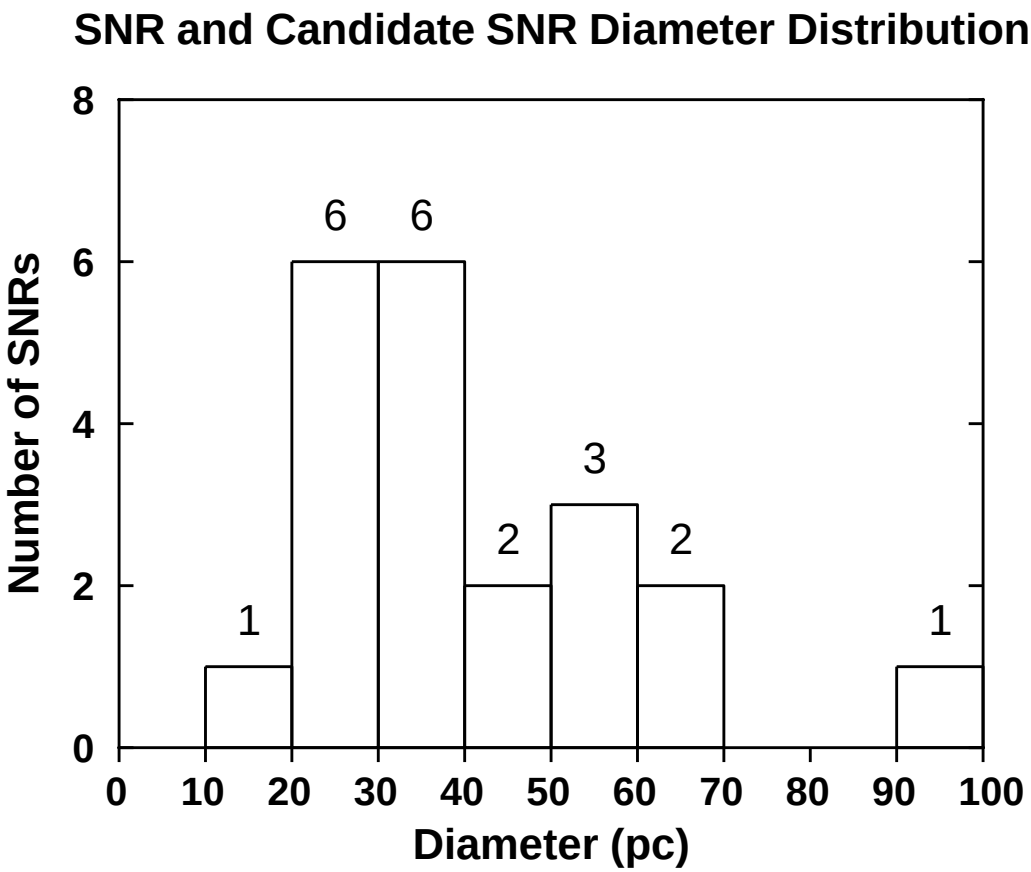

Figure 4.15 SNR diameter distribution suggesting most SMC remnants are in their adiabatic phase.

While these studies are usually performed using Hα observations, we use average 2.37 GHz H II diameters in Fig. 4.16 to attempt to find if such a relation exists, excluding J010326-720308 as a suspected giant H II region. Although the values for N_0 (295) and D_0 (9.2 pc) do not agree with those reported by Ye (1992) (158 and 44 pc, respectively) the fit is definitely a good one with a r^2 of 0.99. Improved radio resolution and sensitivity with the added bonus of less dust obscuration may eventually make such methods useful to the understanding of H II region evolution.

4.7.7 2-D Distribution of SNRs and H II Regions

In order to understand the distribution of SNRs and H II regions, we plotted their positions against a 1.42 – 2.37 GHz spectral index radio image of the SMC (Fig. 4.17). This image was created by smoothing the 2.37 GHz image to a 98″ beam using the MIRIAD task CONVOL and aligning it with the 1.42 GHz image using REGRID. The task MATHS (masking noise below 5σ) allowed the spectral index between the two frequencies to be represented as intensity on the image.

We note that the H II regions outline the main Bar and interior of the SMC while the SNRs are found at the extreme ends of the Bar. The hollowed out areas of steeper spectral index suggests several more SNRs to exist further within the main Bar; these are hard to distinguish from H II regions using radio frequencies alone.

Confusion between H II regions and SNRs can clearly be seen. The wide expanse of several H II regions also cause flux confusion with background galaxies and AGNs. The two dominant areas at the north and south ends of the Bar represent the richest areas not only in radio but also in the optical domain.

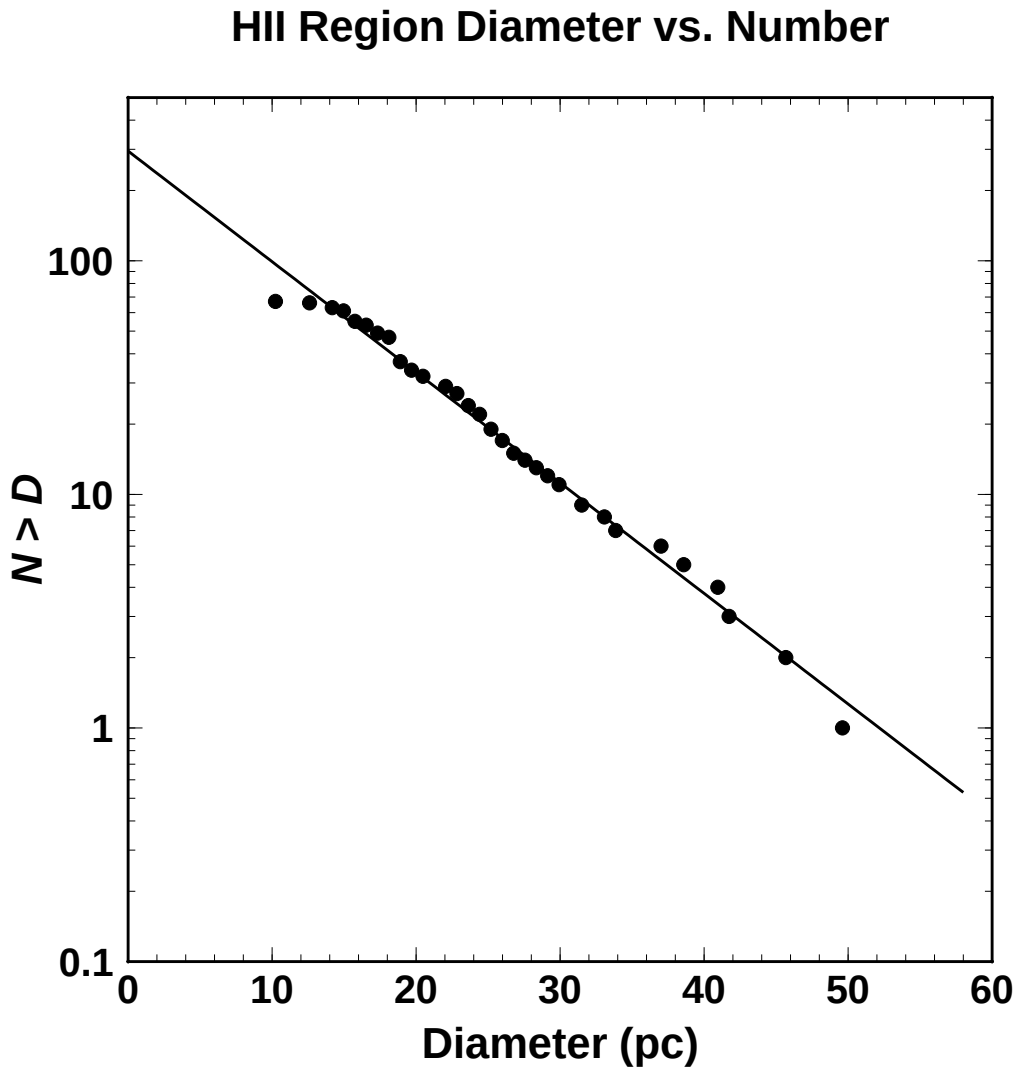

Figure 4.16 H II region number-diameter relation on a log-linear plot. This data fits a line, $N(> D) = 295e^{-D/9.2\pm0.2}$ with $r^2 = 0.99$.

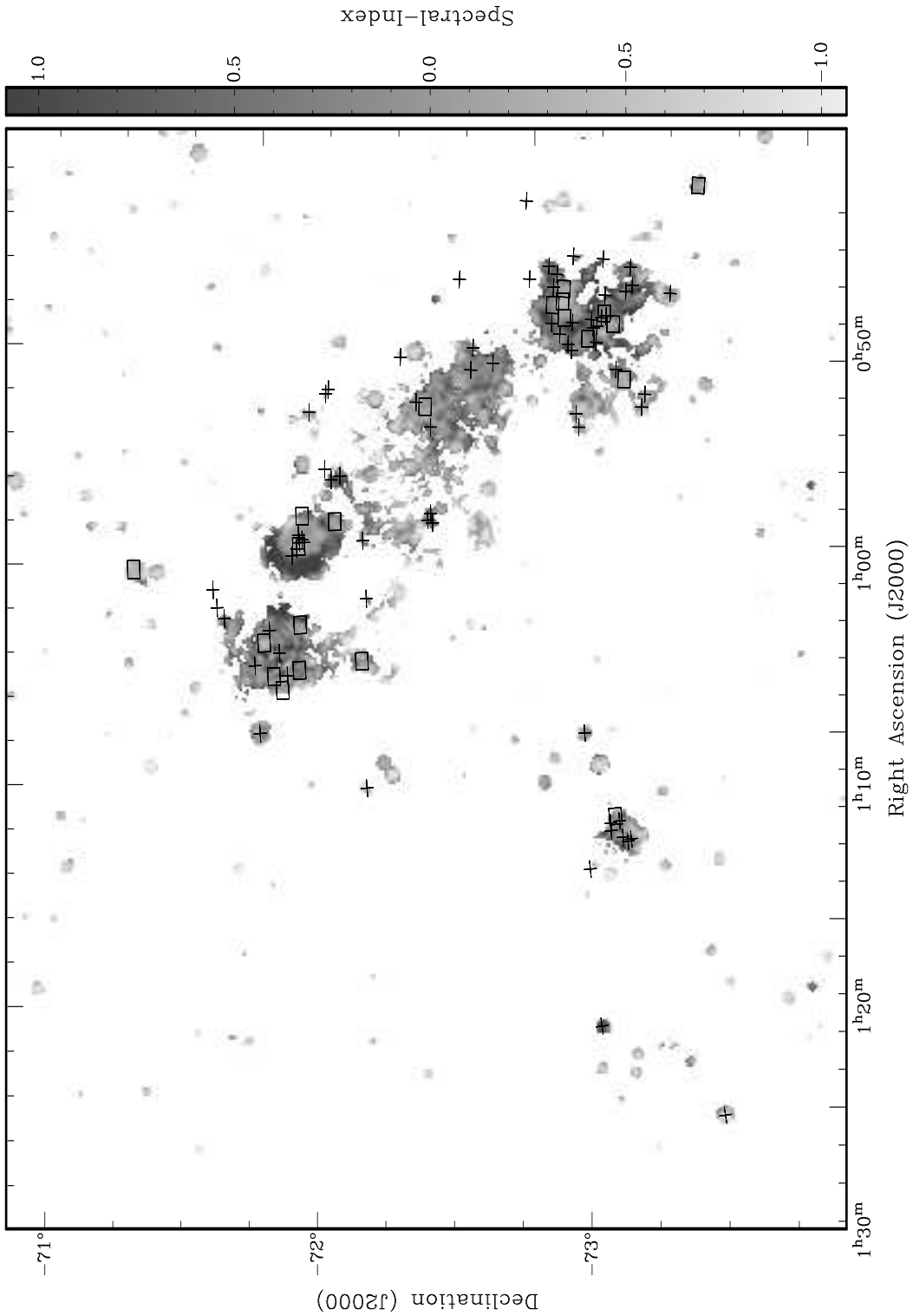

Figure 4.17 The distribution of SNRs (boxes) and H II regions (crosses) throughout the SMC Field superimposed over a 1.42 – 2.37 GHz spectral index radio image. In this map, the spectral index is shown as 'intensity' as calculated from the MIRIAD task MATHS.

Table 4.7 Candidate X-ray SNRs with no optical or radio SNR identifications. (a: denotes *ASCA* hardness ratio (HR) instead of *ROSAT* HR2, defined as HR = [H – S]/[H + S] where H represents counts between 2.0–7.0 keV and S between 0.7–2.0 keV.)

Name	Coordinates		HR2	Other names and references
	R.A. (J2000)	Dec (J2000)	(*ROSAT*)	
No. 6, Yokogawa et al. (2003)	00 36 09.2	–72 21 05	-0.79 ± 0.35^a	No. 211, Haberl et al. (2000); No. 4, Sasaki et al. (2000)
No. 45, Yokogawa et al. (2003)	00 53 29.2	–73 36 40	-0.79 ± 0.51^a	
No. 165, Kahabka et al. (1999)	01 01 51.3	–72 49 03	0.12 ± 0.27	RX-J0101.8-7249
No. 223, Kahabka et al. (1999)	01 12 43.6	–72 07 25	1	RX-J0112.7-7207
No. 245, Kahabka et al. (1999)	01 19 26.7	–73 01 19	0.62 ± 0.06	RX-J0119.4-7301; No. 66, Wang & Wu (1992)

4.7.8 Comparison of Multi-Frequency Datasets

Pannuti et al. (2000) have compared datasets of SNRs selected by radio, X-ray and optical criteria in order to explore selection effects that occur due to the environments of SNRs as well as available resolution and sensitivity. The Venn diagram shown in Fig. 4.18 summarizes the number of SNRs and candidate SNRs within the SMC according to their radio, X-ray and optical emission, not according to the criteria by which they were originally selected. Given the distribution of SNRs near or within relatively dense H II regions as shown in Fig. 4.17, it is not surprising that most objects have been observed in X-ray and radio since these denser regions support such emission processes. However, the SMC is near enough that optical emission from these SNRs can also be detected, minimizing the selection effect seen in more distant galaxies such as NGC 300.

We find a number of X-ray SNR candidates listed in several recent surveys with no optical or radio emission (Table 4.7). Kahabka et al. (1999) found three (3) X-ray candidate SNRs in the SMC: sources RX J0101.8-7249, RX J0112.7-7207 and RX J0119.4-7201. The latter was originally discovered using the *Einstein* observatory and named BKGS 30, but it was not classified as a SNR. Yokogawa et al. (2003) also found two soft X-ray SNR candidates (No. 6 and No. 45) using data from the *ASCA* mission. The coordinates for No. 6 are $\alpha = 00^h36^m09.2^s$, $\delta = -72^\circ21'05''$ (J2000) and for No. 45; $\alpha = 00^h53^m29.2^s$, $\delta = -73^\circ36'40''$ (J2000). This brings the total number of X-ray candidate SNRs with no radio or optical counterparts to five (5). Future surveys with *Chandra* and *XMM-Newton* will be needed to verify that these sources are SNRs.

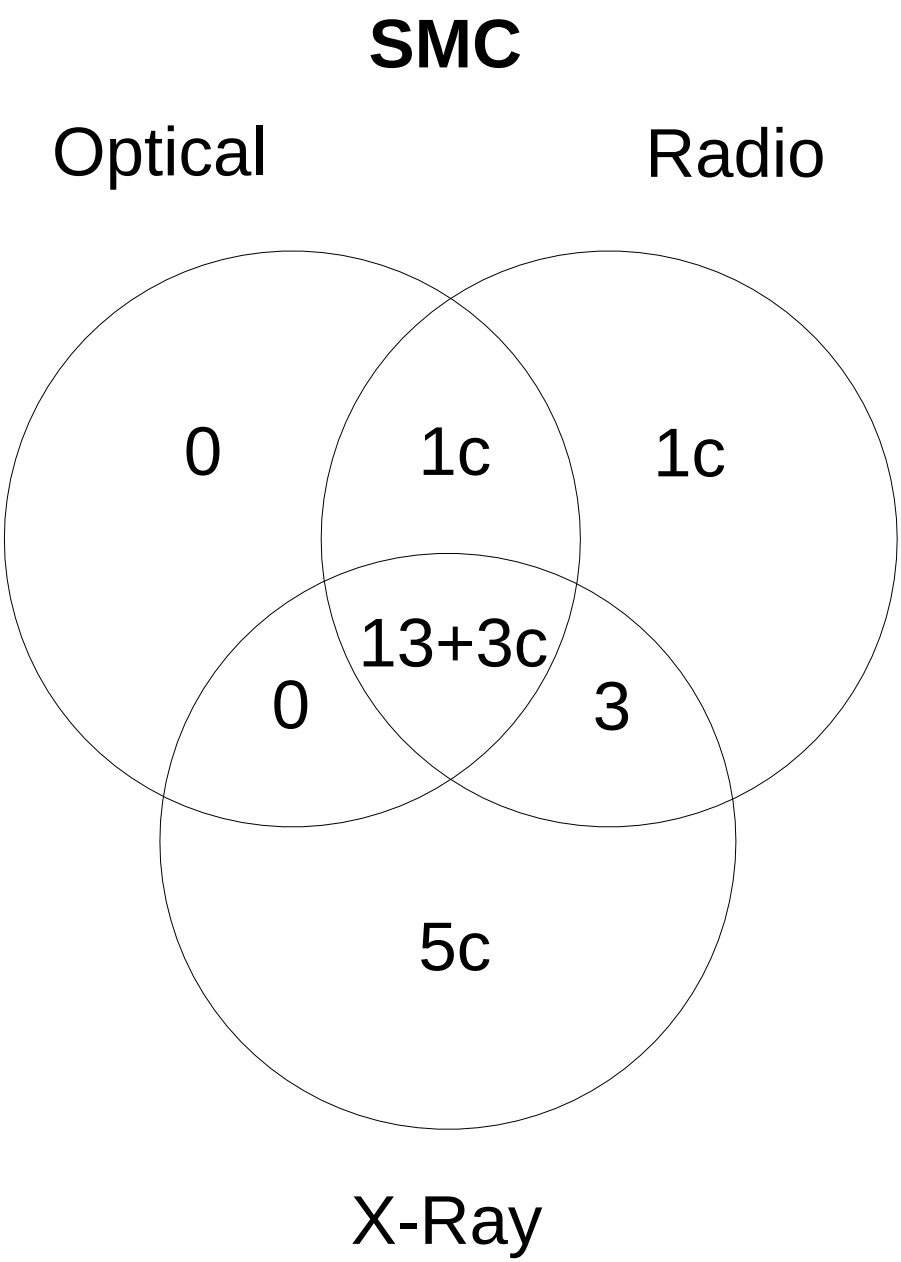

Figure 4.18 Venn diagram of SNRs and candidate SNRs in different electromagnetic domains. Candidates are denoted by the letter ‘c’.

4.8 SNR References, Images and Notes

This was originally an appendix in the published version of this chapter. Its purpose was to present some of the more interesting information about previously studied radio SNRs.

SNR J004637-730823: (B0044-734; Figs. 4.1 and 4.19; Ye 1988; Rosado et al. 1994; Dickel et al. 2001) Part of the large H II region N S19; the remnant cannot be detected in the optical domain.

SNR J004728-730601: (B0045-733; Figs. 4.1 and 4.19; Ye 1988; Rosado et al. 1994; Dickel et al. 2001) Also located near the H II region N S19 and is visible at optical, X-ray and radio wavelengths.

SNR J004716-730811: (B0045-734; Figs. 4.1, 4.19 and 4.20(a); Mills et al. 1982; Mills et al. 1984; Mathewson et al. 1983; Rosado et al. 1994; Dickel et al. 2001) The brightest radio SNR in the SMC, it has a diffuse disk and filament extending from the core also detected in Hα, suggesting the presence of thermal emission.

SNR J004821-731931: (B0046-735; Figs. 4.1 and 4.20(b); Ye 1988; Rosado et al. 1994; Mills et al. 1982; Mills et al. 1984) Discovered by cross-identifying a radio source and a filamentary shell with strong [S II] emission (Mathewson & Clarke 1973), this remnant's optical counterpart shows a diffuse knot with filaments.

SNR J004907-731402: (B0047-735; Figs. 4.1 and 4.20(c); Mathewson et al. 1984; Mills et al. 1984; Filipović et al. 1998b) This remnant's radio image appears patchy, consisting of three separate nuclei; at X-ray energies, it has a central core with two diffuse extensions.

SNR J005110-732212: (B0049-736; Figs. 4.1 and 4.20(d); Ye 1988; Mills et al. 1982; Mills et al. 1984; Mathewson et al. 1984) At 2.37 GHz, this SNR has a more or less typical morphology with a defined shell,

offset center and no nearby bright H II regions or background sources.

SNR J005240-723820: (B0050-728; Figs. 4.3 and 4.20(e); Ye 1988; Rosado et al. 1994; Mathewson et al. 1984; Mills et al. 1984) This large (95 ± 4 pc) patchy radio SNR is near the large H II region N S50; its radio spectral index (-1.03 ± 0.05) is steep, possibly because of lower frequency confusion with N S50 and nearby background sources.

SNR J005800-721101: (B0056-724; Figs. 4.2 and 4.20(f); Ye 1988; Ye et al. 1991) This SNR is located in the giant nebula N S66 and has a flat spectral index (0.02 ± 0.18); exclusion of the MOST 843 MHz flux density gives a more typical SNR spectral index of –0.54.

SNR J005817-721814: (B0056-725; Figs. 4.2 and 4.20(g); Ye 1988; Mathewson et al. 1984) This SNR has a defined structure consisting of a diffuse shell with circular appearance; it has an X-ray 0.1 – 4.0 keV luminosity (IKT 16) of 1.0×10^{37} ergs s^{-1}.

SNR J005927-721010: (B0057-724; Figs. 4.2 and 4.20(g); Ye 1988; Ye et al. 1991; Mills et al. 1982) Confused within N S66, we used SNR J005927-711010's X-ray dimensions ($204'' \times 144''$) to determine its flux density at 1.42 GHz and 2.37 GHz; when used with other available values, the result was a spectral index of -0.81 ± 0.27.

SNR J010023-713322: (B0058-718; Fig. 4.20(h); Ye 1988; Mathewson et al. 1984; Mills et al. 1984) This SNR exhibits a very typical shell morphology with a radio circular diffuse region.

SNR J010313-720958: (B0101-724; Fig. 4.20(i); Mathewson et al. 1983; Mills et al. 1982; Mills et al. 1984; Hughes & Smith 1994; Ye et al. 1995) This faint radio SNR has radio emission extending evenly in

each direction except the east, there faint extensions are devoid of features.

SNR J010402-720149: (B0102-723; Fig. 4.20(j); Ye 1988; Dopita et al. 1981; Tuohy et al. 1983; Sasaki et al. 2001; Amy & Ball 1993; Hayashi 1994) Possibly the smallest and youngest known SNR in the SMC, this oxygen-rich bright object has an outer blast wave in X-ray (Gaetz et al. 2000) consistent with the interpretation that synchrotron radiation originates behind the blast wave, but outward of more typical X-ray emission.

SNR J010524-720923: (B0104-722; Fig. 4.5(h); Filipović 2000) This SNR has a very diffuse radio morphology, consisting of several clumps or core areas in a ring; this is not as obvious in radio as in Hα.

SNR J010505-722319: (B0103-726; Fig. 4.20(k); Ye 1988; Mills et al. 1982; Mills et al. 1984) Possibly the oldest (1.8×10^4 yr) example of an oxygen-rich SNR (Park et al. 2003) and suggested as a more evolved version of IKT 22 (van der Heyden et al. 2004), its radio structure is typical, showing a diffuse circular shell with several brighter clumps.

SNR J010619-720527: (B0104-723; Fig. 4.20(l); Ye 1988; Mathewson et al. 1984; Mills et al. 1984; Hughes & Smith 1994) This is the dimmest radio SNR in the SMC and has a flat spectral index ($+0.19 \pm 0.28$), most likely due to a lack of measurable flux at 4.80 and 8.64 GHz. The U.K. Schmidt red plate image of this SNR reveals a diffuse optical shell.

4.9 Chapter Summary

In this chapter, we have presented the statistics of sixteen (16) SNRs and five (5) new candidate SNRs within the SMC along with images and tables listing their details. An additional three (3) new radio sources may be

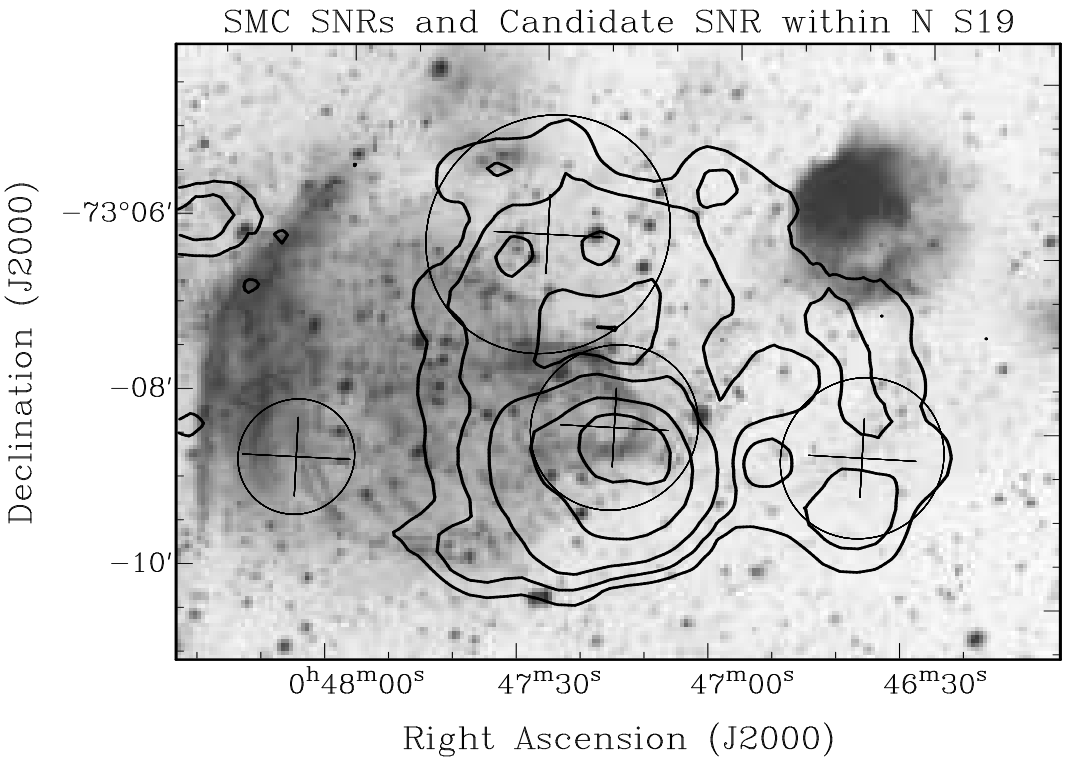

Figure 4.19 N S19 H II region containing SNRs J004637-730823, J004728-730601, J004716-730811 and candidate SNR J004806-730842. This Hα image has 2.37 GHz – Hα contours at 0.02, 0.03, 0.05, 0.1 and 0.15 mJy pixel^{-1}. Circles mark size and location of sources.

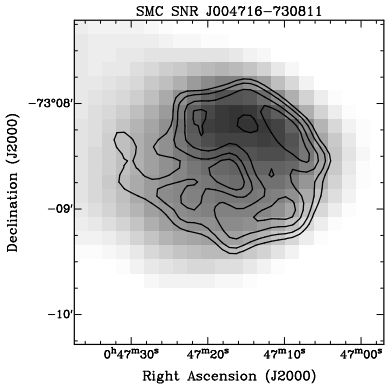

(a) SNR J004716-730811 4.8 GHz image and 8.64 GHz contours (0.7, 1.0, 1.5 and 2 mJy beam^{-1}).

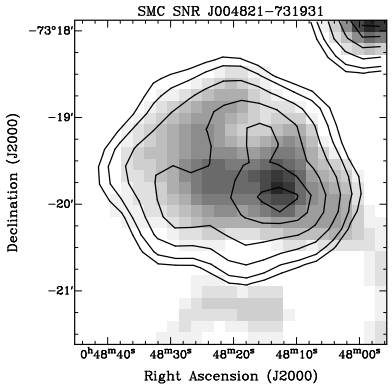

(b) SNR J004821-731931 4.8 GHz image and 2.37 GHz contours (4, 5, 7, 10, 13, and 15 mJy beam^{-1}).

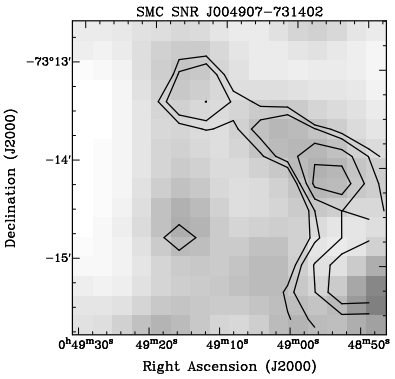

(c) 2.37 GHz image with MOST 843 MHz contours of SNR J004907-731402 (image center). Contours are 2.5, 3, 4 and 5 mJy beam^{-1}. The SNR is patchy, consisting of three centers of emission at 11, 2 and 7 o'clock.

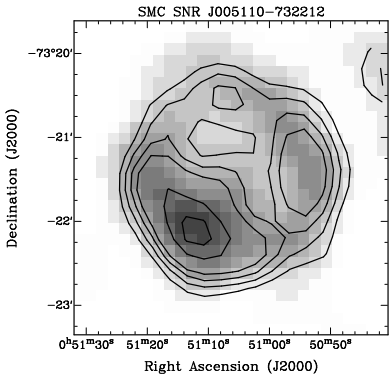

(d) SNR J005110-732212 4.8 GHz image with 2.37 GHz contours (4, 5, 6, 7, 10 and 12 mJy beam^{-1}).

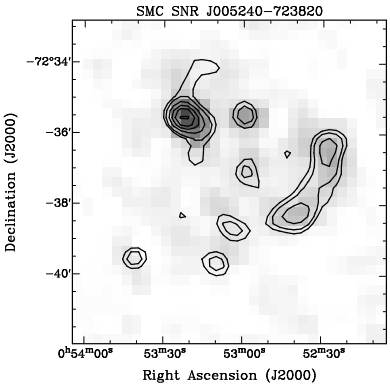

(e) SNR J005240-723820 MOST 843 MHz image with 2.37 GHz contours. Contours are 5, 6, 8, 10, 12, 15 and 20 mJy beam^{-1}.

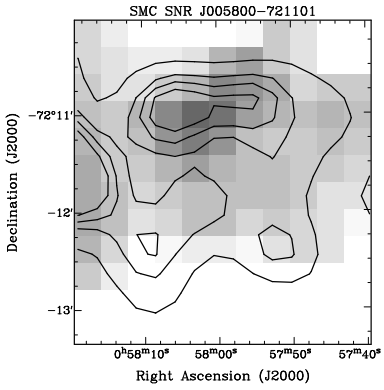

(f) SNR J005800-721101 MOST 843 MHz image with 2.37 GHz contours. Contours are 3, 4, 4.5 and 5 mJy beam^{-1}.

Figure 4.20 Radio images of known SNRs. ATCA beam sizes for 1.42, 2.37, 4.80 and 8.64 GHz are 98″, 40″, 30″and 15″, respectively. Sensitivities are 1.8, 0.4, 0.8 and 0.4 mJy beam^{-1}, respectively.

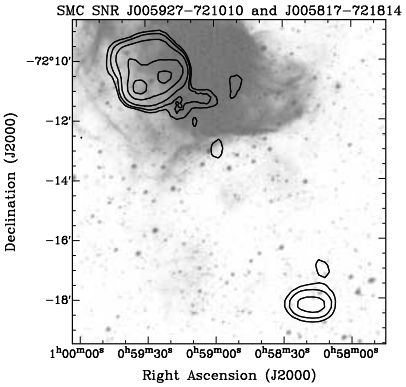

(g) Hα image with 2.37 GHz – Hα difference image contours of the N S66 H II region containing SNRs J005927-721010 (upper left) and J005817-721814 (lower right). Contours are 0.02, 0.03, 0.05, 0.1 and 0.15 mJy pixel^{-1}.

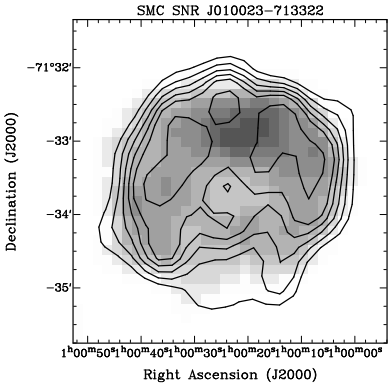

(h) SNR J010023-713322 4.8 GHz image with 2.37 GHz contours (3, 4, 5, 6, 7, 9 and 12 mJy beam^{-1}).

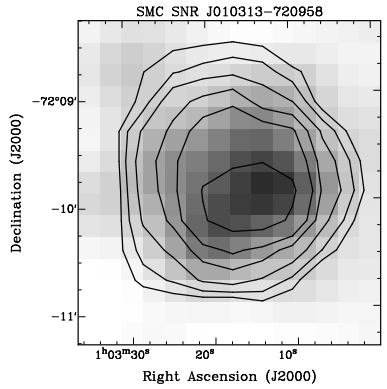

(i) SNR J010313-720958 2.37 GHz image with MOST 843 MHz contours (5, 7, 10, 15, 20 and 30 mJy beam^{-1}).

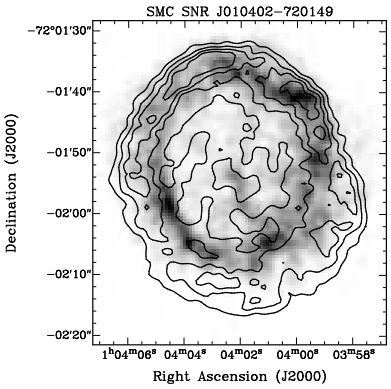

(j) SNR J010402-720149 *Chandra* (0.6-1.5 keV) X-ray image with high resolution (2″) 4.8 GHz contours (0.2, 0.4, 0.6 and 0.8 mJy beam^{-1}).

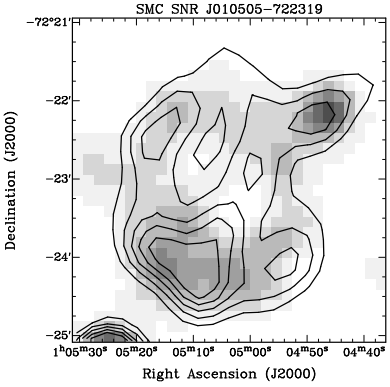

(k) SNR J010505-722319 4.8 GHz image with 2.37 GHz contours (3, 4, 5, 6, and 7 mJy beam^{-1}).

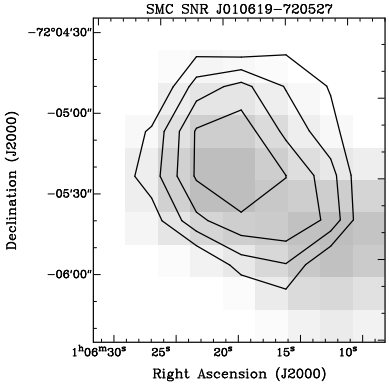

(l) SNR J010619-720527 2.37 Ghz image with MOST 843 GHz contours (3, 4, 5 and 6 mJy beam^{-1}).

Figure 4.20 (Cont.) Radio images of known SNRs. ATCA beam sizes for 1.42, 2.37, 4.80 and 8.64 GHz are 98″, 40″, 30″and 15″, respectively. Sensitivities are 1.8, 0.4, 0.8 and 0.4 mJy beam^{-1}, respectively.

SNR candidates but only further detailed study could verify this. We also discussed the SMC H II regions and presented subtraction images of four regions within the cloud. These subtraction images add insight to the environment of all of these objects.

Based on this study, we make the following conclusions:

1.) Comparisons of multi-frequency diameters of SNRs suggest that as a group, they cannot be selected between the optical, X-ray and radio domains. Improved X-ray resolutions from newer missions such as *Chandra* and *XMM-Newton* should improve our understanding of these relationships.

2.) The relation between the optical and radio diameter of H II regions reveal that radio may not detect a significant portion of a source. With the advent of higher resolution radio telescopes, this makes the accurate determination of flux density and spectral index difficult since boundaries are unreliable. H II regions are also heterogeneous sources causing flux density measurements to be unreliable.

3.) The spectral index distribution is as expected for SNRs and candidate SNRs in the SMC with a mean value of -0.63 (s.d.=0.43).

4.) In the SMC, background sources with steep spectral indices tend to be hard X-ray sources while SNRs have softer X-ray spectra.

5.) The Surface Brightness vs. Diameter relation is not useful for the characterization of SNRs in the SMC. However, the range of SNR surface brightness values are similar to that for the Galaxy although determination of a completeness limit is constrained by confusion with H II regions.

6.) The SNR Integral Number-Diameter relation may be divided into a younger population in their adiabatic phase and an older incomplete sample due to selection effects. The usefulness of this relation has been questioned by Berkhuijsen (1987). It is possible to find a similar relation for H II regions, but the significance to H II region evolution is uncertain.

7.) The 2-D distribution of SNRs and H II regions in the SMC suggest that several SNRs probably exist within the interior of the main Bar, but are confused within the dominant H II regions.

8.) Most of the SNRs within the SMC have emission from the optical, radio and X-ray domain except for several (five) X-ray candidates that have yet to be confirmed.

CHAPTER 5

THE SMALL MAGELLANIC CLOUD – SNR OPTICAL SPECTRA

5.1 Original Abstract

We present an analysis of optical long-slit spectra and estimated line ratios for eleven of the sixteen known radio supernova remnants (SNRs) in the Small Magellanic Cloud (SMC) using observations made with the 2.3-meter Advanced Technology Telescope and Double Beam Spectrograph at Siding Springs Observatory in Australia[1]. We also present spectra and estimated line ratios for a twelfth source; a previously reported candidate radio SNR, J004100-733648. Our new data for this source confirm its classification as an SNR. We find that these shocks show no evolutionary trends, implying that reported relationships between diameter and line ratios may instead be due to selection effects. We have also used the estimated line ratios in the spectra of these SNRs – which we assume to be dominated by the interstellar medium (ISM) at this stage of their evolution – to derive an estimate of $10^{-4.1}$ (relative to hydrogen) for the abundances of metals in the ISM of the SMC. This value is in general agreement with other values previously published in the literature.

5.2 Introduction

Multi-wavelength studies of supernova remnants (SNRs) allow us to understand the crucial physics that underlies the interactions between these sources and the surrounding interstellar medium (ISM). Unfortunately, the distances to many Galactic SNRs are uncertain by a factor of 2, leading to a factor of 4 uncertainty in luminosity and of 5.5 in the calculated energy release of the initiating supernova (SN; Seward et al. 2005). At a distance of $\sim$ 65 kpc (Feast 1999), the SMC is a prime target for the astrophysical research of objects including SNRs and H II regions. This is because these sources are located at a known distance, yet close enough to allow a detailed analysis of each individual remnant.

We recently presented a series of papers using ATCA radio-continuum observations at 1.42 GHz (λ = 21 cm) and 2.37 GHz (λ = 12.7 cm) centered at RA (J2000) = 00^h55^m and Dec (J2000)=–72°50′ and covering a $\sim$ 20 square degree field of the sky in the direction of the SMC. Parkes single-dish data were added to provide missing short-spacing as outlined in Stanimirović et al. (1999). Additional observations in selected regions of the SMC at 4.80 GHz (λ = 6.25 cm) and 8.64 GHz (λ = 3.5 cm) were also presented in these

[1] This article was published in Monthly Notices of the Royal Astronomical Society, volume 376, pages 1793–1804 (2007). Co-authors include G. L. White, M. D. Filipović and T. G. Pannuti; see 'Contribution of Others' section for more information.

works.

The flux uncertainties (rms) were 1.8 mJy beam^{-1}, 0.4 mJy beam^{-1}, 0.8 mJy beam^{-1} and 0.4 mJy beam^{-1} at the frequencies of 1.42 GHz, 2.37 GHz, 4.80 GHz and 8.64 GHz, respectively, while the image resolution was 98″, 40″, 30″and 15″, respectively. More details and the resulting catalogue can be found in Staveley-Smith et al. (1997) and Filipović et al. (2002) (hereafter known as Paper I).

An initial classification of sources was presented in Chapter 3 (Payne et al. 2004a). In that effort, we used criteria including identification with previously known sources detected at other wavelengths, source extension and morphology, position and radio spectral index. Appendix A, Table 1 is a complete list which summarizes the detected sources and their properties. A complete table is also available in a machine-readable format from CDS (**http://vizier.cfa.harvard.edu/viz-bin/VizieR?-source=J/MNRAS/355/44**).

Chapter 4 presented a statistical analysis of all 16 confirmed SNRs and five new candidate remnants. Three other sources having some SNR characteristics were also presented. To better understand the environments containing SNRs, we scaled[2] Hα images of four SMC regions (southwest Bar, N S66, N S76 and N S83) and subtracted their flux from the ATCA 2.37 GHz radio image.

Reid et al. (2006) used these subtraction techniques to study the N S66 region using 1.42, 2.37, 4.8 and 8.64 GHz and scaled Hα images. In that paper, we presented preliminary optical long-slit observations of this region using the 2.3-meter Advanced Technology Telescope (ATT) and double beam spectrograph (DBS) at the Siding Spring Observatory in Australia. The present chapter now presents new optical spectroscopic observations of radio SNRs and candidate SNRs in the SMC.

As noted by Fesen & Hurford (1996), an extensive list of optical emission lines associated with H II regions and Planetary Nebulae (PNe) has been developed, but such lines are of limited use for the study of SNRs. This is because the lines observed in the spectra of H II regions or PNe are not seen in SNRs or have different relative intensities. For example, PNe have many weak permitted lines of C, N and O. Few permitted optical lines (such as O I, Na I, Ca II and Fe I) are reported in the observed spectra of SNRs. Emission lines in SNRs do cover an enormous range of ionisation stages and only a small percentage of Galactic and Magellanic Cloud optical SNRs have been well studied (see Fesen & Hurford 1996 for a complete discussion). In fact, the paper by Fesen & Hurford (1996) is one of few extensive compilations of observed emission lines of SNRs found in the literature. Limited emission line lists can also be found, e.g., in Osterbrock & Ferland (2006) [3].

[2]The scaling was arbitrary such that the minimal flux over large portions of the difference image was close to zero but not negative.

[3]See tables and references in their Chapter 12.

SNRs have strong forbidden lines indicative of shocked material (e.g. [S II], [N II], [O I], [O II] and [O III]). The line ratio [O III](λ4959 + λ5007)/[O III](λ4363) is always observed to be less than 30 in SNRs. However, the λ4363 line is often too weak and the sky Hg I λ4358 too strong to permit its use. As we know, the best optical discriminator of new candidate SNRs is the use of the ratio of [S II](λ6716 + λ6731)/Hα(λ6563) in combination with the presence of strong [O I](λ6300 + λ6364) and [O II](λ3727) lines (Fesen, Blair & Kirshner 1985). This is especially important where the [S II]/Hα ratio alone is inconclusive ($0.4 <$ [S II]/Hα < 0.67).

This chapter is organized as follows: Section 5.3 details observations, spectral extraction and reduction methods. A sample one-dimensional spectrum typical of a SNR shock is presented. Resultant line fluxes are listed in Section 5.4. Section 5.5 gives a detailed spectral analysis which includes line ratios, electron densities and abundances. Section 5.6 summarizes the results.

5.3 Observations and Data Reduction

In August 2005, we obtained long-slit spectra of sources in the SMC and LMC using the DBS and 2.3-meter ATT at the Siding Springs Observatory in Australia. The visible waveband (3200–9000 Å) of this general purpose spectrograph is split by a dichroic at around 6000 Å and feeds two similar spectrographs, with red and blue optimised detectors. 300B (300 lpmm) and 316R (316 lpmm) gratings allowed a spectral resolution of 5 Å. We used a slit size $2.5'' \times 4'$ with a $0.96''$pixel^{-1} spatial resolution. In general, exposure times for each spectrum were limited to 500 s. Positional accuracy is estimated to be better than $12''$ in either RA or Dec.

Follow up spectral observations of selected SMC SNR targets were conducted January 2006, using the 1.9-meter telescope and Cassegrain spectrograph at the South African Astronomical Observatory (SAAO) in Sutherland. Spectra were obtained using grating number 7 (300 lpmm) between 4000 and 7000 Å having a spectral resolution of 5 Å. For these, the slit size was $1.5'' \times 1.5'$ with a spatial resolution of $0.74''$pixel^{-1}. Exposure times were limited to 800 s with a positional accuracy of $\sim 10''$.

Exposures of all SMC radio SNRs and candidate SNRs listed in Payne et al. (2004a) were obtained during these observations at position angles[4] 0 and 90 degrees. The center of the slit was placed at the radio center coordinate of each SNR. Figs. 5.1 and 5.2 shows Hα images and radio contours of SNRs for which shocked regions were extracted. In these figures, we make use of combined 4×300 s CTIO 0.9-meter (Fig. 5.1; Cheng et al. 1993) and wide-field optical CCD images (Fig. 5.2) obtained at the Curtis Schmidt Telescope at CTIO

[4]Defined as the slit angle east of north.

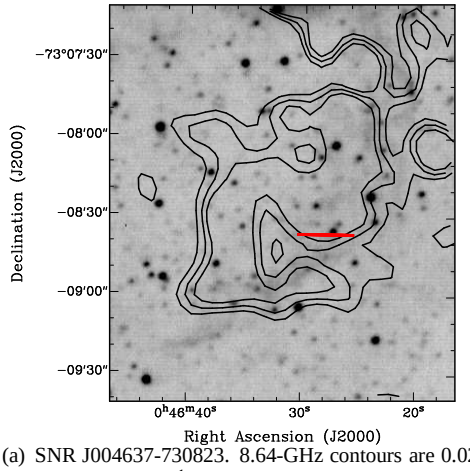

(a) SNR J004637-730823. 8.64-GHz contours are 0.02, 0.04 and 0.06 mJy beam^{-1}.

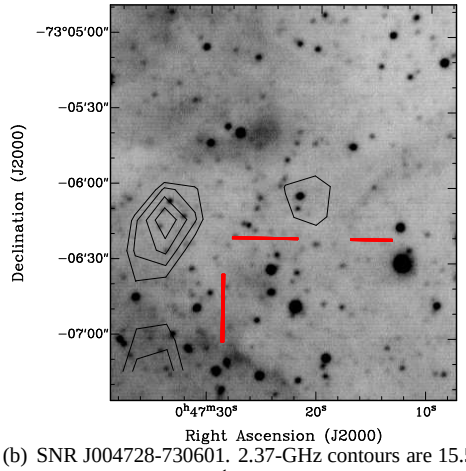

(b) SNR J004728-730601. 2.37-GHz contours are 15.5, 16.0, 16.5 and 17.0 mJy beam^{-1}.

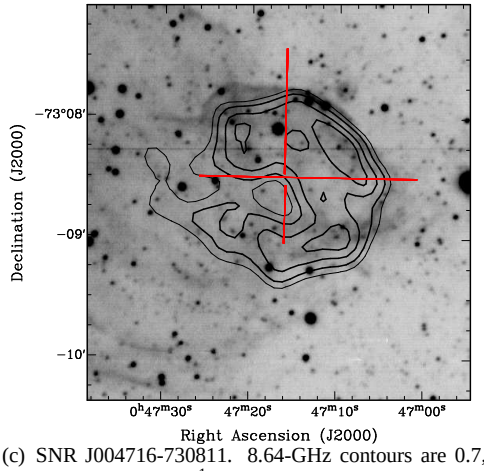

(c) SNR J004716-730811. 8.64-GHz contours are 0.7, 1.0, 1.5 and 2.0 mJy beam^{-1}.

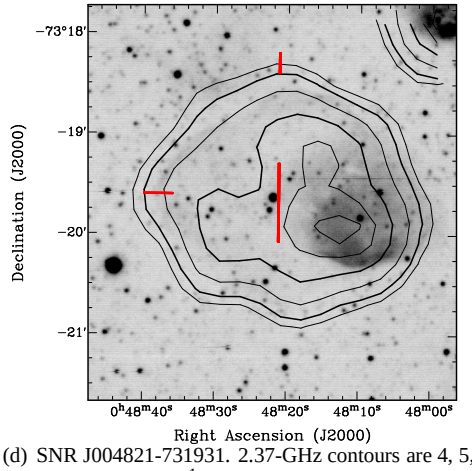

(d) SNR J004821-731931. 2.37-GHz contours are 4, 5, 7, 10, 13 and 15 mJy beam^{-1}.

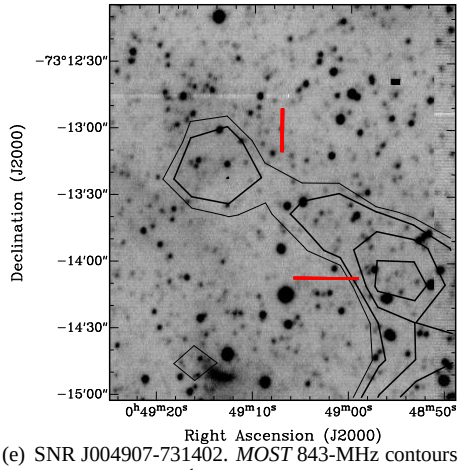

(e) SNR J004907-731402. *MOST* 843-MHz contours are 2.5, 3, 4 and 5 mJy beam^{-1}.

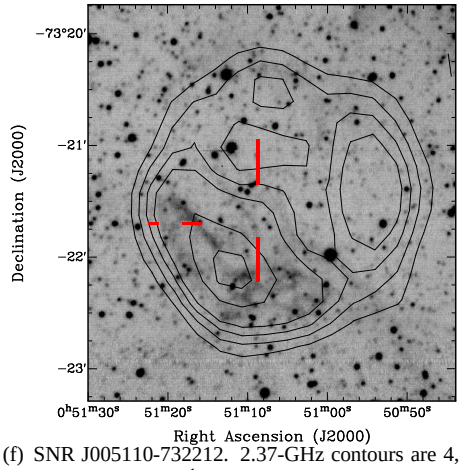

(f) SNR J005110-732212. 2.37-GHz contours are 4, 5, 6, 7, 10 and 12 mJy beam^{-1}.

Figure 5.1 CTIO 0.9-meter Hα images and radio contours of SNRs in the SMC with slit positions marked.

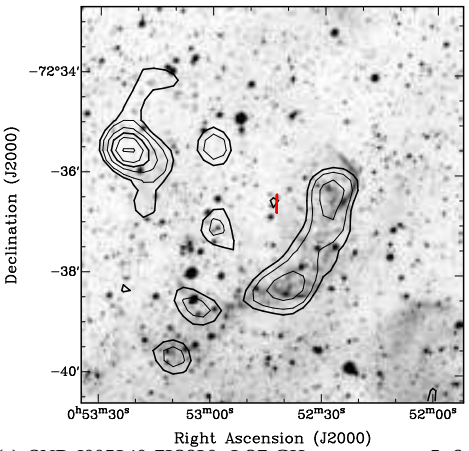

(a) SNR J005240-723820. 2.37-GHz contours are 5, 6, 8, 10, 12, 15 and 20 mJy beam^{-1}.

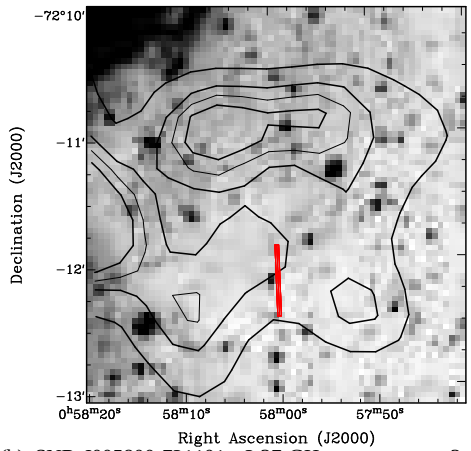

(b) SNR J005800-721101. 2.37-GHz contours are 3, 4, 4.5 and 5 mJy beam^{-1}.

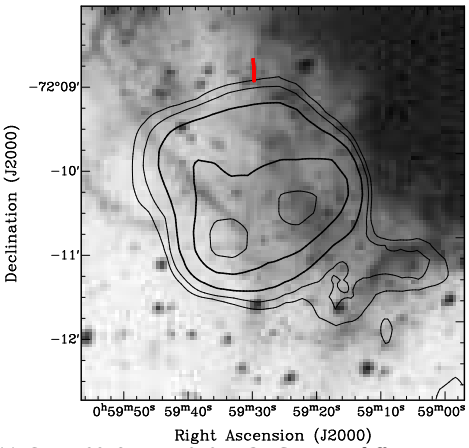

(c) SNR J005927-721010. 2.37 GHz-Hα difference contours are 0.02, 0.03, 0.05, 0.1 and 0.15 mJy pixel^{-1}.

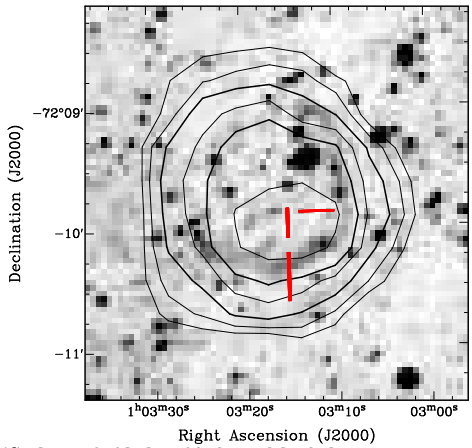

(d) SNR J010313-720958. *MOST* 843-MHz contours are 5, 7, 10, 15, 20 and 30 mJy beam^{-1}.

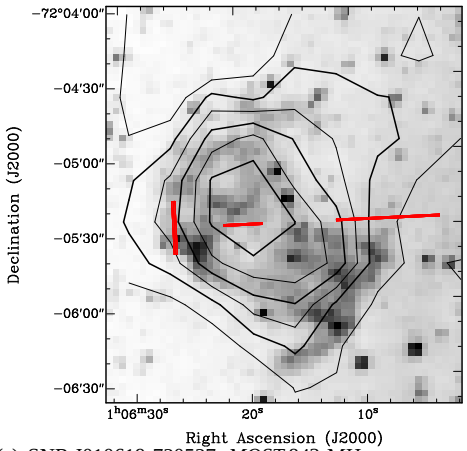

(e) SNR J010619-720527. *MOST* 843-MHz contours are 1, 2, 3, 4, 5 and 6 mJy beam^{-1}.

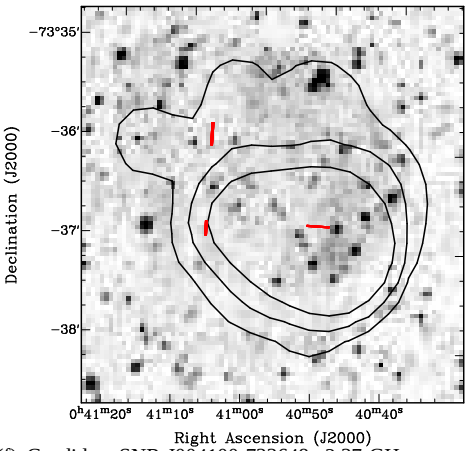

(f) Candidate SNR J004100-733648. 2.37-GHz contours are 2, 4 and 8 mJy beam^{-1}.

Figure 5.2 CTIO Curtis Schmidt Hα images and radio contours of SNRs in the SMC with slit positions marked.

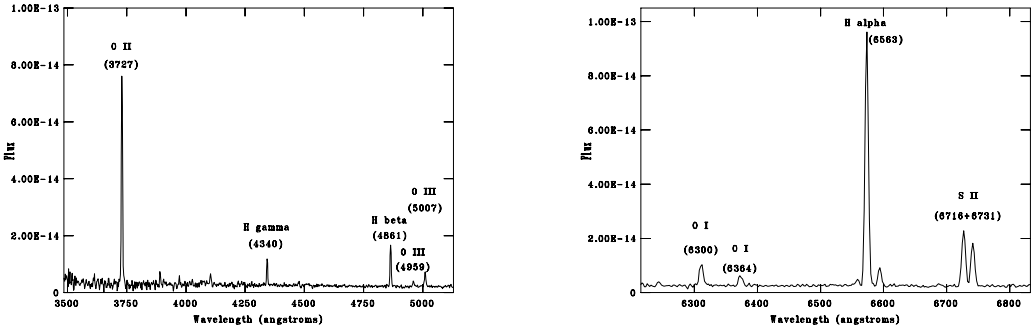

(a) Blue spectrum SNR J004716-730811.

(b) Red spectrum SNR J004716-730811.

Figure 5.3 Sample spectra for the SNR J004716-730811 from 2.3-meter DBS spectrograph reduced using IRAF. Locations of spectral lines important in the identification of SNRs are marked.

in November 1999. The 0.9-meter Hα image has a pixel resolution of $\sim 0.4''$ but only covers the central SMC. The wide-field Curtis Schmidt Hα image covers a much larger region of the SMC with 2048×2048 pixels at a resolution of $\sim 3''$. The latter image was reduced and aligned using standard procedures in IRAF as described in detail by Danforth et al. (2002).

Spectral data reduction included bias subtraction and flat-field correction followed by cosmic-ray hit cleaning using the IRAF software package (and FIGARO's task 'bclean'). Extraction (task 'extractor'), including background sky subtraction, of data obtained at the slit positions shown in Figs. 5.1 and 5.2 were based on the presence of [S II] emission lines and location. We created one-dimensional spectra, wavelength calibrated using standard lines from the NeAr/FeAr arcs (DBS) and the CuAr arc (SAAO). Flux calibration was applied using the spectrometric standard stars, LTT 7379 (DBS) and EG 21 (SAAO).

Fig. 5.3 shows an example of a one-dimensional DBS spectrum for SNR J004716-730811. IRAF's task 'splot' allowed the final resultant spectra to be viewed and line statistics were found using the features within that software. Spectra with [S II]/Hα ratios ≥ 0.4 were chosen for additional analysis and are included here.

5.4 Results

In Table 5.1, we present the result of extractions using the criterion of a [S II]/Hα ratio ≥ 0.4. It includes the most recent radio name for each remnant, the previous (B1950) name common in the literature, the observed slit position and flux density ($\times 10^{-14}$ ergs cm^{-2} s^{-1}) of each emission line found at position angles 0° and 90°. Listed emission lines include [O II] (λ3727), [O III] (λ4363, λ4959 and λ5007), [O I] (λ6300 and λ6364), [N II] (λ6550 and λ6585), [S II] (λ6716 and λ6731), Hδ (λ4102), Hγ (λ4340), Hβ (λ4861) and Hα (λ6563). We

find the average 90% measurement confidence interval for these flux values to be $\pm 0.5 \times 10^{-14}$ ergs cm^{-2} s^{-1}. These errors were calculated using Monte-Carlo simulation techniques found in the task 'splot' for a sample number of 100 and a sensitivity of 1×10^{-16} ergs cm^{-2} s^{-1}Å^{-1}. Table 5.2 lists additional emission lines found in the spectra with relative strengths compared to Hβ. We find only common lines typically associated with SNRs as described by Fesen & Hurford (1996).

As pointed out by Haffner, Reynolds & Tufte (1999), areas of faint Hα background emission can have [S II]/Hα ratios which approach 0.4 or higher (see their Fig. 5 where R = 2.4×10^{-7} ergs cm^{-2} s^{-1} sr^{-1}) which could be confused with shocked regions. However, inspection of Figs. 5.1 and 5.2 suggests our selected slit regions are within or near regions of radio and Hα emission associated with known or suspected SNRs. More importantly, the presence of strong SNR associated emission lines, including [O I] and [O II] as noted in Section 5.5.1, support the assertion that we have extracted shocked regions.

All values are shown at their rest wavelengths. To find radial velocities, we used task 'emsao'[5] using spectra from DBS blue. This task finds individual emission lines, computes redshifts and combines them into a single radial velocity. Values for individual shocks are listed in Table 5.4. We find an average radial velocity of 222.2 ± 55.7 km s^{-1}; a systematic SMC radial velocity of 158 ± 4 km s^{-1} is reported by Huchtmeier & Richter (1986).

We extracted three shocked regions for SNR candidate J004100-733648 having intense [S II]/Hα ratios up to 0.8. There is a fairly discrete shell morphology (Fig. 5.2) in Hα and a steep radio spectral index[6] (α=-0.94 ± 0.14). Northward radio extensions are seen overlaying the Hα emission, suggesting this may be a break-out region. The remnant has also been seen in *ROSAT* X-ray observations. Given its shell morphology in both radio and optical, its steep spectral index, the presence of X-ray emission and the presence of highly shocked material, we feel this object is verified as a SNR.

Discrete shocked regions were not selected for five SNRs. SNR J005817-721814 (SNR B0056-725) was reported by Mathewson et al. (1984) as a SNR based on its X-ray position and radio/optical morphology. We found potential shocked regions for this source with [S II]/Hα ratios as high as 0.3; not quite within our criterion of 0.4. Mathewson et al. (1984) noted that SNR B0058-718 (SNR J010023-731122) has a shell like structure in radio with a non-thermal spectral index and thin filaments visible in [S II] and [O III]. This remnant is quite large ($\sim$ 60 pc), which may explain why we could not isolate a dense enough shocked region. Dopita, Tuohy & Mathewson (1981) found that the bright X-ray source, 1E 0102.2-7219 (SNR J010402-720149),

[5] This task is found within the RVSAO suite of IRAF.

[6] Defined such that $S_\nu \propto \nu^\alpha$ where S_ν is flux density and ν is frequency.

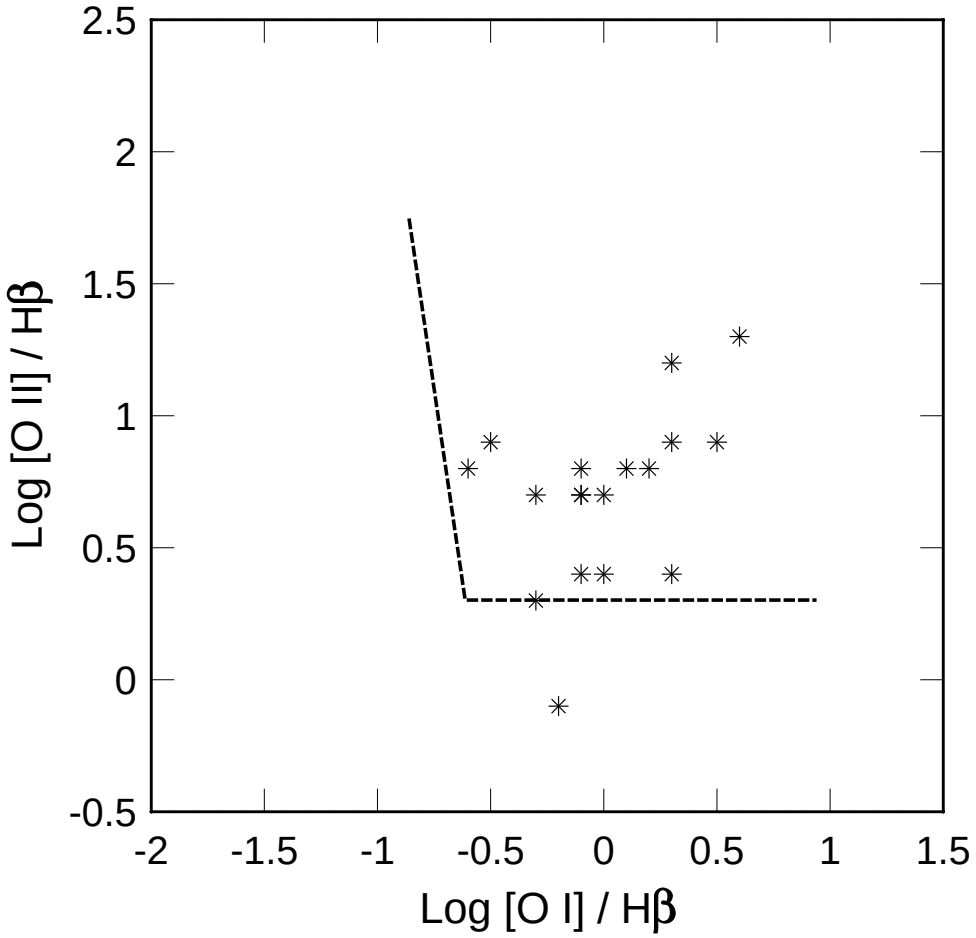

Figure 5.4 Log ([O I]/Hβ) vs. log ([O II]/Hβ) plot for known SMC SNRs with shock [S II]/Hα ratios $\geq$ 0.4. Dotted lines represent boundaries set by Fesen et al. (1985).

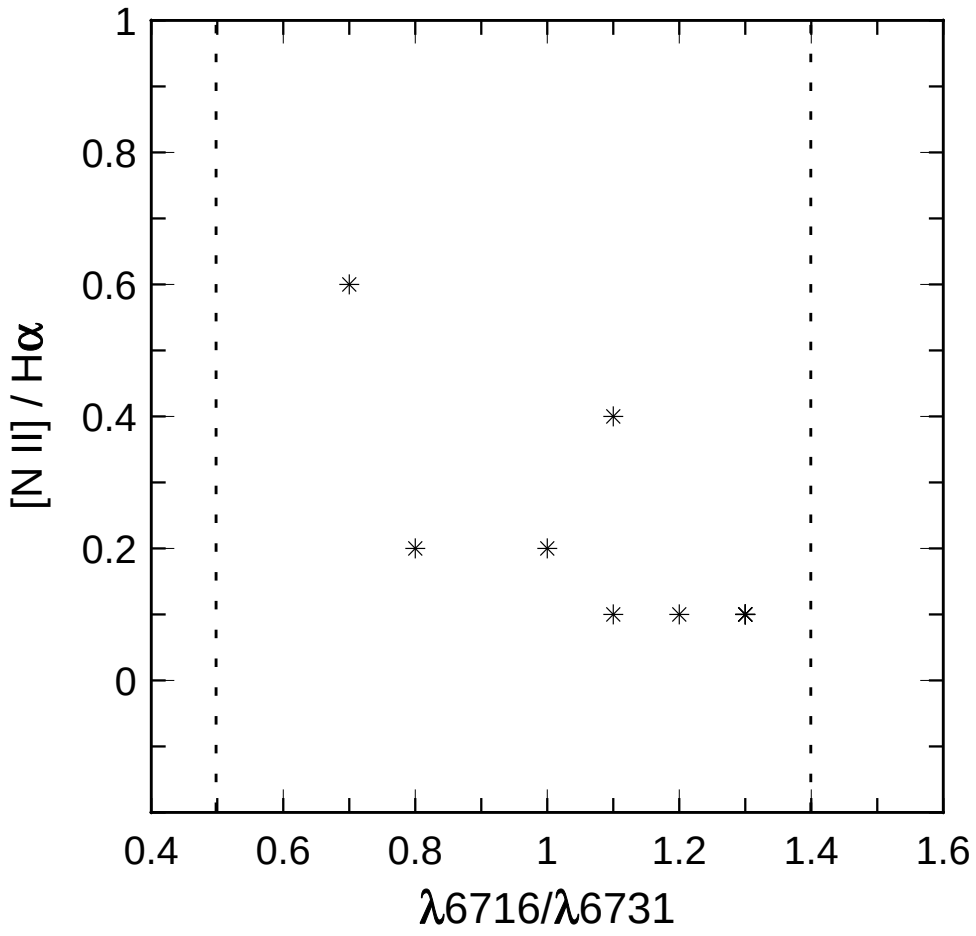

Figure 5.5 The observed SMC [S II] λ6716/λ6731 ratios vs. [N II]/Hα. The dotted line at λ6716/λ6731 = 1.4 and 0.5 indicates the low and high density limit of the ratio. There is no obvious linear trend apparent (r^2 = 0.6), similar to the case for M33 presented in Smith et al. (1993).

is prominent in its [O III] emission and belongs to the class of young SNRs resulting from the explosion of Population I type stars. We selected regions with strong [O III] emission within this remnant, however [S II]/Hα ratios were too marginal (0.2–0.3) for us to include. SNR J010524-720923 has a very diffuse radio morphology consisting of several clumps where shocked regions may exist overlaying a disk-like region seen in Hα. Our slit positions were not co-incident with any shocked region having a [S II]/Hα ratio greater than 0.3. SNR J010505-722319 has several brighter radio clumps incorporated in a diffuse circular shell. This remnant is also a larger ($\sim$ 66 pc) diffuse object in which our slit positions could not detect a deeply shocked region ([S II]/Hα ratio no greater than 0.2).

We were not able to extract any shocked regions from the other SNR candidates listed in Chapter 4 (Payne et al. 2004a; SNR J004806-730842, SNR J004748-731727, SNR J010539-720341 and SNR J011333-731704). All of these are located deep within H II regions which prevent the clean isolation of shocked regions.

SAAO spectral observations of ATCA SMC 163, DEM S 142 and ATCA SMC 487, sources with some SNR characteristics, were also carefully examined. Spectra extracted at our slit positions did not reveal any shocked regions for these objects, and so their status as remnants cannot be verified.

5.4.1 Extinction Estimate

We estimate extinction values for our data using Balmer emission lines Hα (λ6563), Hβ (λ4861), Hγ (λ4340) and Hδ (λ4102). From these, Balmer decrements were calculated as Hα/Hβ, Hγ/Hβ and Hδ/Hβ. Characteristic extinction curves are presented by Osterbrock & Ferland (2006) and expected intrinsic Balmer decrements are based on Case B recombination[7]. Table 5.3 shows individual values for E(B – V) based on these decrements.

Balmer decrements for Hγ/Hβ and Hδ/Hβ, both obtained from the same detector (DBS blue), give similar negative colour excesses, E(B – V). Colour excesses obtained from the Hα/Hβ decrement, using both DBS red and DBS blue detectors, are different. Although data from both detectors have been calibrated during reduction, flux values across detectors do not exactly match. We can find nothing in the literature that discusses this issue and there is no other correction we can currently safely apply.

Given Table 5.3 and an SMC E(B – V) of 0.037 mag reported by Schlegel et al. (1998), we have decided not to correct our data for reddening. None of the ratios obtained, except [O I]/Hβ, use line fluxes from both

[7] This is an approximation for cases characterized by large optical depth, where every Lyman-line photon is scattered many times and is eventually converted into lower-series photons.

detectors, so these values are felt to be unaffected. In the case of [O I]/Hβ as discussed in Section 5.5.1, it should be noted that their values may represent an upper limit.

Although the spectra were calibrated with a flux standard, it is critical to emphasize that the line flux densities are not photometric. In fact, comparison of flux standards showed significant variation throughout the night due to nonphotometric conditions. However, in all cases the sensitivity function (the correction for wavelength-dependent sensitivity of the CCD) of standards agree to within 1.5%. This is important since it allows the calculation of accurate line ratios.

5.5 Spectral Analysis

In Table 5.4, we show for each extracted spectrum, location and radial velocity with error as determined by task 'emsao' (Kurtz & Mink 1998). This table also shows estimated radio diameter (2.37-GHz; from Chapter 4), selected line ratios ([O III]/Hβ, [O I]/Hα, [N II]/Hα, [S II]/Hα, λ6731/Hα, λ6716/λ6731, log [O I]/Hβ and log [O II]/Hβ) and derived electron density.

5.5.1 Shock Verification

As noted in Section 5.2, a useful discriminator between SNRs and H II regions may be based on [S II], Hα, [O I] and [O II] line strengths where good sky [O I] subtraction is possible (Fesen 1981; Blair, Kirshner & Chevalier 1982). Fesen et al. (1985) note that [O I]/Hβ and [O II]/Hβ ratios in the spectra of SNRs are usually much larger than those for H II regions. They present graphs showing the logarithmic values of these ratios of Galactic, M31 and M33 remnants. Despite limitations of the [O I]/Hβ ratio as discussed in Section 5.4.1 we show a similar plot (Fig. 5.4) using values from Table 5.4. Given [S II]/Hα ratio and shock location with these oxygen line strengths, we are more confident that we have extracted SNR shocked regions.

5.5.2 Temperatures and Electron Densities

Ions including [O III] and [N II] have energy-level structures that produce emission lines from different excitation energies. The relative rates of excitation depend very strongly on temperature and may be used to measure electron temperature. The only practical probe for the measurement of electron temperature in our case is the [O III] forbidden line ratio[8] as presented in Figure 5.1 by Osterbrock & Ferland (2006). However,

[8] Defined as (λ4959 + λ5007)/λ4363.

Table 5.1 Selected line fluxes (at rest wavelengths) of SMC SNRs from spectroscopic observations for position angles 0° and 90°. The mean 90% confidence error of the flux is 0.5×10^{-14} ergs cm^{-2} s^{-1}.

Position Angle 0°

Object Name (J2000)	Other Name (B1950)	R.A. (J2000)	Dec 1 (J2000)	Dec 2 (J2000)	Emission Line Flux ($\times 10^{-14}$ ergs cm^{-2} s^{-1})														
					3727 Å [O II]	4102 Å Hδ	4340 Å Hγ	4363 Å [O III]	4861 Å Hβ	4959 Å [O III]	5007 Å [O III]	6300 Å [O I]	6364 Å [O I]	6550 Å [N II]	6563 Å Hα	6585 Å [N II]	6716 Å [S II]	6731 Å [S II]
Confirmed SNRs																			
J004728-730601	B0045-733	00 47 28.6	–73 07 02.4	–73 06 35.6	16.4				1.1			1.3	0.9	0.6	3.6	1.0	2.5	1.7
J004716-730811	B0045-734	00 47 16.1	–73 09 02.8	–73 08 34.0	26.2	2.3	2.7		4.4			1.6	1.6	0.8	24.2	2.0	5.2	4.0
		00 47 16.1	–73 08 28.3	–73 07 25.9	46.0	2.2	5.1		9.0	1.3	3.8	6.0	3.3	1.4	61.2	5.1	14.3	10.7
J004821-731931	B0046-735	00 48 21.2	–73 20 04.6	–73 19 17.6	8.4	0.5	0.7		1.3			1.6		0.4	9.2	1.0	2.5	1.7
		00 48 21.2	–73 18 23.8	–73 18 11.3	1.9	0.2	0.3		0.2			0.5	0.2	0.2	3.5	0.4	0.5	1.0
J004907-731402	B0047-735	00 49 07.1	–73 13 10.2	–73 12 51.0								0.9		0.1	0.8	0.1	0.4	0.2
J005110-732212	B0049-736	00 51 08.7	–73 22 12.8	–73 21 49.8	8.5	1.7	2.1		1.9			1.4		0.2	7.6	0.6	2.0	1.6
		00 51 08.7	–73 21 21.0	–73 20 57.0	2.0	0.9	0.5		0.2	0.4	0.4	0.5			0.9		0.4	
J005240-723820	B0050-728	00 52 42.5	–72 36 47.1	–72 36 25.0	3.9				0.2			0.8		0.3	4.8	0.2	1.0	0.8
J005800-721101	B0056-724	00 58 00.0	–72 12 25.5	–72 11 51.9	3.3	3.0	1.7		1.8	1.3	3.3	1.0		0.2	5.5	0.3	1.0	1.0
J005927-721010	B0057-724	00 59 27.4	–72 09 01.8	–72 08 45.5	29.3	3.0	3.2		3.7	5.1	16.8	0.5	0.7	0.1	1.2	0.5	1.2	0.8
J010313-720958	B0101-724	01 03 15.3	–72 10 36.4	–72 10 12.4	1.0	2.0	1.5		1.2			0.8		0.4	1.9	0.3	0.5	0.3
		01 03 15.3	–72 10 04.7	–72 09 50.3	7.2	1.4	1.4	0.3	1.5	1.3	3.6	0.7		0.2	4.7	0.5	1.1	0.6
J010619-720527	B0104-723	01 06 26.0	–72 05 37.5	–72 05 16.4	8.1	1.2	1.9		3.4	0.2	0.8	2.6	0.7	0.3	20.2	0.9	4.1	3.3
SNR Candidates																			
J004100-733648	B0039-735	00 41 06.5	–73 36 57.6	–73 36 49.0								0.2		0.1	0.3	0.1	0.2	0.1
		00 41 06.5	–73 36 02.9	–73 35 49.4			0.1		0.3			0.4		0.1	0.8	0.2	0.2	0.2

Position Angle 90°

Object Name (J2000)	Other Name (B1950)	Dec (J2000)	R.A. 1 (J2000)	R.A. 2 (J2000)	Emission Line Flux ($\times 10^{-14}$ ergs cm^{-2} s^{-1})														
					3727 Å [O II]	4102 Å Hδ	4340 Å Hγ	4363 Å [O III]	4861 Å Hβ	4959 Å [O III]	5007 Å [O III]	6300 Å [O I]	6364 Å [O I]	6550 Å [N II]	6563 Å Hα	6585 Å [N II]	6716 Å [S II]	6731 Å [S II]
Confirmed SNRs																			
J004637-730823	B0044-734	–73 08 37.0	00 46 25.5	00 46 30.4	13.1		1.1		1.9	0.8	2.8	2.5	0.4	0.4	9.8	1.8	2.6	1.5
J004728-730601	B0045-733	–73 06 21.0	00 47 13.3	00 47 17.0	1.0				0.3					0.1	1.7	0.1	0.4	0.5
		–73 06 21.0	00 47 21.9	00 47 27.8	8.2				0.8					0.1	5.8	0.4	1.6	1.2
J004716-730811	B0045-734	–73 08 30.0	00 47 01.0	00 47 25.9	55.3	4.8	5.1		9.3			11.1	2.2	2.0	59.5	4.5	16.9	11.5
J004821-731931	B0046-735	–73 19 36.0	00 48 35.9	00 48 39.9								1.4	0.6	0.2	3.7	0.4	2.2	1.5
J004907-731402	B0047-735	–73 14 07.0	00 48 59.1	00 49 05.8								1.2	0.4	0.2	0.8	0.2	0.2	0.3
J005110-732212	B0049-736	–73 21 42.0	00 51 15.9	00 51 18.1	0.9						0.2	0.9	0.4	0.2	5.4	0.4	1.1	0.9
		–73 21 42.0	00 51 21.2	00 51 22.4	0.9	0.4	0.2		0.3	0.2	0.3	0.4	0.2	0.1	2.2	0.2	0.4	0.4
J010313-720958	B0101-734	–72 09 52.0	01 03 10.3	01 03 14.0	5.9	2.7	2.4		0.9	0.2	1.0	0.2		0.0	1.6	0.2	0.6	0.5
J010619-720527	B0104-723	–72 05 27.0	01 06 03.0	01 06 11.9	23.2	2.0	2.6		4.7	1.6	4.0	2.2	1.2	0.5	22.8	1.3	5.3	4.1
		–72 05 27.0	01 06 18.4	01 06 21.7	7.9	1.4	1.7		2.8	0.4	0.8	1.7	0.7	0.4	14.3	0.7	3.1	2.3
SNR Candidates																			
J004100-733648	B0039-735	–73 36 48.0	00 40 48.9	00 40 52.1			0.2					0.2		0.1	0.5	0.0	0.2	0.1

as seen in Table 5.1, the [O III] line (λ4363) is available for only one shock, making temperature determinations impossible except in that instance. Other temperature sensitive line ratios listed in Osterbrock & Ferland (2006) are not available within our wavelength range or sensitivity.

By contrast, comparison of the intensity of two lines of the same ion, emitted by different levels with similar excitation energies are dependent only on the ratio of collision strengths. This allows an estimate of the average electron density to be made, as discussed in Osterbrock & Ferland (2006). We estimate the electron density for each of our shocks based on [S II] ratios (λ6716/λ6731) using the Space Telescope Science Data Analysis System task 'nebular.temden', assuming a temperature of 10 000 K. This online calculator uses a five-level atom approximation from De Robertis et al. (1987). Some λ6716/λ6731 ratios have nonphysical measure values ≥ 1.4 and were set to the low-density limit (< 100 cm^{-3}). A high-density limit of a few thousand cm^{-3} for ratios ≤ 0.5 is also present. Values reported here cover this entire range with a dataset mode of a few hundred.

5.5.3 ISM Abundance of the SMC

During the evolution of SNRs, the enriched ejecta is quickly overwhelmed by ISM swept-up by the expanding blast wave. The swept-up mass M_{sw} can be expressed as

$$M_{\rm sw} = \frac{4}{3}\pi R^3 \rho \approx 0.12\, n_0\, R_{\rm pc}^3\, M_\odot, \tag{5.1}$$

where ρ is the mass density of the pre-SNR ISM and R is the radius of the SNR (Smith et al. 1993). The ambient density, n_0, of SNRs can vary from 10^{-3} to 10^3 cm^{-3}. Choosing a nominal ambient density of 1 cm^{-3} implies that all of the remnants in our sample have much more interstellar material than ejecta from the original supernova explosion ($> 200\ M_\odot$ based on our smallest radius). Thus, if one can use line ratios to find gas abundances, the results reveal more information about the abundances of the ISM into which a SNR is expanding.

The grid of shock models presented by Dopita et al. (1984) is perhaps the most applicable for SNR abundance determination. However, estimates may be adversely affected by low shock velocities as noted by Blair & Kirshner (1985). Smith et al. (1993) notes that the [N II] line intensity falls off for shock velocities less than ~ 80 km s^{-1} and the λ6731 line varies little down to 50 km s^{-1}. Therefore, the use of Figure 8 in Dopita et al. (1984) (which compares the ratios [N II]/Hα and λ6731/Hα) should yield abundances which are not susceptible to variations in shock conditions corresponding to a limiting shock velocity of ~ 80 km s^{-1}.

Further, Figure 5 in Dopita et al. (1984) indicates that line ratios such as [O III]λ5007 to Hβ > 1 suggest shock velocities > 100 km s^{-1}. Inspection of Table 5.1 confirms that the majority of our values do exceed a ratio of 1.

In Table 5.5 we list SMC SNR abundances based on the grid presented in Fig. 8 of Dopita et al. (1984). We adopt the generalized "metal" abundance formally defined there as

$$\log A = 0.8 + \frac{1}{3}\left[\log\left(\frac{N}{H}\right) + \log\left(\frac{O}{H}\right) + \log\left(\frac{S}{H}\right)\right]. \quad (5.2)$$

Smith et al. (1993) notes that while individual abundance estimates may not be very precise using this method, mean abundances can be accurately derived[9].

Technically, λ6731/Hα ratios $\geq$ 0.55 saturate the [S II] line and should be excluded from any abundance determinations. However, for only one of the sources considered in this chapter – the known SMC SNR J005927-721010 – does this line ratio attain such a high value, namely 0.7, indicative of an enhanced oxygen abundance. But, inclusion of this value is felt to give the data, if anything, a more realistic upper limit.

Russell & Dopita (1990) presented abundance estimates of the Magellanic Clouds based primarily on an analysis of H II regions and a limited number of SNRs. Table 8 (Russell & Dopita 1990) review average SMC and LMC H II region abundances found in the literature, including that for oxygen in units of log(O/H) + 12. Their oxygen abundance value of 8.13 ± 0.10 does compare reasonably to our value of 8.0 ± 0.3. Our estimate of nitrogen abundance is slightly higher (7.1 ± 0.3 vs. 6.55 ± 0.13). Comparison of log A 'metal' averages of our and their individual abundance values show they are very close (−4.1 ± 0.3 vs. −4.03 ± 0.10). Welty (2001) notes that on average, SMC stars and H II regions have metallicities 0.6 – 0.7 dex below solar values. This all agrees with our values for SMC SNRs within the limits of error given in Table 5.5.

5.5.4 SNR Evolution

Systematic variations in [N II]/Hα correlated with the density sensitive [S II] λ6716/λ6731 ratio in Galactic SNRs have been reported by Daltabuit, D'Odorico & Sabbadin (1976). The conclusion implied that both ratios are correlated with SNR diameters and could be used to map evolutionary trends. These relationships have been questioned by Smith et al. (1993) as originating from selection effects instead.

Fig. 5.5 shows a graph of [N II]/Hα ratios vs. λ6716/λ6731 ratios for our SMC SNR sample. No apparent

[9] The use of Fig. 8 (Dopita et al. 1984) requires an assumed ratio of oxygen to sulfur of 42.8.

linear trend can be seen; the polynomial regression coefficient of multiple determination, r^2, was 0.6[10]. In Fig. 5.6, we show abundance and density-sensitive ratios observed in our sample as a function of SNR diameter[11]. We see no significant linear correlation in any of these four plots; the best r^2 was 0.02 in the case of [S II]/Hα vs. diameter. Given our results, we agree with Smith et al. (1993) that intensity ratios tell little about SNR evolution.

5.6 Chapter Summary

The diverse nature of individual SNRs is most likely the result of their unique environment rather than evolutionary stage.

In this chapter, we have:

1. selected shocked regions from 11 of 16 known radio SNRs and 1 radio candidate SNR based on a [S II]/Hα ratio equal or greater than 0.4. All but one of these also have strong [O I] and [O II] lines.

2. confirmed the radio candidate J004100-733648 as a bona fide SNR.

3. calculated line ratios for SNR shocks based on line intensities, using these to estimate their electron density.

4. searched these spectra for 'other' emission lines, finding typical lines as reported by Fesen & Hurford (1996) for SNR shocks.

5. found average SMC 'metal' abundances, assuming shock velocities $\geq$ 80 km s^{-1}, which agree with values found in the literature based on different calculation methods, including H II region observations.

6. demonstrated that abundance and electron density sensitive line ratios do not show an evolutionary trend. Theory predicts and our values imply that these ratios are actually dependent on the swept-up ISM.

[10] A value of 1.0 gives a perfect explanation of the data.

[11] As discussed in Chapter 4 of this series we could find no statistical difference in radio and optical diameters of SMC SNRs as observed with present instrumentation.

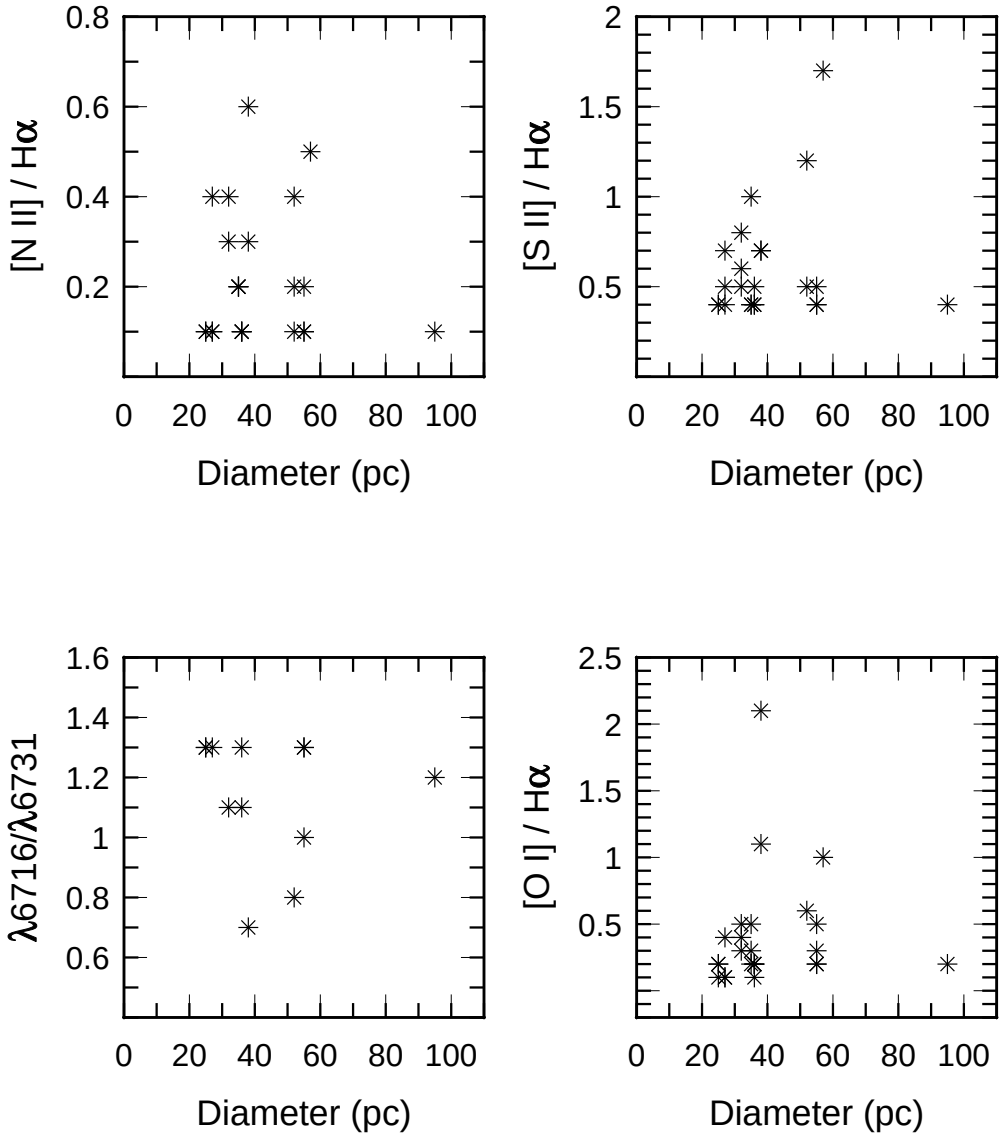

Figure 5.6 Comparisons of abundance and density sensitive line ratios to SNR diameters. Unphysical λ6716/λ6731 density ratios $\geq$ 1.4 and $\leq$ 0.5 have been excluded. Given r^2 values of 0.0004, 0.02, 0.03 and 0.008, respectively, we find that no obvious linear evolutionary trend is evident in any of these graphs.

Table 5.2 Other emission lines found for each extracted spectrum at Position Angles 0°and 90°. Strengths as compared to Hβ are listed in parentheses (1 = flux much greater than Hβ; 2 = flux about equal to Hβ; 3 = flux much less than Hβ). Although common in SMC SNRs, He I 3888.65 and H I 3889.05 are too close to be readily identified at a spectral resolution of 5 Å. Forbidden lines are in brackets [ ] and line reference is Fesen & Hurford (1996).

Position Angle 0°

Object	R.A.	Dec 1	Dec 2	Other Emission Lines (rest wavelength in Å)
				Confirmed SNRs
J004728-730601	00 47 28.6	–73 07 02.4	–73 06 35.6	
J004716-730811	00 47 16.1	–73 09 02.8	–73 08 34.0	Ca II λ3968.47 (3)
	00 47 16.1	–73 08 28.3	–73 07 25.9	Ca II λ3968.47 (3), He I λ5876 blend (3)
J004821-731931	00 48 21.2	–73 20 04.6	–73 19 17.6	
	00 48 21.2	–73 18 23.8	–73 18 11.3	
J004907-731402	00 49 07.1	–73 13 10.2	–73 12 51.0	Na I λ5889.95 (1)
J005110-732212	00 51 08.7	–73 22 12.8	–73 21 49.8	H I λ3835.38 (2), Hϵ λ3970.07 (2)
	00 51 08.7	–73 21 21.0	–73 20 57.0	Na I λ5889.95 (1)
J005240-723820	00 52 42.5	–72 36 47.1	–72 36 25.0	Na I λ5889.95 (1)
J005800-721101	00 58 00.0	–72 12 25.5	–72 11 51.9	
J005927-721010	00 59 27.4	–72 09 01.8	–72 08 45.5	[Ne III] λ3868.75 (2), Hϵ λ3970.07(3)
J010313-720958	01 03 15.3	–72 10 36.4	–72 10 12.4	Hϵ λ3970.07 (2), He I λ4026.19 (3), Na I λ5889.95 (3)
	01 03 15.3	–72 10 04.7	–72 09 50.3	He I λ3797.90 (3), H I λ3835.38 (3), [Ne III] λ3868.75 (3), Ca II λ3968.47 (2), He I λ4471.48, λ4471.69 (3)
J010619-720527	01 06 26.0	–72 05 37.5	–72 05 16.4	Ca II λ3968.47 (3), [S II] λ4068.60 (3), [S II] λ4076.35 (3)
				SNR Candidates
J004100-733648	00 41 06.5	–73 36 57.6	–73 36 49.0	
	00 41 06.5	–73 36 02.9	–73 35 49.4	

Position Angle 90°

Object	Dec	R.A. 1	R.A. 2	Other Emission Lines (rest wavelength in Å)
				Confirmed SNRs
J004637-730823	–73 08 37.0	00 46 25.5	00 46 30.4	[Ne III] λ3868.75 (3)
J004728-730601	–73 06 21.0	00 47 13.3	00 47 17.0	
	–73 06 21.0	00 47 21.9	00 47 27.8	
J004716-730811	–73 08 30.0	00 47 01.0	00 47 25.9	
J004821-731931	–73 19 36.0	00 48 35.9	00 48 39.9	
J004907-731402	–73 14 07.0	00 48 59.1	00 49 05.8	Na I λ5889.95 (1)
J005110-732212	–73 21 42.0	00 51 15.9	00 51 18.1	He I λ5876 blend (1), Na I λ5889.95 (1)
	–73 21 42.0	00 51 21.2	00 51 22.4	Ca II λ3968.47 (2), Na I λ5889.95 (1)
J010313-720958	–72 09 52.0	01 03 10.3	01 03 14.0	H I λ3750.15 (1), H I λ3770.63 (1), H I λ3797.90 (1), H I λ3835.38 (1), Ca II λ3933.66 (1), Ca II λ3968.47 (1)
J010619-720527	–72 05 27.0	01 06 03.0	01 06 11.9	[Ne III] λ3868.75 (3), Ca II λ3968.47 (3), He I λ5876 blend (3)
	–72 05 27.0	01 06 18.4	01 06 21.7	Ca II λ3968.47 (3), He I λ5876 blend (3)
				SNR Candidates
J004100-733648	–73 36 48.0	00 40 48.9	00 40 52.1	

Table 5.3 Extinction values based on Balmer decrements.

Position Angle 0°

Object Name (J2000)	Other Name (B1950)	R.A. (J2000)	Dec 1 (J2000)	Dec 2 (J2000)	E(B – V) based on Hα/Hβ	Hγ/Hβ	Hδ/Hβ
			Confirmed SNRs				
J004728-730601	B0045-733	00 47 28.6	–73 07 02.4	–73 06 35.6	0.2		
J004716-730811	B0045-734	00 47 16.1	–73 09 02.8	–73 08 34.0	0.7	–0.6	–1.0
		00 47 16.1	–73 08 28.3	–73 07 25.9	0.9	–0.4	0.1
J004821-731931	B0046-735	00 48 21.2	–73 20 04.6	–73 19 17.6	0.9	–0.2	–0.5
		00 48 21.2	–73 18 23.8	–73 18 11.3	1.7	–2.7	–2.1
J004907-731402	B0047-735	00 49 07.1	–73 13 10.2	–73 12 51.0			
J005110-732212	B0049-736	00 51 08.7	–73 22 12.8	–73 21 49.8	0.4	–2.0	–1.9
		00 51 08.7	–73 21 21.0	–73 20 57.0	0.3	–3.4	–4.0
J005240-723820	B0050-728	00 52 42.5	–72 36 47.1	–72 36 25.0	2.0		
J005800-721101	B0056-724	00 58 00.0	–72 12 25.5	–72 11 51.9	0.1	–1.6	–2.8
J005927-721010	B0057-724	00 59 27.4	–72 09 01.8	–72 08 45.5	–2.1	–1.3	–1.7
J010313-720958	B0101-724	01 03 15.3	–72 10 36.4	–72 10 12.4	–0.5	–2.2	–2.8
		01 03 15.3	–72 10 04.7	–72 09 50.3	0.1	–1.6	–1.9
J010619-720527	B0104-723	01 06 26.0	–72 05 37.5	–72 05 16.4	0.7	–0.3	–0.4
			SNR Candidates				
J004100-733648	B0039-735	00 41 06.5	–73 36 57.6	–73 36 49.0			
		00 41 06.5	–73 36 02.9	–73 35 49.4	–0.1	1.8	

Position Angle 90°

Object Name (J2000)	Other Name (B1950)	Dec (J2000)	R.A. 1 (J2000)	R.A. 2 (J2000)	E(B – V) based on Hα/Hβ	Hγ/Hβ	Hδ/Hβ
			Confirmed SNRs				
J004637-730823	B0044-734	–73 08 37.0	00 46 25.5	00 46 30.4	0.6	–0.4	
J004728-730601	B0045-733	–73 06 21.0	00 47 13.3	00 47 17.0	0.6		
		–73 06 21.0	00 47 21.9	00 47 27.8	1.0		
J004716-730811	B0045-734	–73 08 30.0	00 47 01.0	00 47 25.9	0.8	–0.3	–1.0
J004821-731931	B0046-735	–73 19 36.0	00 48 35.9	00 48 39.9			
J004907-731402	B0047-735	–73 14 07.0	00 48 59.1	00 49 05.8			
J005110-732212	B0049-736	–73 21 42.0	00 51 15.9	00 51 18.1			
		–73 21 42.0	00 51 21.2	00 51 22.4	0.8	–0.9	–2.4
J010313-720958	B0101-734	–72 09 52.0	01 03 10.3	01 03 14.0	–0.4	–4.0	–3.8
J010619-720527	B0104-723	–72 05 27.0	01 06 03.0	01 06 11.9	0.5	–0.3	–0.8
		–72 05 27.0	01 06 18.4	01 06 21.7	0.6	–0.5	–0.9
			SNR Candidates				
J004100-733648	B0039-735	–73 36 48.0	00 40 48.9	00 40 52.1			

Table 5.4 Selected line ratios and statistics. Wavelengths are laboratory values given in Å.

Position Angle 0°

Object Name	R.A. (J2000)	Dec 1 (J2000)	Dec 2 (J2000)	Rad. Velocity (km s^{-1})	2.37-GHz Diameter (pc)	[O III]/Hβ (λ4959 + λ5007)/λ4861	[O I]/Hα (λ6300 + λ6364)/λ6563	[N II]/Hα (λ6550 + λ6585)/λ6563	[S II]/Hα (λ6716 + λ6731)/λ6563	6731/Hα λ6731/λ6563	[S II] ratio λ6716/λ6731	Log ([O I]/Hβ)	Log ([O II]/Hβ)	Electron Density (cm^{-3})
						Confirmed SNRs								
J004728-730601	00 47 28.6	–73 07 02.4	–73 06 35.6	232.2 ± 51.2	52.0		0.6	0.4	1.2	0.5	1.4	0.3	1.2	< 100
J004716-730811	00 47 16.1	–73 09 02.8	–73 08 34.0	179.8 ± 35.0	36.0		0.1	0.1	0.4	0.2	1.3	–0.1	0.8	121
	00 47 16.1	–73 08 28.3	–73 07 25.9	189.4 ± 44.9	36.0	0.6	0.2	0.1	0.4	0.2	1.3	0.0	0.7	121
J004821-731931	00 48 21.2	–73 20 04.6	–73 19 17.6	216.0 ± 22.7	35.0		0.2	0.2	0.4	0.2	1.5	0.1	0.8	< 100
	00 48 21.2	–73 18 23.8	–73 18 11.3	282.9 ± 57.3	35.0		0.2	0.2	0.4	0.3	0.5	0.5	0.9	(a)
J004907-731402	00 49 07.1	–73 13 10.2	–73 12 51.0		38.0		1.1	0.3	0.7	0.2	2.3			< 100
J005110-732212	00 51 08.7	–73 22 12.8	–73 21 49.8	138.7 ± 37.1	55.0		0.2	0.1	0.5	0.2	1.3	–0.1	0.7	121
	00 51 08.7	–73 21 21.0	–73 20 57.0		55.0	3.3	0.5		0.4			0.3	0.9	
J005240-723820	00 52 42.5	–72 36 47.1	–72 36 25.0	184.9 ± 40.4	95.0		0.2	0.1	0.4	0.2	1.2	0.6	1.3	240
J005800-721101	00 58 00.0	–72 12 25.5	–72 11 51.9	72.3 ± 162.2	36.0	2.6	0.2	0.1	0.4	0.2	1.1	–0.3	0.3	395
J005927-721010	00 59 27.4	–72 09 01.8	–72 08 45.5	84.9 ± 49.8	57.0	5.8	1.0	0.5	1.7	0.7	1.6	–0.5	0.9	< 100
J010313-720958	01 03 15.3	–72 10 36.4	–72 10 12.4	220.9 ± 34.4	27.0		0.4	0.4	0.5	0.2	1.6	–0.2	–0.1	< 100
	01 03 15.3	–72 10 04.7	–72 09 50.3	188.0 ± 18.8	27.0	3.3	0.1	0.1	0.4	0.1	1.7	–0.3	0.7	< 100
J010619-720527	01 06 26.0	–72 05 37.5	–72 05 16.4	216.2 ± 25.1	25.0	0.3	0.2	0.1	0.4	0.2	1.3	0.0	0.4	121
						SNR Candidates								
J004100-733648	00 41 06.5	–73 36 57.6	–73 36 49.0		32.0		0.4	0.4	0.8	0.3	2.1			< 100
	00 41 06.5	–73 36 02.9	–73 35 49.4	107.5 ± 94.1	32.0		0.5	0.4	0.5	0.3	1.1	0.1		395

Position Angle 90°

Object Name	Dec (J2000)	R.A. 1 (J2000)	R.A. 2 (J2000)	Rad. Velocity (km s^{-1})	2.37-GHz Diameter (pc)	[O III]/Hβ (λ4959 + λ5007)/λ4861	[O I]/Hα (λ6300 + λ6364)/λ6563	[N II]/Hα (λ6550 + λ6585)/λ6563	[S II]/Hα (λ6716 + λ6731)/λ6563	6731/Hα λ6731/λ6563	[S II] ratio λ6716/λ6731	Log ([O I]/Hβ)	Log ([O II]/Hβ)	Electron Density (cm^{-3})
						Confirmed SNRs								
J004637-730823	–73 08 37.0	00 46 25.5	00 46 30.4	344.9 ± 45.0	35.0	1.9	0.3	0.2	0.4	0.2	1.7	0.2	0.8	< 100
J004728-730601	–73 06 21.0	00 47 13.3	00 47 17.0	274.3 ± 32.7	52.0			0.2	0.5	0.3	0.8		0.5	1 385
	–73 06 21.0	00 47 21.9	00 47 27.8	337.5 ± 40.8	52.0			0.1	0.5	0.2	1.4		1.0	< 100
J004716-730811	–73 08 30.0	00 47 01.0	00 47 25.9	325.7 ± 72.5	36.0		0.2	0.1	0.5	0.2	1.5	0.2	0.8	< 100
J004821-731931	–73 19 36.0	00 48 35.9	00 48 39.9		35.0		0.5	0.2	1.0	0.4	1.5			< 100
J004907-731402	–73 14 07.0	00 48 59.1	00 49 05.8		38.0		2.1	0.6	0.7	0.4	0.7			2 231
J005110-732212	–73 21 42.0	00 51 15.9	00 51 18.1	220.1 ± 64.8	55.0		0.2	0.1	0.4	0.2	1.3			121
	–73 21 42.0	00 51 21.2	00 51 22.4	289.2 ± 160.0	55.0	1.3	0.3	0.2	0.4	0.2	1.0	0.3	0.4	606
J010313-720958	–72 09 52.0	01 03 10.3	01 03 14.0		27.0	1.4	0.1	0.1	0.7	0.3	1.3	–0.6	0.8	121
J010619-720527	–72 05 27.0	01 06 03.0	01 06 11.9	297.3 ± 43.5	25.0	1.2	0.1	0.1	0.4	0.2	1.3	–0.1	0.7	121
	–72 05 27.0	01 06 18.4	01 06 21.7	293.8 ± 38.1	25.0	0.4	0.2	0.1	0.4	0.2	1.3	–0.1	0.4	121
						SNR Candidates								
J004100-733648	–73 36 48.0	00 40 48.9	00 40 52.1		32.0		0.3	0.3	0.6	0.2	1.7			< 100

Table 5.5 SMC SNR abundances based on the grid shown in Figure 8 of Dopita et al. (1984). (a) denotes that no line intensities are available for [N II] or λ6731.

Position Angle 0°

Object Name	R.A. (J2000)	Dec 1 (J2000)	Dec 2 (J2000)	N abundance log(N/H)+12	O abundance log(O/H)+12	"Metal" Abundance log A
			Confirmed SNRs			
J004728-730601	00 47 28.6	–73 07 02.4	–73 06 35.6	7.4	8.5	–3.6
J004716-730811	00 47 16.1	–73 09 02.8	–73 08 34.0	6.8	7.9	–4.2
	00 47 16.1	–73 08 28.3	–73 07 25.9	6.8	7.6	–4.4
J004821-731931	00 48 21.2	–73 20 04.6	–73 19 17.6	6.8	7.6	–4.4
	00 48 21.2	–73 18 23.8	–73 18 11.3	7.1	8.2	–3.9
J004907-731402	00 49 07.1	–73 13 10.2	–73 12 51.0	7.1	7.9	–4.1
J005110-732212	00 51 08.7	–73 22 12.8	–73 21 49.8	6.8	7.9	–4.2
	00 51 08.7	–73 21 21.0	–73 20 57.0	a	a	a
J005240-723820	00 52 42.5	–72 36 47.1	–72 36 25.0	6.8	7.9	–4.2
J005800-721101	00 58 00.0	–72 12 25.5	–72 11 51.9	6.8	7.9	–4.2
J005927-721010	00 59 27.4	–72 09 01.8	–72 08 45.5	8.0	9.1	–3.0
J010313-720958	01 03 15.3	–72 10 36.4	–72 10 12.4	7.4	7.9	–4.0
	01 03 15.3	–72 10 04.7	–72 09 50.3	6.8	7.6	–4.4
J010619-720527	01 06 26.0	–72 05 37.5	–72 05 16.4	6.8	7.9	–4.2
			SNR Candidates			
J004100-733648	00 41 06.5	–73 36 57.6	–73 36 49.0	7.4	8.2	–3.8
	00 41 06.5	–73 36 02.9	–73 35 49.4	7.4	8.2	–3.8

Position Angle 90°

Object Name	Dec (J2000)	R.A. 1 (J2000)	R.A. 2 (J2000)	N abundance log(N/H)+12	O abundance log(O/H)+12	"Metal" Abundance log A
			Confirmed SNRs			
J004637-730823	–73 08 37.0	00 46 25.5	00 46 30.4	7.1	7.6	–4.3
J004728-730601	–73 06 21.0	00 47 13.3	00 47 17.0	7.1	8.2	–3.9
	–73 06 21.0	00 47 21.9	00 47 27.8	6.8	7.9	–4.2
J004716-730811	–73 08 30.0	00 47 01.0	00 47 25.9	6.8	7.9	–4.2
J004821-731931	–73 19 36.0	00 48 35.9	00 48 39.9	7.1	8.5	–3.7
J004907-731402	–73 14 07.0	00 48 59.1	00 49 05.8	7.7	8.5	–3.5
J005110-732212	–73 21 42.0	00 51 15.9	00 51 18.1	6.8	7.9	–4.2
	–73 21 42.0	00 51 21.2	00 51 22.4	7.1	7.9	–4.1
J010313-720958	–72 09 52.0	01 03 10.3	01 03 14.0	7.1	8.2	–3.9
J010619-720527	–72 05 27.0	01 06 03.0	01 06 11.9	6.8	7.9	–4.2
	–72 05 27.0	01 06 18.4	01 06 21.7	6.8	7.9	–4.2
			SNR Candidates			
J004100-733648	–73 36 48.0	00 40 48.9	00 40 52.1	7.1	7.9	–4.1

Average Abundances

SNR Sample	N abundance log(N/H)+12	O abundance log(O/H)+12	"Metal" Abundance log A
SMC SNRs (This work)	7.1	8.0	–4.1
Standard deviation	0.3	0.3	0.3
SMC H II Regions based on Russell & Dopita (1990)	6.55	8.13	–4.03
Standard deviation	0.13	0.10	0.10
Galactic SNRs based on Fesen et al. (1985)	7.94	8.84	–3.18
Standard deviation	0.25	0.28	0.29

CHAPTER 6

FINAL SUMMARY AND CONCLUSIONS

Observations in this thesis have focused on the selection of radio SNRs that have the required properties in that domain with co-identifications in the optical and X-ray. Because X-ray and radio emission are expected to occur in a denser ISM, it is not surprising most of these are embedded in star forming locations including H II regions and OB Associations. We find two microquasar and two radio planetary nebulae candidates in the SMC, and one microquasar candidate in NGC 300. Followup observations reveal these objects are also intimately associated with the local ISM and will be the subject of future papers.

In NGC 300, analysis of ATCA and VLA images reveal a total of 18 radio SNRs; all associated with HII regions, OB associations or both. One of these have no optical component, while only 3 have X-ray counterparts. The latter situation is most likely due to sensitivity limitations of current X-ray telescopes. The luminosity function of these sources does suggest the sample is not complete. Unfortunately, not much can be said about their evolutionary stage since it was not yet possible to resolve radio diameters at the distance of 2.02 Mpc.

The selection criteria discern an additional 3 radio SNR candidates, 3 background sources and at least 2 background candidates. Ten other sources could be background sources, but currently are confused with SNRs or H II regions.

Since the SMC is much closer ($\sim$ 65 kpc), here we have a more complete sample of radio SNRs, a finding verified by their luminosity function. Using a selection criteria similar to that for NGC 300, we verify 16 previously confirmed radio SNRs and identify five new candidates. One of these candidates is confirmed by optical spectroscopy. Here, it is possible to include morphology and extension (diameter) in the selection criteria.

Only one of these radio candidates have no optical or X-ray emission detection; none are remotely isolated from an H II region. Difference images of selected H II regions also support this finding. Most are the result of Type II SNe; however, at least four may have Type Ia SNe progenitors as shown in Table 4.1.

Our instrumentation could not discern major differences in diameters between SNRs in radio, optical and X-ray. Radio observations may not always include the entire source, complicating boundary and flux density measurements. This may cause errors in spectral index determination.

This is especially true in H II regions, where radio and optical diameters do not match at all. Most radio diameters cluster at the radio resolution, whereas optical diameters are much more diverse. This makes

determination of spectral index for these sources unreliable, since their boundaries are very uncertain.

We find the location of background sources to be fairly uniform across the SMC, with an 81% correlation to the expected number (Wall 1994). Because of improved sensitivity and resolution, these sources have spectral indices steeper on average than previous studies. However, these spectral indices also have a wide range, presumably due to contamination with H II regions or confusion with H II compact sources.

Observed SMC SNRs appear fairly well evolved; a histogram of SNRs diameter suggests most are in the adiabatic stage or beyond. This is also evident in the integral number-diameter relation, $N(\leq D) \propto D$, whose slope has a bimodal character. This suggests there exists one population of SNRs in their adiabatic stage and another in a more advanced 'snowplow' or mixing phase.

Despite the fact that these remnants are in similar phases of evolution, which may be related to diameter, there does not appear to be a clear diameter relation to surface brightness, density or abundance. Using the swept-up mass relation given in equation 5.1, the smallest possible SNR radius of $\sim$ 9 pc (SMC SNR J010402-720149) implies a mass of $\sim$ 87 $M_{\odot}$. This is greater than 200 $M_{\odot}$ if one consider only remnants with available spectra (Chapter 5). This is unlikely to represent the mass of the progenitor star's ejecta, but may explain why abundance determinations average to the metallicity of the SMC.

Thus, the results in this thesis are consistent with the idea that most currently observable extragalactic radio SNRs are formed within star forming regions. Massive progenitor stars are created in this relatively dense ISM that eventually become mature SNRs. In the case of the SMC, we find abundance estimates from their optical spectra to reflect on average those of the ISM proper.

BIBLIOGRAPHY

Chapter 1 and Appendix B

Aharonian F. A., Akhperjanian A. G., Aye K. -M., et al., 2004, Nature, 432, 75

Alves D. R., 2004, New Astronomy Reviews, 48, 659

Arbutina B., Urošević D., Stanković M., Tešić L., 2004, MNRAS, 350, 346

Arbutina B., Urošević D., 2005, MNRAS, 360, 76

Asvarov A. I., 2003, in Ostrowski M., Sikora M., eds., Proceedings, Particle Acceleration in Astrophysics. Astronomical Observatory of the Jagiellonian University, Cracow, Poland

Badenes C., Bravo E., Borkowski K. J., Domínguez I., 2003, ApJ, 593, 358

Ballet J., 2005, Proceedings, 35th COSPAR Scientific Assembly. Paris, France, p. 765

Bamba A., Yamazaki R., Ueno M., Koyama K., 2004, AdSpR, 33, 376

Barbon R., Ciatti F., Rosino L., 1979, A&A, 72, 287

Berkhuijsen E. M., 1986, A&A, 166, 257

Berkhuijsen E. M., 1987, A&A, 181, 398

Bhatnager S., 2001, Ph.D. Thesis, University of Pune

Blondin J. M., Wright E. B., Barkowski K. J., Reynolds S. P., 1998, ApJ, 500, 342

Blair W. P., Kirshner R. P., Chevalier R. A., 1981, ApJ, 247, 879

Blair W. P., Long K. S., 1997, ApJS, 108, 261

Blair W. P., Fesen R. A., Schlegel E. M., AJ, 121, 1497

Blair W. P., Ghavamian P., Sankrit R., Danforth C. W., 2006, ApJS, 165, 480

Branch D., Livio M., Yungelson L. R., Boffi F. R., Baron E., 1995, PASP, 107, 1019

Branch D., Benetti S., Kasen D. et al., 2002, ApJ, 566, 1005

Braun R., Walterbos R. A. M., 1993, A&AS, 98, 327

Carpano S., Wilms J., Schirmer M., Kendziorra E., 2004, Mem. S.A.It, 75, 486

Charles P. A., Seward F. D., 1995, Exploring the X-ray Universe. Cambridge University Press, Cambridge, UK, p. 66

Chevalier R. A., 1977, ARA&A, 15, 175

Chevalier R. A., Kirshner R. P., Raymond J. C., 1980, ApJ, 235, 186

Chevalier R. A., 1996, in McCray R., Wang Z., eds., Preceedings International Astronomical Union Colloquium 145, Supernovae and Supernova Remnants. Cambridge University Press, Cambridge, UK, p. 399

Chevalier R., 1998, Mem. S. A. It., 69, 977

Chu Y.-H., Kennicutt R. C., 1988, AJ, 96, 1874

Cioffi D. F., McKee C. F., Bertschinger E., 1988, ApJ, 334, 252

Clark D. H., Caswell J. L., 1976, MNRAS, 174, 267

Clayton D. D., Craddock W. L., 1965, ApJ, 142, 189

Cox D. P., 1972, ApJ, 178, 159

Daltabuit E., D'Odorico S., Sabbadin F., 1976, A&A, 52, 93

Danforth C. W., Sankrit R., Blair W. P. et al., 2003, ApJ, 586, 1179

Decourchelle A., Ellison D. C., SSRv, 99, 219

De Grus R., O'Connel R. W., Becker G. D., Chevalier R. A., Gallagher J. S. III, 2000, AJ, 119, 681

Deharveng L., Caplan J., Lequenx J., Azzopardi M., Breysacher J., Tarenghi M., Westerlund. B. 1988, A&AS, 73, 407

de Vaucouleurs G., de Vaucouleurs A., Corwin H. G., Jr., Buta R. J., Paturel G., Fouque´ P., 1991, Third Reference Catalogue of Bright Galaxies (RC3). Springer-Verlag, New York

Dickel J., D'Odorico S., Silverman A., 1985, AJ, 90, 414

Dickel J., Milne D. K., 1998, AJ, 115, 1057

Dickel J. R., 2005, in Sjouwerman L. O. Dyer K. K., eds., X-ray and Radio Connections. http://www.aoc.nrao.edu/events/xraydio , 2005xrrc.procE4.04D

Diehl R., Timmes F. X., 1998, PASP, 110, 637

D'Odorico S., Dopita M. A., and Benvenuti P., 1980, A&AS, 40, 67

Dulk G. A., Slee O. B., 1975, ApJ, 199, 61

Duric N., Viallefond F., Goss W. M., van der Hulst J. M., 1993, A&AS, 99, 217

Duric N., 2000, in Berkhuijsen E. M., Beck R., Walterbos R. A. M., eds. Proceedings 232. WE-Heraeus-Seminar 22 – 25 May 2000, Bad Honnef, Germany, p. 127

Duric N., 2000, in Berkhuijsen E. M., Beck R., Walterbos R. A. M., eds. Proceedings 232. WE-Heraeus-Seminar 22 – 25 May 2000, Bad Honnef, Germany, p. 179

Dunne B. C., Points S. C., Chu Y.-H., 2001, ApJS, 136, 119

Dwarkadas V., 2004, in Hoflich P., Kumar P., Wheeler J. C., eds., Cosmic explosions in three dimensions : asymmetries in supernovae and gamma-ray bursts. Cambridge University Press, Cambridge, UK, p. 74

Dwek E., Rice W. L., 1987, ApJ, 320, L27

Dyer K. K., 2001, Ph.D. Thesis, North Carolina State University

Dyer K. K., Reynolds S. P., Borkowski K. J., 2004, ApJ, 600, 752

Feast M. W., 1991, in Haynes R., Milne D., eds., Proceedings IAU Symposium 148, The Magellanic Clouds. Kluwer, Dordrecht, Germany, p. 1

Feast M., 1999, in Whitelock P., Cannon R., eds., Proceedings IAU Symposium 192, The Stellar Content of Local Group Galaxies. Astron. Soc. Pac., San Francisco, p. 51

Fesen R. A., Blair W. P., Kirshner R. P., 1985, ApJ, 292, 29

Fesen R. A., Hurford A. P., 1996, ApJS, 106, 563

Filipović M. D., Pietsch, W., Haynes R. F., et al., 1998a, A&AS, 127, 119

Filipović M. D., Haynes R. F., White G. L., Jones P. A., 1998b, A&AS, 130, 421

Filippenko A. V., Barth A. J., Bower G. C., Ho L. C., 1995, AJ, 110, 2261

Gaensler B. M., 2003, in Bandiera R., Maiolino R., Mannucci F., eds., Texas in Tuscany. XXI Symposium on Relativistic Astrophysics, Florence, Italy, 9 – 13 December 2002, World Scientific Publishing, Singapore, p. 297 – 304

Ghavamian P., Raymond J., Smith R. C., Hartigan P., 2001, ApJ, 547, 995

Ghavamian P., Blair W. P., Long K. S., Sasaki M., Gaetz T. J., Plucinsky P. P., 2005, AJ, 130, 539

Gordon S. M., Kirshner R. P., Duric N., Long K. S., 1993, ApJ, 418, 743

Gordon S. M., 1994, Ph.D. Thesis, University of New Mexico

Gordon S. M., Kirshner R. P., Long K. S., Blair W. P., Duric N., Smith R. C., 1998, ApJS, 117, 89

Gordon S. M., Duric N., Kirshner R. P., Goss W. M., Viallefond F., 1999, ApJS, 120, 247

Green D. A., 1988, in Araki et al., eds., Proceedings of Workshop, Supernova Shells and Their Birth Events. Springer-Verlag, Berlin, Germany

Green D. A., 1998, A Catalogue of Galactic Supernova Remnants. MRAO, UK (available on the WWW at http://www.mrao.cam.ac.uk/surveys/snrs/)

Green D. A., 2004, BASI, 32, 335

Greenhouse M. A., et al., 1997, ApJ, 476, 105

Guseinov O. H., Ankay A., Sezer A., Tagieva S. O., 2003, A&AT, 22, 273

Harkness R. P., Wheeler J. C., Margon B. et al., 1987, ApJ, 317, 355

Haberl F., Pietsch W., 1999, A&AS, 139, 277

Haberl F., Filipović M. D., Pietsch W., Kahabka P., 2000, A&AS, 142, 41

Haberl F., Pietsch W., 2001, A&A, 373, 438

Henize K. G., 1956, ApJS, 2, 315

Hodge P. W., 1969, ApJS, 157, 73

Hyman S. D., Lacey C. K., Weiler K. W., Van Dyk S. D., 2000, AJ, 119, 1711

Insertis F. M., Rees M. J., 1991, MNRAS, 252, 82

Iyudin A. F. et al., 1998, Nature, 396, 142

Jenkins L. P., Roberts T. P., Warwick R. S., Kilgard R. E., Ward M. J., 2004, MNRAS, 349, 404

Jones T. W., Rudnick L., Jun B-I. et al., 1998, PASP, 110, 125

Kassim N. E., 1989, ApJ, 347, 915

Kaufman M., Bash F. N., Kennicutt R. C., Hodge P. W., 1987, ApJ, 319, 61

Kong, A. K. H., Di Stefano, R. 2003, ApJ, 590, L13

Kong A. K. H., Sjouwerman L. O., Williams B. F., Garcia M. R., Dickel J. R., 2003, ApJ, 590, 21

Kong A. K. H., Sjouwerman L. O., Williams B. F., 2004, AJ, 128, 2783

Lacey C., Duric N., Goss W. M., 1997, ApJS, 109, 417

Lacey C. K., Lazio T. J. W., Kassim N. E., et al., 2001, ApJ, 559, 954

Lacey C. K., Duric N., 2001, ApJ, 560, 719

Lacey C. K., Goss W. M., Mizouni L. K., 2007, AJ, 133, 2156

Laming J. M., 2000, ApJS, 127, 409

Leibundgut B., 2000, A&ARv, 10, 179

Long K. S., Helfand D. J., Grabelsky D. A., 1981, ApJ, 248, 925

Long K. S., Blair W. P., Kirshner R. P., Winkler P. F., 1990, ApJS, 72, 61

Long K. S., 1996, in McCray R., Wang Z., eds., Proceedings International Astronomical Union Colloquium 145, Supernovae and Supernova Remnants. Cambridge University Press, Cambridge, UK, p. 349

Long K. S., Charles P. A., Blair W. P., Gordon S. M., 1996, ApJ, 466, 750

Longair M. S., 1992, High Energy Astrophysics. Cambridge University Press, Cambridge, UK, p. 76 – 79

Lucy L. B., 1991, ApJ, 383, 308

Magnier E. A. et al., 1995, A&AS, 114, 215

Magnier E. A., Primini F. A., Prins S., van Paradus J., Lewin W., 1997, ApJ, 490, 649

Mathewson D. S., Healey J. R., 1964, in Kerr F.J., Rodgers A. W., eds., Proceedings International Astronomical Union Symposium 20, The Galaxy and the Magellanic Clouds. Australian Academy of Sciences, Canberra, Australia, p. 283

Mathewson D. S., Clarke J. N., 1972, ApJ, 178, 105

Mathewson D. S., Clarke J. N., 1973a, ApJ, 180, 725

Mathewson D. S., Clarke J. N., 1973b, ApJ, 182, 697

Mathewson D. S., Ford V. L., Dopita M. A., Tuohy I. R., Long K. S., Helfand D. J., 1983a IAUS, 101, 541

Mathewson D. S., Ford V. L., Dopita M. A., Tuohy I. R., Long K. S., Helfand D. J., 1983b, ApJS, 51, 345

Mathewson D. S., Ford V. L., Dopita M. A., Tuohy I. R., Mills B. Y., Turtle A. J., 1984, ApJS, 55, 189

Mathewson D. S., Ford V. L., Tuohy I. R., Mills B. Y., Turtle A. J., Helfand D. J., 1985, ApJS, 58, 197

Matonick D. M., Fesen R. A., 1997, ApJS, 112, 49

Matonick D. M., Fesen R. A., Blair W. P., Knox S. L., 1997, ApJS, 113, 333

McDonald A. R., Muxlow T. W. B., Wills K. A., Pedlar A., Beswick R. J., 2002, MNRAS, 334, 912

McGee R. X., Newton L. M., 1972, Aust. J. Phys., 29, 329

McKee C. F., Ostriker J. P., 1977, ApJ, 218, 148

Meikle W. P. S., Spyromilio J., Allen D. A., Varani G. -F., Cumming R. J., 1993, MNRAS, 261, 535

Minkowski R., 1941, PASP, 53, 224

Motizuki Y., Kumagai S., 2004, NewAR, 48, 69

Muxlow T. W. B., Pedlar A., Wilkinson P. N., Axon D. J., Sanders E. M., de Bruyn A. G., 1994, MNRAS, 266, 455

Paczyński B., 1998, ApJ, 494, 45

Pannuti T. G., Duric N., Lacey C K., Goss W. M., Hoopes C. G., Walterbos R. A. M., Magnor M., 2000, ApJ, 544, 780

Pannuti T. G., 2000, Ph.D. Thesis, University of New Mexico

Pannuti T. G., Duric N., Lacey C. K., Ferguson A. M. N., Magnor M. A., Mendelowitz C., 2002, ApJ, 565, 966

Pannuti T. G., Allen G. E., Houck J. C., Sturner S. J., 2003, ApJ, 593, 377

Pedlar A., Muxlow T. W. B., Garrett M. A., Diamond P., Wills K. A., Wilkinson P. N., Alef W., 1999, MNRAS, 307, 761

Pence W. D., Snowden S. L., Mukai K., Kuntz K. D., 2001, ApJ, 561, 189

Pohl M., 2001, ICRC, 27I, 147

Poveda A., Woltjer L., 1968, AJ, 73, 65

Rakowski C. E., 2005, AdSpR, 35, 1017

Reach W. T., Rho J., Tappe A., Pannuti T. G., et al., 2006, AJ, 131, 1479

Read, A. M., Ponman, T. J., Strickland, D. K. 1997, MNRAS, 286, 626

Read A. M., Pietsch W., 1999, A&A, 341, 8

Read, A. M., Pietsch, W. 2001, A&A, 373, 473

Reich W., 2002, in Becker W., Lesch H., Truṁper J., eds., Proceeding of 270 WE-Heraeus Seminar, Neutron Stars, Pulsars and Supernova Remnants. Max-Plank-Institut fuŕ extraterrestrische Physik, Garching bei Muñchen, Germany, p. 1

Reynolds S. P., 1988, in Verschuur G. L., Kellermann K. I., eds., Galactic and Extragalactic Radio Astronomy. Springer-Verlag, Berlin, Germany, p. 457

Reynolds S. P., Keohane J. W., 1999, ApJ, 525, 368

Reynolds S. P., 2005, in Sjouwerman L. O. Dyer K. K., eds., X-ray and Radio Connections. http://www.aoc.nrao.edu/events/xraydio , 2005xrrc.procE4.00R

Rho J., Petre R., 1998, ApJ, 503, 167

Rho J., Reach W., 2003, RevMexAA, 15, 263

Riley, J. D., Pedlar A., Muxlow T. W. B., McDonald A. R., Beswick R. J., Wills K. A., 2004, preprint (astro-ph/0405114)

Rohlfs K., Wilson T. L., 2004, Tools of Radio Astronomy. Springer-Verlag, Berlin, Germany

Rubin V. C., Kumar C. K., Ford W. K., 1972, ApJ, 177, 31

Saken J. M., Fesen R. A., Shull J. M., 1992, ApJS, 81, 715

Salter C. J., Brown R. L., 1988, in Verschuur G. L., Kellermann K. I., eds., Galactic and Extragalactic Radio Astronomy. Springer-Verlag, Berlin, Germany p. 1 – 34

Schlegel E. M., Pannuti T. G., 2003, AJ, 125, 3025

Schulman E., Bregman J. N., 1995, ApJ, 441, 568

Seaquist E. R., Stanković M., 2007, ApJ, 659, 347

Seward F. D., Mitchell M., 1981, ApJ, 243, 736

Shklovskii I. S., 1960, Sov. Astron.-AJ, 4, 243

Smith N., Weidong L., Foley R. J., et al., 2007, ApJ, 666, 1116

Smith R. C., Kirshner R. P., Blair W. P., Long K. S., Winkler P. F., 1993, ApJ, 407, 564

Smith R. C., Chu Y.-H., MacLow M.-M., oey M. S., Klein U., 1994, AJ, 108, 1266

Smith R. C. et al., 1998, PASA, 15, 163

Snowden S. L., Mukai K., Pence W., Kuntz K. D., AJ, 121, 3001

Stappers B. W., Gaensler B. M., Kaspi V. M., van der Klis M., Lewin W. H. G., 2003, Science, 299, 1372

Stephenson F. R., Green D. A., 2002, Historical Supernovae and their Remnants. Oxford University Press, Oxford, England, 34

Stevens I. R., Strickland D. K., Wills K. A., 1999, preprint (astro-ph/9909044)

Supper R. et al., 1997, A&A, 317, 328

Swartz D. A., Ghosh K. K., McCollough M. L., Pannuti T. G., Tennant A. F., Wu K., 2003, ApJS, 144, 213

Truelove J. K., McKee C. F., ApSS, 120, 299

Trushkin S. A., BSAO, 1998, 46, 62

Tully R. B., 1988, Nearby Galaxies Catalog, Cambridge, Cambridge University Press

Turner J. L., Ho P. T. P., 1994, ApJ, 421, 122

Turatto M., 2003, LNP, 598, 21

Urošević D., 2002, Serb. Astron. J., 165, 27

Urošević D., 2003, ApSS, 283, 75

Urošević D., Pannuti T. G., Duric N., Theodorou A., 2005, A&A, 435, 437

van den Bergh S., 1988, PASP, 100, 1486

van der Swaluw E., 2001, Ph.D. Thesis, Universiteit Utrecht

van der Heyden K. J., Bleeker J. A. M., Kaastra J. S., 2004, A&A, 421, 1031

Van Dyk S. D., 1992, AJ, 103, 1788

Vink J., 2004a, NuPhS, 132, 21

Vink J., 2004b, AdSpR, 33, 356

Walterbos R. A. M., Braun R., 1992, A&AS, 92, 625

Wang Q. D., 1999, ApJ, 517, 27

Weiler K. W., 1983, The Observatory, 103, 85

Weiler K. W., Sramek R. A., 1988, ARA&A, 26. 295

Weiler K. W., Panagia N., Montes M. J., Sramek R. A., 2002, ARA&A, 40, 387

Weisskopf M. C., Brinkman B., Canizares C., et al., PASP, 114, 1

Wright M., Dickel J., Koralesky B., Rudnick L., 1999, ApJ, 518, 284

Westerlund B. E., 1997, The Magellanic Clouds. Cambridge University Press, Cambridge, UK

White G. L., Malin D. F., Lee S. et al., 1987, IAUC, 4327, 1

Whiteoak J. B. Z., Green A. J., 1996, A&AS, 118, 329

Williams B. F., Schmitt M. D., Winkler P. F., 1995, BAAS, 27, 883

Williams B. F., Sjouwerman L. O., Kong A. K. H., Gelfand J. D., Garcia M. R., Murray S. S., 2004, ApJ, 615, 720

Williams, R. M., Ph.D. Thesis, University of Illinois

Williams, R. M., Chu Y.-H., Dickel J. R., Petre R., Smith R. C., Tavarez M., 1999, ApJS, 123, 467

Williams, R., Chu Y.-H., Dickel J., Smith R. C., Milne D., Winkler P. F., 1999, ApJ, 514, 798

Williams R. M., Chu Y. -H., Gruendl R., 2006, AJ, 132, 1877

Wills K. A., Pedlar A., Muxlow T. W. B., Wilkinson P. N., 1997, MNRAS, 291, 517

Woltjer L., 1972, ARA&A, 10, 129

Xu J.-W., Zhang X.-Z., Hau J.-L., 2005, ChJAA, 5, 165

Ye T., 1988, Ph.D. Thesis, Sydney University

Ye T., Turtle A. J., Kennicutt R. C., 1991, MNRAS, 249, 722

Yusef-Zadeh F., Wardle M., Rho J., Sakano M., 2003, ApJ, 585, 319

Zombeck M. V., 1990, Handbook of Astronomy and Astrophysics (second edition). Cambridge University Press, Cambridge, UK

Chapter 2

Blair W. P., Long K. S., 1997, ApJS, 108, 261 (BL97)

Braun R., Walterbos R. A. M., 1993, A&AS, 98, 327

Chen C. H. R., Chu Y.-H., 1998, AAS, 193.7405C

Deharveng L., Caplan J., Lequenx J., Azzopardi M., Breysacher J., Tarenghi M., Westerlund B., 1988, A&AS, 73, 407

Dyer K. K., Reynolds S. P., 1999, ApJ, 526, 365

Dubus G., 2003, in Combes F., Barret D., Contini T., eds., Semaine de l'Astrophysique Française, EdP-Sciences, Conference Series. Bordeaux, France, 202

Dunne B. C., Points S. C., Chu Y., 2001, ApJS, 136, 119

Ehle M., et al., 2003, *XMM-Newton* Users' Handbook. http://xmm.vilspa.esa.es/

Filipović M. D., Haynes,R. F., White G. L., Jones P. A., 1998, A&AS, 130, 421

Freedman W. L., Madore B. F., Gibson B. K., et al., 2001, ApJ, 553, 47F

Gooch R., 1996, ADASS, 5, 80

Gordon S. M., Kirschner R. P., Long K. S., Blair W. P., Duric N., Smith R. C., 1998, ApJS, 117, 89

Gordon S. M., Duric N., Kirshner R. P., Goss W. M., Viallefond F., 1999, ApJS, 120, 247

Greisen E. W., 2003, in Heck A. ed., AIPS, the VLA and the VLBA, Information Handling in Astronomy - - Historical Vistas. Kluwer Academic Publishers, Dordrech, 285, 109

Haberl F., Filipović M. D., Pietsch W., Kahabka P., 2000, A&AS, 142, 41

Kim S. C., Sung H., Lee M. G., 2002, JKAS, 35, 9

Kong A. K. H., Di Stefano R., 2003, ApJ, 590, L13

Koyama K., Kinugasa K., Matsuzaki K., Nishiuchi M., Sugizaki M., Torii K., Yamauchi S., Aschenbach B., 1997, PASJ, 49L, 7K

Lacey C. K., Duric N., 2001, ApJ, 560, 719

Loiseau N., 2003, Users' Guide to the *XMM-Newton* Science Analysis System. http://xmm.vilspar.esa.es/

Mitchell K. J., Condon J. J., 1985, AJ, 90, 1957

McGee R. X., Newton L. M., 1972, Aust. J. Phys., 25, 619

Pannuti T. G., Duric N., Lacey C. K., Goss W. M., Hoopes C. G., Walterbos R. A. M., Magnor M. A., 2000, ApJ, 544, 780

Pannuti T. G., Duric N., Lacey C. K., Ferguson A. M. N., Magnor M. A., Mendelowitz C., 2002, ApJ, 565, 966

Pietrzyński G., Gieren W., Fouqué P., Pont F., 2001, A&A, 371, 497

Read A. M., Pietsch W., 2001, A&A, 373, 473

Read A. M., Ponman T. J., Strickland D. K., 1997, MNRAS, 286, 626

Sault B., Killeen N., 2003, MIRIAD users Guide. Australia Telescope National Facility

Soffner T., Meńdez R. H., Jacoby G. H., Ciardullo R., Roth M. M., Kudritzki R. P., 1996, A&A, 306, 9S

Tully R., 1988, Nearby Galaxies Catalog. Cambridge University Press, Cambridge

Trümper J., 1982, Adv. Space Res., 2, 241

Williams R. M., Chu Y.-H., Dickel J. R., Petre R., Smith R. C., Tavarez M., 1999, ApJS, 123, 467

Chapter 3

Bock D. C.-J., Large M. I., Sadler E. M., 1999, AJ, 117, 1578

Bruhweiler F. C., Klinglesmith D. A., Gull T. R., Sofia S., 1987, ApJ, 317, 152

Budding E., Jones K. L., Slee O. B., Watson L., 1999, MNRAS, 305, 966

Clarke J. N., Little A. G., Mills B. Y., 1976, Aust. J. Phys. Astrophys. Suppl., 40, 1

Crawford F., Kaspi V. M., Manchester R. N., Lyne A. G., Camilo F., DÁmico N., 2001, ApJ, 553, 367

Davies R. D., Elliott K. H., Meaburn J., 1976, Memoirs Royal Astron. Soc., 81, 89

Dgani R., Soker N., 1998, ApJ, 499, 83

Dickel J. R., Williams R. M., Carter L. M., Milne D. K., Petre R., Amy S. W., 2001, AJ, 122, 849

Dubus G., 2003, in Combes F., Barret D., Contini T., eds., SF2A-2003: Semaine de l'Astrophysique Française. EdP-Sciences, Les Ulis, p. 473

Feast M., 1999, in Whitelock P., Cannon R., eds., Proceedings IAU Symposium 192, The Stellar Content of Local Group Galaxies. Astron. Soc. Pac., San Francisco, p. 51

Filipović M. D., Jones P. A., White G. L., Haynes R. F., Klein U., Wielebinski R., 1997, A&AS, 121, 321

Filipović M. D., Haynes R. F., White G. L., Jones P. A., 1998, A&AS, 130, 421

Filipović M. D., Bohlsen T., Goldstein G., Reid W., Staveley-Smith L., Jones P. A., Nohejl K., 2002, MNRAS, 335, 1085 (Paper I)

Haberl F., Filipović M. D., Pietsch W., Kahabka P., 2000, A&AS, 142, 41

Henize K. G., 1956, ApJS, 2, 315

Hodge P. W., Snow T. P., 1975, AJ, 80, 9

Inoue H., Koyama K., Tanaka Y., 1983, in Danziger I. J., Gorenstein P., eds., Proceedings IAU Symposium 101, Supernova Remnants and their X-ray Emission. Reidel, Dordrecht, p. 535

Israel F. P., Johansson L. E. B., Lequeux J., et al., 1993, A&A, 276, 25

Jacoby G. H., DeMarco O., 2002, AJ, 123, 269

Kahabka P., Pietsch W., Filipović M. D., Haberl F., 1999, A&AS, 136, 81

Large M. I., Mills B. Y., Little A. G., Crawford D. F., Sutton J. M., 1981, MNRAS, 194, 693

Lorimer D. R., Yates J. A., Lyne A. G., Gould D. M., 1995, MNRAS, 273, 411

McGee R. X., Newton L. M., 1972, AuJPh, 25, 619

McGee R. X., Newton L. M., Butler P. W., 1976, AuJPh, 29, 329

McKibben Nail V., Whitney C. A., Wade C. M., 1953, Proceedings of the National Academy of Sciences, 39, 1168

Marx M., Dickey J. M., Mebold U., 1997, A&AS, 126, 325

Marx-Zimmer M., Herbstmeier U., Dickey J. M., Zimmer F., Staveley-Smith L., Mebold U., 2000, A&A, 354, 787

Meyssonnier N., Azzopardi M., 1993, A&AS, 102, 451

Morgan D. H., 1995, A&AS, 112, 445

Otrupcek R. E., Wright A. E., 1991, PASA, 9, 170

Rosado M., Coarer E., Georgelin Y. P., Viale A., 1993, in Baschek B., Klare G., Lequeux J., eds., Proceedings of the second European Meeting on the Magellanic Cloud 328, New Aspects of the Magellanic Cloud Research. Springer-Verlag, Berlin, p. 226

Sanduleak N., MacConnell D. J., Philip A. G. D., 1978, PASP, 90, 621

Sasaki M., Haberl F., Pietsch W., 2000, A&AS, 147, 75

Schwering P. B. W., Israel P. F., 1990, Atlas and Catalogue of Infrared Sources in the Magellanic Clouds. Kluwer, Dordrecht

Seward F. D., Mitchell M., 1981, ApJ, 243, 736

Sinnott R. W., 1988, NGC 2000. Cambridge University Press, Cambridge

Staveley-Smith L., Sault R. J., Hatzidimitroiu D., Kesteven M. J., McConnell D., 1997, MNRAS, 289, 225

Turtle A. J., Ye T., Amy S. W., Nicholls J., 1998, PASA, 15, 280

Wall J. V., 1994, AuJPh, 47, 625

Wang Q., Wu X., 1992, ApJS, 78, 391

Wright A. E., Griffith M., Burke B., Ekers R. D., 1994, ApJS, 91, 111

Ye T., 1988, PhD Thesis, Sydney University

Zijlstra A. A., van Hoof P. A. M., Chapman J. M., Loup C., 1994, A&A, 290, 228

Chapter 4

Aschenbach B., 1998, Nature, 396, 141

Amy S. W., Ball L., 1993, ApJ, 411, 761

Arbutina B., Urošević D., Stanković M., Tešić L., 2004, MNRAS, 350, 346

Bolatto A. D., Leroy A., Israel F. P., Jackson J. M., 2003, ApJ, 595, 167

Berkhuijsen E. M., 1987, A&A, 181, 398

Caplan J., Ye T., Deharveng L., Turtle A. J., Kennicutt R. C., 1996, A&A, 307, 403

Chu Y.-H., Kennicutt R. C., 1988, AJ, 95, 1111

Danforth C. W., Howk J. C., Fullerton A. W., Blair W. P., Sembach K. R. 2002, ApJS, 139, 81

Danforth C. W., Sankrit R., Blair W. P., Howk J. C., Chu Y. -H., 2003, ApJ, 586, 1179

Davies R. D., Elliott K. H., Meaburn J., 1976, MmRAS, 81, 89

Dickel J. R., Williams R. M., Carter L. M., Milne D. K., Petre R., Amy S. W., 2001, AJ, 122, 849

Dopita M. A., Tuohy I. R., Mathewson D. S., 1981, ApJ, 248, 105

Edge W. R. T., Coe M. J., Galache J. L., McBride V. A., Corbet R. H. D., Markwardt C. B., Laycock S., 2004, MNRAS, 353, 1286

Feast M., 1999, in Whitelock P., Cannon R., eds., Proceedings IAU Symposium 192, The Stellar Content of Local Group Galaxies. Astron. Soc. Pac., San Francisco, p. 51

Filipović M. D., Haynes R. F., White G. L., Jones P. A., 1998a, A&AS, 130, 421

Filipović M. D., Pietsch W., Haynes R. F. et al., 1998b, A&AS, 127, 119

Filipović M. D., Haberl F., Pietsch W., Morgan D. H., 2000, A&A, 353, 129

Filipović M. D., Bohlsen T., Goldstein G., Reid W., Staveley-Smith L., Jones P. A., Nohejl K., 2002, MNRAS, 335, 1085

Gaensler B. M., Hendrick S. P., Reynolds S. P., Borkowski K. J., 2003, ApJ, 594, 111

Gaetz T. J., Butt Y. M., Edgar R. J., Eriksen K. A., Plucinsky P. P., Schlegel E. M., Smith R. K., 2000, ApJ, 534, 47

Green D. A., 2004, Bull. Astr. Soc. India, 32, 335

Haberl F., Filipović M. D., Pietsch W., Kahabka P., 2000, A&AS, 142, 41

Hayashi I., Koyama K., Ozaki M., Miyata E., Tsunemi H., Hughes J. P., Petre R., 1994, PASJ, 46, 121

Henize K. G., 1956, ApJS, 2, 315

Hughes J. P., Smith R. C., 1994, AJ, 107, 1363

Inoue H., Koyama K., Tanaka Y., 1983, in Danziger I. J., Gorenstein P., eds., Proceedings IAU Symposium 101, Supernova Remnants and their X-ray Emission. Reidel, Dordrecht, p. 535

Kahabka P., Pietsch W., Filipović M. D., Haberl F., 1999, A&AS, 136, 81

Long K. S., 1983, in Danziger I. J., Gorenstein P., eds., Proceedings IAU Symposium 101, Supernova Remnants and their X-ray Emission. Reidel, Dordrecht, p. 525

Mathewson D. S., Clarke J. N., 1972, ApJ, 178, 105

Mathewson D. S., Clarke J. N., 1973, ApJ, 182, 697

Mathewson D. S., Ford V. L., Dopita M. A., Tuohy I. R., Long K. S., Helfand D. J., 1983, ApJS, 51, 345

Mathewson D. S., Ford V. L., Dopita M. A., Tuohy I. R., Long K. S., Helfand D. J., 1984, ApJS, 55, 189

Matonick D. M., Fesen R. A., 1997, ApJS, 112, 49

McGee R. X., Newton L. M., 1972, Aust. J. Phys., 25, 581

Mills B. Y., Little A. G., Durdin J. M., Kesteven M. J., 1982, MNRAS, 200, 1007

Mills B. Y., 1983, in Danziger I. J., Gorenstein P., eds., Proceedings IAU Symposium 101, Supernova Remnants and their X-ray Emission. Reidel, Dordrecht, p. 551

Mills B. Y, Turtle A. J., Little A. G., Durdin M. J., 1984, Aust. J. Phys., 37, 321

Milne D. K., Caswell J. L., Haynes R. F., 1980, 191, 469

Pannuti T. G., Duric N., Lacey C. K., Goss W. M., Hoopes C. G., Walterbos R. A. M., Magnor M. A., 2000, ApJ, 544, 780

Park S., Hughes J. P., Burrows D. N., Slane P. O., Nousek J. A., Garmire G. P., 2003, ApJ, 598, 95

Payne J. L., Filipović M. D., Reid W., Jones P. A., Staveley-Smith L., White G. L., 2004a, MNRAS, 355, 44

Payne J. L., Filipović M. D., Pannuti T. G., Jones P. A., Duric N., White G. L., Carpano S., 2004b, A&A, 425, 443

Rosado M., Le Coarer E., Georgelin Y. P., 1994, Rev. Mex. Astron. Astrofis., 29, 97

Sasaki M., Haberl F., Pietsch W., 2000, A&AS, 147, 75

Sasaki M., Stadlbauer T. F. X., Haberl F., Filipović M. D., Bennie P. J., 2001, A&A, 365, 237

Stanimirović S., Staveley-Smith L., Dickey J. M., Sault R. J., Snowden S. L., 1999, MNRAS, 302, 417

Staveley-Smith L., Sault R. J., Hatzidimitroiu D., Kesteven M. J., McConnell D., 1997, MNRAS, 289, 225

Testor G., Lortet M.-C., 1987, A&A, 178, 25

Trushkin S. A., 1998, BSAO, 46, 62

Tuohy I. R., Dopita M. A., Mathewson D. S., Long K. S., Helfand D. J., 1983, in Danziger I.J., Gorenstein P., eds., Proceedings IAU Symposium 101, Supernova Remnants and their X-ray Emission. Reidel, Dordrecht, p. 559

van der Heyden K. J., Bleeker J. A. M., Kaastra J. S., 2004, A&A, 421, 1031

Wang Q., Wu X., 1992, ApJS, 78, 391

Westerlund B. E., 1997a, The Magellanic Clouds. Cambridge University Press, Cambridge, p. 32

Westerlund B. E., 1997b, The Magellanic Clouds. Cambridge University Press, Cambridge, p. 91

Woltjer L., 1972, ARA&A, 10, 129

Ye T., 1988, PhD Thesis, Sydney University

Ye T., Turtle A. J., Kennicutt R. C., 1991, MNRAS, 249, 722

Ye T., 1992, MNRAS, 255, 32

Ye T., Amy S. W., Wang Q. D., Ball L., Dickel J., 1995, MNRAS, 275, 1218

Yokogawa J., Imanishi K., Tsujimoto M., Koyama K., Nishiuchi M., 2003, PASJ, 55, 161

Chapter 5

Blair W. P., Kirshner R. P., Chevalier R. A., 1982, ApJ, 254, 50

Blair W. P., Kirshner R. P., 1985, ApJ, 289, 582

Cheng K. P., Hintzen P., Smith E. P., Angione F., Talbert N., Collins N., Stecher T., 1993, in Hollenbach D. J., Thronson H. A., Shull J. M., eds., Proceedings Third Teton Summer School on Astrophysics, The Evolution of Galaxies and their Environment. NASA, Ames Research Center, Moffett Field, p. 38

Daltabuit E., D'Odorico S., Sabbadin F., 1976, A&A, 52, 93

Danforth C. W., Howk J. C., Fullerton A. W., Blair W. P., Sembach K. R. 2002, ApJS, 139, 81

De Robertis M. M., Dufour R., Hunt R., 1987, JRASC, 81, 195

Dopita M. A., Tuohy I. R., Mathewson D. S., 1981, ApJ, 248, 105

Dopita M. A., Binette L., D'Odorico S., Benvenuti P., 1984, ApJ, 276, 653

Feast M., 1999, in Whitelock P., Cannon R., eds., Proceedings IAU Symposium 192, The Stellar Content of Local Group Galaxies. Astron. Soc. Pac., San Francisco, p. 51

Fesen R. A., 1981, Ph.D. Thesis, University of Michigan

Fesen R. A., Blair W. P., Kirshner R. P., 1985, ApJ, 292, 29

Fesen R. A., Hurford A. P., 1996, ApJS 106, 563

Filipović M. D., Bohlsen T., Goldstein G., Reid W., Staveley-Smith L., Jones P. A., Nohejl K., 2002, MNRAS, 335, 1085

Haffner L. M., Reynolds R. J., Tufte S. L., 1999, ApJ, 523, 223

Huchtmeier W. K., Richter O. G., 1986, A&AS, 63, 323

Kurtz M. J., Mink D. J., 1998, PASP, 110, 934

Mathewson D. S., Ford V. L., Dopita M. A., Tuohy I. R., Mills B. Y., Turtle A. J., 1984, ApJS, 55, 189

Osterbrock D. E., Ferland G. J., 2006, Astrophysics of Gaseous Nebulae and Active Galactic Nuclei (second edition). University Science Books, Sausalito

Payne J. L., Filipović M. D., Reid W., Jones P. A., Staveley-Smith L., White G. L., 2004a, MNRAS, 355, 44

Reid W. A., Payne J. L., Filipović M. D., Danforth C. W., Jones P. A., White G. L., Staveley-Smith L., 2006, MNRAS, 367, 1379

Russell S. C., Dopita M. A., 1990, ApJS, 74, 93

Schlegel D. J., Finkbeiner D. P., Davis M., 1998, ApJ, 500, 525

Seward F. D., Williams R. M., Chu Y. -H., Dickel J. R., Smith R. C., Points S. D., 2006, ApJ, 640, 327

Smith R. C., Kirshner R. P., Blair W. P., Long K. S., Winkler P. F., 1993, ApJ, 407, 564

Stanimirović S., Staveley-Smith L., Dickey J. M., Sault R. J., Snowden S. L., 1999, MNRAS, 302, 417

Staveley-Smith L., Sault R. J., Hatzidimitroiu D., Kesteven M. J., McConnell D., 1997, MNRAS, 289, 225

Welty D. E., 2001, preprint (astro-ph/0110377)

APPENDIX A

CATALOGUE OF ATCA SMC SOURCES

Chapter 3 gave a sample of the catalogue listing 717 classified ATCA sources. Here, I include all sources in the catalogue and columns 1 – 15. The complete catalogue can be found at:

http://vizier.cfa.harvard.edu/viz-bin/VizieR?-source=J/MNRAS/355/44 .

Table 1 includes the following columns:

Column 1 – Our ATCA source number.

Column 2 – The group name; separate sources individually defined at one frequency but linked in a lower one.

Column 3 – The ATCA name based on Right Ascension and Declination; hours, minutes, seconds and degrees, minutes, seconds.

Column 4 – The J2000 positions.

Column 5 – Flux density at 408 MHz; from the MC4 (Clarke et al. 1976) catalogue.

Column 6 – Flux density at 843 MHz; from the SUMSS (Bock et al. 1999) catalogue.

Column 7 – Flux density at 843 MHz; from the MOST (Ye 1988) catalogue.

Column 8 – Flux density at 1.42 GHz; ATCA, this work.

Column 9 – Flux density at 2.37 GHz; ATCA, this work.

Column 10 – Flux density at 4.8 GHz; ATCA, this work.

Column 11 – Flux density at 8.64 GHz; ATCA, this work.

Column 12 – 0.1 – 4.0 keV X-ray luminosities in units of ergs s^{-1}; from X-ray catalogues listed in Table 3.1.

Column 13 – Spectral index and standard error.

Column 14 – Estimated flux density at 1 GHz based on spectral index.

Column 15 – Source type according to past work and here.

Table 1 Catalogue of the ATCA SMC sources.

1	2	3	4		5	6	7	8	9	10	11	12	13	14	15
ATCA	Group	ATCA	J2000		S_{408MHz} MC4	S_{843MHz} SUMSS	S_{843MHz} MOST	$S_{1.42GHz}$ ATCA	$S_{2.37GHz}$ ATCA	$S_{4.8GHz}$ ATCA	$S_{8.64GHz}$ ATCA	X-ray Luminosity	$\alpha \pm \Delta\alpha$	S_{1GHz} est.	Type (previous vs. here)
No.	Name	Name	R.A.	Dec	(Jy)	(Jy)	(Jy)	(Jy)	(Jy)	(Jy)	(Jy)	(ergs s^{-1})		(Jy)	
001		J002907-735348	00 29 07.33	–73 53 48.2		0.1222	0.1260	0.0571	0.0060				–2.80 0.37	0.088	BKG BKG
002		J003025-731813	00 30 25.00	–73 18 13.1		0.0569	0.0567		0.0030				–2.85 0.00	0.035	BKG BKG
003		J003036-735148	00 30 36.62	–73 51 48.4		0.0481	0.0417		0.0029				–2.65 0.07	0.028	BKG BKG
004		J003006-740011	00 30 06.35	–74 00 11.0		0.1048	0.0768	0.0763	0.0177				–1.45 0.35	0.079	BKG BKG
005		J003034-742914	00 30 34.83	–74 29 14.3	0.33	0.1766	0.1250	0.1134	0.0514				–1.00 0.11	0.133	BKG BKG
006		J003131-743032	00 31 31.52	–74 30 32.3		0.0465	0.0489	0.0233	0.0187				–0.95 0.12	0.039	BKG BKG
007		J003140-743448	00 31 40.41	–74 34 48.0		0.0940	0.0715	0.0555	0.0422				–0.65 0.12	0.073	BKG BKG
008		J003255-714549	00 32 55.29	–71 45 49.5		0.1039		0.0379	0.0084				–2.43 0.17	0.075	BKG BKG
009		J003252-722933	00 32 52.50	–72 29 33.7		0.0474	0.0485	0.0785	0.0368				–0.14 0.31	0.052	BKG bkg
010		J003232-730649	00 32 32.39	–73 06 49.7		0.1601	0.0732	0.1036	0.0467				–0.75 0.37	0.102	BKG BKG
011		J003242-733154	00 32 42.62	–73 31 54.6		0.0870	0.0846	0.0383	0.0202				–1.41 0.04	0.066	BKG BKG
012		J003234-734138	00 32 34.57	–73 41 38.9		0.0072			0.0066				–0.08 0.14	0.007	BKG bkg
013		J003208-735037	00 32 08.89	–73 50 37.9		0.0416	0.0446	0.0311	0.0088				–1.45 0.24	0.037	BKG BKG
014		J003249-741857	00 32 49.20	–74 18 57.5		0.0735	0.0720	0.0434	0.0276				–0.94 0.02	0.062	BKG BKG
015		J003314-705556	00 33 14.25	–70 55 56.9	0.34	0.1548		0.0439	0.0046				–2.38 0.38	0.062	BKG BKG
016		J003325-722343	00 33 25.05	–72 23 43.2					0.0014						BKG bkg
017		J003356-722843	00 33 56.98	–72 28 43.3		0.0323	0.0330	0.0280	0.0120				–0.91 0.18	0.030	BKG BKG
018		J003327-723719	00 33 27.81	–72 37 19.1		0.0237	0.0196		0.0036				–1.73 0.09	0.016	BKG BKG
019		J003347-731441	00 33 47.58	–73 14 41.3		0.0098			0.0013				–1.95 0.14	0.007	BKG BKG
020		J003310-740344	00 33 10.97	–74 03 44.0		0.0295	0.0187	0.0076	0.0118				–0.81 0.43	0.018	BKG BKG
021		J003305-742124	00 33 05.39	–74 21 24.1		0.0164	0.0153		0.0045				–1.22 0.03	0.013	BKG BKG
022		J003357-742323	00 33 57.57	–74 23 23.5		0.0455	0.0462	0.0344	0.0186				–0.84 0.08	0.041	BKG BKG
023		J003341-743054	00 33 41.15	–74 30 54.9		0.0223	0.0140	0.0162	0.0084				–0.67 0.24	0.017	BKG BKG
024		J003310-745519	00 33 10.74	–74 55 19.1		0.0394		0.0111	0.0115				–1.20 0.42	0.026	BKG BKG
025		J003426-715448	00 34 26.94	–71 54 48.2		0.0073			0.0022				–1.16 0.14	0.006	BKG BKG
026		J003454-713559	00 34 54.60	–71 35 59.2		0.0117			0.0023				–1.57 0.14	0.009	BKG BKG
027		J003424-721145	00 34 24.29	–72 11 45.7	0.47	0.2402	0.2360	0.1666	0.0748				–1.01 0.07	0.200	BKG BKG
028		J003435-722756	00 34 35.28	–72 27 56.1		0.0077			0.0035				–0.76 0.14	0.007	BKG BKG
029	0034-7333	J003413-733328	00 34 13.76	–73 33 28.4	1.16	0.5050	0.3530	0.4696	0.2127				–0.84 0.19	0.458	BKG BKG
030	0034-7333	J003426-733513	00 34 26.74	–73 35 13.4		0.2091	0.1550		0.0870				–0.70 0.15	0.160	BKG BKG
031		J003511-710957	00 35 11.29	–71 09 57.0		0.0837		0.0564	0.0187				–1.45 0.23	0.074	BKG BKG
032		J003536-714602	00 35 36.64	–71 46 02.9		0.0235		0.0133	0.0075				–1.11 0.00	0.020	BKG BKG
033		J003547-721116	00 35 47.93	–72 11 16.2		0.0091	0.0120		0.0034				–1.09 0.13	0.009	BKG BKG
034		J003530-723655	00 35 30.85	–72 36 55.5		0.0165	0.0129	0.0147	0.0167				0.12 0.11	0.015	BKG bkg
035		J003551-725303	00 35 51.88	–72 53 03.8		0.0368	0.0376	0.0332	0.0195				–0.59 0.11	0.035	BKG bkg
036		J003523-732224	00 35 23.98	–73 22 24.5		0.0396	0.0408	0.0180	0.0176				–0.87 0.19	0.032	BKG BKG
037		J003544-735210	00 35 44.67	–73 52 10.6		0.0224	0.0195	0.0099	0.0078				–1.00 0.14	0.017	BKG BKG
038		J003646-705312	00 36 46.30	–70 53 12.6		0.0078			0.0013				–1.73 0.14	0.006	BKG BKG
039		J003647-713609	00 36 47.34	–71 36 09.2		0.0319		0.0193	0.0125				–0.91 0.02	0.027	BKG BKG
040		J003659-713813	00 36 59.25	–71 38 13.6		0.0087		0.0262	0.0087				0.01 0.71	0.013	BKG bkg
041		J003625-714637	00 36 25.94	–71 46 37.5		0.0208		0.0125	0.0040				–1.59 0.21	0.018	BKG BKG
042		J003636-715126	00 36 36.64	–71 51 26.3		0.0083			0.0026				–1.12 0.14	0.007	BKG BKG
043		J003633-715143	00 36 33.78	–71 51 43.3				0.0548							BKG bkg
044	0036-7209	J003624-720853	00 36 24.45	–72 08 53.7		0.0358			0.0049				–1.92 0.14	0.026	BKG BKG
045	0036-7209	J003619-720951	00 36 19.24	–72 09 51.5		0.0501	0.0668	0.0585	0.0190				–0.97 0.31	0.054	BKG BKG
046		J003624-725344	00 36 24.37	–72 53 44.3		0.0157		0.0454	0.0263				0.50 0.52	0.022	BKG bkg
047		J003609-725401	00 36 09.60	–72 54 01.6		0.0098			0.0312				1.12 0.14	0.012	BKG bkg
048		J003608-742925	00 36 08.53	–74 29 25.0		0.0097			0.0016				–1.74 0.14	0.007	BKG BKG
049		J003653-744428	00 36 53.67	–74 44 28.7					0.0021						BKG bkg
050		J003703-704727	00 37 03.13	–70 47 27.0		0.0221		0.0117	0.0099				–0.78 0.15	0.018	BKG BKG

Table 1 Catalogue of the ATCA SMC sources.

1	2	3	4		5	6	7	8	9	10	11	12	13	14	15
ATCA	Group	ATCA	J2000		S_{408MHz} MC4	S_{843MHz} SUMSS	S_{843MHz} MOST	$S_{1.42GHz}$ ATCA	$S_{2.37GHz}$ ATCA	$S_{4.8GHz}$ ATCA	$S_{8.64GHz}$ ATCA	X-ray Luminosity	$\alpha \pm \Delta\alpha$	S_{1GHz} est.	Type (previous vs. here)
No.	Name	Name	R.A.	Dec	(Jy)	(Jy)	(Jy)	(Jy)	(Jy)	(Jy)	(Jy)	(ergs s^{-1})		(Jy)	
051		J003715-705641	00 37 15.73	–70 56 41.2		0.0091		0.0095	0.0101				0.10 0.01	0.009	bkg
052		J003743-710737	00 37 43.32	–71 07 37.0		0.0745		0.0616	0.0358				–0.71 0.12	0.070	BKG BKG
053		J003709-712111	00 37 09.31	–71 21 11.4		0.0121			0.0021				–1.69 0.14	0.009	BKG BKG
054		J003708-714001	00 37 08.88	–71 40 01.6		0.0360			0.0129				–0.99 0.14	0.030	BKG BKG
055		J003740-714109	00 37 40.26	–71 41 09.1					0.0013						BKG bkg
056		J003701-714907	00 37 01.80	–71 49 07.3		0.0106			0.0042				–0.90 0.14	0.009	BKG BKG
057		J003756-720602	00 37 56.09	–72 06 02.8				0.0098	0.0033				–2.13 0.28	0.021	BKG BKG
058		J003755-725203	00 37 55.22	–72 52 03.4	0.53	0.2815	0.2080	0.1735	0.0990				–0.92 0.09	0.220	BKG BKG
059		J003749-735128	00 37 49.93	–73 51 28.5		0.0195		0.0233	0.0133				–0.37 0.24	0.021	BKG bkg
060		J003717-751410	00 37 17.89	–75 14 10.4		0.0521		0.0253	0.0036				–2.58 0.40	0.041	BKG BKG
061		J003745-751202	00 37 45.49	–75 12 02.0				0.0462							BKG bkg
062		J003855-704940	00 38 55.91	–70 49 40.3		0.0061			0.0015				–1.36 0.14	0.005	BKG BKG
063		J003850-720851	00 38 50.40	–72 08 51.4		0.0097	0.0122	0.0462	0.0055				–0.34 0.89	0.014	BKG bkg
064		J003819-723419	00 38 19.42	–72 34 19.0		0.0193	0.0176	0.0233	0.0063				–0.90 0.39	0.018	BKG BKG
065		J003857-724853	00 38 57.99	–72 48 53.9					0.0019						BKG bkg
066		J003802-730435	00 38 02.02	–73 04 35.6				0.0117	0.0052				–1.58 0.28	0.020	BKG BKG
067		J003850-731059	00 38 50.59	–73 10 59.5		0.0129	0.0115	0.0307	0.0148				0.34 0.41	0.015	BKG bkg
068		J003809-735025	00 38 09.10	–73 50 25.3	0.36	0.2013	0.1910	0.1597	0.1013				–0.69 0.05	0.186	BKG BKG
069		J003824-742213	00 38 24.37	–74 22 13.5	0.71	0.4620	0.4340	0.2772	0.1599				–0.85 0.06	0.362	BKG BKG
070		J003805-745030	00 38 05.23	–74 50 30.7		0.0362		0.0166	0.0171				–0.73 0.26	0.028	BKG BKG
071		J003944-705250	00 39 44.04	–70 52 50.4		0.0429		0.0319	0.0206				–0.71 0.05	0.039	BKG BKG
072		J003951-705513	00 39 51.33	–70 55 13.2		0.0202			0.0030				–1.85 0.14	0.015	BKG BKG
073		J003947-713736	00 39 47.26	–71 37 36.4	0.54	0.1362	0.2320	0.0935	0.0551				–1.29 0.14	0.153	BKG BKG
074		J003939-714144	00 39 39.71	–71 41 44.3	0.47	0.1613	0.2770	0.0949	0.0497				–1.30 0.14	0.157	BKG BKG
075		J003927-715248	00 39 27.05	–71 52 48.6		0.0418		0.0246	0.0167				–0.89 0.04	0.035	BKG BKG
076		J003921-720355	00 39 21.40	–72 03 55.4				0.0123	0.0076				–0.94 0.28	0.017	BKG BKG
077	0039-7243	J003904-724338	00 39 04.43	–72 43 38.6		0.0140	0.0143	0.0088	0.0058				–0.87 0.02	0.012	BKG BKG
078	0039-7243	J003921-724313	00 39 21.93	–72 43 13.7		0.0075			0.0014				–1.62 0.14	0.006	BKG BKG
079		J003901-725731	00 39 01.24	–72 57 31.2		0.0157		0.0155	0.0050				–1.10 0.36	0.016	BKG BKG
080		J003942-735624	00 39 42.32	–73 56 24.3		0.0086	0.0117		0.0042				–0.84 0.15	0.009	BKG BKG
081		J003936-742018	00 39 36.19	–74 20 18.0		0.0299	0.0355		0.0138				–0.83 0.08	0.028	BKG BKG
082		J004028-703514	00 40 28.89	–70 35 14.3		0.0432		0.0231	0.0032				–2.51 0.44	0.035	BKG BKG
083		J004051-712200	00 40 51.62	–71 22 00.7		0.0099		0.0084	0.0030				–1.15 0.28	0.009	BKG BKG
084		J004047-714601	00 40 47.81	–71 46 01.1	1.04	0.5515	0.7670	0.4630	0.2951				–0.71 0.08	0.568	BKG BKG
085		J004023-723808	00 40 23.32	–72 38 08.6		0.0131	0.0116	0.0167	0.0085				–0.27 0.25	0.013	BKG bkg
086	0040-7336	J004050-733657	00 40 50.30	–73 36 57.5		0.1519		0.1581	0.0841	0.0525	0.0308		–0.74 0.08	0.161	BKG BKG
087	0040-7336	J004100-733648	00 41 00.10	–73 36 48.6	0.11		0.0608	0.0791	0.0455	0.0133	0.0062		–0.94 0.14	0.065	SNR snr
088		J004125-705745	00 41 25.37	–70 57 45.3		0.0660	0.0532	0.0672	0.0676				0.14 0.09	0.061	BKG bkg
089		J004133-711103	00 41 33.40	–71 11 03.0		0.0086	0.0123		0.0037				–0.99 0.17	0.009	BKG BKG
090		J004111-715902	00 41 11.61	–71 59 02.5		0.0119			0.0056				–0.73 0.14	0.011	BKG BKG
091		J004159-720511	00 41 59.49	–72 05 11.2				0.0334	0.0179				–1.22 0.28	0.051	BKG BKG
092		J004144-721823	00 41 44.47	–72 18 23.6					0.0014						BKG bkg
093		J004124-734708	00 41 24.31	–73 47 08.1		0.0076	0.0100		0.0021				–1.38 0.13	0.007	BKG BKG
094		J004123-740701	00 41 23.74	–74 07 01.0		0.0099	0.0116		0.0029				–1.26 0.08	0.009	BKG BKG
095		J004153-743336	00 41 53.85	–74 33 36.0		0.0083			0.0030				–0.98 0.14	0.007	BKG BKG
096		J004205-711725	00 42 05.32	–71 17 25.3		0.0258		0.0124	0.0129				–0.67 0.25	0.020	BKG BKG
097		J004209-721446	00 42 09.08	–72 14 46.4		0.0176	0.0167	0.0081	0.0070				–0.92 0.15	0.014	BKG BKG
098		J004211-722510	00 42 11.42	–72 25 10.5					0.0026						bkg bkg
099		J004239-723324	00 42 39.10	–72 33 24.7		0.0171	0.0205	0.0100	0.0095				–0.71 0.16	0.016	BKG BKG
100		J004216-725910	00 42 16.79	–72 59 10.5					0.0026						HII hii

Table 1 Catalogue of the ATCA SMC sources.

1	2	3	4		5	6	7	8	9	10	11	12	13	14	15
ATCA	Group	ATCA	J2000		S_{408MHz} MC4	S_{843MHz} SUMSS	S_{843MHz} MOST	$S_{1.42GHz}$ ATCA	$S_{2.37GHz}$ ATCA	$S_{4.8GHz}$ ATCA	$S_{8.64GHz}$ ATCA	X-ray Luminosity	$\alpha \pm \Delta\alpha$	S_{1GHz} est.	Type (previous vs. here)
No.	Name	Name	R.A.	Dec	(Jy)	(Jy)	(Jy)	(Jy)	(Jy)	(Jy)	(Jy)	(ergs s^{-1})		(Jy)	
101		J004226-730419	00 42 26.16	–73 04 19.0	0.26	0.1497	0.1490	0.0904	0.0500				–0.94 0.05	0.121	BKG BKG
102		J004202-730722	00 42 02.26	–73 07 22.7	0.48	0.2473	0.1490	0.1696	0.0920				–0.87 0.16	0.193	BKG BKG
103		J004219-731047	00 42 19.33	–73 10 47.3		0.0308	0.0114	0.0143	0.0117				–0.46 0.41	0.017	B/H B/H
104		J004213-740325	00 42 13.61	–74 03 25.7					0.0026						BKG bkg
105		J004230-742846	00 42 30.97	–74 28 46.5		0.0136	0.0148		0.0053				–0.95 0.04	0.012	BKG BKG
106		J004229-745452	00 42 29.80	–74 54 52.3				0.0044	0.0054				0.40 0.28	0.004	bkg
107		J004226-751357	00 42 26.81	–75 13 57.3		0.0757		0.0503	0.0070				–2.30 0.51	0.066	BKG BKG
108		J004328-704143	00 43 28.76	–70 41 43.1	1.58	0.7775		0.6048	0.2230				–1.05 0.13	0.663	BKG BKG
109		J004334-705519	00 43 34.39	–70 55 19.6		0.0507	0.0398	0.0269	0.0130				–1.18 0.11	0.037	BKG BKG
110		J004312-710422	00 43 12.11	–71 04 22.1		0.0559	0.0449	0.0431	0.0283				–0.53 0.11	0.047	BKG bkg
111		J004341-711522	00 43 41.45	–71 15 22.3		0.0124	0.0117		0.0031				–1.31 0.03	0.010	BKG BKG
112		J004341-712230	00 43 41.20	–71 22 30.5					0.0051						BKG bkg
113		J004334-713204	00 43 34.03	–71 32 04.8		0.0524	0.0431	0.0326	0.0211				–0.78 0.08	0.042	BKG BKG
114		J004318-714059	00 43 18.04	–71 40 59.5			0.0486	0.0281	0.0152				–1.12 0.03	0.041	BKG BKG
115		J004339-720347	00 43 39.90	–72 03 47.2		0.0622		0.0392	0.0192				–1.14 0.09	0.053	BKG BKG
116		J004331-721025	00 43 31.49	–72 10 25.3		0.0220	0.0251	0.0184	0.0131				–0.56 0.06	0.022	BKG bkg
117		J004336-730223	00 43 36.65	–73 02 23.6					0.0056						bkg PN
118		J004348-732319	00 43 48.48	–73 23 19.4		0.0190	0.0158	0.0466	0.0073				–0.58 0.71	0.020	BKG bkg
119		J004346-732554	00 43 46.41	–73 25 54.7		0.0410	0.0627		0.0162				–1.10 0.21	0.042	BKG BKG
120		J004306-732827	00 43 06.19	–73 28 27.9		0.0293	0.0296	0.0392	0.0144				–0.58 0.32	0.030	BKG bkg
121		J004317-735516	00 43 17.73	–73 55 16.2		0.0114	0.0100		0.0029				–1.26 0.06	0.009	BKG BKG
122		J004318-742719	00 43 18.16	–74 27 19.9				0.0485							bkg bkg
123		J004452-704844	00 44 52.95	–70 48 44.2		0.0296	0.0328	0.0277	0.0108				–0.95 0.21	0.029	BKG BKG
124		J004459-711440	00 44 59.73	–71 14 40.3		0.0395		0.0274	0.0181				–0.76 0.02	0.035	BKG BKG
125		J004414-724302	00 44 14.01	–72 43 02.6		0.0218	0.0299	0.0290	0.0176				–0.30 0.20	0.026	BKG bkg
126		J004457-731010	00 44 57.46	–73 10 10.9				0.0109	0.0117	0.0024	0.0037		–0.81 0.29	0.016	HII hii
127		J004343-732941	00 43 43.91	–73 29 41.6				0.0032	0.0020				–0.92 0.28	0.004	BKG BKG
128		J004414-733318	00 44 14.86	–73 33 18.1		0.0070			0.0045				–0.43 0.14	0.007	BKG bkg
129		J004438-733703	00 44 38.95	–73 37 03.9		0.0200	0.0296	0.0246	0.0091				–0.86 0.30	0.023	BKG BKG
130		J004452-734538	00 44 52.01	–73 45 38.6		0.0325	0.0345	0.0219	0.0161				–0.72 0.04	0.029	BKG BKG
131		J004421-744316	00 44 21.57	–74 43 16.5		0.0372		0.0209	0.0143				–0.93 0.06	0.031	BKG BKG
132		J004416-750219	00 44 16.51	–75 02 19.8		0.0143		0.0179	0.0130				–0.09 0.18	0.015	BKG bkg
133		J004555-704646	00 45 55.45	–70 46 46.9		0.0227			0.0091				–0.88 0.14	0.020	BKG BKG
134		J004501-710257	00 45 01.20	–71 02 57.6					0.0027						BKG bkg
135		J004535-712315	00 45 35.43	–71 23 15.8		0.0348	0.0367	0.0254	0.0132				–0.94 0.08	0.031	BKG BKG
136		J004548-714932	00 45 48.59	–71 49 32.8		0.0096			0.0061				–0.44 0.14	0.009	Bkg bkg
137		J004504-715612	00 45 04.31	–71 56 12.2		0.0124	0.0387	0.0086	0.0074				–1.12 0.51	0.017	BKG BKG
138		J004534-720403	00 45 34.75	–72 04 03.0		0.0090	0.0138		0.0038				–1.04 0.21	0.009	BKG BKG
139		J004548-724138	00 45 48.54	–72 41 38.1					0.0029						BKG bkg
140		J004530-730453	00 45 30.78	–73 04 53.6				0.0350	0.0874	0.0625	0.0559		0.15 0.23	0.047	HII HII
141		J004554-730645	00 45 54.57	–73 06 45.9					0.0165						HII hii
142		J004552-731339	00 45 52.33	–73 13 39.1					0.0078						BKG bkg
143		J004522-731520	00 45 22.33	–73 15 20.2				0.0103	0.0301	0.0057	0.0011		–1.41 0.51	0.038	BKG BKG
144		J004501-731647	00 45 01.96	–73 16 47.3				0.0098	0.0122	0.0024	0.0044		–0.69 0.33	0.014	HII hii
145		J004523-732250	00 45 23.62	–73 22 50.4				0.0902	0.6255	0.0389	0.0422		–0.90 0.68	0.300	HII hii
146		J004529-745058	00 45 29.28	–74 50 58.6		0.0130		0.0122	0.0074				–0.54 0.14	0.013	BKG bkg
147		J004529-750135	00 45 29.10	–75 01 35.1					0.0018						BKG bkg
148		J004632-705858	00 46 32.03	–70 58 58.6		0.0485	0.0513	0.0560	0.0323				–0.36 0.17	0.050	BKG bkg
149		J004622-710042	00 46 22.61	–71 00 42.1		0.0147	0.0149		0.0059				–0.89 0.01	0.013	BKG BKG
150		J004616-711615	00 46 16.66	–71 16 15.4		0.0169	0.0120	0.0055	0.0033				–1.45 0.18	0.011	BKG BKG

Table 1 Catalogue of the ATCA SMC sources.

1	2	3	4		5	6	7	8	9	10	11	12	13	14	15
ATCA	Group	ATCA	J2000		S_{408MHz} MC4	S_{843MHz} SUMSS	S_{843MHz} MOST	$S_{1.42GHz}$ ATCA	$S_{2.37GHz}$ ATCA	$S_{4.8GHz}$ ATCA	$S_{8.64GHz}$ ATCA	X-ray Luminosity	$\alpha \pm \Delta\alpha$	S_{1GHz} est.	Type (previous vs. here)
No.	Name	Name	R.A.	Dec	(Jy)	(Jy)	(Jy)	(Jy)	(Jy)	(Jy)	(Jy)	(ergs s^{-1})		(Jy)	
151		J004650-713923	00 46 50.49	–71 39 23.2					0.0043						bkg bkg
152	0046-7201	J004621-720154	00 46 21.22	–72 01 54.2		0.0512	0.0411	0.0614	0.0139				–0.99 0.45	0.045	BKG BKG
153	0046-7201	J004608-720203	00 46 08.16	–72 02 03.9		0.0591	0.0557		0.0219				–0.93 0.03	0.049	BKG BKG
154		J004623-722724	00 46 23.39	–72 27 24.5		0.0144	0.0154	0.0285	0.0073				–0.51 0.50	0.016	BKG bkg
155		J004620-724514	00 46 20.44	–72 45 14.2					0.0013						HII hii
156		J004611-730043	00 46 11.93	–73 00 43.3				0.0030	0.0030				0.00 0.28	0.003	HII HII
157		J004633-730604	00 46 33.48	–73 06 04.7				0.1307	0.1176	0.0613	0.0196		–1.04 0.18	0.238	HII hii
158		J004637-730823	00 46 37.64	–73 08 23.2			0.0400	0.0679	0.0211				–0.61 0.55	0.048	SNR SNR
159		J004652-731731	00 46 52.93	–73 17 31.2					0.0053						HII hii
160	0046-7322	J004639-732204	00 46 39.58	–73 22 04.3				0.0377	0.0381	0.0014	0.0088		–1.30 0.75	0.057	HII hii
161	0046-7322	J004619-732324	00 46 19.32	–73 23 24.8				0.0266	0.0392	0.0073	0.0042		–1.21 0.28	0.060	HII hii
162		J004645-732704	00 46 45.56	–73 27 04.6					0.0307						bkg bkg
163		J004640-733150	00 46 40.59	–73 31 50.9				0.0902	0.0454	0.0398	0.0352		–0.47 0.12	0.088	HII hii
164		J004659-734527	00 46 59.39	–73 45 27.0					0.0036						bkg bkg
165		J004635-735344	00 46 35.17	–73 53 44.9		0.0071			0.0042				–0.51 0.14	0.007	BKG bkg
166		J004603-741336	00 46 03.43	–74 13 36.0		0.0327	0.0244	0.0148	0.0102				–1.01 0.14	0.023	BKG BKG
167		J004610-741804	00 46 10.95	–74 18 04.1		0.0091			0.0054				–0.51 0.14	0.008	BKG bkg
168		J004633-742509	00 46 33.55	–74 25 09.0		0.0111			0.0016				–1.87 0.14	0.008	BKG BKG
169		J004646-743407	00 46 46.46	–74 34 07.1		0.0152	0.0145	0.0164	0.0055				–0.85 0.30	0.014	BKG BKG
170		J004602-744005	00 46 02.10	–74 40 05.2		0.0583		0.0379	0.0271				–0.74 0.03	0.051	BKG BKG
171		J004750-705756	00 47 50.27	–70 57 56.9		0.0434	0.0488	0.0272	0.0208				–0.79 0.08	0.039	BKG BKG
172		J004725-712727	00 47 25.05	–71 27 27.9		0.0061			0.0016				–1.30 0.14	0.005	BKG BKG
173		J004703-714959	00 47 03.94	–71 49 59.3		0.0450	0.0402	0.0196	0.0167				–0.96 0.16	0.034	BKG BKG
174		J004718-723947	00 47 18.15	–72 39 47.4		0.0085		0.0280	0.0222				0.93 0.46	0.013	BKG XRB
175		J004733-730456	00 47 33.18	–73 04 56.2				0.1133							bkg bkg
176		J004701-730521	00 47 01.35	–73 05 21.3				0.0414	0.0177				–1.66 0.28	0.074	BKG BKG
177		J004728-730601	00 47 28.58	–73 06 01.5			0.0360	0.1381	0.0284	0.0368	0.0244	0.6	–0.36 0.29	0.059	SNR SNR
178		J004716-730811	00 47 16.61	–73 08 11.5	0.70		0.4600	0.4576	0.3410	0.2881	0.0891	5.8	–0.57 0.11	0.478	SNR SNR
179		J004724-732159	00 47 24.36	–73 21 59.3					0.0448						BKG bkg
180		J004712-745933	00 47 12.87	–74 59 33.0		0.0214		0.0165	0.0111				–0.64 0.05	0.020	BKG BKG
181		J004732-750057	00 47 32.15	–75 00 57.4		0.0222			0.0083				–0.95 0.14	0.019	BKG BKG
182		J004706-750241	00 47 06.08	–75 02 41.5		0.0144			0.0072				–0.67 0.14	0.013	BKG BKG
183		J004835-710322	00 48 35.30	–71 03 22.5	0.18	0.0507	0.0245	0.0431	0.0185				–1.12 0.33	0.044	BKG BKG
184		J004851-710510	00 48 51.21	–71 05 10.5		0.0197	0.0243	0.0227	0.0114				–0.57 0.20	0.021	BKG bkg
185		J004816-711406	00 48 16.06	–71 14 06.9		0.0413	0.0334	0.0207	0.0145				–0.93 0.10	0.031	BKG BKG
186		J004837-712839	00 48 37.17	–71 28 39.1					0.0014						BKG bkg
187		J004826-720025	00 48 26.29	–72 00 25.9					0.0016						bkg bkg
188		J004850-725125	00 48 50.84	–72 51 25.0		0.0101	0.0142	0.0063	0.0103				–0.25 0.31	0.010	B/H B/H
189		J004823-730557	00 48 23.68	–73 05 57.2				0.0638	0.0342				–1.22 0.28	0.098	HII hii
190		J004856-730748	00 48 56.30	–73 07 48.8				0.1431	0.1271	0.0772	0.0356		–0.77 0.11	0.217	HII hii
191		J004806-730842	00 48 06.06	–73 08 42.7				0.0826	0.1047	0.0609			–0.22 0.20	0.105	SNR snr
192		J004819-731032	00 48 19.16	–73 10 32.3					0.0087						HII HII
193		J004748-731727	00 47 48.64	–73 17 27.4				0.0329	0.0266	0.0164			–0.58 0.04	0.042	SNR snr
194	0048-7314	J004802-731653	00 48 02.79	–73 16 53.4	0.16			0.1037	0.1009	0.0557			–0.40 0.06	0.118	SNR hii
195	0048-7314	J004756-731752	00 47 56.82	–73 17 52.5					0.0649						HII hii
196		J004809-731442	00 48 09.22	–73 14 42.6				0.0648	0.0562	0.0415			–0.37 0.02	0.075	HII hii
197	0048-7315	J004828-731556	00 48 28.18	–73 15 56.9				0.0547	0.0228	0.0378			–0.24 0.39	0.045	HII hii
198	0048-7315	J004834-731509	00 48 34.04	–73 15 09.8					0.0205	0.0142	0.0224		0.05 0.21	0.017	HII HII
199		J004821-731931	00 48 21.24	–73 19 31.6	0.40		0.1640	0.1478	0.1120	0.0340	0.0131	0.6	–1.06 0.11	0.176	SNR SNR
200		J004836-733056	00 48 36.64	–73 30 56.1		0.0101	0.0126	0.0225	0.0107				0.08 0.37	0.013	B/H B/H

Table 1 Catalogue of the ATCA SMC sources.

1	2	3	4		5	6	7	8	9	10	11	12	13	14	15
ATCA	Group	ATCA	J2000		S_{408MHz} MC4	S_{843MHz} SUMSS	S_{843MHz} MOST	$S_{1.42GHz}$ ATCA	$S_{2.37GHz}$ ATCA	$S_{4.8GHz}$ ATCA	$S_{8.64GHz}$ ATCA	X-ray Luminosity	$\alpha \pm \Delta\alpha$	S_{1GHz} est.	Type (previous vs. here)
No.	Name	Name	R.A.	Dec	(Jy)	(Jy)	(Jy)	(Jy)	(Jy)	(Jy)	(Jy)	(ergs s^{-1})		(Jy)	
201		J004834-734428	00 48 34.20	–73 44 28.3		0.0071		0.0055	0.0043				–0.49	0.007	BKG bkg
202		J004843-740733	00 48 43.55	–74 07 33.1		0.0189	0.0197	0.0134	0.0078				–0.86 0.05	0.017	BKG BKG
203		J004808-741206	00 48 08.38	–74 12 06.9		0.1608	0.1680	0.1183	0.0761				–0.73 0.04	0.147	BKG BKG
204		J004806-742007	00 48 06.09	–74 20 07.1					0.0021						BKG bkg
205		J004832-743313	00 48 32.00	–74 33 13.2		0.0060		0.0074	0.0034				–0.55 0.32	0.006	BKG bkg
206		J004936-705213	00 49 36.90	–70 52 13.9		0.0104	0.0149	0.0089	0.0137				0.02 0.24	0.012	BKG bkg
207		J004906-710345	00 49 06.68	–71 03 45.5	0.27	0.0702	0.0433	0.0151	0.0241				–1.50 0.35	0.049	BKG BKG
208		J004924-710530	00 49 24.72	–71 05 30.2		0.0467	0.0371	0.0406	0.0174				–0.77 0.23	0.039	BKG BKG
209		J004905-712654	00 49 05.42	–71 26 54.0					0.0013						BKG bkg
210		J004923-712659	00 49 23.01	–71 26 59.7		0.0270	0.0319	0.0193	0.0124				–0.83 0.07	0.026	BKG BKG
211		J004954-715151	00 49 54.15	–71 51 51.6		0.0252	0.0246	0.0241	0.0183				–0.28 0.06	0.024	BKG bkg
212		J004958-720538	00 49 58.14	–72 05 38.6		0.0085			0.0039				–0.75 0.14	0.007	Bkg BKG
213		J004915-720922	00 49 15.34	–72 09 22.7					0.0031						bkg bkg
214		J004933-721902	00 49 33.37	–72 19 02.9		0.0517	0.0426	0.0744	0.0267				–0.41 0.38	0.050	BKG bkg
215		J004917-722007	00 49 17.23	–72 20 07.2					0.0117						bkg bkg
216		J004939-723541	00 49 39.03	–72 35 41.8		0.0097			0.0094				–0.03 0.14	0.010	Bkg bkg
217		J004956-723555	00 49 56.83	–72 35 55.2	0.37	0.1878	0.1720	0.1612	0.0729				–0.85 0.10	0.169	B/H B/H
218		J004935-724642	00 49 35.72	–72 46 42.2		0.0305	0.0314	0.0336	0.0196				–0.39 0.16	0.031	BKG bkg
219		J004943-724843	00 49 43.23	–72 48 43.0				0.0203	0.0222				0.18 0.28	0.019	HII HII
220		J004925-730940	00 49 25.80	–73 09 40.5					0.0066						HII hii
221		J004944-731030	00 49 44.88	–73 10 30.4				0.0277	0.0228				–0.38 0.28	0.032	HII hii
222		J004907-731402	00 49 07.75	–73 14 02.0			0.0370	0.2810	0.0193			0.6	–0.62 1.52	0.073	SNR SNR
223		J004918-731551	00 49 18.25	–73 15 51.0					0.0114						HII hii
224		J004916-732050	00 49 16.59	–73 20 50.1		0.0176	0.0224	0.0411		0.0052	0.0006		–1.40 0.32	0.025	BKG BKG
225		J004928-732626	00 49 28.74	–73 26 26.6		0.0094	0.0145	0.0371	0.0136				0.34 0.57	0.015	B/H B/H
226		J004902-734455	00 49 02.62	–73 44 55.6		0.0198	0.0204	0.0143	0.0086				–0.80 0.05	0.018	BKG BKG
227		J004936-741553	00 49 36.64	–74 15 53.2		0.0599	0.0476	0.0379	0.0248				–0.73 0.10	0.047	BKG BKG
228	0049-7446	J004909-744630	00 49 09.85	–74 46 30.4		0.0217		0.0134	0.0105				–0.70 0.08	0.019	BKG BKG
229	0049-7446	J004920-744712	00 49 20.55	–74 47 12.9		0.0078		0.0067	0.0033				–0.83 0.18	0.007	BKG BKG
230		J004918-745700	00 49 18.59	–74 57 00.5		0.1142		0.0759	0.0493				–0.81 0.01	0.100	BKG BKG
231		J005040-703929	00 50 40.32	–70 39 29.4		0.0389		0.0274	0.0053				–1.93 0.42	0.035	BKG BKG
232		J005025-705307	00 50 25.13	–70 53 07.7		0.0073			0.0038				–0.63 0.14	0.007	BKG BKG
233		J005041-715826	00 50 41.27	–71 58 26.1		0.0117	0.0107		0.0026				–1.41 0.04	0.009	BKG BKG
234		J005015-723241	00 50 15.61	–72 32 41.1				0.0091	0.0109				0.35 0.28	0.008	HII HII
235		J005049-724819	00 50 49.66	–72 48 19.4						0.0282	0.0093		–1.89 0.24	0.544	HII hii
236		J005028-725311	00 50 28.11	–72 53 11.5				0.2117	0.1541	0.0967	0.0569		–0.72 0.03	0.282	HII hii
237		J005016-730320	00 50 16.60	–73 03 20.3		0.0496	0.0421	0.0359	0.0312				–0.38 0.07	0.042	BKG bkg
238		J005056-731248	00 50 56.22	–73 12 48.8				0.0166	0.0127	0.0042			–1.16 0.17	0.028	BKG BKG
239		J005032-730711	00 50 32.73	–73 07 11.3					0.0080						bkg bkg
240		J005052-731701	00 50 52.45	–73 17 01.1				0.0086	0.0092				0.13 0.28	0.008	Bkg bkg
241		J005040-732022	00 50 40.47	–73 20 22.5				0.0095	0.0193				1.38 0.28	0.006	HII HII
242		J005009-734139	00 50 09.34	–73 41 39.3		0.0106	0.0119	0.0080	0.0061				–0.60 0.05	0.010	BKG bkg
243		J005115-713059	00 51 15.31	–71 30 59.8		0.0267	0.0260	0.0118	0.0090				–1.09 0.13	0.021	BKG BKG
244		J005153-721650	00 51 53.36	–72 16 50.9					0.0138						HII hii
245		J005147-725053	00 51 47.38	–72 50 53.7				0.0380	0.0103	0.0063			–1.43 0.30	0.051	BKG BKG
246		J005141-725555	00 51 41.16	–72 55 55.5		0.0782	0.0781	0.0701	0.0426	0.0227			–0.71 0.07	0.075	BKG BKG
247		J005147-730453	00 51 47.56	–73 04 53.2		0.0180	0.0240	0.0062	0.0062				–1.28 0.32	0.015	BKG BKG
248		J005140-731339	00 51 40.38	–73 13 39.9		0.0126		0.0390	0.0195	0.0116			–0.20 0.36	0.021	BKG bkg
249		J005110-732212	00 51 10.24	–73 22 12.5			0.1550	0.1017	0.0788	0.0550	0.0301	3.0	–0.66 0.04	0.137	SNR SNR
250		J005155-732650	00 51 55.47	–73 26 50.9				0.0333	0.0445				0.57 0.28	0.027	HII HII

Table 1 Catalogue of the ATCA SMC sources.

1	2	3	4		5	6	7	8	9	10	11	12	13	14	15
ATCA	Group	ATCA	J2000		S_{408MHz} MC4	S_{843MHz} SUMSS	S_{843MHz} MOST	$S_{1.42GHz}$ ATCA	$S_{2.37GHz}$ ATCA	$S_{4.8GHz}$ ATCA	$S_{8.64GHz}$ ATCA	X-ray Luminosity	$\alpha \pm \Delta\alpha$	S_{1GHz} est.	Type (previous vs. here)
No.	Name	Name	R.A.	Dec	(Jy)	(Jy)	(Jy)	(Jy)	(Jy)	(Jy)	(Jy)	(ergs s^{-1})		(Jy)	
251		J005117-734002	00 51 17.24	–73 40 02.3		0.0981	0.0807	0.0976	0.0543				–0.42 0.19	0.088	BKG bkg
252		J005240-711909	00 52 40.12	–71 19 09.5		0.0069			0.0014				–1.54 0.14	0.005	BKG BKG
253		J005254-720132	00 52 54.25	–72 01 32.2		0.0236	0.0168	0.0165	0.0141				–0.34 0.14	0.019	B/H B/H
254		J005206-721615	00 52 06.60	–72 16 15.7				0.0235	0.0114				–1.41 0.28	0.039	HII hii
255		J005218-722708	00 52 18.81	–72 27 08.7	0.54	0.2911	0.2630	0.2087	0.1176				–0.83 0.05	0.251	BKG BKG
256		J005259-723520	00 52 59.68	–72 35 20.9		0.0142	0.0132	0.0205	0.0391				0.99 0.07	0.016	BKG bkg
257		J005227-723619	00 52 27.46	–72 36 19.5				0.0586	0.0607				0.07 0.28	0.057	HII HII
258		J005240-723820	00 52 40.58	–72 38 20.3			0.3050	0.2160	0.1096	0.0486	0.0310		–1.03 0.05	0.273	SNR SNR
259		J005218-730155	00 52 18.26	–73 01 55.2		0.0388	0.0435	0.0251	0.0163				–0.90 0.05	0.035	BKG BKG
260		J005211-730854	00 52 11.65	–73 08 54.3		0.0082	0.0119		0.0083				–0.17 0.18	0.010	BKG bkg
261		J005258-731144	00 52 58.24	–73 11 44.5				0.0105	0.0117				0.21 0.28	0.010	HII HII
262		J005238-731246	00 52 38.08	–73 12 46.1	0.21	0.1640	0.1620	0.1447	0.0745	0.0277	0.0180		–0.88 0.08	0.134	BKG BKG
263		J005235-732610	00 52 35.72	–73 26 10.9					0.0054						HII hii
264		J005203-733238	00 52 03.25	–73 32 38.1		0.0094			0.0071				–0.27 0.14	0.009	Bkg bkg
265		J005205-733725	00 52 05.47	–73 37 25.4		0.0137			0.0067				–0.69 0.14	0.012	BKG BKG
266		J005249-741133	00 52 49.82	–74 11 33.7		0.0077			0.0020				–1.30 0.14	0.006	BKG BKG
267		J005228-743745	00 52 28.07	–74 37 45.3		0.0086			0.0022				–1.32 0.14	0.007	BKG BKG
268		J005355-703810	00 53 55.98	–70 38 10.3		0.0572		0.0058	0.0040				–2.58 0.61	0.027	BKG BKG
269		J005351-703958	00 53 51.80	–70 39 58.7		0.0449		0.0669	0.0074				–1.74 0.84	0.051	BKG BKG
270		J005348-715001	00 53 48.20	–71 50 01.2		0.0169	0.0159	0.0139	0.0061				–0.90 0.17	0.015	BKG BKG
271		J005347-715901	00 53 47.66	–71 59 01.5					0.0013						bkg bkg
272		J005318-720905	00 53 18.20	–72 09 05.6		0.0203	0.0181	0.0349	0.0109				–0.39 0.44	0.021	B/H bkg
273		J005300-721238	00 53 00.34	–72 12 38.5				0.0290	0.0382				0.54 0.28	0.024	HII HII
274		J005326-723021	00 53 26.85	–72 30 21.4		0.0126			0.0102				–0.20 0.14	0.012	Bkg bkg
275		J005337-723145	00 53 37.59	–72 31 45.4	0.25	0.1323	0.1220	0.1231	0.0424	0.0220			–0.92 0.37	0.059	BKG BKG
276		J005321-723533	00 53 21.05	–72 35 33.7		0.0415	0.0297	0.2084	0.0361	0.0108	0.0060		–0.92 0.37	0.059	BKG BKG
277		J005341-723934	00 53 41.14	–72 39 34.7				0.0161	0.0399	0.0046	0.0044		–1.04 0.43	0.038	HII hii
278		J005328-725524	00 53 28.59	–72 55 24.0		0.0133	0.0179	0.0155	0.0138				–0.10 0.13	0.015	BKG bkg
279		J005338-731221	00 53 38.87	–73 12 21.5				0.0130	0.0265				1.39 0.28	0.008	HII HII
280		J005307-743904	00 53 07.65	–74 39 04.9				0.0276	0.0207				–0.56 0.28	0.034	BKG bkg
281		J005325-745557	00 53 25.44	–74 55 57.7					0.0035						BKG bkg
282		J005344-751441	00 53 44.61	–75 14 41.3		0.0189		0.0138	0.0018				–2.27 0.56	0.017	BKG BKG
283		J005457-710340	00 54 57.53	–71 03 40.5		0.0164	0.0117		0.0031				–1.45 0.16	0.011	BKG BKG
284		J005453-713138	00 54 53.31	–71 31 38.5		0.0244	0.0287	0.0179	0.0114				–0.81 0.07	0.023	BKG BKG
285		J005428-720158	00 54 28.16	–72 01 58.9		0.0086	0.0104		0.0026				–1.25 0.09	0.008	BKG BKG
286		J005404-721343	00 54 04.95	–72 13 43.8		0.0122	0.0122	0.0272	0.0094				–0.08 0.46	0.014	BKG bkg
287		J005408-722420	00 54 08.70	–72 24 20.5		0.0132	0.0113	0.0143	0.0061				–0.58 0.26	0.012	BKG bkg
288		J005441-722958	00 54 41.37	–72 29 58.8		0.0118	0.0114	0.0104	0.0095				–0.20 0.02	0.011	BKG bkg
289		J005439-724501	00 54 39.52	–72 45 01.5		0.0170	0.0170	0.0280	0.0111				–0.28 0.36	0.018	BKG bkg
290		J005423-725259	00 54 23.38	–72 52 59.7		0.0563	0.0575	0.0642	0.0287				–0.58 0.23	0.056	BKG bkg
291		J005449-725347	00 54 49.11	–72 53 47.9		0.0231	0.0257	0.0216	0.0146				–0.47 0.08	0.023	BKG bkg
292		J005448-731646	00 54 48.87	–73 16 46.0		0.0177	0.0208	0.0175	0.0114				–0.47 0.11	0.018	BKG bkg
293		J005409-731709	00 54 09.92	–73 17 09.6					0.0053						bkg bkg
294		J005434-733848	00 54 34.36	–73 38 48.5		0.0135	0.0112	0.0053	0.0041				–1.11 0.16	0.010	BKG BKG
295		J005411-734016	00 54 11.62	–73 40 16.9		0.0170	0.0171	0.0198	0.0077				–0.67 0.27	0.017	BKG BKG
296		J005448-735858	00 54 48.06	–73 58 58.4		0.0135	0.0121		0.0031				–1.37 0.05	0.010	BKG BKG
297		J005425-741720	00 54 25.07	–74 17 20.8		0.0085	0.0119		0.0037				–0.97 0.16	0.009	BKG BKG
298		J005449-744940	00 54 49.49	–74 49 40.7		0.0121		0.0083	0.0081				–0.39 0.11	0.011	BKG bkg
299		J005527-710227	00 55 27.08	–71 02 27.6					0.0013						BKG bkg
300		J005554-710327	00 55 54.53	–71 03 27.8					0.0096						BKG bkg

Table 1 Catalogue of the ATCA SMC sources.

1	2	3	4		5	6	7	8	9	10	11	12	13	14	15
ATCA	Group	ATCA	J2000		S_{408MHz} MC4	S_{843MHz} SUMSS	S_{843MHz} MOST	$S_{1.42GHz}$ ATCA	$S_{2.37GHz}$ ATCA	$S_{4.8GHz}$ ATCA	$S_{8.64GHz}$ ATCA	X-ray Luminosity	$\alpha \pm \Delta\alpha$	S_{1GHz} est.	Type (previous vs. here)
No.	Name	Name	R.A.	Dec	(Jy)	(Jy)	(Jy)	(Jy)	(Jy)	(Jy)	(Jy)	(ergs s^{-1})		(Jy)	
301		J005503-712104	00 55 03.34	–71 21 04.2		0.0394	0.0389	0.0326	0.0167				–0.78 0.12	0.036	BKG BKG
302		J005519-714449	00 55 19.41	–71 44 49.1		0.0322	0.0334	0.0219	0.0120				–0.95 0.05	0.028	BKG BKG
303	0055-7210	J005523-721055	00 55 23.53	–72 10 55.2	0.31	0.1329	0.0971	0.1230	0.1254				–0.45 0.23	0.144	BKG bkg
304	0055-7210	J005539-721055	00 55 39.21	–72 10 55.5		0.0959	0.0650	0.1671	0.0550				–0.18 0.49	0.091	BKG bkg
305		J005544-721608	00 55 44.65	–72 16 08.5					0.0089						HII hii
306		J005558-722609	00 55 58.32	–72 26 09.8		0.1295	0.1220	0.1339	0.0798	0.0646			–0.41 0.08	0.124	BKG bkg
307		J005531-723122	00 55 31.96	–72 31 22.8		0.0351	0.0270	0.1625	0.0798				1.14 0.60	0.046	BKG bkg
308		J005534-723523	00 55 34.75	–72 35 23.2		0.0938	0.0598	0.1192	0.0382				–0.51 0.44	0.079	BKG bkg
309		J005508-723711	00 55 08.03	–72 37 11.5		0.0261	0.0183	0.1477	0.0162				0.08 1.03	0.032	BKG bkg
310		J005554-742236	00 55 54.56	–74 22 36.2		0.0065			0.0074				0.13 0.14	0.007	Bkg bkg
311		J005537-743927	00 55 37.22	–74 39 27.6	0.31	0.1703	0.1940	0.0874	0.0392				–1.20 0.11	0.128	BKG BKG
312		J005607-703848	00 56 07.83	–70 38 48.2	0.30	0.1420		0.0637	0.0154				–1.64 0.20	0.085	BKG BKG
313		J005642-704141	00 56 42.84	–70 41 41.8				0.0143	0.0026				–3.33 0.28	0.046	BKG BKG
314		J005611-710708	00 56 11.35	–71 07 08.5	1.53	0.8299	0.8860	0.6394	0.3934				–0.75 0.03	0.774	BKG BKG
315		J005652-712301	00 56 52.73	–71 23 01.3	0.16	0.1287	0.1320	0.0785	0.0447				–0.75 0.11	0.099	BKG BKG
316		J005622-715111	00 56 22.38	–71 51 11.9		0.0312	0.0326	0.0313	0.0103				–0.99 0.27	0.030	BKG BKG
317		J005602-720908	00 56 02.06	–72 09 08.7		0.0105	0.0109	0.0334	0.0065				–0.23 0.69	0.013	BKG bkg
318	0056-7218	J005616-721732	00 56 16.13	–72 17 32.1					0.0994	0.0211	0.0021	1.0	–2.96 0.29	1.506	HII hii
319	0056-7218	J005610-721833	00 56 10.10	–72 18 33.9				0.0551				1.0			bkg bkg
320	0056-7218	J005604-721931	00 56 04.63	–72 19 31.2					0.0266	0.0112		1.0	–1.23 0.20	0.077	HII hii
321		J005643-725207	00 56 43.94	–72 52 07.5		0.1118	0.1060	0.1086	0.0287				–1.17 0.33	0.101	BKG BKG
322		J005632-735710	00 56 32.52	–73 57 10.5		0.0258	0.0237	0.0158	0.0108				–0.81 0.04	0.021	BKG BKG
323		J005636-740316	00 56 36.91	–74 03 16.6		0.0262	0.0241	0.0227	0.0296				0.13 0.10	0.025	BKG bkg
324		J005712-703404	00 57 12.25	–70 34 04.7				0.0243							BKG bkg
325		J005712-703707	00 57 12.59	–70 37 07.1				0.0243							BKG bkg
326		J005715-704047	00 57 15.73	–70 40 47.2		0.1388		0.1340	0.0637				–0.75 0.23	0.137	BKG BKG
327		J005738-710848	00 57 38.35	–71 08 48.7		0.0375	0.0444	0.0398	0.0173				–0.76 0.21	0.039	BKG BKG
328		J005746-711727	00 57 46.82	–71 17 27.4		0.0120		0.0141	0.0030				–1.34 0.56	0.013	BKG BKG
329		J005755-715658	00 57 55.57	–71 56 58.8		0.0078		0.0248	0.0097				0.22 0.68	0.011	BKG bkg
330		J005737-715924	00 57 37.84	–71 59 24.6		0.0132	0.0166	0.0170	0.0068				–0.66 0.28	0.015	BKG BKG
331		J005703-721630	00 57 03.50	–72 16 30.3		0.0243	0.0295	0.0527	0.0157	0.0047	0.0028		–1.08 0.21	0.032	BKG BKG
332		J005729-723220	00 57 29.00	–72 32 20.7				0.0256	0.0081	0.0113	0.0062		–0.61 0.24	0.023	BKG PN
333		J005741-724158	00 57 41.92	–72 41 58.4		0.0206	0.0214	0.0314	0.0186				–0.03 0.23	0.023	BKG bkg
334		J005750-730606	00 57 50.64	–73 06 06.4					0.0051						bkg bkg
335		J005735-731302	00 57 35.60	–73 13 02.2					0.0014						bkg bkg
336		J005748-732551	00 57 48.30	–73 25 51.9					0.0008						bkg bkg
337		J005714-733452	00 57 14.93	–73 34 52.2		0.0188		0.0157	0.0084				–0.78 0.15	0.018	BKG BKG
338		J005758-740215	00 57 58.12	–74 02 15.5		0.0064			0.0013				–1.54 0.14	0.005	BKG BKG
339		J005722-740315	00 57 22.09	–74 03 15.2		0.0317	0.0306	0.0194	0.0126				–0.88 0.02	0.027	BKG BKG
340		J005732-741244	00 57 32.39	–74 12 44.6	1.76	0.8706	0.8830	0.4673	0.2209				–1.18 0.06	0.671	BKG BKG
341		J005730-744216	00 57 30.36	–74 42 16.9		0.0306		0.0209	0.0151				–0.68 0.02	0.027	BKG BKG
342		J005815-712352	00 58 15.59	–71 23 52.1		0.0564	0.0283	0.0312	0.0241				–0.49 0.28	0.037	BKG bkg
343		J005820-713041	00 58 20.65	–71 30 41.5		0.0520	0.0571	0.0427	0.0246				–0.74 0.09	0.049	BKG BKG
344		J005824-720045	00 58 24.62	–72 00 45.4		0.0188	0.0221	0.0256	0.0099				–0.59 0.30	0.020	BKG bkg
345		J005800-721101	00 58 00.00	–72 11 01.4			0.0520	0.0697	0.0530				0.02 0.18	0.057	SNR SNR e
346		J005832-721400	00 58 32.37	–72 14 00.6					0.0181						bkg bkg
347		J005817-721814	00 58 17.39	–72 18 14.5			0.0870	0.0713	0.0591	0.0351	0.0143	1.0	–0.74 0.10	0.091	SNR SNR
348	0058-7239	J005816-723852	00 58 16.26	–72 38 52.1					0.0201	0.0112			–0.83 0.20	0.041	HII hii
349	0058-7239	J005824-723955	00 58 24.71	–72 39 55.0				0.0044	0.0214	0.0092			0.50 0.69	0.006	HII HII
350	0058-7239	J005756-723932	00 57 56.96	–72 39 32.2					0.0265	0.0087			–1.58 0.20	0.103	HII hii

Table 1 Catalogue of the ATCA SMC sources.

1	2	3	4		5	6	7	8	9	10	11	12	13	14	15
ATCA	Group	ATCA	J2000		S_{408MHz} MC4	S_{843MHz} SUMSS	S_{843MHz} MOST	$S_{1.42GHz}$ ATCA	$S_{2.37GHz}$ ATCA	$S_{4.8GHz}$ ATCA	$S_{8.64GHz}$ ATCA	X-ray Luminosity	$\alpha \pm \Delta\alpha$	S_{1GHz} est.	Type (previous vs. here)
No.	Name	Name	R.A.	Dec	(Jy)	(Jy)	(Jy)	(Jy)	(Jy)	(Jy)	(Jy)	(ergs s^{-1})		(Jy)	
351		J005831-725106	00 58 31.61	–72 51 06.7		0.0126			0.0247	0.0050	0.0010		–1.08 0.43	0.021	BKG BKG
352		J005846-730506	00 58 46.90	–73 05 06.3				0.0061	0.0034				–1.14 0.28	0.009	BKG BKG
353		J005819-732937	00 58 19.92	–73 29 37.3		0.0063			0.0081				0.24 0.14	0.007	BKG bkg
354		J005813-735953	00 58 13.22	–73 59 53.1		0.0215	0.0212	0.0146	0.0085				–0.88 0.04	0.019	BKG BKG
355		J005831-740148	00 58 31.31	–74 01 48.4		0.0166	0.0197	0.0124	0.0085				–0.73 0.07	0.016	BKG BKG
356		J005848-743514	00 58 48.86	–74 35 14.8		0.0293	0.0310	0.0138	0.0121				–0.94 0.16	0.024	BKG BKG
357		J005845-744654	00 58 45.81	–74 46 54.5		0.0167		0.0086	0.0065				–0.91 0.12	0.013	BKG BKG
358		J005904-704901	00 59 04.30	–70 49 01.5	0.34	0.1539	0.3400	0.0958	0.0449				–1.20 0.24	0.149	BKG BKG
359		J005948-705031	00 59 48.92	–70 50 31.3		0.0147		0.0169	0.0148				0.01 0.09	0.015	BKG bkg
360		J005950-705159	00 59 50.73	–70 51 59.7		0.0176			0.0097				–0.58 0.14	0.016	BKG bkg
361	0059-7210	J005953-720840	00 59 53.54	–72 08 40.2				0.0655	0.1836				2.01 0.28	0.032	HII HII
362	0059-7210	J005855-721010	00 58 55.15	–72 10 10.0				0.2459	0.2544	0.1682	0.0778		–0.64 0.14	0.372	HII hii
363	0059-7210	J005908-721056	00 59 08.39	–72 10 56.8				0.2459	0.2043	0.2065	0.1105		–0.39 0.11	0.296	SNR hii
364	0059-7210	J005916-721020	00 59 16.09	–72 10 20.2	1.01			0.1720	0.2107	0.1745	0.0430		–0.88 0.16	0.396	HII hii
365	0059-7210	J005916-721120	00 59 16.32	–72 11 20.5				0.2680	0.0986				–1.95 0.28	0.531	HII hii
366	0059-7210	J005927-721010	00 59 27.42	–72 10 10.2			0.4100	0.3700	0.3280	0.3074	0.0435		–0.81 0.27	0.500	SNR SNR
367	0059-7210	J005934-720942	00 59 34.23	–72 09 42.4				0.1274	0.0898			5.5	–0.68 0.28	0.162	HII hii
368		J005904-721446	00 59 04.00	–72 14 46.3					0.0104						bkg bkg
369		J005917-721721	00 59 17.73	–72 17 21.6					0.0094						BKG bkg
370		J005914-722423	00 59 14.09	–72 24 23.1				0.0115	0.0130				0.24 0.28	0.011	HII HII
371		J005900-723419	00 59 00.40	–72 34 19.4				0.1232							bkg bkg
372		J005906-735205	00 59 06.45	–73 52 05.4		0.0372	0.0333	0.0247	0.0212				–0.51 0.07	0.032	BKG bkg
373		J005906-745455	00 59 06.40	–74 54 55.1		0.0077			0.0063				–0.19 0.14	0.007	BKG bkg
374		J005906-745851	00 59 06.51	–74 58 51.4		0.0252		0.0196	0.0089				–1.01 0.18	0.023	BKG BKG
375		J010012-704026	01 00 12.40	–70 40 26.8		0.0144		0.0065	0.0029				–1.55 0.01	0.011	BKG BKG
376		J010051-705016	01 00 51.48	–70 50 16.6		0.0075			0.0027				–0.99 0.14	0.006	BKG BKG
377		J010043-712137	01 00 43.44	–71 21 37.8		0.0141	0.0151	0.0208	0.0060				–0.72 0.40	0.015	BKG BKG
378		J010023-713322	01 00 23.26	–71 33 22.6	0.48		0.2390	0.2059	0.1248	0.0879	0.0370		–0.78 0.06	0.241	SNR SNR
379		J010059-713528	01 00 59.18	–71 35 28.6		0.0109		0.0253	0.0128	0.0079	0.0054		–0.45 0.19	0.017	BKG bkg
380		J010029-713827	01 00 29.72	–71 38 27.2	0.33	0.1919	0.2180	0.1490	0.0824	0.0400	0.0255		–0.87 0.04	0.172	BKG BKG
381		J010019-714437	01 00 19.91	–71 44 37.0		0.0095			0.0015				–1.79 0.14	0.007	Bkg BKG
382		J010030-730006	01 00 30.92	–73 00 06.9		0.0193	0.0181	0.0324	0.0074				–0.71 0.51	0.020	BKG BKG
383		J010053-734043	01 00 53.90	–73 40 43.5		0.0121	0.0113	0.0126	0.0064				–0.52 0.19	0.011	BKG bkg
384		J010053-734209	01 00 53.54	–73 42 09.1		0.0078			0.0013				–1.73 0.14	0.006	Bkg BKG
385		J010014-742527	01 00 14.12	–74 25 27.1		0.0095			0.0015				–1.79 0.14	0.007	BKG BKG
386		J010041-744630	01 00 41.04	–74 46 30.6					0.0044						BKG bkg
387		J010045-745415	01 00 45.03	–74 54 15.3		0.0654		0.0376	0.0229				–1.02 0.02	0.055	BKG BKG
388		J010125-715054	01 01 25.24	–71 50 54.0				0.0208	0.0042				–3.12 0.28	0.062	HII hii
389		J010144-723227	01 01 44.20	–72 32 27.7		0.0219	0.0297	0.1055	0.0150				–0.21 0.85	0.033	BKG bkg
390		J010140-725516	01 01 40.90	–72 55 16.7		0.0113			0.0034				–1.16 0.14	0.009	Bkg BKG
391		J010156-734249	01 01 56.58	–73 42 49.8		0.0146	0.0135	0.0289	0.0058				–0.65 0.58	0.016	BKG BKG
392		J010142-742336	01 01 42.77	–74 23 36.0		0.0126	0.0122		0.0030				–1.37 0.02	0.010	BKG BKG
393		J010112-744102	01 01 12.52	–74 41 02.6		0.0217		0.0099	0.0103				–0.72 0.26	0.017	BKG BKG
394		J010258-703921	01 02 58.88	–70 39 21.1		0.0366		0.0281					–0.51 0.27	0.034	BKG bkg
395		J010254-710044	01 02 54.64	–71 00 44.9					0.0016						BKG bkg
396		J010239-710218	01 02 39.53	–71 02 18.6		0.0101	0.0100		0.0026				–1.31 0.01	0.008	BKG BKG
397		J010203-710319	01 02 03.90	–71 03 19.0		0.0093			0.0034				–0.97 0.14	0.008	BKG BKG
398		J010222-712724	01 02 22.04	–71 27 24.0		0.0250	0.0246	0.0219	0.0122				–0.64 0.12	0.023	BKG BKG
399		J010255-713633	01 02 55.75	–71 36 33.3		0.0276	0.0327	0.0471	0.0177				–0.38 0.36	0.032	BKG bkg
400		J010216-715140	01 02 16.92	–71 51 40.7				0.0064	0.0074				0.28 0.28	0.006	HII HII

Table 1 Catalogue of the ATCA SMC sources.

1	2	3	4		5	6	7	8	9	10	11	12	13	14	15
ATCA	Group	ATCA	J2000		S_{408MHz} MC4	S_{843MHz} SUMSS	S_{843MHz} MOST	$S_{1.42GHz}$ ATCA	$S_{2.37GHz}$ ATCA	$S_{4.8GHz}$ ATCA	$S_{8.64GHz}$ ATCA	X-ray Luminosity	$\alpha \pm \Delta\alpha$	S_{1GHz} est.	Type (previous vs. here)
No.	Name	Name	R.A.	Dec	(Jy)	(Jy)	(Jy)	(Jy)	(Jy)	(Jy)	(Jy)	(ergs s^{-1})		(Jy)	
401		J010248-715312	01 02 48.41	–71 53 12.2				0.0328	0.0233	0.0149	0.0131		–0.52 0.05	0.037	HII hii
402		J010203-722450	01 02 03.74	–72 24 50.2				0.0094	0.0111				0.33 0.28	0.008	HII HII
403		J010227-734738	01 02 27.62	–73 47 38.9		0.0142		0.0159	0.0033				–1.41 0.55	0.015	BKG BKG
404		J010221-735322	01 02 21.11	–73 53 22.4		0.0314	0.0270	0.0160	0.0099				–1.05 0.07	0.024	BKG BKG
405		J010234-741535	01 02 34.23	–74 15 35.6		0.0397	0.0411	0.0301	0.0159				–0.87 0.09	0.036	BKG BKG
406		J010226-742703	01 02 26.36	–74 27 03.0		0.0111	0.0105	0.0076	0.0025				–1.35 0.19	0.009	BKG BKG
407	0102-7435	J010258-743345	01 02 58.13	–74 33 45.6		0.0199	0.0168		0.0044				–1.38 0.08	0.014	BKG BKG
408	0102-7435	J010256-743533	01 02 56.58	–74 35 33.5		0.0338	0.0306	0.0350	0.0152				–0.64 0.23	0.031	BKG BKG
409	0102-7435	J010330-743431	01 03 30.50	–74 34 31.7					0.0067						BKG bkg
410		J010228-750029	01 02 28.68	–75 00 29.9		0.0149			0.0042				–1.23 0.14	0.012	BKG BKG
411		J010201-750236	01 02 01.44	–75 02 36.1					0.0041						BKG bkg
412		J010319-704648	01 03 19.68	–70 46 48.9		0.0063		0.0088	0.0044				–0.34 0.33	0.007	BKG bkg
413		J010322-711146	01 03 22.70	–71 11 46.7				0.0170							BKG bkg
414		J010358-711253	01 03 58.83	–71 12 53.6		0.0229	0.0192	0.0182	0.0076				–0.92 0.20	0.019	BKG BKG
415		J010346-712413	01 03 46.94	–71 24 13.1				0.0078	0.0039				–1.35 0.28	0.013	BKG BKG
416		J010331-712919	01 03 31.10	–71 29 19.0					0.0013						BKG bkg
417		J010304-715333	01 03 04.01	–71 53 33.7				0.0051	0.0148	0.0164	0.0006		–1.05 0.82	0.019	BKG BKG
418		J010326-720308	01 03 26.36	–72 03 08.9	0.67			0.1224	0.3314				–0.58 0.43	0.320	HII hii
419		J010313-720958	01 03 13.74	–72 09 58.9			0.1400	0.0952	0.0859			2.4	–0.47 0.09	0.123	SNR SNR
420		J010320-721348	01 03 20.77	–72 13 48.7		0.0178	0.0166	0.0126	0.0103				–0.51 0.04	0.016	BKG bkg
421		J010328-724724	01 03 28.72	–72 47 24.8		0.0287	0.0160	0.0461	0.0177				–0.03 0.49	0.025	BKG bkg
422		J010339-725042	01 03 39.53	–72 50 42.9		0.0164	0.0173	0.0168	0.0101				–0.45 0.13	0.016	BKG bkg
423		J010330-725152	01 03 30.58	–72 51 52.1					0.0061						bkg bkg
424		J010327-730024	01 03 27.03	–73 00 24.8		0.0244	0.0227	0.0268	0.0093				–0.79 0.30	0.023	BKG BKG
425		J010331-750705	01 03 31.55	–75 07 05.1		0.1278		0.0819	0.0359				–1.23 0.13	0.111	BKG BKG
426		J010458-703733	01 04 58.25	–70 37 33.2		0.0351		0.0342	0.0095				–1.26 0.41	0.035	BKG BKG
427		J010411-705604	01 04 11.98	–70 56 04.4		0.0162	0.0186	0.0192	0.0059				–0.93 0.33	0.017	BKG BKG
428		J010425-711305	01 04 25.43	–71 13 05.1		0.0103		0.0068	0.0037				–0.99 0.07	0.009	BKG BKG
429		J010441-713123	01 04 41.27	–71 31 23.8		0.0349	0.0337	0.0433	0.0262				–0.19 0.18	0.035	BKG bkg
430		J010402-720149	01 04 02.01	–72 01 49.9	0.65		0.3969	0.2780	0.2221	0.1416	0.0816	157.0	–0.65 0.02	0.364	SNR SNR
431		J010432-720508	01 04 32.35	–72 05 08.9				0.0074	0.0296				2.71 0.28	0.003	HII HII
432		J010430-720721	01 04 30.88	–72 07 21.9		0.0544	0.0596	0.1645	0.0374	0.0130			–0.87 0.39	0.073	BKG BKG
433		J010404-724345	01 04 04.32	–72 43 45.5		0.0167	0.0203	0.0168	0.0086				–0.68 0.17	0.017	BKG BKG
434		J010410-733808	01 04 10.91	–73 38 08.6					0.0054						BKG bkg
435		J010404-735126	01 04 04.95	–73 51 26.0		0.0146	0.0138	0.0141	0.0067				–0.66 0.19	0.014	BKG BKG
436		J010425-742734	01 04 25.53	–74 27 34.0		0.0192	0.0219	0.0126	0.0105				–0.67 0.09	0.018	BKG BKG
437		J010442-745715	01 04 42.63	–74 57 15.8		0.0078			0.0019				–1.37 0.14	0.006	BKG BKG
438		J010442-750137	01 04 42.29	–75 01 37.2					0.0033						BKG bkg
439		J010522-705204	01 05 22.50	–70 52 04.3		0.0130	0.0120	0.0158	0.0080				–0.35 0.23	0.013	BKG bkg
440		J010557-710457	01 05 57.53	–71 04 57.2		0.0383	0.0461	0.0301	0.0188				–0.77 0.08	0.037	BKG BKG
441		J010509-712846	01 05 09.68	–71 28 46.3			0.0105		0.0024				–1.43 0.14	0.008	BKG BKG
442		J010556-714608	01 05 56.46	–71 46 08.5		0.0767	0.0784	0.0552	0.0319				–0.84 0.05	0.069	BKG BKG
443		J010550-715816	01 05 51.00	–71 58 16.3						0.0766					bkg bkg
444		J010505-715936	01 05 05.77	–71 59 36.3				0.2572	0.2602	0.0672	0.0121		–1.74 0.29	0.735	HII hii
445		J010539-720341	01 05 39.20	–72 03 41.7				0.0509	0.0396	0.0191	0.0014		–1.89 0.44	0.156	SNR snr
446		J010538-720643	01 05 38.34	–72 06 43.4				0.0301	0.0235				–0.48 0.28	0.036	HII hii
447		J010524-720923	01 05 24.20	–72 09 23.4			0.0657	0.0496	0.0404			2.6	–0.47 0.02	0.060	SNR SNR
448		J010501-721035	01 05 01.26	–72 10 35.5				0.0959	0.0833	0.0048	0.0032		–2.17 0.37	0.273	BKG BKG
449		J010531-721334	01 05 31.82	–72 13 34.8		0.0196		0.0924	0.0207	0.0093	0.0100		–0.64 0.34	0.037	BKG BKG
450		J010537-722258	01 05 37.70	–72 22 58.1						0.0040					bkg bkg

Table 1 Catalogue of the ATCA SMC sources.

1	2	3	4		5	6	7	8	9	10	11	12	13	14	15
ATCA	Group	ATCA	J2000		S_{408MHz} MC4	S_{843MHz} SUMSS	S_{843MHz} MOST	$S_{1.42GHz}$ ATCA	$S_{2.37GHz}$ ATCA	$S_{4.8GHz}$ ATCA	$S_{8.64GHz}$ ATCA	X-ray Luminosity	$\alpha \pm \Delta\alpha$	S_{1GHz} est.	Type (previous vs. here)
No.	Name	Name	R.A.	Dec	(Jy)	(Jy)	(Jy)	(Jy)	(Jy)	(Jy)	(Jy)	(ergs s^{-1})		(Jy)	
451		J010505-722319	01 05 05.62	–72 23 19.0			0.1140	0.0940	0.0649	0.0429	0.0230	16.8	–0.68 0.05	0.112	SNR SNR
452		J010525-722525	01 05 25.00	–72 25 25.4		0.0474	0.0511	0.0951	0.0241	0.0141	0.0063		–0.93 0.19	0.057	BKG BKG
453		J010532-723020	01 05 32.56	–72 30 20.4				0.0606							bkg bkg
454		J010551-725936	01 05 51.02	–72 59 36.1		0.0078			0.0012				–1.81 0.14	0.006	Bkg BKG
455		J010523-731519	01 05 23.84	–73 15 19.7		0.0342	0.0392	0.0283	0.0148				–0.84 0.11	0.033	BKG BKG
456		J010558-732515	01 05 58.95	–73 25 15.9		0.0135	0.0182		0.0053				–1.05 0.14	0.013	BKG BKG
457		J010516-735742	01 05 16.16	–73 57 42.4		0.0148	0.0165	0.0182	0.0072				–0.65 0.27	0.015	BKG BKG
458		J010536-740007	01 05 36.75	–74 00 07.1		0.0272	0.0256	0.0183	0.0152				–0.55 0.05	0.024	BKG bkg
459	0105-7432	J010536-743202	01 05 36.12	–74 32 02.3		0.0093		0.0235	0.0107				0.14 0.55	0.013	BKG bkg
460	0105-7432	J010532-743332	01 05 32.65	–74 33 32.0		0.0110	0.0116		0.0026				–1.42 0.03	0.009	BKG BKG
461		J010544-750549	01 05 44.08	–75 05 49.7		0.0276		0.0200	0.0124				–0.77 0.05	0.025	BKG BKG
462		J010620-704143	01 06 20.98	–70 41 43.1		0.0237		0.0193	0.0078				–1.07 0.23	0.022	BKG BKG
463		J010612-710215	01 06 12.38	–71 02 15.8				0.0469							BKG bkg
464	0106-7119	J010652-711928	01 06 52.36	–71 19 28.5				0.0066	0.0026				–1.82 0.28	0.012	BKG BKG
465	0106-7119	J010644-712002	01 06 44.49	–71 20 02.4		0.0072			0.0045				–0.46 0.14	0.007	BKG bkg
466		J010632-714824	01 06 32.10	–71 48 24.2				0.0117	0.0023				–3.18 0.28	0.036	BKG BKG
467		J010619-705114	01 06 19.25	–70 51 14.8		0.0134	0.0150	0.0056	0.0025				–1.69 0.05	0.011	BKG BKG
468		J010619-720527	01 06 19.49	–72 05 27.8			0.0150	0.0108	0.0182			3.4	0.19 0.28	0.013	SNR SNR
469		J010651-721843	01 06 51.21	–72 18 43.6		0.0118	0.0126	0.0176	0.0025				–1.32 0.58	0.012	BKG BKG
470		J010648-725806	01 06 48.57	–72 58 06.7		0.0140	0.0156	0.0155	0.0071				–0.63 0.21	0.014	BKG BKG
471		J010656-731320	01 06 56.99	–73 13 20.9		0.0116	0.0120		0.0038				–1.10 0.02	0.010	BKG BKG
472		J010613-734959	01 06 13.39	–73 49 59.9		0.0244	0.0236	0.0143	0.0079				–1.07 0.03	0.020	BKG BKG
473		J010659-735456	01 06 59.85	–73 54 56.3		0.0111	0.0118	0.0213	0.0047				–0.67 0.53	0.012	BKG BKG
474		J010645-741933	01 06 45.83	–74 19 33.3		0.0076	0.0112		0.0094				0.02 0.19	0.009	BKG bkg
475		J010611-744123	01 06 11.85	–74 41 23.1		0.0125		0.0077	0.0053				–0.83 0.03	0.011	BKG BKG
476		J010601-745900	01 06 01.00	–74 59 00.3					0.0068						BKG bkg
477		J010611-750442	01 06 11.35	–75 04 42.9					0.0015						BKG bkg
478		J010748-705215	01 07 48.23	–70 52 15.7		0.0073		0.0192	0.0083				0.13 0.58	0.010	BKG bkg
479		J010720-711746	01 07 20.68	–71 17 46.2		0.0066			0.0018				–1.26 0.14	0.005	BKG BKG
480		J010756-712540	01 07 56.47	–71 25 40.8		0.0117	0.0147	0.0146	0.0098				–0.24 0.16	0.013	BKG bkg
481		J010721-713731	01 07 21.29	–71 37 31.7					0.0029						BKG bkg
482		J010708-714307	01 07 08.35	–71 43 07.5		0.0457	0.0452	0.0337	0.0145				–1.06 0.14	0.040	BKG BKG
483		J010750-714510	01 07 50.18	–71 45 10.5					0.0036						BKG bkg
484		J010716-732949	01 07 16.72	–73 29 49.2		0.0280	0.0279	0.0185	0.0088				–1.09 0.09	0.024	BKG BKG
485		J010844-704655	01 08 44.07	–70 46 55.5		0.0257		0.0155	0.0090				–1.02 0.02	0.022	BKG BKG
486		J010807-713948	01 08 07.28	–71 39 48.1		0.0211	0.0219	0.0296	0.0077				–0.84 0.42	0.022	BKG BKG
487		J010819-715956	01 08 19.60	–71 59 56.6				0.1150	0.0970	0.0506	0.0329		–0.73 0.05	0.161	HII hii
488		J010808-720908	01 08 08.69	–72 09 08.6		0.0103	0.0145		0.0023				–1.62 0.17	0.009	BKG BKG
489		J010839-724715	01 08 39.22	–72 47 15.1		0.0378	0.0376	0.0321	0.0107				–1.13 0.24	0.034	BKG BKG
490		J010812-725739	01 08 12.37	–72 57 39.0		0.0140			0.0062				–0.79 0.14	0.012	Bkg BKG
491		J010848-741932	01 08 48.43	–74 19 32.2		0.0158	0.0103	0.0143	0.0068				–0.53 0.28	0.013	BKG bkg
492		J010817-745521	01 08 17.37	–74 55 21.3					0.0067						BKG bkg
493		J010929-704208	01 09 29.36	–70 42 08.3		0.0202		0.0090	0.0079				–0.91 0.22	0.015	BKG BKG
494		J010940-705006	01 09 40.32	–70 50 06.6		0.0084			0.0042				–0.67 0.14	0.007	BKG BKG
495		J010955-711342	01 09 55.61	–71 13 42.9		0.0064			0.0020				–1.13 0.14	0.005	BKG BKG
496		J010900-713309	01 09 00.98	–71 33 09.4					0.0036						BKG bkg
497		J010931-713455	01 09 31.34	–71 34 55.6	0.47	0.2350	0.2301	0.1538	0.0762				–1.01 0.05	0.196	BKG BKG
498		J010957-713544	01 09 57.62	–71 35 44.8		0.0145			0.0052				–0.99 0.14	0.012	BKG BKG
499		J010935-713821	01 09 35.70	–71 38 21.7		0.0153			0.0051				–1.06 0.14	0.013	BKG BKG
500		J010916-722035	01 09 16.99	–72 20 35.0		0.0149			0.0033				–1.46 0.14	0.012	BKG BKG

Table 1 Catalogue of the ATCA SMC sources.

1 ATCA No.	2 Group Name	3 ATCA Name	4 J2000 R.A.	Dec	5 S_{408MHz} MC4 (Jy)	6 S_{843MHz} SUMSS (Jy)	7 S_{843MHz} MOST (Jy)	8 $S_{1.42GHz}$ ATCA (Jy)	9 $S_{2.37GHz}$ ATCA (Jy)	10 $S_{4.8GHz}$ ATCA (Jy)	11 $S_{8.64GHz}$ ATCA (Jy)	12 X-ray Luminosity (ergs s^{-1})	13 $\alpha \pm \Delta\alpha$	14 S_{1GHz} est. (Jy)	15 Type (previous vs. here)
501		J010927-722224	01 09 27.11	–72 22 24.0		0.0110			0.0032				–1.20 0.14	0.009	BKG BKG
502		J010914-722934	01 09 14.14	–72 29 34.7		0.0097		0.0087	0.0041				–0.83 0.21	0.009	BKG BKG
503		J010919-725600	01 09 19.30	–72 56 00.8		0.0400	0.0425	0.0228	0.0185				–0.81 0.10	0.035	BKG BKG
504		J010920-731044	01 09 20.32	–73 10 44.6					0.0060						bkg bkg
505		J010913-731140	01 09 13.15	–73 11 40.3			0.0502	0.0975	0.0547				0.09 0.40	0.063	HII HII
506		J010912-731734	01 09 12.09	–73 17 34.8		0.0078			0.0073				–0.06 0.14	0.008	Bkg bkg
507		J010901-731806	01 09 01.19	–73 18 06.7		0.0257	0.0267	0.0361	0.0258				0.05 0.16	0.028	BKG bkg
508		J010905-734927	01 09 05.00	–73 49 27.9		0.0087			0.0043				–0.68 0.14	0.008	BKG BKG
509		J010929-740558	01 09 29.39	–74 05 58.8		0.0109	0.0111		0.0053				–0.71 0.01	0.010	BKG BKG
510		J011053-704257	01 10 53.14	–70 42 57.1		0.0242		0.0267	0.0082				–1.04 0.42	0.025	BKG BKG
511		J011019-704817	01 10 19.50	–70 48 17.2		0.0077		0.0072	0.0032				–0.85 0.24	0.008	BKG BKG
512		J011048-711419	01 10 48.56	–71 14 19.7		0.0146	0.0175	0.0197	0.0066				–0.74 0.33	0.016	BKG BKG
513		J011016-713950	01 10 16.09	–71 39 50.7				0.0044	0.0036				–0.39 0.28	0.005	BKG bkg
514		J011034-720030	01 10 34.81	–72 00 30.0		0.0067			0.0017				–1.33 0.14	0.005	Bkg BKG
515		J011050-721026	01 10 50.54	–72 10 26.8		0.0165	0.0170	0.0250	0.0105				–0.34 0.32	0.018	BKG bkg
516		J011005-722649	01 10 05.34	–72 26 49.3		0.0995	0.1280	0.1638	0.1193	0.0734	0.0298		–0.52 0.15	0.135	BKG bkg
517		J011039-722828	01 10 39.44	–72 28 28.0	0.51	0.3307	0.1690	0.2362	0.1362	0.0678	0.0184		–0.98 0.13	0.238	BKG BKG
518		J011030-723308	01 10 30.78	–72 33 08.9		0.0143	0.0154		0.0035				–1.40 0.04	0.012	BKG BKG
519		J011056-724254	01 10 56.34	–72 42 54.7				0.2266	0.0669				–2.38 0.28	0.522	BKG BKG
520		J011021-730438	01 10 21.37	–73 04 38.3		0.0624	0.0592	0.0649	0.0393				–0.37 0.14	0.060	BKG bkg
521		J011050-731425	01 10 50.78	–73 14 25.7	2.10	1.1511	1.3800	0.8424	0.5016				–0.81 0.06	1.067	BKG BKG
522		J011028-745105	01 10 28.21	–74 51 05.2		0.0257		0.0129	0.0099				–0.92 0.13	0.020	BKG BKG
523		J011031-745354	01 10 31.09	–74 53 54.5		0.0212		0.0189	0.0121				–0.54 0.11	0.020	BKG bkg
524		J011134-711415	01 11 34.21	–71 14 15.2		0.0502	0.0621	0.0383	0.0301				–0.61 0.09	0.050	BKG BKG
525		J011149-711901	01 11 49.38	–71 19 01.2		0.0361	0.0176	0.0181	0.0108				–0.80 0.30	0.022	BKG BKG
526		J011116-715135	01 11 16.00	–71 51 35.7		0.0108	0.0105	0.0097	0.0025				–1.29 0.32	0.010	BKG BKG
527		J011115-722247	01 11 15.83	–72 22 47.2				0.0349	0.0557				0.91 0.28	0.025	HII HII
528		J011103-723532	01 11 03.46	–72 35 32.9		0.0070			0.0026				–0.96 0.14	0.006	Bkg BKG
529		J011124-724223	01 11 24.56	–72 42 23.9				0.1919							bkg bkg
530		J011153-725119	01 11 53.18	–72 51 19.3		0.0105	0.0130		0.0037				–1.11 0.10	0.010	BKG BKG
531		J011132-730210	01 11 32.46	–73 02 10.4		0.0840	0.0780	0.1115	0.0774				0.02 0.17	0.086	BKG bkg
532		J011128-732932	01 11 28.68	–73 29 32.1					0.0086						bkg bkg
533		J011157-734130	01 11 57.98	–73 41 30.4		0.0322	0.0345	0.0245	0.0119				–0.96 0.11	0.029	BKG BKG
534		J011113-743339	01 11 13.98	–74 33 39.7		0.0079			0.0021				–1.28 0.14	0.006	BKG BKG
535		J011227-724803	01 12 27.24	–72 48 03.8		0.0159	0.0198	0.0415	0.0077				–0.58 0.64	0.020	BKG bkg
536		J011247-731526	01 12 47.79	–73 15 26.9		0.0134	0.0150	0.0137	0.0090				–0.40 0.11	0.014	BKG bkg
537		J011225-732752	01 12 25.75	–73 27 52.2		0.0487	0.0490	0.0447	0.0262				–0.56 0.11	0.046	BKG bkg
538		J011223-741213	01 12 23.05	–74 12 13.3		0.0484		0.0326	0.0225				–0.74 0.01	0.043	BKG BKG
539		J011216-742309	01 12 16.55	–74 23 09.1		0.0148			0.0036				–1.37 0.14	0.012	BKG BKG
540		J011231-750617	01 12 31.30	–75 06 17.8		0.0180			0.0081				–0.77 0.14	0.016	BKG BKG
541		J011355-702554	01 13 55.87	–70 25 54.9				0.0395							BKG bkg
542	0113-7114	J011358-711424	01 13 58.11	–71 14 24.9		0.0602	0.0453	0.0624	0.0220				–0.73 0.33	0.052	BKG BKG
543	0113-7114	J011344-711519	01 13 44.01	–71 15 19.5		0.0493	0.0519		0.0211				–0.85 0.03	0.044	BKG BKG
544		J011338-714120	01 13 38.64	–71 41 20.6		0.0204	0.0248	0.0130	0.0078				–1.03 0.08	0.019	BKG BKG
545		J011302-714901	01 13 02.10	–71 49 01.4			0.0126	0.0060	0.0036				–1.21 0.07	0.010	BKG BKG
546		J011353-731557	01 13 53.49	–73 15 57.1					0.0111						hii hii
547		J011333-731704	01 13 33.80	–73 17 04.4				0.0398	0.0701	0.0424	0.0349		–0.17 0.17	0.055	SNR snr
548		J011348-731753	01 13 48.75	–73 17 53.0				0.1811	0.1709				–0.11 0.28	0.188	HII HII
549		J011302-740709	01 13 02.41	–74 07 09.2		0.0060		0.0282	0.0041				–0.36 1.12	0.010	BKG bkg
550		J011332-740758	01 13 32.58	–74 07 58.3		0.0518	0.0590	0.0314	0.0176				–1.11 0.05	0.046	BKG BKG

Table 1 Catalogue of the ATCA SMC sources.

1	2	3	4		5	6	7	8	9	10	11	12	13	14	15
ATCA	Group	ATCA	J2000		S_{408MHz} MC4	S_{843MHz} SUMSS	S_{843MHz} MOST	$S_{1.42GHz}$ ATCA	$S_{2.37GHz}$ ATCA	$S_{4.8GHz}$ ATCA	$S_{8.64GHz}$ ATCA	X-ray Luminosity	$\alpha \pm \Delta\alpha$	S_{1GHz} est.	Type (previous vs. here)
No.	Name	Name	R.A.	Dec	(Jy)	(Jy)	(Jy)	(Jy)	(Jy)	(Jy)	(Jy)	(ergs s^{-1})		(Jy)	
551		J011357-742655	01 13 57.21	–74 26 55.7		0.0086			0.0034				–0.90 0.14	0.007	BKG BKG
552		J011318-743450	01 13 18.55	–74 34 50.7		0.0140		0.0104	0.0090				–0.43 0.05	0.013	BKG bkg
553		J011448-705508	01 14 48.42	–70 55 08.8				0.0057	0.0029				–1.32 0.28	0.009	BKG BKG
554		J011435-715249	01 14 35.78	–71 52 49.2	0.12	0.0797	0.0827	0.0801	0.0294				–0.71 0.16	0.071	BKG BKG
555		J011416-731549	01 14 16.92	–73 15 49.3					0.0182						hii hii
556		J011439-731821	01 14 39.47	–73 18 21.8				0.0557	0.0859	0.0778	0.0539		–0.04 0.15	0.071	HII HII
557		J011404-732005	01 14 04.93	–73 20 05.1	0.24	0.1215	0.1130	0.0868	0.0703	0.2880	0.0220		–0.43 0.26	0.130	B/H bkg
558	0114-7319	J011453-731921	01 14 53.46	–73 19 21.0				0.0168	0.0248				0.76 0.28	0.013	HII HII
559	0114-7319	J011447-732007	01 14 47.09	–73 20 07.0				0.0275	0.0297				0.15 0.28	0.026	HII HII
560		J011432-732148	01 14 32.22	–73 21 48.8		0.1563	0.1780	0.1886	0.1101	0.0481	0.0274		–0.80 0.10	0.176	B/H BKG
561		J011415-732706	01 14 15.81	–73 27 06.7					0.0015						bkg bkg
562		J011457-732805	01 14 57.78	–73 28 05.1		0.0117			0.0036				–1.14 0.14	0.010	Bkg BKG
563		J011428-733306	01 14 28.31	–73 33 06.2		0.0089			0.0022				–1.35 0.14	0.007	Bkg BKG
564		J011412-740912	01 14 12.70	–74 09 12.1				0.0057	0.0019				–2.15 0.28	0.012	Bkg BKG
565		J011449-741804	01 14 49.58	–74 18 04.1					0.0018						BKG bkg
566		J011447-742047	01 14 47.68	–74 20 47.1					0.0030						BKG bkg
567		J011456-743400	01 14 56.35	–74 34 00.9		0.0081			0.0020				–1.35 0.14	0.006	BKG BKG
568		J011500-703707	01 15 00.85	–70 37 07.4		0.0078			0.0031				–0.89 0.14	0.007	BKG BKG
569		J011559-710442	01 15 59.83	–71 04 42.0		0.0338	0.0374	0.0218	0.0136				–0.93 0.04	0.030	BKG BKG
570		J011548-714007	01 15 48.08	–71 40 07.7		0.0087		0.0091	0.0025				–1.20 0.44	0.009	BKG BKG
571	0115-7200	J011517-715931	01 15 17.83	–71 59 31.4			0.0116		0.0028				–1.38 0.14	0.009	BKG BKG
572	0115-7200	J011534-720006	01 15 34.10	–72 00 06.7		0.0243	0.0304	0.0425	0.0106				–0.75 0.47	0.028	BKG BKG
573		J011525-723005	01 15 25.50	–72 30 05.3					0.0018						bkg bkg
574		J011528-741112	01 15 28.59	–74 11 12.8		0.0075			0.0021				–1.23 0.14	0.006	BKG BKG
575		J011551-741107	01 15 51.87	–74 11 07.5		0.0086		0.0068	0.0024				–1.23 0.26	0.008	BKG BKG
576		J011506-743645	01 15 06.37	–74 36 45.4		0.0079		0.0097	0.0036				–0.76 0.39	0.008	BKG BKG
577		J011623-702950	01 16 23.88	–70 29 50.8		0.0684			0.0027				–3.13 0.14	0.040	BKG BKG
578		J011611-711029	01 16 11.19	–71 10 29.2		0.0348	0.0366	0.0228	0.0149				–0.85 0.02	0.031	BKG BKG
579		J011635-712602	01 16 35.58	–71 26 02.6		0.0305	0.0273	0.0157	0.0060				–1.49 0.10	0.023	BKG BKG
580		J011608-731029	01 16 08.51	–73 10 29.5				0.0111	0.0323				2.09 0.28	0.005	HII HII
581		J011628-731440	01 16 28.94	–73 14 40.8	0.24	0.1391	0.1340	0.0880	0.1709				–0.27 0.22	0.146	B/H bkg
582		J011616-732655	01 16 16.78	–73 26 55.4	0.16	0.0674	0.0634	0.0492	0.0299				–0.91 0.08	0.063	BKG BKG
583		J011611-733858	01 16 11.88	–73 38 58.7	0.33	0.1443	0.1330	0.0933	0.0566				–0.98 0.05	0.127	BKG BKG
584		J011649-734233	01 16 49.78	–73 42 33.3					0.0041						bkg bkg
585		J011604-735358	01 16 04.51	–73 53 58.9		0.0141		0.0109	0.0070				–0.68 0.06	0.013	BKG BKG
586		J011609-742813	01 16 09.75	–74 28 13.8		0.0398		0.0186	0.0150				–0.95 0.17	0.031	BKG BKG
587		J011606-743213	01 16 06.47	–74 32 13.7		0.0086		0.0078	0.0053				–0.47 0.10	0.008	BKG bkg
588		J011645-743535	01 16 45.89	–74 35 35.0				0.0113	0.0139				0.40 0.28	0.010	Bkg bkg
589		J011603-744327	01 16 03.04	–74 43 27.2		0.0373		0.0184	0.0116				–1.13 0.08	0.030	BKG BKG
590		J011719-703438	01 17 19.13	–70 34 38.2		0.0145		0.0163	0.0020				–1.91 0.72	0.015	BKG BKG
591		J011719-710043	01 17 19.29	–71 00 43.7		0.0110			0.0016				–1.87 0.14	0.008	BKG BKG
592		J011719-714118	01 17 19.59	–71 41 18.2		0.0285	0.0205	0.0173	0.0078				–1.05 0.18	0.021	BKG BKG
593		J011758-721911	01 17 58.04	–72 19 11.9		0.0185	0.0201	0.0140	0.0062				–1.05 0.13	0.017	BKG BKG
594		J011722-730917	01 17 22.04	–73 09 17.6		0.0228	0.0203	0.0133	0.0096				–0.79 0.06	0.019	BKG BKG
595		J011731-743339	01 17 31.86	–74 33 39.0		0.0097		0.0175	0.0086				–0.11 0.42	0.012	BKG bkg
596		J011726-744659	01 17 26.00	–74 46 59.7		0.0129		0.0071	0.0037				–1.21 0.02	0.011	BKG BKG
597		J011759-745003	01 17 59.86	–74 50 03.7		0.0243		0.0109	0.0056				–1.42 0.04	0.019	BKG BKG
598		J011744-745545	01 17 44.13	–74 55 45.4		0.0089			0.0031				–1.02 0.14	0.007	BKG BKG
599		J011724-745837	01 17 24.71	–74 58 37.8					0.0041						BKG bkg
600		J011841-715216	01 18 41.76	–71 52 16.1		0.0260	0.0190	0.0125	0.0111				–0.71 0.17	0.019	BKG BKG

Table 1 Catalogue of the ATCA SMC sources.

1	2	3	4		5	6	7	8	9	10	11	12	13	14	15
ATCA	Group	ATCA	J2000		S_{408MHz} MC4	S_{843MHz} SUMSS	S_{843MHz} MOST	$S_{1.42GHz}$ ATCA	$S_{2.37GHz}$ ATCA	$S_{4.8GHz}$ ATCA	$S_{8.64GHz}$ ATCA	X-ray Luminosity	$\alpha \pm \Delta\alpha$	S_{1GHz} est.	Type (previous vs. here)
No.	Name	Name	R.A.	Dec	(Jy)	(Jy)	(Jy)	(Jy)	(Jy)	(Jy)	(Jy)	(ergs s^{-1})		(Jy)	
601		J011834-720647	01 18 34.19	–72 06 47.7		0.0195	0.0195	0.0109	0.0057				–1.18 0.02	0.016	BKG BKG
602		J011856-724258	01 18 56.71	–72 42 58.3		0.0119			0.0017				–1.88 0.14	0.009	Bkg BKG
603		J011836-725724	01 18 36.81	–72 57 24.1		0.0109		0.0109	0.0057				–0.63 0.21	0.011	BKG BKG
604		J011825-731754	01 18 25.37	–73 17 54.2		0.0098			0.0058				–0.51 0.14	0.009	Bkg bkg
605		J011850-742610	01 18 50.77	–74 26 10.5		0.0096			0.0032				–1.06 0.14	0.008	BKG BKG
606		J011846-744438	01 18 46.60	–74 44 38.6				0.0109	0.0043				–1.82 0.28	0.021	BKG BKG
607		J011806-745824	01 18 06.34	–74 58 24.3		0.0324		0.0244	0.0104				–1.10 0.19	0.030	BKG BKG
608		J011918-710531	01 19 18.50	–71 05 31.6	0.36	0.1589	0.1600	0.1078	0.0636				–0.96 0.04	0.144	BKG BKG
609		J011934-725933	01 19 34.29	–72 59 33.1		0.0069			0.0016				–1.41 0.14	0.005	BKG BKG
610		J011909-744211	01 19 09.07	–74 42 11.1		0.0334		0.0202	0.0126				–0.94 0.01	0.028	BKG BKG
611		J011910-750146	01 19 10.61	–75 01 46.8		0.0131		0.0065	0.0049				–0.95 0.13	0.010	BKG BKG
612		J011958-750311	01 19 58.28	–75 03 11.6		0.0197		0.0133	0.0059				–1.17 0.14	0.017	BKG BKG
613		J012011-703608	01 20 11.50	–70 36 08.6		0.0340			0.0096				–1.22 0.14	0.028	BKG BKG
614		J012037-703845	01 20 37.49	–70 38 45.8	0.22	0.1158		0.0943	0.0452				–0.85 0.09	0.105	BKG BKG
615		J012055-711043	01 20 55.62	–71 10 43.4		0.0080			0.0012				–1.84 0.14	0.006	BKG BKG
616		J012027-712641	01 20 27.04	–71 26 41.2		0.0200	0.0125	0.0070	0.0030				–1.60 0.19	0.012	BKG BKG
617		J012035-713326	01 20 35.64	–71 33 26.3		0.0088			0.0017				–1.59 0.14	0.007	BKG BKG
618		J012037-713627	01 20 37.17	–71 36 27.9					0.0015						BKG bkg
619		J012023-721956	01 20 23.56	–72 19 56.9		0.0325	0.0345	0.0204	0.0136				–0.88 0.03	0.029	BKG BKG
620		J012007-725014	01 20 07.50	–72 50 14.5		0.0200	0.0163	0.0165	0.0071				–0.83 0.21	0.017	BKG BKG
621		J012055-733456	01 20 55.04	–73 34 56.6		0.0551	0.0377	0.0458	0.0316				–0.32 0.18	0.045	BKG bkg
622		J012004-745742	01 20 04.57	–74 57 42.8					0.0045						BKG bkg
623		J012036-750634	01 20 36.43	–75 06 34.7		0.0151		0.0405	0.0172				0.13 0.59	0.021	BKG bkg
624		J012153-712004	01 21 53.54	–71 20 04.5		0.0064			0.0017				–1.28 0.14	0.005	BKG BKG
625		J012128-714335	01 21 28.63	–71 43 35.9		0.0177	0.0184	0.0089	0.0053				–1.20 0.05	0.014	BKG BKG
626		J012154-715531	01 21 54.26	–71 55 31.2		0.0253	0.0170	0.0142	0.0081				–0.89 0.17	0.018	BKG BKG
627		J012129-721547	01 21 29.23	–72 15 47.8					0.0014						BKG bkg
628		J012150-740012	01 21 50.87	–74 00 12.0		0.1019	0.0841	0.0739	0.0408				–0.76 0.12	0.084	BKG BKG
629		J012208-702921	01 22 08.05	–70 29 21.3		0.0753		0.0313	0.0042				–2.79 0.37	0.057	BKG BKG
630		J012251-705428	01 22 51.77	–70 54 28.2		0.0079		0.0150	0.0111				0.33 0.30	0.010	BKG bkg
631		J012223-713414	01 22 23.68	–71 34 14.6		0.0069			0.0018				–1.30 0.14	0.006	BKG BKG
632		J012209-713953	01 22 09.77	–71 39 53.7		0.0386	0.0376	0.0231	0.0149				–0.91 0.02	0.032	BKG BKG
633		J012207-714733	01 22 07.06	–71 47 33.6		0.0092			0.0020				–1.48 0.14	0.007	BKG BKG
634		J012233-714725	01 22 33.94	–71 47 25.2		0.0131		0.0217	0.0148				0.12 0.29	0.015	BKG bkg
635		J012258-714850	01 22 58.02	–71 48 50.7		0.0094	0.0122		0.0029				–1.26 0.13	0.009	BKG BKG
636		J012250-715043	01 22 50.58	–71 50 43.9		0.0748	0.0596	0.0533	0.0291				–0.77 0.13	0.061	BKG BKG
637		J012220-730356	01 22 20.83	–73 03 56.3		0.0131	0.0121		0.0029				–1.42 0.04	0.010	BKG BKG
638		J012254-731429	01 22 54.39	–73 14 29.5					0.0047						BKG bkg
639		J012236-733819	01 22 36.01	–73 38 19.2		0.0612	0.0589	0.0402	0.0234				–0.90 0.04	0.052	BKG BKG
640		J012238-741018	01 22 38.45	–74 10 18.3		0.0392		0.0139	0.0143				–0.98 0.34	0.028	BKG BKG
641		J012247-742631	01 22 47.21	–74 26 31.9		0.0107		0.0074	0.0041				–0.93 0.07	0.009	BKG BKG
642		J012248-743526	01 22 48.61	–74 35 26.6		0.0096		0.0069	0.0026				–1.26 0.21	0.009	BKG BKG
643		J012200-744638	01 22 00.29	–74 46 38.9		0.0274		0.0173	0.0137				–0.67 0.07	0.024	BKG BKG
644		J012257-751506	01 22 57.96	–75 15 06.1	1.64	0.8717		0.2752	0.0152				–2.54 0.54	0.305	BKG BKG
645		J012335-703236	01 23 35.39	–70 32 36.5		0.0241			0.0047				–1.58 0.14	0.018	BKG BKG
646		J012320-703739	01 23 20.64	–70 37 39.0		0.0515		0.0258	0.0189				–0.97 0.12	0.041	BKG BKG
647		J012306-711120	01 23 06.20	–71 11 20.9		0.0157			0.0041				–1.30 0.14	0.013	BKG BKG
648		J012324-714735	01 23 24.19	–71 47 35.7		0.0098			0.0012				–2.03 0.14	0.007	BKG BKG
649		J012330-721815	01 23 30.53	–72 18 15.3		0.0295	0.0288	0.0181	0.0150				–0.67 0.07	0.025	BKG BKG
650		J012318-723606	01 23 18.40	–72 36 06.1		0.0105	0.0119		0.0046				–0.86 0.06	0.010	BKG BKG

Table 1 Catalogue of the ATCA SMC sources.

1	2	3	4		5	6	7	8	9	10	11	12	13	14	15
ATCA	Group	ATCA	J2000		S_{408MHz} MC4	S_{843MHz} SUMSS	S_{843MHz} MOST	$S_{1.42GHz}$ ATCA	$S_{2.37GHz}$ ATCA	$S_{4.8GHz}$ ATCA	$S_{8.64GHz}$ ATCA	X-ray Luminosity	$\alpha \pm \Delta\alpha$	S_{1GHz} est.	Type (previous vs. here)
No.	Name	Name	R.A.	Dec	(Jy)	(Jy)	(Jy)	(Jy)	(Jy)	(Jy)	(Jy)	(ergs s^{-1})		(Jy)	
651		J012312-732847	01 23 12.32	–73 28 47.7					0.0033						BKG bkg
652		J012320-734527	01 23 20.82	–73 45 27.2					0.0090						BKG bkg
653		J012349-735039	01 23 49.67	–73 50 39.8	0.38	0.1893	0.1740	0.1056	0.0638				–1.02 0.02	0.152	BKG BKG
654		J012324-735558	01 23 24.00	–73 55 58.3		0.0216	0.0280	0.0316	0.0321				0.28 0.12	0.026	BKG bkg
655		J012324-740242	01 23 24.09	–74 02 42.0		0.0150			0.0059				–0.90 0.14	0.013	BKG BKG
656		J012310-741813	01 23 10.36	–74 18 13.0		0.0075		0.0059	0.0045				–0.49 0.01	0.007	BKG bkg
657		J012352-744140	01 23 52.55	–74 41 40.9		0.0562		0.0415	0.0211				–0.95 0.12	0.051	BKG BKG
658		J012311-745416	01 23 11.02	–74 54 16.5		0.0139		0.0132	0.0061				–0.80 0.24	0.014	BKG BKG
659		J012415-704152	01 24 15.57	–70 41 52.6		0.0175			0.0058				–1.07 0.14	0.015	BKG BKG
660		J012417-711204	01 24 17.86	–71 12 04.6		0.0250		0.0109	0.0108				–0.81 0.26	0.019	BKG BKG
661		J012433-712646	01 24 33.65	–71 26 46.0		0.0541		0.0308	0.0221				–0.87 0.07	0.045	BKG BKG
662		J012455-720630	01 24 55.36	–72 06 30.3		0.0155	0.0122	0.0063	0.0027				–1.57 0.10	0.011	BKG BKG
663		J012408-730905	01 24 08.24	–73 09 05.5				0.0941	0.0925	0.0106	0.1092		–0.31 0.69	0.083	HII hii
664		J012416-734115	01 24 16.43	–73 41 15.0					0.0015						BKG bkg
665		J012542-712939	01 25 42.33	–71 29 39.0		0.0091			0.0012				–1.96 0.14	0.007	BKG BKG
666		J012525-714906	01 25 25.77	–71 49 06.9		0.0063			0.0037				–0.52 0.14	0.006	BKG bkg
667		J012548-715136	01 25 48.42	–71 51 36.5		0.0366	0.0305	0.0087	0.0053				–1.86 0.22	0.023	BKG BKG
668	0125-7229	J012522-722923	01 25 22.34	–72 29 23.4		0.0606	0.0370		0.0265				–0.56 0.24	0.043	BKG bkg
669	0125-7229	J012530-722948	01 25 30.12	–72 29 48.7				0.0342	0.0177				–1.29 0.28	0.054	BKG BKG
670		J012546-731604	01 25 46.58	–73 16 04.6		0.0902	0.0895	0.0649	0.0378	0.0172			–0.94 0.05	0.081	BKG BKG
671		J012536-732250	01 25 36.51	–73 22 50.8				0.0735	0.0627	0.0228			–0.99 0.18	0.118	BKG BKG
672		J012559-735418	01 25 59.65	–73 54 18.4		0.0338	0.0315	0.0180	0.0109				–1.07 0.04	0.027	BKG BKG
673		J012535-735634	01 25 35.04	–73 56 34.9		0.0283	0.0234	0.0188	0.0099				–0.89 0.11	0.023	BKG BKG
674		J012550-740008	01 25 50.65	–74 00 08.3		0.0176		0.0076	0.0042				–1.39 0.08	0.013	BKG BKG
675		J012624-705023	01 26 24.55	–70 50 23.8		0.0554		0.0213	0.0050				–2.33 0.17	0.041	BKG BKG
676		J012617-730754	01 26 17.45	–73 07 54.2		0.0876	0.0617	0.0529	0.0326				–0.77 0.15	0.065	BKG BKG
677		J012639-731503	01 26 39.97	–73 15 03.0		0.0934	0.0982	0.0586	0.0367				–0.93 0.02	0.082	BKG BKG
678		J012650-731635	01 26 50.55	–73 16 35.4					0.0046						BKG bkg
679		J012629-732715	01 26 29.17	–73 27 15.4		0.0552	0.0575	0.0382	0.0310	0.0186			–0.62 0.03	0.050	BKG BKG
680		J012647-734320	01 26 47.87	–73 43 20.3		0.0081	0.0109		0.0029				–1.14 0.14	0.008	BKG BKG
681		J012649-740313	01 26 49.26	–74 03 13.2		0.0087		0.0068	0.0029				–1.06 0.20	0.008	BKG BKG
682		J012640-741622	01 26 40.85	–74 16 22.2		0.0086			0.0022				–1.32 0.14	0.007	BKG BKG
683		J012633-744852	01 26 33.39	–74 48 52.1		0.0100			0.0014				–1.90 0.14	0.007	BKG BKG
684		J012656-751113	01 26 56.00	–75 11 13.8		0.0761		0.0289	0.0028				–3.19 0.45	0.056	BKG BKG
685		J012733-713640	01 27 33.97	–71 36 40.7		0.1044	0.0725	0.0496	0.0184				–1.46 0.19	0.071	BKG BKG
686		J012705-715051	01 27 05.76	–71 50 51.9		0.0068		0.0100	0.0015				–1.46 0.74	0.008	BKG BKG
687		J012758-720534	01 27 58.50	–72 05 34.5		0.0300	0.0261	0.0118	0.0057				–1.55 0.07	0.021	BKG BKG
688		J012712-730951	01 27 12.04	–73 09 51.9				0.0260							BKG bkg
689		J012753-731105	01 27 53.04	–73 11 05.3		0.0145	0.0169	0.0130	0.0099				–0.44 0.07	0.015	BKG bkg
690		J012823-715437	01 28 23.15	–71 54 37.1		0.0167		0.0107	0.0022				–1.96 0.37	0.014	BKG BKG
691		J012814-730801	01 28 14.99	–73 08 01.1		0.0132	0.0155	0.0076	0.0046				–1.11 0.07	0.012	BKG BKG
692		J012828-734141	01 28 28.78	–73 41 41.7		0.0114	0.0138		0.0069				–0.58 0.09	0.011	BKG bkg
693		J012805-741110	01 28 05.92	–74 11 10.1		0.0111		0.0078	0.0035				–1.12 0.15	0.010	BKG BKG
694		J012815-744152	01 28 15.57	–74 41 52.5					0.0019						BKG bkg
695		J012834-750947	01 28 34.48	–75 09 47.5				0.0134							BKG bkg
696		J012812-751257	01 28 12.78	–75 12 57.0		0.4004		0.1087					–2.50 0.27	0.261	BKG BKG
697		J012904-715159	01 29 04.59	–71 51 59.4		0.0257		0.0354					0.61 0.27	0.029	BKG bkg
698		J012928-730643	01 29 28.13	–73 06 43.8		0.0068	0.0100		0.0026				–1.12 0.19	0.007	BKG BKG
699		J012924-733150	01 29 24.80	–73 31 50.6		0.0228	0.0305		0.0161				–0.48 0.14	0.024	BKG bkg
700		J012930-733313	01 29 30.26	–73 33 13.4	0.30		0.1670	0.2480	0.1109	0.1270	0.0509		–0.50 0.11	0.199	B/H hii

Table 1 Catalogue of the ATCA SMC sources.

1 ATCA No.	2 Group Name	3 ATCA Name	4 J2000 R.A.	4 J2000 Dec	5 S_{408MHz} MC4 (Jy)	6 S_{843MHz} SUMSS (Jy)	7 S_{843MHz} MOST (Jy)	8 $S_{1.42GHz}$ ATCA (Jy)	9 $S_{2.37GHz}$ ATCA (Jy)	10 $S_{4.8GHz}$ ATCA (Jy)	11 $S_{8.64GHz}$ ATCA (Jy)	12 X-ray Luminosity (ergs s^{-1})	13 $\alpha \pm \Delta\alpha$	14 S_{1GHz} est. (Jy)	15 Type (previous vs. here)
701		J013032-731740	01 30 32.44	–73 17 40.2		0.0479	0.0505	0.0222	0.0113				–1.43 0.03	0.038	BKG BKG
702		J013013-742025	01 30 13.87	–74 20 25.8		0.0142		0.0147	0.0207				0.36 0.10	0.014	BKG bkg
703		J013016-742540	01 30 16.75	–74 25 40.7		0.0069		0.0079	0.0038				–0.58 0.28	0.007	BKG bkg
704		J013024-743930	01 30 24.50	–74 39 30.0				0.0102	0.0119				0.30 0.28	0.009	BKG bkg
705		J013146-734958	01 31 46.05	–73 49 58.1		0.0294		0.0176	0.0036				–2.03 0.35	0.025	BKG BKG
706		J013124-740042	01 31 24.09	–74 00 42.5		0.0365	0.0397	0.0308	0.0083				–1.37 0.28	0.033	BKG BKG
707		J013156-741726	01 31 56.72	–74 17 26.1		0.0082			0.0019				–1.42 0.14	0.006	BKG BKG
708		J013109-745842	01 31 09.62	–74 58 42.1		0.0180			0.0029				–1.77 0.14	0.013	BKG BKG
709		J013232-724008	01 32 32.50	–72 40 08.8	0.58	0.3590	0.3830						–0.62 0.05	0.334	BKG BKG
710		J013216-733905	01 32 16.37	–73 39 05.8	0.20	0.0643			0.0036				–2.32 0.20	0.031	BKG BKG
711		J013229-734126	01 32 29.71	–73 41 26.9		0.0514			0.0054				–2.18 0.14	0.035	BKG BKG
712		J013243-734414	01 32 43.02	–73 44 14.5		0.0681		0.0310	0.0049				–2.54 0.35	0.053	BKG BKG
713		J013212-742016	01 32 12.31	–74 20 16.3		0.0108		0.0100	0.0018				–1.73 0.53	0.011	BKG BKG
714		J013245-743357	01 32 45.43	–74 33 57.5		0.0120		0.0120	0.0035				–1.19 0.40	0.012	BKG BKG
715		J013309-742917	01 33 09.03	–74 29 17.1		0.0561		0.0382	0.0127				–1.44 0.24	0.050	BKG BKG
716		J013328-743636	01 33 28.81	–74 36 36.8		0.0378		0.0273	0.0121				–1.10 0.16	0.034	BKG BKG
717		J013342-744610	01 33 42.37	–74 46 10.0		0.0590		0.0440	0.0073				–2.02 0.49	0.054	BKG BKG

Table 2 Overview of extragalactic optical SNR sample properties (adapted from Matonick & Fesen 1997 and references therein). Type and inclination, *i*, are taken from Tully (1988). Note that 'Mode' is the peak of respective histograms[1].

Galaxy[1]	Type	*i* (deg)	R (Mpc)	D_{galaxy} (kpc)	M (H I) ($10^9 M_\odot$)	Number SNRs	SNR Diameter (pc) Mode	SNR Diameter (pc) Max	SNR Hα (ergs cm^{-2}s^{-1}) Mode	SNR [S II]/Hα Mode
LMC	Sm	35	0.055	10.6	0.8	28	30	90	...	0.60
SMC	Im	61	0.063	4.7	0.8	11	58	62	...	0.70
M31	Sb	78	0.69	31.2	4.0	221	32	195	4.4×10^{-15}	0.52
M33	Scd	56	0.84	12.8	1.8	98	35	126	1.3×10^{-14}	0.65
NGC 300	Sd	46	2.1	11.7	2.4	28	43	200	4.5×10^{-15}	0.75
NGC 2403	Scd	62	3.2	19.9	3.6	35	70	170	2.0×10^{-14}	0.58
NGC 7793	Sdm	50	3.4	8.5	0.7	28	32	260	2.0×10^{-14}	0.50
M81	Sab	60	3.6	21.2	3.0	41	30	130	2.0×10^{-15}	0.67
NGC 5204	Sm	53	4.8	6.1	0.6	3	40	60	5.5×10^{-15}	0.58
M101	Scd	0	5.4	37.4	11.3	93	30	300	3.2×10^{-15}	0.55
NGC 6946	Scd	42	5.5	23.8	6.3	27	30	180	2.4×10^{-15}	0.55
NGC 5585	Sd	51	7.0	10.4	1.4	5	60	130	1.4×10^{-14}	0.59

APPENDIX B

SUPPLEMENTAL EXTRAGALACTIC SNR RESEARCH NOTES

This section contains supplemental discussion and notes that were not used in the thesis proper. It is hoped this may be a useful 'state of the art' summary for other researchers in the field.

After the work of Mathewson & Clarke (1973a), a number of observers have carried out surveys in the optical, X-ray and radio realms to find SNRs in other galaxies. S. D'Odorico, W. P. Blair, R. P. Kirshner, R. A. Chevalier and M. A. Dopita performed optical interference surveys in the late 1970's and early 1980's identifying ~ 40 SNRs in Local Group spirals (Long 1996). Radio surveys at this time were less successful, detecting only about 20 SNRs during the 1980s; some previously detected as optical SNRs. X-ray studies also yielded slow progress during this time with only a few SNRs detected. X-ray surveys of the Magellanic Clouds (MCs) using the *Einstein* Observatory was a notable exception. Long et al. (1981) reported that of 97 sources found in the Large Magellanic Cloud, a surprising number were SNRs. Six definite SNRs and 25 suspected SNRs were reported based on temporal, spatial and spectral information.

More recently, Matonick & Fesen (1997) presented an overview of optical extragalactic SNR searches (Table 2), combining their results with SNRs found within the MCs, M31, M33, NGC 300 and NGC 7793. The average (mode) diameter of these SNRs was ~ 40 pc, suggesting they are selected for evolutionary stage.

[1]SNR references for Table 2: LMC, Mathewson et al. (1983b, 1984, 1985), Chu & Kennicutt (1988), van den Bergh (1988), Smith et al. (1994); SMC, Mathewson & Clarke (1972, 1973b), Mathewson et al. (1983b, 1984); M31, D'Odorico et al. (1980), Blair et al. (1981), Walterbos & Braun (1992), Braun & Walterbos (1993), Magnier et al. (1995); M33, Gordon (1994); NGC 300 and NGC 7793, Blair & Long (1997); the rest, Matonick & Fesen (1997).

Large Magellanic Cloud

The Large Magellanic Cloud is the second closest galaxy to the Milky Way, with only the Sagittarius Dwarf Spheroidal ($\sim$ 16 kpc) located closer to the Galactic centre. Alves (2004) reviewed distance and structure studies of the Large Magellanic Cloud (LMC), finding that the average of 14 recent measurements converge to a modulus of 18.50 ± 0.02 magnitude ($\sim$ 50.1 kpc). These results demonstrate a high level of consistency and the possibility that a consensus on the LMC distance has been reached.

The de Vaucouleurs model of the LMC as a flattened disc tilted to the plane of the sky ($i = 40\,\mathrm{deg}$) remains one of its best descriptions. This galaxy also has an optical bar that is different from its spiral radio distribution (Filipović et al. 1998b). Estimates of the LMC's thickness range from 100 – 300 pc in its population of young stars to $\sim$ 9 kpc in its older population.

LMC SNRs can be observed at ground-based optical and radio telescopes with resolutions of 0.25 pc. Previous generations of orbital X-ray telescopes could achieve resolutions to 1.5 pc. New instruments (e.g. *Chandra* at 0.5 arcsec) may approach resolutions of 0.13 pc (Weisskopf et al. 2002).

The first identifications of SNRs in the LMC were suggested by Mathewson & Healey (1964). Comparisons of radio observations to Hα nebulae (catalogued by Henize 1956) revealed good agreement for most H II regions except for three suspicious LMC objects (N49, N63A and N132D). They felt these objects were SNRs. Later optical emission-line imaging studies confirmed they were similar to Galactic SNRs. A few years later, Mathewson & Clarke (1973a) searched again for SNRs in the LMC, finding nine. When added to the previous three, they had discovered a total of 12 (Magnier et al. 1995).

In the 1986 collaborative study by Filipović et al. (1998b), they found that from 62 'known' SNRs (excluding SN 1987A), 34 obeyed their identification criteria for SNRs. Four well-known SNRs could not be detected and 24 candidates were named.

As discussed previously, Long et al. (1981) used X-ray observations from the *Einstein* observatory to find SNRs in the LMC. These included six definite SNRs and 25 candidate SNRs and were some of the first X-ray observations of this galaxy.

Mathewson et al. (1983a) discussed the classification of SNR types in the MCs using 32 X-ray sources with optical identifications. These were separated into four classes: the evolved, the oxygen-rich, the Balmer-dominated and the Crab-like. They listed three examples of oxygen-rich SNRs (N132D, 0540-69.3 and 0102-72.3) which had intrinsic X-ray luminosities much greater than Cas A. Balmer-dominated SNRs (0505-67.9, 0509-67.5, 0519-69.0 and 0548-70.4) had strong Balmer lines of hydrogen with very weak [O III] and [S II]

emission. These SNRs may have resulted from Type I SNe since their properties are similar to Galactic Type I SNe (Tycho, Kepler and SN 1006). N157B was suggested as a 'Crab-like' SNR because it had a centrally condensed radio structure, a flat radio spectral index and a non-thermal X-ray spectrum.

Various types of X-ray morphology are mirrored in the optical appearance of remnants (Mathewson et al. 1983b). Optical observations ([OIII], Hα, Hβ and [S II]) using the Anglo-Australian telescope (3.9-meter mirror) and the image photon counting system show that many are circularly symmetric and have limb-brightened shells. In some cases only a fraction of the entire shell is seen. Other remnants have diffuse, sometimes patchy optical emission covering an irregularly shaped area roughly the size of their X-ray regions. 'Crab-like' X-ray objects are dominated by a single bright knot of emission. They also noted that X-ray and optical sizes agreed to better than 20%.

There were some notable exceptions to this 'rule of size' which included N157B's brightest optical knot. This was displaced by 30″ from N157's X-ray emission. Another remnant, N63A, had a bright X-ray shell nearly three times its optical diameter. They found that N132D and N49B also had X-ray diameters significantly larger than their optical extent. The issue of a SNR's size at different wavelength domains continue to require further study.

D. S. Mathewson and F. D. Seward used *Einstein* data to categorize SNR morphology. Later, Williams et al. (1999) classified 31 X-ray SNRs within the LMC, this time using archival *ROSAT* data. They included SNR morphology catagories such as shell-type, diffuse face, centrally brightened, point-source dominated and irregular.

Williams et al. (1999) model their observations based on the evolution of SNRs. They suggest the observed X-ray emission is initially generated at the shock front, where the freshly shocked million kelvin gas is prominent; this results in a shell-type morphology. As the front encounters and envelops clumps in the surrounding ISM, these clumps are shock-heated and lag behind. Such clumps evaporate into the interior of the SNR, causing local increases in gas density raising the surface brightness of interior X-rays to detectable levels. This results in a diffuse face morphology leading to a centrally brightened one when the interior density rises due to clump evaporation. Their model may be modified by additional factors, such as the presence of a central neutron star.

Haberl & Pietsch (1999) published a catalogue of *ROSAT* X-ray sources in the LMC containing 144 likely identifications. 46 sources were associated with SNRs and candidates, most already detected by previous X-ray missions. Observations were analysed in five energy bands (soft: 0.1–0.4 keV, hard: 0.5–2.0 keV, hard1: 0.5–0.9 keV, hard2: 0.9–2.0 keV and broad: 0.1–2.4 keV). From preliminary investigations of the

data, F. Haberl showed that both extent and likelihood in combination with hardness ratios[2] can be used the identify SNRs. They give a very restrictive (and rather technical) classification scheme (see their Table 3).

Haberl & Pietsch (1999) named eight new Position Sensitive Proportional Counter (PSPC) sources as SNRs. They also found one promising new SNR candidate with extended X-ray emission located far north of other SNRs in the LMC.

There are also some unusual SNRs in the LMC as noted by Dickel (2005) which include LMC N11L and N49. Images in radio, optical and X-ray show that N11L has an extended region and a one-sided "jet" structure as noted by Williams et al. (1999). Is this the result of a γ-ray burst when the remnant's progenitor exploded? N49 has within its boundary the site of a γ-ray event that occurred on March 5, 1979. This area has been found to fluctuate and is classified as the Soft Gamma-ray Repeater, SGR 0525-66. This association needs further investigation.

M31

In addition to the MC's, there have been a number of SNR searches in other nearby galaxies. Perhaps one of the first and most notable was the catalogue compiled by D'Odorico et al. (1980). This catalogue presented coordinates and finding charts of optical SNR candidates in several nearby galaxies including M31, NGC 253, IC 1613, IC 342, M33, NGC 2403 and NGC 6822. SNRs were detected primarily by comparing photographs of the galaxies in Hα and [S II]. Data was obtained from plates made from the Asiago 1.82-meter telescope, the 48-in Schmidt camera of Hale Observatory and the UK 48-in Schmidt camera at Siding Spring.

At a distance of 780 kpc, the Andromeda galaxy (M31) is the closest spiral galaxy that shares similar morphology, metallicity and size with the Milky Way. This makes it an excellent candidate for comparitive studies of SNRs. D'Odorico et al. (1980) reported 19 candidate SNRs in the Andromeda galaxy with at least one confirmation. These observations had been preceeded eight years by Rubin et al. (1972) who made tentative identifications of 7 SNRs. Blair et al. (1981) used optical image-tube photographs of eight fields within M31 with interference filters to isolate [S II] and Hα + [N II] emission revealing 11 nebulae that resembled SNRs.

[2]Basically, this is the ratio of the difference and sum of counts in two X-ray energy bands that allow a rough determination of the source's spectrum. In the analysis of *ROSAT* data, often two hardness ratios, HR1 and HR2 are defined (e.g. Read & Pietsch 1999). HR1 values are most sensitive to variations in the absorbing column, while HR2 estimates trace the power law index or temperature. It sometimes is useful to compare tabulated values with plots in the literature which show the variation of HR1 and HR2 for simple spectral models (see Haberl & Pietsch 1999 or Kong & Di Stefano 2003 for examples).

The Andromeda SNR list was greatly increased by Braun & Walterbos (1993) who found a sample of 52 'forbidden-line' SNRs using a [S II]:Hα ratio cut-off of 0.5. These observations focused on the spiral arms located in the northeastern half of the galaxy. They also included in this study, 24 previous VLA radio SNR detections (1465 MHz) coinciding with optical remnants. Had they observed the entire disk of M31, there may have been over a hundred remnants with both optical and radio emission. This number does not take into account potential SNR dectections based on radio criteria alone. After assessing the completeness of their sample, they found a SNe rate[3] of 1 in 80 years.

Williams et al. (1995) used pure optical emission-line CCD images ([S II]λ6724:Hα) to identify 105 SNR candidates within M31, of which 13 were previously identified. Their effective resolution of only 5 arcsec was equivalent to 18 pc. Magnier et al. (1995) also used CCD imaging to survey 1.0 square degree of the disk of M31. Utilizing optical line-flux density ratios, a presence or absence of ionising blue stars and optical morphology, they identified 178 SNR candidates, dividing them into three confidence categories. 14 large structures had superbubble characteristics seen in the Milky Way and Magellanic Clouds. Only 15 of their candidates had been found in previous searches.

The presence or absence of ionising blue stars in a resolved (> 4pc in Magnier et al. 1995) region of Hα emission is an interesting concept. Regions that do not contain any ionising blue stars must be ionized by some process (excluding photoionisation) and therefore such regions may be SNRs. If a disk-shaped region contained a bright star in the center, it would be a likely H II region. If a large disk or ring-shaped region contained no blue stars at all, regardless of the [S II] flux density, Magnier et al. (1995) judged it to be a good SNR candidate. A large disk that contained a single blue star which seemed unusually faint or highly offset from the center was also thought to be a potential SNR candidate.

The reason additional criteria are used by Magnier et al. (1995) is because, while the forbidden-line ratio test (e.g. [S II]:Hα) is useful to identify SNRs, it has drawbacks. Such problems include the facts that:

1. Balmer dominated SNRs do not have a high forbidden-line to permitted-line ratio;
2. the presence of O and B stars can deplete ionisation states, degrading the forbidden-line flux density;
3. stellar wind shocks in bubbles and H II regions can raise the forbidden-line flux density; and,
4. a wide range of [S II]:Hα ratios are observed for both H II regions and SNRs, giving a faint boundary between these two classes in some instances. This is because certain SNRs, including those that are

[3]This only included Ib and II SNe since Ia SNe, located in the bulge, were most likely outside of their field of view.

"Balmer" dominated, do not show high forbidden-line to permitted-line ratios. In addition, the presence of O and B stars can deplete ionization states and ratios, while stellar wind shocks in bubbles and H II regions can raise ratios.

Magnier et al. (1995) also give approximate lower-limit $\Sigma - D$ relationships for SNRs in different electromagnetic domains. These are written in log form with k values that represent scaling constants:

$$\log \Sigma_{\mathrm{H}\alpha} = -1.0 \log D + k_{\mathrm{H}\alpha} \tag{1}$$

$$\log \Sigma_{\mathrm{Radio}} = -1.5 \log D + k_{\mathrm{Radio}} \tag{2}$$

$$\log \Sigma_{\mathrm{X-ray}} = -4.0 \log D + k_{\mathrm{X-ray}}. \tag{3}$$

These equations imply that optical observations have a relative advantage for identifying large SNRs while X-ray observations have an advantage for observing the smallest SNRs. They note that optical SNR searches are currently the most efficient method to find extragalactic SNRs. This is because extinction is not large for external galaxies and, there are many 2-meter (or larger) optical telescopes with available observing time. Significant sensitivity limitations of both X-ray and radio also give the advantage to optical observations of extragalactic SNRs.

X-ray surveys of M31 include Supper et al. (1997) who found 17 *ROSAT* PSPC counterparts to previously identified SNRs and Magnier et al. (1995) with six distinct *ROSAT* HRI counterparts. The lower number of HRI detected SNRs reported by Magnier et al. (1995) is most likely because *ROSAT's* HRI detector had a lower sensitivity than the PSPC detector and their study covered a smaller portion of M31. In addition, the absence of detected X-ray energy from most optically identified SNRs may imply that the local ISM density is simply too low (< 0.1 cm^{-3}; Magnier et al. 1995).

SNRs embedded within a high density ISM have also been found. Kong et al. (2003) reported a SNR (Braun 101) in the center of the Andromeda galaxy at radio, X-ray and optical wavelengths. A more recent paper by Williams et al. (2004) notes that a total of five SNRs have been resolved by *Chandra* in an 37 ks X-ray image centered at the galaxy's nucleus. As deeper studies become available it is expected this number will rise rapidly.

M33

SNR studies in M33 have the advantage that this galaxy has a favorable tilt ($\sim 55^{\circ}$) and a disk that covers a small portion of the sky ($\sim$ 0.4 square degrees; Magnier et al. 1995). Since M33 is relatively close ($\sim$ 840 kpc), it has received a fair amount of attention beginning with the first SNR identification by S. D'Odorico in 1978. Further work by D'Odorico et al. (1980) raised the number to 19.

Long et al. (1990) discovered 30 emission nebulae within M33 they identify as SNRs based on strong [S II] emission. They used the prime focus CCD camera on the Kitt Peak Mayall 4-meter telescope to obtain images from 18 fields covering the central 15′. These candidates were confirmed as SNRs by later spectroscopic observations bringing the total number of SNRs in that galaxy to about 50. From this information, they estimated a SNe rate of one every 26–300 years and their sample follows a $N(< D) \propto D^{2.1}$ relation. Spectroscopic observations were performed using the Multiple Mirror Telescope (MMT) and the Red Channel long-slit CCD spectrograph over a two year period (Smith et al. 1993). Significant [O I] emission, another distinguishing characteristic of shocked gas, was observed in the majority of the remnants.

Duric et al. (1993) presented a radio atlas of optically identified SNRs in M33 using radio-continuum data obtained from the VLA and the Westerbork Synthesis Radio Telescope (WSRT) at 4.84 and 1.42 GHz. They reported the detection of 26 SNRs confirming previous radio detections of 9 sources. These SNRs ranged from a diameter of 10 pc to 100 pc with an average of 35 pc. This suggested most are similar in size to the Cygnus Loop. SNRs within M33 accounted for less than 5% of the integrated radio emission at 20 cm, allowing SNRs to be plausible sources for all cosmic rays within this galaxy. Their cumulative radio luminosity function, represented by a power law, S^{β}, showed the SNRs to have a power index of –0.8. The brightest radio SNR had a radio power much smaller than Cas A and they did not find a significant $\Sigma - D$ relation.

Studies by Gordon et al. (1999) also did not find any statistically significant SNR relationship between flux density and diameter. They used high-sensitivity maps at 20 and 6 cm with the VLA and WSRT to compile the largest ever sample of extragalactic radio supernova remnants. Fifty-three SNRs were confirmed through a combination of radio and optical techniques. They also found 26 non-thermal radio sources associated with H II regions, suspecting that many of them contained SNRs. The spectral index of SNRs associated with these regions tended to be flatter because of radio H II region contributions.

In this study, high quality optical Hα images were used to model thermal radio emission from H II regions. These were subtracted from non-thermal radio emission allowing flux densities from 14 of 19 SNRs to be

corrected. Gordon (1993) had used a similar technique to uncover an embedded remnant in the giant H II region NGC 592 found within M33.

Even though the SNR luminosity function showed no indication of a break other than that imposed by the flux density limit of their data, Gordon et al. (1999) were able to estimate the amount of cosmic-ray acceleration in M33. They reported the total radio emission from SNRs was approximately 2 to 3% of the total synchrotron emission from the galaxy. This value further supports the idea that SNRs are a primary source of cosmic-ray acceleration.

A new optical sample of SNRs in M33 was recently presented by Gordon et al. (1998). They identified 98 SNR candidates, of which 53 were previously unknown, using optical images obtained with the Kitt Peak 4-meter telescope and 4-in interference filters ([S II], Hα+ [N II] and 610.5 nm continuum). Using the MMT and Red Channel long-slit CCD spectrograph, they obtained spectra of 27 SNR candidates increasing the total number of spectra to 72; the largest sample in any galaxy. Only 39 of these optically selected SNRs have no radio counterpart. Gordon et al. (1998) calculated the integral number-diameter relation, assuming a minimum SNR diameter of 8 pc and a maximum of 35 pc, finding a slope of 2.0. This is consistent with most observed SNRs being in the Sedov-Taylor phase allowing them to derive a SNe rate of one every 360 years.

Gordon et al. (1998) used spectroscopic line ratios to explain the effects of evolution and abundance variation in their SNR sample. They found trends between line ratios and SNR diameters, suggesting the existence of an evolutionary trend. They also found a correlation between [N II]:Hα and galactocentric distance. This implied the existence of an abundance gradient.

Long et al. (1996) published one of the first major X-ray surveys of M33, using a 50.4 ks *ROSAT* PSPC image to identify 37 sources. Ten of these were coincident with previously known optical SNRs. They determined a hardness ratio for each of their sources and added 11 potential candidates using their spectral softness criteria[4].

A catalogue of 184 *ROSAT* X-ray sources within 50′ of the center of M33 was reported by Haberl & Pietsch (2001). They found 16 sources that coincided in position with known SNRs, although one was likely a foreground star and two others showed time variability[5] in their X-ray energies. 12 of the SNRs were detected in radio, optical and X-ray wavelength bands. They felt these results were consistent with a theoretical picture in which radio and X-ray emission is dependent on ambient gas density. Haberl & Pietsch (2001) named only 3 SNR candidates based on X-ray hardness; less than 11 candidates named by Duric

[4](H–S)/(H+S) < 0, with S representing counts in the 0.1–1.0 keV energy range and H in the 1.0–2.4 keV energy range.

[5]This is significant since SNRs are not variable objects.

(2000b). The reason for this is that a refined hardness ratio classification by Haberl & Pietsch (2001) allowed differentiation between supersoft sources, foreground stars and SNRs within the more general class of soft sources used by Duric (2000b).

Haberl & Pietsch (2001) compared the X-ray luminosity distribution of SNRs within M33 with those of the MCs, all normalized to a distance of $\sim$ 50 kpc. They found the ratio of faint to bright (relative to 1.9×10^{35}ergs s^{-1}) SNRs in the SMC (3.25) is different than the LMC (1.42). This may be due to higher metal abundances in the LMC, causing SNRs there to be brighter at *ROSAT* wavelengths. Previously reported metal abundances (as measured by the O abundance) in M33 are similar to those of the LMC (0.34 versus 0.5 solar at 15′ off-center, respectively). From this information, they estimate that there are 20 faint SNRs in M33 at 1.7×10^{36}ergs^{-1}. This is far below the luminosity of 10^{39}ergs^{-1} found for the diffuse X-ray emission of M33 by Schulman & Bregman (1995).

Using archival *Chandra* images of M33, Ghavamian et al. (2005) identified X-ray SNRs through comparison with candidates identified from elevated [S II]/Hα optical ratios and radio spectral indices. They also examined *XMM-Newton* data from M33. Of the 98 'known' optical SNRs in M33, they found 22 $> 3\sigma$ in the soft band (0.35–1.1 keV). They also identified one source with radio, but no optical emission, that may also be an X-ray SNR. Two soft X-ray sources suspected of being SNRs where found in the optical on cross-comparison suggesting that there may be 100 optical SNRs within M33. In total, the number of SNRs with X-ray emission in M33 may be as high as 37, when *XMM-Newton* observations are added.

ISM Density and SNR Evolution within M31 and M33

There are currently over 300 known SNRs in M31 and M33, an extensive set of data having important implications for the evolution of these remnants and their interaction with their local ISM. The study of these remnants help to shed important information about Galactic SNRs and their environments.

The evolution of SNRs can be framed in the context of a 'nature vs. nurture' debate (Duric 2000a). Is SNR evolution governed by initial conditions at birth or is it governed by the medium through which the SNR expands?

The ISM is not a simple entity and is strongly shaped by the SNR precursor itself. The strength of the stellar wind and the size of the cavity is a function of the mass of the progenitor star. The radiative signatures of SNRs are a function of the medium in which they evolve. The amount of optical line emission from shocked interstellar clouds, radio-continuum emission from accelerated cosmic ray electrons and X-ray emission from shock heated gas, all increase with a higher ambient gas density. This can be tested given the

large number of SNRs known to exist within these two galaxies alone. The interaction of the ISM with the SNR shock front is responsible for the electromagnetic emission we receive from these objects.

The shock thermalizes the expanding energy of the remnant. It increases the local density, temperature and turbulence of gas in the post-shock region and the density of cosmic rays. Shocks also increase local magnetic field strength through compression and turbulent amplification.

Estimates of metallicity are obtained for these galaxies by comparing metal line intensities relative to hydrogen. The [N II]:Hα line ratio is a common example that has been estimated for both M31 and M33. Using this ratio, Duric (2000a) notes that there is a metallicity drop of roughly 10% per kpc away from the center of each of these galaxies.

SNR X-ray emission depend on the blast energy (E_0) and the density of the ISM (n_e). Magnier et al. (1997) gives a dependence of surface brightness, Σ_χ, on these parameters as:

$$\Sigma_\chi \propto E_0^{1/2} n_e^{3/2} D^{-1/2}. \quad (4)$$

Magnier et al. (1997) suggested that the detection of only 6 *ROSAT* High Resolution Imager (HRI) SNRs in a portion of M31 containing 91 optically identified SNRs was due to intrinsic faintness at X-ray energies. They placed an upper density limit of 0.1 cm^{-3} on the ambient gas of those SNRs not detected in their X-ray surveys. This implies that optically identified SNRs are selected in regions of low density ISM. The [S II]/Hα search method is biased against denser H II or star forming regions.

Because of the dependence on higher ambient densities, X-ray SNRs correlate more closely with radio SNRs in both M33 and M31. Radio wavelengths may be a more sensitive probe of the ambient gas density than X-ray. This is because radio telescopes such as the VLA and ATCA have a relatively higher sensitivity than X-ray telescopes. Studies with *Chandra* and *XMM-Newton* may soon change this.

Ghavamian et al. (2005) has used X-ray luminosity separations between M33, SMC and LMC to suggest that this may be related to the ISM of these galaxies. This is in line with the idea that SNRs probe the ISM as they expand out. Higher luminosities of the LMC SNRs may be related to the particularly high metallicity of the ISM suspected there. By this line of reasoning, the progressively fainter luminosity distributions of M33 and the SMC may be caused by progressively lower metallicities.

M82

M82 is an irregular, almost edge-on galaxy located at a distance of 3.2 Mpc. This galaxy has been the

focus of several radio SNR studies in its starburst region. Unfortunately, there is also high visual extinction in the majority of the starburst regions preventing optical detection of SN or SNRs.

However, the radio SNR population of M82 is very interesting. In more recent times, Muxlow et al. (1994) used MERLIN (Multi-Element Radio-Linked Interferometer Network) at 5 GHz (6 cm) to image the central 700 pc finding more than 40 discrete sources. These were resolved by the MERLIN 50 mas beam confirming these sources to be primarily SNRs. Several of these SNRs show complete shells or structure consistent with partial shells. 23 of these objects follow a $\Sigma - D$ relation similar to that found in the LMC and our Galaxy (different from the slope discussed in section 1.10). These are compact remnants with diameters up to 3 pc which follow a linear $N(< D)$ relation. This linear relation implies that the remnants are still in their free expansion phase (diameter $\propto$ time). The authors estimate a 0.05 yr^{-1} supernova rate if the shells are expanding at 5000 km s^{-1}. Assuming this constant expansion rate, they felt that the average age for this group of remnants is about 200 years. This is expected since this is a starburst region.

Pedlar et al. (1999) used the European Very Long Baseline Interferometry (VLBI) Network (EVN) at 18 cm to study five of these compact remnants comparing them to previous studies. Four of the sources show shell type structures which, when combined with their lack of strong radio variability, non-thermal radio spectrum and small linear size, strongly supports their identification as young SNRs. Comparison of the structure of 43.31 + 592 in 1997 with earlier epoch EVN measurements taken in 1986 shows that the remnant is expanding at $\sim 10^4$ km s^{-1}. The most luminous remnant, 41.95 + 575, has a much lower expansion velocity of less than 4000 km s^{-1}. They speculate that it either originates from a very massive star, or is contained in a high density medium. Riley et al. (2004) used global VLBI observations in two epochs (1998 and 2001) to calculate expansion velocities of these two objects. They find that 41.95 + 575 and 43.31 + 592 have expansion velocities of 2500 ± 1200 km s^{-1} and 7350 ± 2100 km s^{-1}, respectively. Flux densities also decreased in line with expectations of 8.5% per year.

X-ray surveys of SNRs in M82 are relatively rare. Stevens et al. (1999) reported *ROSAT* HRI X-ray emission from two sources which co-identify with radio SN or young SNRs in M82. One of these is 41.95 + 575, the luminous remnant analyzed by Pedlar et al. (1999) and discussed above. The other X-ray source that co-identifies with radio source 44.01 + 596 is less certain as a radio SN and may represent an AGN.

Pedlar et al. (1999) note that it is clear that in M82, SN events are taking place in an environment different from both our Galaxy and the interstellar medium of many of the external galaxies in which radio SNe have been observed. The starburst regions contain large numbers of high-density molecular clouds. They argue that 43.31 + 592 may no longer be in free expansion. Equating the swept-up volume with an ejected mass of

$\sim 5\ M_{\odot}$, a guess, they infer a density of ~ 1000 atom cm^{-3}. A similar argument for 41.95 + 575 implies an ambient density of $> 10^4$ atom cm^{-3}.

Pedlar et al. (1999) also make a valid point about the classic distinction usually drawn between radio SNe and radio SNRs. Classically, the former are characterized by the interaction of the SN shock wave with the circumstellar medium and the latter occur when the shock wave interacts with the ISM. This somewhat simplistic distinction between radio SNe and radio SNRs is becoming less clear and several extragalactic radio SNe have been found to have flux density decay times measured in decades rather than years. Interactions with a dense circumstellar medium may allow these objects to miss the adiabatic Sedov-Taylor phase altogether. One of the reasons that radio observations of these compact objects in M82 is so important is because up to this point, there has been little observational information about the radio properties of SNe events with ages between a few decades and several hundred years[6].

M82 was also studied by MERLIN at 408 MHz. This study by Wills et al. (1997) used images of the central starburst region detecting 20 SNRs at this frequency. They felt the lower number of SNRs found as compared to the 6 cm images was due to a difference in free-free absorption by ionized gas. In fact, seven of their SNRs showed low-frequency turnovers in their spectra consistent with free-free absorption. The remaining 14 remnants showed no evidence of a low-frequency turnover.

Wills et al. (1997) found a mean optically thin spectral index of –0.6 for the remnants detected at 408 MHz. They calculated emission measures[7] for these remnants and previous groups detected at higher frequencies. Their remnants have emission measures an order of magnitude smaller than previous groups. If it is assumed that the ionized gas distribution in these regions are approximately uniform, this means that the 408 MHz SNRs are embedded towards the near side of the entire distribution of radio SNRs found within M82.

Observations were also made by McDonald et al. (2002) using the Very Large Array (VLA) in its 'A' configuration at 15 GHz and MERLIN at 5 GHz, enabling a spectral analysis of the compact radio structure on a scale of < 1.6 arcsec. Inclusion of the Pie Town Very Long Baseline Array antenna increased the

[6]For example, the luminous radio source J1228+441 in NGC 4449 has been cited as a rare chance to study an object between the oldest known radio SN (1923A in M83) and Cas A, thought to be ~ 330 years old (Lacey et al. 2007). In that paper, they discuss the radio light curves and spectral index variations of J1228+441 over a 30 year period. J1228+441 is one of the few known intermediate-age SNRs, with an age between a range of 60 to 200 years.

[7]Without getting into the formulas for this which can be readily referenced in Wills et al. (1997), one can think of the emission measure as directly proportional to the free-free optical depth. Hence, the smaller the optical depth as it approaches zero, the thinner the medium.

resolution of the VLA observations by a factor of two. They brought the total number of compact sources in M82 to at least 61 in the central region. 30 of these are SN related, 16 are H II regions and 15 (14 of which are most likely older SNRs) have yet to be identified. Of 15 newly identified H II regions, all have steep 'inverted' spectra which implies that these sources become optically thick between 5 and 15 GHz. Five of the above sources represent additional SNRs, identified by their steep, negative spectral indices at higher frequencies. At lower frequencies, these objects experience a turnover in their spectra near 1.4 GHz, requiring emission measures in the foreground ionized gas of $\sim 10^7$ cm^{-6} pc in order to be seen at these wavelengths. However, since these remnants are obscured at lower radio frequencies, they may represent those SNRs embedded deeper within M82 and hence behind a greater amount of ionized gas.

Greenhouse et al. (1997) used [Fe II] 1.644 μm Fabry-Perot imaging observations of M82 to trace a population of SNR substantially older than those found at 6 cm by Muxlow et al. (1994). Six [Fe II] compact sources are included in this list that spans at least a factor of 2 in size and a factor of 10–20 in age. The size contrast between the [Fe II] and the 6 cm remnants in M82 is similar to that exhibited by the Cygnus Loop (age $\sim$ 5000 years) and Cas A (age $\sim$ 300 years).

Although there is a scarcity of optical SNR observations within M82, De Grus et al. (2000) found 10 compact Hα sources in a poststarburst region northeast of the center of this galaxy. These objects have Hα luminosities and sizes consistent with Type II SNRs. These are some of the first candidates for optically visible SNRs in M82 outside the heavily obscured central starburst. A region farther from the core was also examined and found to lack any SNR candidates suggesting that star formation in the galaxy has propagated inward toward the present day starburst core. Observations of these sources to obtain [S II] to Hα ratios are needed.

Seaquist & Stanković (2007) present an alternative hypothesis for the origin of the compact non-thermal radio (CNRs) sources discussed above. They claim most may be wind-driven bubbles (WDB) associated with very young super star clusters. The motivation for this is the low amount of variability in the radio sample that implies an SNR age > 1000 years and their small size (diameters up to 4 pc) suggesting an age of only a few hundred years. In the new scenario, the strong wind from a young cluster energizes a hot expanding bubble, which sweeps ISM to form a thin and dense radiative shell. The mechanism for non-thermal emission from accelerated relativistic electrons would be similar for that occurring at the SNR shock, making some aspects of this model indistinguishable. They use known parameters to predict shell mass and age, suggesting the WDB hypothesis appears to be a plausible alternative to the SNR picture. Future observations, especially in the infrared, in order to associate young clusters with these CNRs may answer puzzles about the radio

population of M82. This may include the steep slope (β) found in the $\Sigma - D$ relation by Urošević et al. (2005).

Other Nearby Spiral Galaxies

There are numerous other spiral galaxies that have been the focus of extragalactic SNR studies. Only a few of the most important surveys can be mentioned here.

Matonick & Fesen (1997) presented results of an optical search for SNRs in the spiral galaxies NGC 5204 (3 SNRs), NGC 5585 (5 SNRs), NGC 6946 (27 SNRs), M81 (41 SNRs) and M101 (93 SNRs). Their 1993 and 1994 observations resulted in interference-filter images created with the 1.3-meter McGraw-Hill telescope at the Michigan-Dartmouth-MIT (MDM) observatory. After the inclusion of 35 SNRs within NGC 2403 (Matonick et al. 1997), they doubled the number of galaxies searched and increased the number of known extragalactic SNRs by about 50%. Since none of their SNRs were found inside H II regions and their criteria biased against detecting large, faint SNRs, there may be 4 times as many SNRs in each of these target galaxies. A spatial distribution analysis of detected SNRs in NGC 2403, M81 and M101, indicated strong associations with star-forming regions. This suggested a significant fraction were the result of SNe II or Ib/c explosions. Thirty one SNRs had estimated diameters greater than 100 pc, larger than possible for a single SNR within a ISM density of 0.1 to 1.0 cm^{-3}. These objects are most likely combinations of multiple SNRs and massive stellar winds.

The method used by Matonick & Fesen (1997) to select their sample of SNRs was rather unique. First, they selected a sample of objects for follow-up spectroscopy by blinking continuum-subtracted [S II] and Hα images, searching for nebulae as bright or brighter in [S II] as in Hα. Spectra of 39 such nebulae were obtained using the 2.4-meter Hiltner telescope at MDM with the MK III spectrograph. Next, they constructed 'difference' images of the original datasets by subtracting 0.4 times the Hα flux densities from the [S II] flux densities, setting any negative pixels to zero. This image was used to find SNRs. Measurements of total flux density from each SNR candidate with corrections using data obtained from the known 39 measured spectra allowed final determination of [S II]/Hα ratios.

NGC 7793 is a almost face-on ($i = 53.7$ deg) Sd galaxy whose overall spiral pattern is nearly lost in a general confusion of H II regions and star formation. Its distance of about 3.38 Mpc corresponds to a linear distance of about 16.5 pc $arcsec^{-1}$. Read & Pietsch (1999) reported the results of *ROSAT* PSPC spectral imaging observations of NGC 7793. These consisted of two separate observations about six months apart with a total observation time of 23.8 ks. This study found seven sources within the optical confines of NGC 7793, two of which are probable SNRs including Blair & Long (1997) 7793–S26. They analysed these by

creating hardness ratios and spectral models[8]. Since the observations were separated by six months, source variability was also determined.

Pannuti et al. (2002) also performed a multi-wavelength study of NGC 7793, again using VLA observations at the 6 and 20 cm wavelength, optical studies by Blair & Long (1997) and *ROSAT* observations reported by Read & Pietsch (1999). An Hα image of the galaxy created with the 1.5-meter telescope at the Cerro tololo Inter-American Observatory was also used. Pannuti et al. (2002) cross-referenced H II regions to Hodge (1969); a large study in which NGC 7793 was but one of twenty galaxies that had its H II region population surveyed and catalogued for future purposes.

Pannuti et al. (2002) found that N7793-S26 was the only optically identified SNR having both X-ray and non-thermal radio emission. The extreme radio luminosity of N7793-S26 and its large filamentary structure suggested that it was created by multiple SNe. Another optically identified SNR, N7793-S11, was found to have some radio emission. Their search for non-thermal radio sources (3σ or above) close to or within H II regions yielded five additional candidate radio SNRs. One of these also had an X-ray counterpart. A X-ray image search for candidate SNRs did not reveal any new sources other than those found by radio and optical methods. This was most likely due to the presence of considerable diffuse X-ray emission throughout the entire disk of NGC 7793. Compared to results obtained from NGC 300, only the most luminous X-ray and radio SNR populations of NGC 7793 could be sampled.

Schlegel & Pannuti (2003) studied X-ray sources in NGC 2403 using *Chandra* data. They also analysed *Einstein*, *ROSAT* and *ASCA* observations of this galaxy to search for time variability from the detected sources. Only one of the 35 optically identified SNRs was clearly associated with an X-ray source. Three other optically identified SNRs may also have X-ray counterparts and so can be considered candidate X-ray SNRs. A search for X-ray counterparts to candidate radio sources (2) reported by Turner & Ho (1994) yielded a coincidence with only one, TH-2.

Kaufman et al. (1987) studied 42 giant H II regions in M81 using Hα and VLA (6 and 20 cm) radio continuum observations. They found five sources containing significant non-thermal radio contributions suspected to represent SNRs, possibly embedded within OB associations. Preliminary [S II]/Hα analysis of two of these potential SNRs (No. 138 and 198) further support the idea that they may be embedded.

Chandra X-ray observations of M81 found a total of 177 sources to a limiting luminosity of $\sim 3 \times 10^{36}$ergs s^{-1} as reported by Swartz et al. (2003). They find five SNRs coincident with optical ones found by Matonick & Fesen (1997). This included X6, a highly luminous X-ray source first discovered by *Einstein*.

[8]These included power law, thermal bremsstrahlung, blackbody and Raymond-Smith hot plasma models.

According to Swartz et al. (2003), the X-ray emission from X6 is from a $\sim 18 M_{\odot}$ object accreting near its Eddington limit and not a SNR. All four remaining candidates are located along spiral arms, each suspected to be the product of SNe resulting from the core-collapse of young massive stars. Swartz et al. (2003) also observed SN 1993J, which at an age of 2594 days, displayed a complex thermal spectrum from a reverse shock rich in Fe-L and highly ionized Mg, Si and S but lacking O. This very young SNR has a hard X-ray component thought to be emitted from its forward shock.

Pence et al. (2001) used 98.2 ks *Chandra* observations to find 12 X-ray detections coincident with optical SNRs within M101. Their field of view contains at least 54 optical SNRs. They report that two of these 'SNR' sources were variable and hence actually represent compact objects.

This galaxy was also thought to host five hypernova remnants (HNRs) defined as luminous discrete X-ray sources with SNR counterparts. These were first reported by Wang (1999) based on a 230 ks *ROSAT* HRI image of M101. He inferred a blast-wave energy of 3×10^{52} ergs for SNR NGC 5471B and 3×10^{53} ergs for SNR MF 83. Hypernovae are a factor ≥ 10 more energetic than canonical SNe and are postulated as being responsible for gamma-ray bursts observed at cosmological distances. The superior spatial resolution and astrometry of *Chandra* has now shown that two of these X-ray sources are not directly coincident with SNRs. MF 83 shows temporal variability indicating it may be an accreting X-ray binary (Snowden et al. 2001). The two remaining HNR candidates were within the field of view of *XMM-Newton* observations presented by Jenkins et al. (2004). They find no evidence to support the HNR scenario although they find no conclusive evidence to rule out NGC 5471B as a HNR.

Lacey et al. (1997) used the VLA to survey NGC 6946 at 6 and 20 cm, identifying 118 compact radio sources. Using spectral index, they reported 37 non-thermal candidate sources as possible SNRs or background sources. Their 2″ resolution images were later analysed by Hyman et al. (2000). They found 15 SNR candidates based on non-thermal spectral indexes with $\alpha < -0.4$, five of which identified with Hα maps created by Van Dyk (1992) using the Kitt Peak 0.9-meter telescope. Their SNR candidate luminosity function (the number distribution of luminosities) has a very steep slope (–1.7 and –2.2 at 6 and 20 cm, respectively) when compared to other extragalactic studies (–0.9 for M31). This may be due to selection effects because of distance. This steep luminosity function index can only be tentative until confirmed by deeper studies.

Lacey & Duric (2001) examined their own sample of candidate radio SNRs in NGC 6946, comparing them with a sample of 27 optical SNRs from Matonick & Fesen (1997). The radio-selected population was found to lie predominately on the spiral arms, while the optical SNRs were found primarily in the interarm regions. Utilizing the properties of these radio-selected SNRs, they conclude that because of the

richer environments of the arm regions, it is the Type II/Ib/Ic (population I) SNRs that are dominant in the production of cosmic rays, by the process of DSA.

At least six SNe have been seen within NGC 6946 during the past 85 years, a number that is rivaled only by M83. In 1994, William Blair and Robert Fesen reported an extraordinarily bright optical SNR within the error circle of a bright *ROSAT* source. This object, listed as No. 16 in Matonick & Fesen (1997) is also a powerful VLA radio source, several times brighter than Cas A. This suggests an interaction of the SNR with a dense ISM or CSM.

Blair et al. (2001) presented *Hubble Space Telescope* (*HST*) narrow-passband Hα and [S II] images of this region suggesting possible scenarios to explain this luminous source. They find two and possibly three loops near massive OB stars suggesting that multiple supernova explosions occurred in relatively close temporal and spatial proximity. Their interpretation of the elliptical [O III] ring is that an older SNR resides in a cavity that was created by its precursor star. This SNR expanded rapidly, depositing its energy only after reaching the cavity wall. In this way, a moderate size (20×30 pc) could be accounted for by an SNR only a few thousand years old. This is much younger than one would estimate from a Sedov-Taylor model ($\sim 25,000$ years) of this remnant. The smaller loop is felt to be a SNR that was formed only a few thousand years after the older one. This is one example of how new observations are explained from previous ones and current SNR theory.

Although not a spiral galaxy, I also include a recent study by Kong et al. (2004) of a SNR (Ho 12) in the nearby (500 kpc) dwarf irregular galaxy NGC 6822. This object was previously observed at X-ray, optical and radio frequencies, but *Chandra* and ground-based data allowed it to be spatially resolved in all three. This SNR is a shell-shaped object with a diameter of about 10″. Kong et al. (2004) was able to fit the *Chandra* spectrum with a nonequilibrium ionisation model with an electron temperature of 2.8 keV. They also calculate an approximate age between 1,700 and 5,800 years.

This concludes my discussion of extragalactic SNR research. As a summary, Table 3 details the current state of SNR radio and X-ray observations.

Table 3 Selected overview of SNR searches with radio and X-ray emission. Candidate SNRs (cSNRs) are specified where possible. (HNR = hypernova remnant)

Galaxy	Radio SNRs & Reference	X-ray SNRs & Reference
LMC	12 SNRs, Mathewson & Clarke (1972, 1973a,b)	6 SNRs, 25 cSNRs, Long et al. (1981)
	34 SNRs, 24 cSNRs, Filipović et al. (1998b)	38 SNRs, 8 cSNRs, Haberl & Pietsch (1999)
SMC	2 SNRs, Mathewson & Clarke (1972, 1973a,b)	1 SNR, 4 cSNRs, Seward & Mitchell (1981)
	10 SNRs, 2 cSNRs, Filipović et al. (1998b)	17 SNRs, 2 cSNRs, Haberl et al. (2000)
M31	24 SNRs, Braun & Walterbos (1993)	6 SNRs, Magnier et al. (1995)
		17 SNRs, Supper et al. (1997)
		5 SNRs, Williams et al. (2004)
M33	26 SNRs, Duric et al. (1993)	10 SNRs, 11 cSNRs, Long et al. (1996)
	53 SNRs, Gordon et al. (1999)	13 SNRs, 3 cSNRs, Haberl & Pietsch (2001)
		37 SNRs, Ghavamian et al. (2005)
NGC 300	3 SNRs, 14 cSNRs, Pannuti et al. (2000)	2 cSNRs, Pannuti et al. (2000)
		3 SNRs, 3 cSNRs, Read & Pietsch (2001)
NGC 7793	2 SNRs, 5 cSNRs, Pannuti et al. (2002)	1 SNR, 1 cSNR, Read & Pietsch (1999)
M81	5 cSNRs, Kaufman et al. (1987)	5 SNRs, Swartz et al. (2003)
M82	30 SNRs, 14cSNRs, McDonald et al. (2002)	
NGC 5204	2 cSNRs, Turner & Ho (1994)	1 SNR, 3 cSNRs, Schlegel & Pannuti (2003)
M101		10 SNRs, Pence et al. (2001)
		5 HNRs, Wang (1999) (4 disputed)
NGC 6946	15 cSNRs, Hyman et al. (2000)	1 SNR, Blair et al. (2001)
NGC 6822	1 SNR, Kong et al. (2004)	1 SNR, Kong et al. (2004)
IC 1613	1 SNR, Dickel et al. (1985)	